

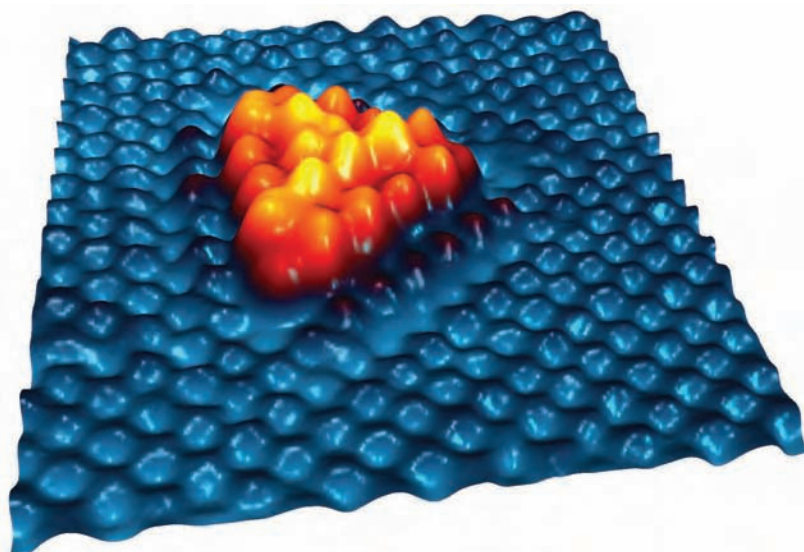


FACULTY OF SCIENCE
UNIVERSITY OF AARHUS

Atomic-scale investigation of MoS₂-based hydrotreating model catalysts

A scanning tunneling microscopy study

PhD Thesis



JAKOB KIBSGAARD



Interdisciplinary Nanoscience Center (iNANO),
and Department of Physics and Astronomy, 2008

**Atomic-scale investigation of
MoS₂-based hydrotreating
model catalysts**

A scanning tunneling microscopy study

JAKOB KIBSGAARD

Interdisciplinary Nanoscience Center (iNANO) and
Department of Physics and Astronomy
University of Aarhus, Denmark

PhD thesis
July 2008

This thesis has been submitted to the Faculty of Science at the University of Aarhus in order to fulfil the requirements for obtaining a PhD degree in physics and nanoscience. The work has been carried out under the supervision of Professor Flemming Besenbacher and Associate Professor Jeppe Vang Lauritsen at the Interdisciplinary Nanoscience Center (iNANO) and the Department of Physics and Astronomy.

2nd edition with minor corrections

—
This document was typeset and compiled in L^AT_EX

April 24, 2009

Contents

List of publications	vii
List of abbreviations	ix
1 Introduction	1
1.1 Introduction	2
1.2 Heterogeneous catalysis	2
1.2.1 Surface science approach	4
1.3 Hydrotreating	6
1.3.1 Hydrodesulfurization	8
1.4 Outline of thesis	9
2 Methods	11
2.1 Scanning tunneling microscopy	12
2.1.1 The principle of STM	12
2.1.2 The Aarhus STM	12
2.1.3 Theory of STM	15
2.1.4 Scanning tunneling spectroscopy	19
2.2 Density functional theory	21
2.2.1 Basic equations in DFT	21
3 A hydrotreating model catalyst	25
3.1 Introduction	26
3.2 The model support	26
3.2.1 The Au(111) surface	27
3.3 Synthesis of MoS ₂ nanoclusters	29
3.4 Crystal structure of MoS ₂	30
3.5 Non-promoted MoS ₂ nanoclusters	30
3.5.1 Morphology of non-promoted MoS ₂ nanoclusters	32
3.5.2 Edge structure of MoS ₂ nanoclusters	33

4	Size-dependent structure of MoS₂ nanoclusters	35
4.1	Introduction	36
4.2	Experimental details	36
4.3	“Magic” sized MoS ₂ nanoclusters	36
4.4	Size-dependent atomic-scale structure	37
4.4.1	(10 $\bar{1}$ 0) Mo edge terminated clusters	37
4.4.2	($\bar{1}$ 010) S edge terminated clusters	40
4.5	Origin of the size effect	41
4.6	Implications for catalysis	42
4.6.1	Sulfur vacancies	43
4.7	Conclusion	46
5	Promoter atoms	47
5.1	Introduction	48
5.2	Experimental details	49
5.3	Characterization of CoMoS and NiMoS	50
5.4	CoMoS	52
5.4.1	Promotional effect of Co	56
5.5	NiMoS	56
5.5.1	NiMoS Type A	58
5.5.2	NiMoS Type B	61
5.6	Comparison with X-ray absorption results	66
5.7	Promoter-dependent (Fe, Co, Ni, and Cu) shape of MoS ₂ nanoclusters	68
5.8	Conclusion	71
6	Support effects	75
6.1	Introduction	76
6.2	Graphite support	76
6.2.1	HOPG surface	77
6.2.2	Experimental details	77
6.2.3	Morphology of graphite-supported MoS ₂ nanoclusters	79
6.2.4	Single-layer MoS ₂ nanoclusters	81
6.2.5	Multi-layer MoS ₂ nanoclusters	85
6.2.6	Atomic-scale structure of multi-layer MoS ₂ edges	87
6.3	TiO ₂ support	90
6.3.1	Rutile TiO ₂	91
6.3.2	Experimental details	91
6.3.3	Morphology of TiO ₂ (110)-supported MoS ₂ nanoplatelets	94
6.3.4	Support-controlled growth of MoS ₂ nanoplatelets	96
6.4	Conclusion	100

7	Mo₆S₆ nanowires	101
7.1	Introduction	102
7.2	Experimental details	102
7.3	Morphology of Mo ₆ S ₆ nanowires	103
7.4	Preference for trimers	104
7.5	Atomic-scale structure of Mo ₆ S ₆ nanowires	105
7.6	Electronic structure of Mo ₆ S ₆ nanowires	109
7.7	Conclusion	110
8	Sulfidation of Co nanoparticles	111
8.1	Introduction	112
8.1.1	Historic background of Fischer-Tropsch synthesis	112
8.1.2	Chemistry of Fischer-Tropsch synthesis	113
8.2	Experimental details	114
8.3	Phase identification	114
8.4	Formation of Co sulfide	116
8.5	Diffusion Co _n S _m complexes	118
8.5.1	Quench-and-look experiments	120
8.6	Structure of cobalt sulfide	121
8.7	Conclusion	123
9	Summary and outlook	125
10	Dansk resumé	129
	Acknowledgements	135
	Bibliography	137

List of publications

- [I] *Cluster-Support Interactions and Morphology of MoS₂ Nanoclusters in a Graphite-Supported Hydrotreating Model Catalyst*
J. Kibsgaard, J. V. Lauritsen, E. Lægsgaard, B. S. Clausen, H. Topsøe, and F. Besenbacher, *Journal of the American Chemical Society* **128**, 13950-13958 (2006).
- [II] *Size-dependent structure of MoS₂ nanocrystals*
J. V. Lauritsen, J. Kibsgaard, S. Helveg, H. Topsøe, B. S. Clausen, E. Lægsgaard, and F. Besenbacher, *Nature Nanotechnology* **2**, 53-58 (2007).
- [III] *Cobalt Growth on Two Related Close-packed Noble Metal Surfaces*
K. Morgenstern, J. Kibsgaard, J. V. Lauritsen, E. Lægsgaard, and F. Besenbacher, *Surface Science* **601**, 1967-1972 (2007).
- [IV] *Location and coordination of promoter atoms in Co- and Ni-promoted MoS₂-based hydrotreating catalysts*
J. V. Lauritsen, J. Kibsgaard, P. G. Moses, B. Hinnemann, J. K. Nørskov, B. S. Clausen, H. Topsøe, E. Lægsgaard, and F. Besenbacher, *Journal of Catalysis* **249**, 220-233 (2007).
- [V] *Recent STM, DFT and HAADF-STEM studies of sulfide-based hydrotreating catalysts: Insight into mechanistic, structural and particle size effects*
F. Besenbacher, M. Brorson, B. S. Clausen, S. Helveg, B. Hinnemann, J. Kibsgaard, J. V. Lauritsen, P. G. Moses, J. K. Nørskov, and H. Topsøe, *Catalysis Today* **130**, 86-96 (2008).
- [VI] *Restructuring of Cobalt Nanoparticles Induced by Formation and Diffusion of Monodisperse Metal-Sulfur Complexes*
J. Kibsgaard, K. Morgenstern, J. V. Lauritsen, E. Lægsgaard, and F. Besenbacher, *Physical Review Letters* **100**, 116104 (2008).
- [VII] *Atomic-scale structure of Mo₆S₆ nanowires*
J. Kibsgaard, A. K. Tuxen, M. Levisen, E. Lægsgaard, S. Gemming, G. Seifert, J. V. Lauritsen, and F. Besenbacher, Submitted

- [VIII] *Promoter-dependent (Fe, Co, Ni, and Cu) structure of MoS₂ nanocrystals*
J. Kibsgaard, A. K. Tuxen, E. Lægsgaard, B. S. Clausen, H. Topsøe, J. V. Lauritsen, and F. Besenbacher, In Preparation
- [IX] *Scanning tunneling microscopy studies of TiO₂-supported hydrotreating catalysts: Anisotropic particle shapes by edge-specific MoS₂-support bonding*
J. Kibsgaard, A. K. Tuxen, E. Lægsgaard, B. S. Clausen, H. Topsøe, J. V. Lauritsen, and F. Besenbacher, In Preparation

List of abbreviations

AES	Auger Electron Spectroscopy
AFM	Atomic Force Microscopy/Microscope
DDS	Direct Desulfurization
DFT	Density Functional Theory
DOS	Density Of States
EXAFS	Extended X-ray Absorption Fine Structure
fcc	face-centered cubic
GGA	Generalized Gradient Approximation
hcp	hexagonally close-packed
HDM	Hydrodemetallization
HDN	Hydrodenitrogenation
HDO	Hydrodeoxygenation
HDS	Hydrodesulfurization
HYD	Hydrogenation
IRAS	Infrared Absorption Spectroscopy
LDA	Local Density Approximation
LDOS	Local Density Of States
ML	Monolayer
PEC	Photoemission Spectroscopy
STM	Scanning Tunneling Microscopy/Microscope
SPM	Scanning Probe Microscopy
TEM	Transmission Electron Microscope
UHV	Ultra High Vacuum
XAS	X-ray Absorption Spectroscopy
XAFS	X-ray Absorption Fine Structure
XANES	X-ray Absorption Near Edge Structure
XDS	X-ray Diffraction Spectroscopy
XPS	X-ray Photoelectron Spectroscopy
XRD	X-ray Diffraction

CHAPTER 1

Introduction

The aim of this introductory chapter is to motivate the work presented in this thesis. First a general introduction to catalysis and in particular the surface science approach to catalysis is given. This general introduction is followed by a more detailed description of the hydrotreating process.

1.1 Introduction

Catalysis is one of the fundamental pillars of modern society. In fact, without the production of ammonia from the catalytic Haber-Bosch process, it is estimated that the global food production would only be able to sustain about half of the current world population [1]. The Haber-Bosch process is thus by many considered to be among the most, if not the most, important invention of the 20th century, and both Fritz Haber and Carl Bosch were awarded the Nobel prize for their development of the process [2, 3].

Today, catalysis really is the workhorse in the chemical industry with approximately $\sim 90\%$ of the products produced in catalytic processes [4]. The vital impact of catalysis is perhaps best illustrated by the fact that products manufactured through catalysis account for $\sim 10\text{-}15\%$ of the gross national product of industrialized countries [5, 6]. More recently environmental concerns have driven the development of specialized catalysts to prevent polluting substances from being released into the environment, with the three-way car exhaust catalyst as probably the most renowned example. The main topic of this thesis is concerned with another highly important environmental catalyst; the hydrotreating catalyst. This type of catalyst is employed to upgrade and clean-up fossil fuels and will be introduced in more detail after a general introduction to heterogeneous catalysis.

1.2 Heterogeneous catalysis

The vast majority of industrial catalytic processes are catalyzed heterogeneously, that is, the catalyst is in a different phase than the reactants and products, and in most cases the catalyst is a solid and the reactants and products are either in the gas or liquid phase. By definition a catalyst is [7]:

a substance that increases the rate of a reaction without modifying the overall standard Gibbs energy change in the reaction; the process is called catalysis.

The capability of a catalyst to increase the reaction rate is of enormous technological importance since for many chemical reactions, the reaction rate is essentially zero even under conditions where the reaction is thermodynamically favorable. This is caused by a large activation energy associated with the formation of an intermediate or the final product. The catalyst offers an alternative reaction pathway that is energetically more favorable, though more complex to describe, compared to the reaction without the catalyst. The overall process can typically be divided into a number of elementary steps, such as adsorption of the reactants on the catalyst, breaking or weakening of adsorbate bonds, adsorbate diffusion, reaction to form products, and finally desorption of the products, which leaves the catalyst unaltered and ready for a new reaction cycle (see Fig. 1.1). The activation barriers of the separate steps in the catalyzed reaction are all (significantly) lower than the activation barrier for the uncatalyzed reaction, which is the reason for the much higher reaction rate of the catalyzed reaction. The catalyst,

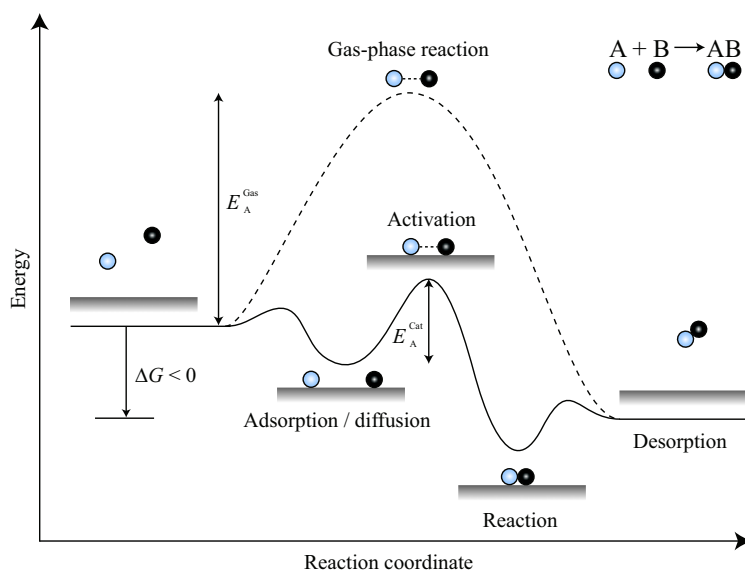


Figure 1.1. Illustration of the elementary steps in a heterogeneous catalytic process. The uncatalyzed reaction is highly activated (dashed line). The alternative reaction pathway offered by the catalytic surface involves more steps, but the barrier of each elementary step is lower than the barrier of the uncatalyzed reaction.

according to definition, does not alter the thermodynamics, i.e. the overall change in Gibbs free energy, ΔG , is the same for both the catalyzed and uncatalyzed reaction pathways. The equilibrium constant is thus unaffected by the catalyst (Fig. 1.1).

The key to understand heterogeneous catalytic processes is the surface of the active catalytic material since the chemical transformation takes place here. Consequently, the reactivity of a catalyst scales directly with the number of exposed active sites at the surface. Furthermore, catalysts often consist of precious metals, and accordingly it is advantageous to disperse the catalytic active material as nanoparticles not only to maximize the number of active sites but also to keep the manufacturing cost of the catalyst low. Hence, in the technical catalyst the active catalytic material is dispersed as nanoparticles onto high surface area supports (100-1000 m²/g), such as alumina, silica, or carbon.

The quest for new catalytic materials and improvement of existing ones has to a large extent rested on costly explorative *trial-and-error* experiments. Consequently, catalysts have often only been characterized in terms of reactivity, selectivity, and stability, and only very little is known about the atomic-scale structure and working principle of catalysts. However, with the recent development of new and more powerful catalyst characterization tools, it has become possible to study catalysis on a fundamental level [5, 6].

1.2.1 Surface science approach

Especially the field of surface science has contributed immensely to the understanding of elementary processes in heterogeneous catalysis. The “surface science approach” to catalysis rests on studies of well-characterized model systems. The high complexity of the technical catalyst is thus stepwise broken down to simplified problems that can be addressed in controlled surface science experiments. The typical approach has been to use idealized single-crystal surfaces kept under ultra-high vacuum (UHV) conditions as a simple model catalyst and investigate their interaction with gas molecules. Such model system studies have provided a tremendous amount of detailed information on a number of different catalytic systems. The most prominent example is the ammonia synthesis through the Haber-Bosch process on an iron-based catalyst. Surface science studies have essentially solved the mechanism of this extremely important catalytic process [5], not least through contributions from Gerhard Ertl, who received the Nobel prize in 2007 for “his studies of chemical processes on solid surfaces” [8].

Though the surface science approach has generated valuable information, two significant gaps are, however, readily identified between the model systems and the real complex technical catalyst. These two gaps are termed the *pressure gap* and *materials gap*, respectively.

The pressure gap is concerned with the enormous difference between UHV compatible pressures ($\leq 10^{-6}$ mbar), which is required for most surface science techniques to be functional, and the typical industrial operating conditions (1-100 bar). The high coverage structures formed at high gas pressures and high temperatures are typically sought mimicked in the low-pressure surface science environment by performing the experiments at low temperature. This approach may, however, lead to kinetic restrictions and other effects different from the industrial conditions.

Significant progress has been made over the past two decades in the development of *in-situ* surface characterization techniques that are capable of bridging the pressure gap. The majority of *in-situ* characterization tools are based on optical principles, e.g. X-ray diffraction spectroscopy (XDS) [9], X-ray absorption spectroscopy (XAS) [10], and photoemission spectroscopy (PES) [11] since electron-based techniques suffer from a low mean-free path of the electrons in a high-pressure environment. Despite the problematic nature of electron-based techniques outside a UHV environment, an environmental transmission electron microscope (ETEM), which is capable of operating at pressures of about 20 mbar and temperatures of about 900°C, has recently been developed at the Haldor Topsøe A/S research laboratories [12]. The ETM technique has successfully been used to follow a reversible reshaping of supported Cu particles induced by pressure gaps [13] and the growth of carbon whiskers on Ni particles in real time [14].

The materials gap is concerned with the disproportion between the technical catalyst, consisting typically of nanometer-sized particles on a highly porous support material, and corresponding model system, e.g. a single-crystal surface. The small size of the catalytic particles increases the density of defects sites, such as steps and kinks, and since the adsorbate interaction with defects often is very different from the interaction found on large flat single-crystal terraces, the model system may not adequately describe the technical catalyst. Furthermore, reducing the dimensions of a material to the nanoscale

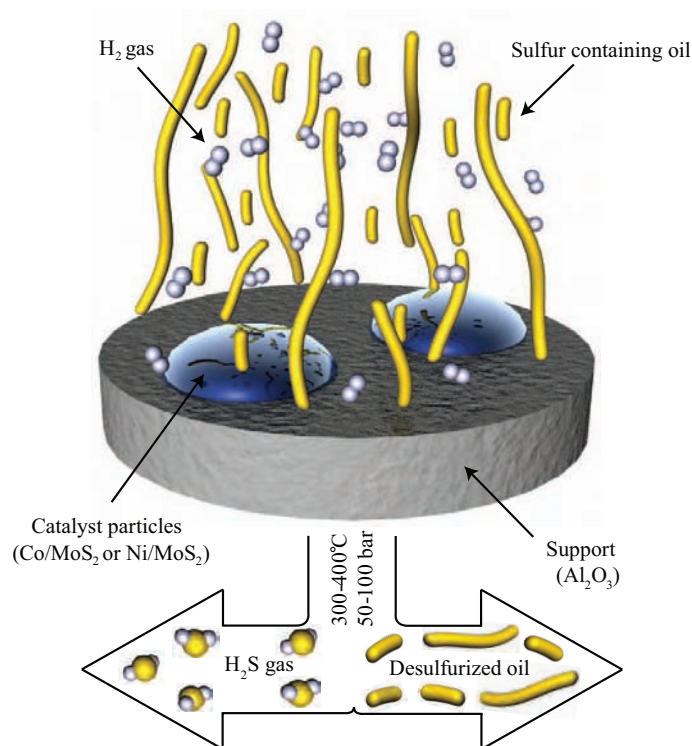


Figure 1.2. Illustration of the hydrodesulfurization process. The sulfur impurities, contained in the hydrocarbon molecules, are removed by trickling a mixture of crude oil and hydrogen gas through a porous support impregnated with the active catalytic particles.

may cause the material to behave quite differently compared to the material on macroscopic dimensions. An excellent example is gold nanoparticles. Whereas bulk gold is noble and notoriously inert, TiO₂-supported gold nanoparticles are capable of oxidizing CO even at low temperatures [15, 16]. Hence, to bridge the materials gap it is desirable to investigate model systems consisting of small particles on flat supports [16–18].

Model systems of supported nanoparticles are, however, a challenge to investigate since most surface science techniques based on diffraction or spectroscopy are averaging techniques. Consequently, these techniques only offer limited information about individual nanoclusters, and crucial information about the catalytical significance, e.g. of defects, is thus typically lost. Scanning probe techniques, such as the scanning tunneling microscope (STM) and the atomic force microscope (AFM), thus stand out as indispensable tools to investigate catalytic nanoparticles due to their unique capability of obtaining real space images with atomic resolution on a localized region of a surface. Especially the exceptionally high resolution of STM has made it possible to address catalytically active sites directly with atomic resolution. Moreover, the recent develop-

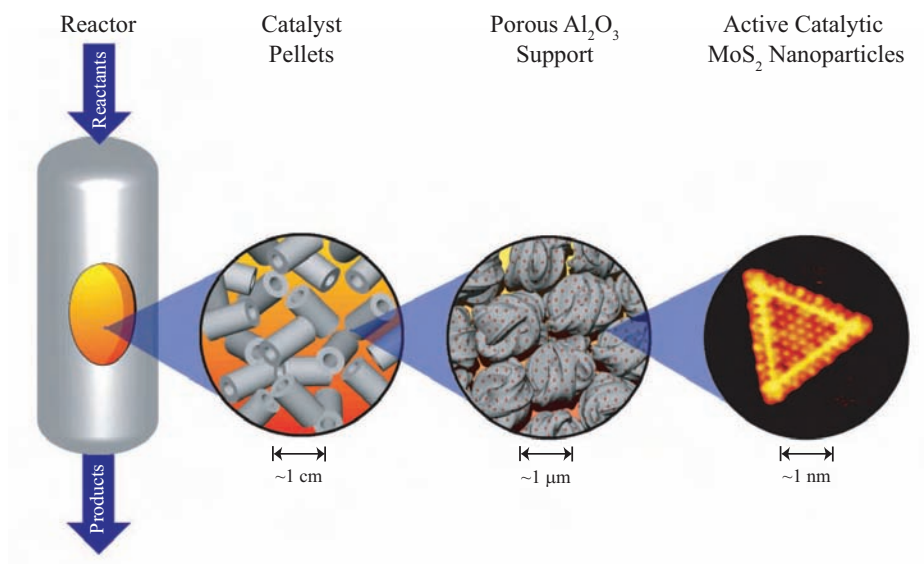


Figure 1.3. Illustration of the great span in length scale involved in the industrial hydrotreating process. Inside a large-scale reactor, highly porous support pellets are present. The pellets typically consist of alumina, and onto these the active highly dispersed MoS₂-based nanoclusters are deposited by wet-chemistry impregnation, which ensures a high contact area with the reactants.

ment of STM systems capable of recording images with atomic resolution at ambient pressures has provided an effective tool for bridging the pressure gap [19, 20].

1.3 Hydrotreating

The main topic of this thesis is hydrotreating catalysis. Hydrotreating covers a broad range of catalytic processes applied to upgrade and process crude oil to comply with current technological and environmental standards. The hydrotreating process is one of the most important catalytic processes, and the annual sales of hydrotreating catalysts represent close to 10% of the total world market for catalysts [21]. In the hydrotreating process, hydrogen is used to saturate unsaturated hydrocarbons (hydrogenation) and remove hetero-atoms, such as sulfur (hydrodesulfurization), nitrogen (hydrodenitrogenation), oxygen (hydrodeoxygenation), and metals (hydrodemetallization). The purpose of removing these impurities is twofold: first of all, the emission of SO₂ and NO_x, when burning S- and N-containing fuels, causes massive acid rain problems, such as forest decline, and secondly to prevent sulfur poisoning of other catalysts in the refineries and the three-way car exhaust catalyst.

In the hydrotreating process, a mixture of crude oil and gaseous hydrogen at elevated temperature and high pressure is trickled through a bed of porous support pellets consist-

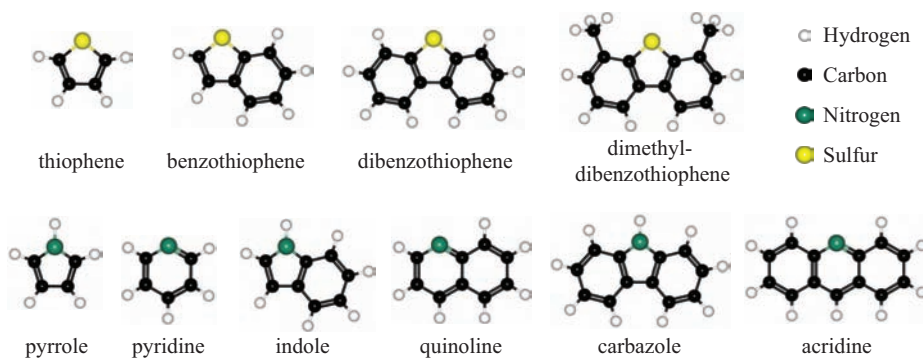


Figure 1.4. Typical sulfur- and nitrogen-containing compounds in crude oil.

ing typically of alumina ($\gamma\text{-Al}_2\text{O}_3$) (illustrated for hydrodesulfurization in Fig. 1.2). The support is impregnated with the active catalytic material in the form of nanometer-sized MoS_2 particles promoted by either Co or Ni. The crude oil feed is generally very inhomogeneous, and the specific impurity content varies significantly with the geographical origin (see Tab. 1.1). Furthermore, since the oil feed is a result of decaying organic material, the diversity of the molecules entering the hydrotreating reaction is large, ranging from simple molecules, such as thiols (R-SH), sulfides ($\text{R-S-R}'$), disulfides ($\text{R-S-S-R}'$), and amines (R-NH_2) to more complex molecules, such as dibenzothiophenes and carbazoles with the impurity atom deeply imbedded in a molecular carbon surrounding (Fig. 1.4). The complexity of the feed demands a highly versatile catalyst to ensure a homogeneous output.

The operating conditions of the catalyst are determined by the composition of the specific oil fraction, but the temperature range is typically $300\text{-}400^\circ\text{C}$ and the pressure $50\text{-}70$ bar. These rather harsh conditions and the great span in length scale involved in catalyst technology (see Fig. 1.3) make it a complicated task to optimize the catalyst performance. Historically, the development of hydrotreating processes dates back to the 1930s, and the alumina-supported bimetallic cobalt-molybdenum catalyst, which is still employed today, was reported as early as 1943 [22].

	Arabian Light	Arabian Heavy	Attacka	Boscan
Sulfur (wt%)	1.8	2.9	0.07	5.2
Nitrogen (wt%)	0.1	0.2	< 0.1	0.7
Oxygen (wt%)	< 0.1	< 0.1	< 0.1	< 0.1

Table 1.1. Typical sulfur, nitrogen, and oxygen impurity levels of crude oil with different geographical origin [21].

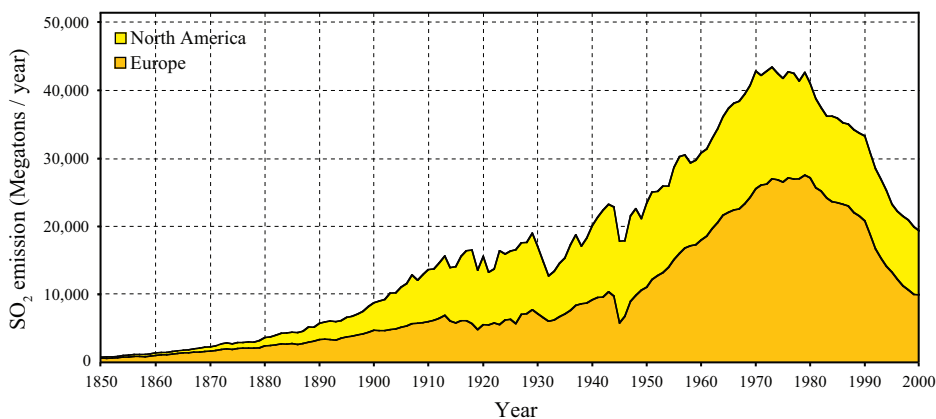


Figure 1.5. The emission of SO₂ from 1850 to 2000 in North America and Europe [25]. The reduction in the emission starting in the early 1980s is directly correlated with implementation of improved hydrotreating processes.

In the early 1980s, there was a general feeling in the industry that the hydrotreating catalyst could not be developed further. However, the hydrotreating catalyst is an excellent example of an industrial catalyst that has undergone a dramatic increase in performance as new and better characterization tools have been developed. During the 1980s, the new detailed insight obtained by these characterization studies lead to new ideas for catalyst preparation, which triggered a dramatic increase in efficiency. The development of the improved catalysts during the 1980s is directly reflected in the SO₂ emission curve in Fig. 1.5.

1.3.1 Hydrodesulfurization

Especially the hydrodesulfurization (HDS) process has recently been subject to increased attention, and stricter legislation in the European Union and the U.S. has imposed severe limits on the sulfur impurity levels in transportation fuels. The legislation in the EU has for example reduced the amount of sulfur in diesel from 350 ppm to better than 50 ppm in 2005, and the limit value will be further tightened to 10 ppm in 2009 [23, 24]. At present, the legal requirements regarding fuel specifications can in principle be fulfilled but only at a considerable cost. The current limit for the sulfur removal is set by the hydrogen consumption, which is a rather expensive resource.

The traditional catalyst characterization techniques, which paved the way for the advances in the 1980s, seem, however, to have reached the limit in terms of providing the desired atomic-scale insight into the structure and working principle of the hydrotreating catalyst. Consequently, further improvement of the catalytic performance calls for new approaches to gain a fundamental atomic-scale understanding of the hydrotreating processes. This has motivated researchers within the field of surface science to take up

the challenge from both an experimental and theoretical point of view.

In this thesis a surface science approach to hydrotreating catalysis is taken. Different MoS₂-based model systems are synthesized and then investigated by STM.

1.4 Outline of thesis

The remaining part of the thesis is structured in the following way:

Chapter 2 The STM technique is introduced. The chapter covers both the principle of operation and the theory that forms the basis for understanding the recorded images. Furthermore, a brief introduction to density functional theory (DFT) is given.

Chapter 3 The preparation of a hydrotreating model catalyst is described in this chapter. Furthermore, the main results of previous studies in the SPM group of non-promoted MoS₂ nanoclusters are briefly summarized as these results form an important foundation for the work presented in the present thesis.

Chapter 4 In this chapter the structural progression of MoS₂ nanoclusters is followed as a function of their size, and it is shown that the equilibrium structure is altered when the cluster size is reduced. The size-dependent structure of the MoS₂ nanoclusters is driven by the tendency to optimize the sulfur excess present at the cluster edges.

Chapter 5 The effects of Co and Ni promoter atoms on the MoS₂-based model catalyst are treated in this chapter. The promoter atoms are found to have a profound influence on the cluster morphology, and the exact position of the promoter atoms is determined from atom-resolved STM images. Despite structural similarities between the Co- and the Ni-promoted model catalysts, differences, which may explain the different catalytic properties of the Co- and Ni-promoted technical catalysts, are found to exist. In the end of the chapter, the study is extended to include Fe and Cu as promoter atoms, and it is shown that the shape of the MoS₂ nanoclusters displays a direct dependence on the type of promoter atom.

Chapter 6 In this chapter the model system is taken one step further with an investigation of MoS₂ nanoclusters on a graphite and a rutile TiO₂ support, respectively, in order to study the effects of a more realistic support. The results show that the support affects the structure of the MoS₂ clusters in terms of, e.g. stacking and cluster shape.

Though the main focus of this thesis is on aspects related to the hydrotreating catalyst, a couple of interesting spin-off studies saw the light of day.

Chapter 7 A spin-off study from the experiments with synthesizing MoS₂ nanoclusters on the graphite support is concerned with the formation of a novel Mo₆S₆ nanowire structure. In this chapter, the synthesis route to elementary pure Mo₆S₆

nanowires is presented, and the detailed atomic-scale structure is revealed using STM and DFT calculations. Furthermore, scanning tunneling spectroscopy (STS) is utilized to explore the electronic properties of the Mo_6S_6 nanowires.

Chapter 8 In this chapter, time-resolved STM is used to investigate a massive sulfur-induced transformation of a homogeneous array of Co nanoparticles into a new cobalt sulfide phase. The underlying atomistic mass-transport process is revealed and, surprisingly, found to be mediated exclusively by the formation and detachment of monosized Co_3S_4 complexes at the perimeter of the Co nanoparticles.

CHAPTER 2

Methods

In this chapter, a detailed description of the concepts and working principles of scanning tunneling microscopy will be given. In addition, a brief section on density functional theory is included.

2.1 Scanning tunneling microscopy

Since the development of the first scanning tunneling microscope (STM) by Gerd Binnig and Heinrich Rohrer in 1982 [26, 27], the STM has revolutionized the field of surface science and has become the technique of choice for revealing the atomic-scale realm of matter. What sets STM apart from other surface science techniques is the unique ability to provide three-dimensional, real-space images with extremely high spatial resolution, which makes it possible to obtain detailed local atomic-scale information about surfaces. The great impact STM has had on surface science was acknowledged in 1986 when the inventors received the Nobel prize [28].

2.1.1 The principle of STM

The working principle of the STM is remarkably simple and rests on the quantum mechanical tunneling phenomenon. By positioning a very sharp metal tip in close proximity ($\sim 5\text{\AA}$) of a conducting surface, the electronic wave functions of the tip and surface will start to overlap, which enables an exchange of electrons in the classically forbidden vacuum gap between the tip and the surface. This is the process referred to as *tunneling* in quantum mechanics.

If a small bias voltage, V_t , is applied to the sample, a net flow of electrons will tunnel from filled sample states into empty tip states or vice versa depending on the polarity of V_t . The net flow of electrons results in a measurable tunnel current, I_t , which is strongly dependent on the distance between the tip and the sample due to the exponential decay of the electronic wave functions into the vacuum gap. This strong exponential dependence of distance secures the ability to achieve images with atomic resolution since a single atom protruding from the tip will carry the main part of the tunnel current, as will become apparent in Section 2.1.3.

In the normal mode of operation, the so-called constant current mode, the STM is raster-scanned across the surface at a fixed bias voltage while keeping the tunneling current constant at a preset value by moving the tip up and down according to a feedback loop. The z position of the tip can now be recorded as a function of the lateral position of the tip resulting in a topographical image of the surface (see Fig. 2.1). One has to be careful in the interpretation of the STM images since constant current STM images reflect the local density of states at the Fermi level projected to the position of the tip apex, as will be shown in Section 2.1.3. The images thus in general reflect a convolution of the geometric and electronic structure of the surface.

2.1.2 The Aarhus STM

The conceptually simple working principle of the STM is in sharp contrast to the actual realization. The positioning and control of a macroscopic STM tip with sub-Ångström precision is a tremendous task bridging almost 9 orders of magnitude. The Aarhus STM [29] used in the presented experimental work is a homebuilt instrument capable of achieving atomic resolution on metal and oxide surfaces on a routine basis. Furthermore,

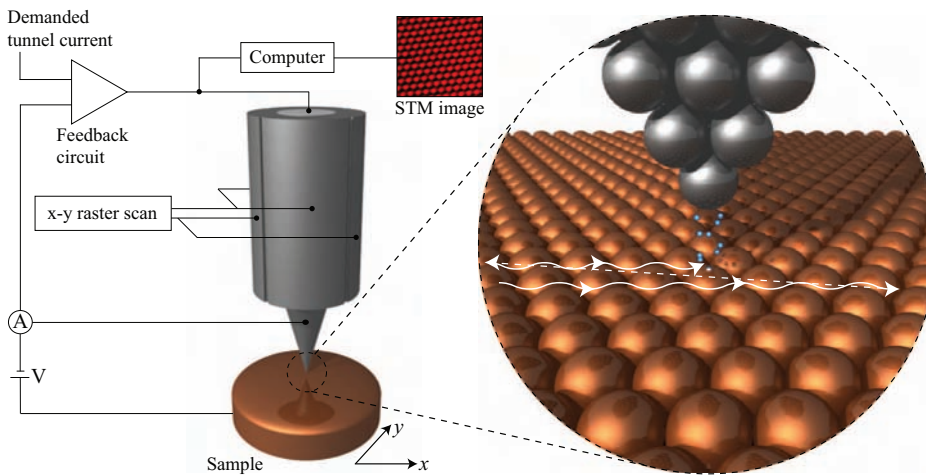


Figure 2.1. Illustration of the basic operating principle behind the STM. The circular zoom-in illustrates schematically the tunneling electrons as the tip is raster-scanned across the surface.

the Aarhus STM allows fast data acquisition due to a compact and rigid design, which makes it possible to observe dynamic processes on the surface.

Figure 2.2 shows a schematic drawing of the Aarhus STM. The sample (A) is mounted in a tantalum sample holder (B), which can be inserted into the STM under two leaf springs (C) ensuring that the sample holder is held rigidly against the top plate (D) of the STM. The top plate, biased with V_t , is both electrically and thermally isolated by three quartz balls (E). The tip (F), which is made from a tungsten wire that has been electrochemically etched to form a sharp apex, is mounted at the end of the piezoelectric scanner tube (G). The scanner tube has thin silver electrodes on the inside as well as on the outside. The lateral scanning motion is achieved by bending the entire tube. The outer electrode is divided into four identical sections, and by applying antisymmetric voltages to opposite electrodes, one side of the scanner tube will expand and the other will contract, which results in the bending of the tube. By biasing the inner electrode with respect to the outer ones, the entire scanner tube will elongate or contract providing sub-Ångström control over the z position of the tip. The scanner tube is attached to a linear motor, the so-called “inchworm” (H) and (I). The inchworm consists of a piezoelectric tube divided into a center electrode and two clamp electrodes (I). By successively opening and closing the clamp electrodes, while contracting and expanding the center electrode, the rod (H), onto which the scanner tube is mounted, can be moved in a worm-like manner. The inchworm is used for coarse positioning of the tip, and movement of 1 mm can be performed in approximately 1 minute. When the motion is towards the sample, it is terminated as soon as a preset tunnel current is detected.

The entire STM (J), which due to its compact design has a high resonance frequency (~ 8 kHz), is mounted in the cradle, which is a stainless steel block (K) suspended by soft springs (O) with a resonance frequency below ~ 2 Hz. During scanning the entire cradle

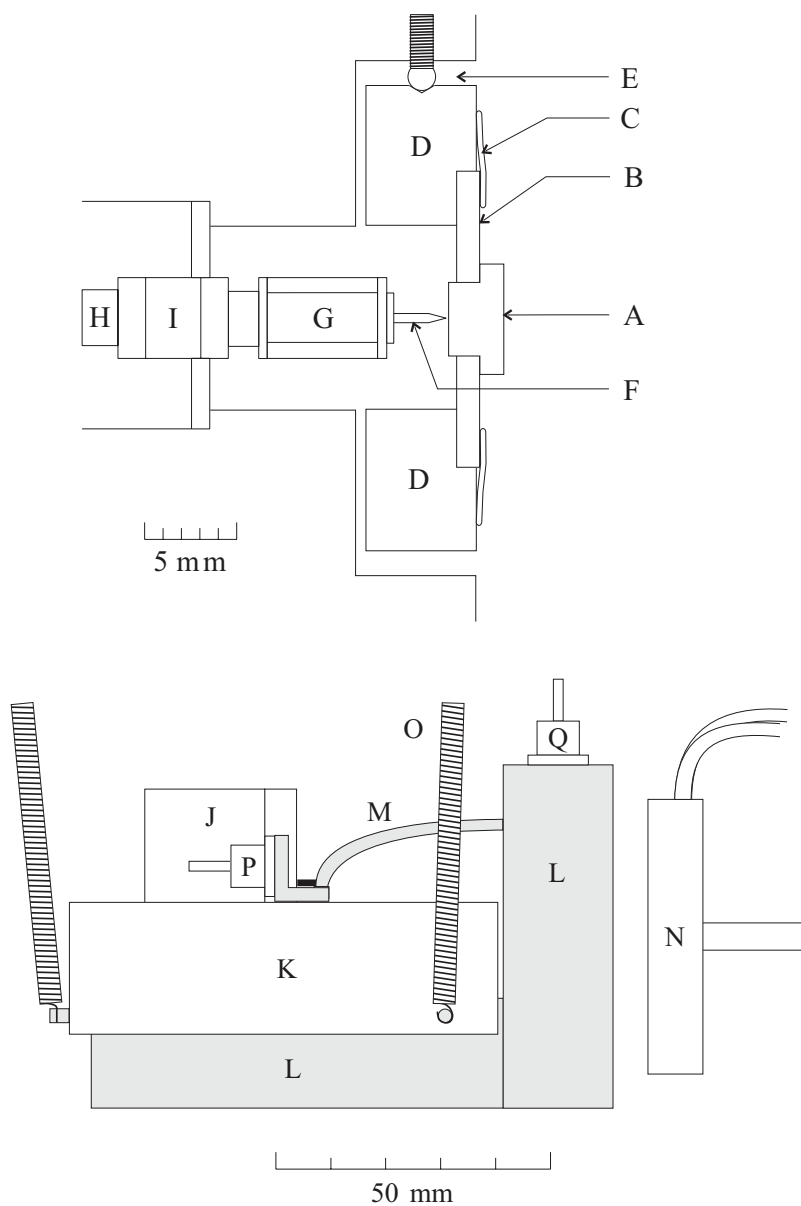


Figure 2.2. Schematic illustration of the Aarhus STM. The illustration at the top shows a cross-section of the STM scanner house (J). The bottom illustration shows a side view of the entire STM cradle. The letters denote: (A) Sample. (B) Sample holder. (C) Leaf springs. (D) STM top plate. (E) Quartz ball. (F) STM tip. (G) Scanner tube. (H), (I) Linear inchworm drive. (K) Stainless steel block. (L) Aluminum blocks. (M) Copper braid. (N) Liquid N₂-cooled Cu block. (O) Suspension springs. (P), (Q) Zener diodes.

hangs freely from these springs. This setup provides excellent damping of any external high frequency vibrations, and no additional vibrational damping is thus needed.

2.1.2.1 STM movies

The compact design of the STM makes fast scanning possible, and several constant current images can be recorded per second. This fast scanning capability is utilized when recording so-called STM movies. These movies are made by recording successive images of the same area of the sample, which gives the possibility to follow dynamic processes, such as diffusion of molecules, on the surface. Another application of the STM movies is to follow slow, e.g. corrosion, processes that occurs on a timescale longer than the normal one-day experiments. An example of such a process is given in Chapter 8, where the transformation of supported metallic Co nanoparticles, exposed to gaseous H_2S , is followed in STM movies with a duration of up to 80 hours. To ensure that the STM movie is recorded at the same position of the surface, drift-correction and more advanced pattern recognition software have been implemented in the scanning software to counteract the drift of the sample relative to the tip.

2.1.3 Theory of STM

STM data are typically presented as colorful 2D images, but sometimes the data are depicted in 3D as the cover illustration of this thesis. Though the look of the 3D STM images is often appealing, and certainly makes nice covers, the 3D STM images could misleadingly lead to the conception that STM depicts the purely geometric structure of the surface. While this interpretation is indeed true on some surfaces, it is, however, not valid in general. In fact, the following will show that the constant current STM images represent contours of constant local density of states (LDOS) at the Fermi level, which implies that STM images often reflect a rather complicated convolution of the electronic and geometric structure of the surface.

In order to give a correct interpretation of STM images, it is essential to know what determines the tunnel current. This is a complicated task because a complete modeling of the tunnel current requires detailed knowledge about the exact geometric and electronic state of both the tip and surface. The most common theoretical description of the tunneling process is thus based on a simplified treatment introduced by Tersoff and Hamann in 1983 [30]. However, before introducing the Tersoff-Hamann approach, a simple one-dimensional model will serve as an introduction to the concept of tunneling and thus STM imaging.

2.1.3.1 One-dimensional model

In a simple one-dimensional model, the vacuum gap can be replaced by a constant potential barrier, U , in the region $0 < z < d$. The wave function, $\psi(z)$, describing an electron with energy $\varepsilon < U$ moving the $+z$ direction in the classically forbidden region, is:

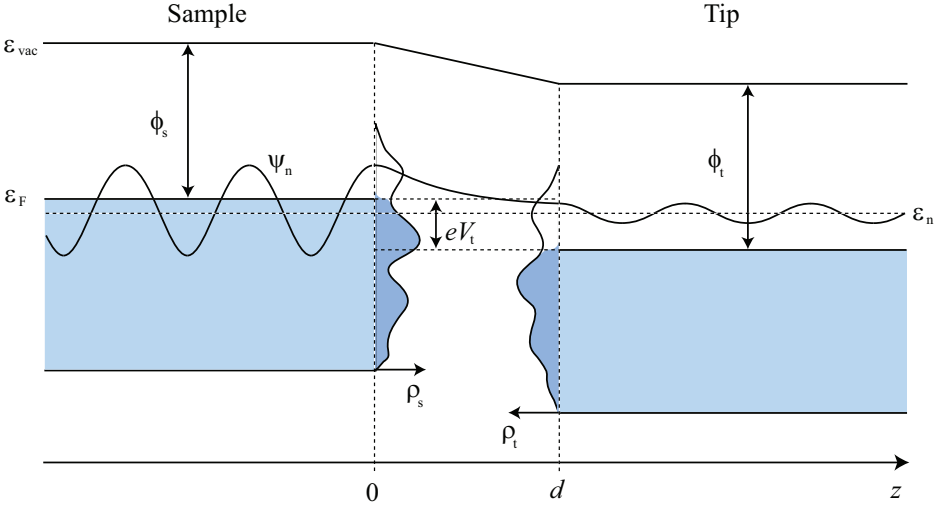


Figure 2.3. Schematic energy diagram of the sample-tip tunnel junction with a width d . A negative bias voltage, V_t , is applied to the sample, i.e. the tunneling proceeds from occupied sample states to empty tip states (occupied states in the tip/sample are shaded blue). Tunneling is only permitted within the small energy interval eV_t . ϕ_s and ϕ_t are the work functions of the sample and tip, respectively. The densities of states of the sample, ρ_s , and tip, ρ_t , are sketched. ψ_n illustrates a wave function with energy ε_n that decays exponentially in the junction but still has a non-zero amplitude at the position of the tip. ε_{vac} is the vacuum energy, and ε_F is the Fermi energy of the sample.

$$\psi(z) = \psi(0)e^{-\kappa z} \quad (2.1)$$

where $\kappa = \sqrt{2m_e(U - \varepsilon)}/\hbar$. The probability w of observing an electron at the end of the potential barrier ($z = d$) is given as:

$$w \propto |\psi(d)|^2 = |\psi(0)|^2 e^{-2\kappa d} \quad (2.2)$$

This exponential decay in the barrier region is illustrated in Fig. 2.3. Accordingly, there is a finite probability for an electron in the n th sample state with an energy, ε_n , between ε_F and $\varepsilon_F - eV_t$, to tunnel to an empty state in the tip. If $eV_t \ll \phi$ then the probability of tunneling is given as¹:

$$w \propto |\psi(d)|^2 = |\psi(0)|^2 e^{-\frac{2}{\hbar} \sqrt{2m_e \phi} d} \quad (2.3)$$

The tunnel current is directly proportional to the total number of sample states within the energy interval eV_t , which leads to:

¹The approximation: $U - \varepsilon = \phi - eV_t \approx \phi$ is used with $\phi = \frac{1}{2}(\phi_s + \phi_t)$.

$$I_t \propto \sum_{\substack{\varepsilon_n = \varepsilon_F - eV_t \\ \varepsilon_n \leq \varepsilon_F}} |\psi_n(d)|^2 \quad (2.4)$$

If the density of electronics states does not vary significantly within the interval $[\varepsilon_F - eV_t; \varepsilon_F]$, the result can be expressed as the *local density of states* $\rho_s(z = d, \varepsilon_F)$ of the sample at the Fermi level and at the position of the tip:

$$I_t \propto V_t \rho_s(z = d, \varepsilon_F) = V_t \rho_s(z = 0, \varepsilon_F) e^{-\frac{2}{\hbar} \sqrt{2m_e \phi} d} \quad (2.5)$$

The above result shows that a constant current STM image reflects the contours of constant local density of states (LDOS) at the Fermi level and at the position of the tip. A similar result can be obtained from the more sound Tersoff-Hamann theory as will be demonstrated in the following section.

2.1.3.2 Tersoff-Hamann theory

The Tersoff-Hamann approach rests on Bardeen's Transfer-Hamiltonian formalism, which treats the tip and surface as two non-interacting systems². Instead of trying to solve the combined problem, Bardeen showed that electronic wave functions of the separate sample and tip subsystems (ψ_s and ψ_t , respectively) can be obtained by solving the stationary Schrödinger equation. The rate of electron transfer, that is, the tunnel current, can then be calculated by time-dependent perturbation theory. This concept was first applied by Tersoff and Hamann as summarized in the following.

A well known result from first-order time-dependent perturbation theory is Fermi's golden rule, which states that the transition rate for an electron to tunnel from an initial (sample) state, ψ_s , to a final (tip) state, ψ_t , is given by:

$$R_{s \rightarrow t} = \frac{2\pi}{\hbar} |M|^2 \delta(\varepsilon_{\psi_s} - \varepsilon_{\psi_t}) \quad (2.6)$$

where the delta function indicates that only elastic tunneling is considered, that is tunneling between states with the same energy at both sides of the gap. Bardeen showed that the tunneling matrix element, M , can be expressed as:

$$M = \frac{\hbar^2}{2m} \int_{S_0} (\psi_s^* \nabla \psi_t - \psi_t \nabla \psi_s^*) d\vec{S} \quad (2.7)$$

where the integration is over any surface lying entirely within the tunnel gap between the tip and the surface [31]. With Fermi's golden rule in mind, the tunnel current from the sample to the tip, for a system with negative bias voltage, V_t , on the sample, can be written as:

$$I_{s \rightarrow t} = 2 \cdot \frac{2\pi e}{\hbar} \int_{-\infty}^{\infty} \underbrace{\rho_s(\varepsilon) f(\varepsilon)}_{\text{\# of filled sample states}} |M|^2 \underbrace{\rho_t(\varepsilon + eV_t) [1 - f(\varepsilon + eV_t)]}_{\text{\# of empty tip states}} d\varepsilon \quad (2.8)$$

²Even though Bardeen's concept was developed long before the invention of the STM, it will be applied to the tip sample situation in the following.

where the factor of two in front accounts for electron spin, $f(\varepsilon)$ is the Fermi distribution function, and ϱ_s and ϱ_t are the density of states (DOS) of the sample and tip, respectively. The Fermi functions $f(\varepsilon) = [1 + \exp((\varepsilon - \varepsilon_F)/k_B T)]^{-1}$ ensure that the tunneling only occurs from filled sample states into empty tip states in accordance with Pauli's exclusion principle.

Though the dominant tunnel current for a negative sample bias will be from the sample to the tip, there will also be a smaller tunnel current flowing in the opposite direction, i.e. from the filled tip states to empty sample states:

$$I_{t \rightarrow s} = \frac{4\pi e}{\hbar} \int_{-\infty}^{\infty} \underbrace{\varrho_s(\varepsilon)[1 - f(\varepsilon)]}_{\text{\# of empty sample states}} |M|^2 \underbrace{\varrho_t(\varepsilon + eV_t)f(\varepsilon + eV_t)}_{\text{\# of filled tip states}} d\varepsilon \quad (2.9)$$

Consequently, the total current flowing from the sample to the tip is:

$$\begin{aligned} I_t &= I_{s \rightarrow t} - I_{t \rightarrow s} \\ &= \frac{4\pi e}{\hbar} \int_{-\infty}^{\infty} |M|^2 \varrho_s(\varepsilon) \varrho_t(\varepsilon + eV_t) [f(\varepsilon) - f(\varepsilon + eV_t)] d\varepsilon \end{aligned} \quad (2.10)$$

For most practical applications of STM, the temperature is low enough for the Fermi distribution to be considered a step function, which simplifies the expression for the tunnel current:

$$I_t \approx \frac{4\pi e}{\hbar} \int_{\varepsilon_F - eV_t}^{\varepsilon_F} |M|^2 \varrho_s(\varepsilon) \varrho_t(\varepsilon + eV_t) d\varepsilon \quad (2.11)$$

If the tunneling matrix element does not change appreciably as a function of energy, it can be separated out in which case the tunnel current can be expressed as a convolution of the surface and tip DOS.

Since the purpose of performing STM is to learn about surface structures, it is unfortunate that the electronic structure of the tip contributes to the tunnel current according to Eq. 2.11 and 2.7. Tersoff and Hamann tackled this problem by assuming a simple s -wave model for the tip with the spherically symmetric wave functions centered at the center of curvature of the tip, \vec{r}_0 . In this approximation the tunnel current, in the limit of small bias voltage and low temperature, can be expressed as:

$$I_t \propto V_t \sum_s |\psi_s(\vec{r}_0)|^2 \delta(\varepsilon_s - \varepsilon_F) = V_t \rho_s(\varepsilon_F, \vec{r}_0) \quad (2.12)$$

where the sum extends over sample states evaluated at \vec{r}_0 . Accordingly, the tunnel current is proportional to the LDOS, $\rho_s(\varepsilon_F, \vec{r}_0)$, at the Fermi level evaluated at the position of the tip. The Tersoff-Hamann model provides a conceptual simple framework for interpreting STM images, and for this reason, it is still the most widely used model.

In the above expression, the strong dependence of the tunnel current on the distance between the tip and the sample relies on the exponential decay of ψ_s into the vacuum

barrier. The expression for the tunnel current can, as for the simple model, be further rewritten as:

$$I_t \propto V_t \cdot \exp\left(-\frac{\sqrt{8m_e\phi}}{\hbar}z\right) \quad (2.13)$$

where m_e is the electron mass, ϕ is the average work function of the tip and surface representing the effective tunneling barrier, and z is the distance between the tip and the sample. This expression is similar to the result of the simple model in Eq. 2.5. For a typical value of the work function around 4 – 5 eV [32], a difference of 1 Å in the tip/surface distance will change the tunnel current by approximately an order of magnitude. This ensures that imaging with atomic resolution is indeed possible.

It is important to keep in mind that the STM images reflect the LDOS of the surface at the position of the tip. On metal surfaces, the LDOS generally coincide with the geometrical topography of the surface, but for band gap materials, such as MoS₂ and TiO₂ or surfaces with directional bonding like graphite, the STM images reflect in general a convolution of the geometric and the electronic structure of the surface. In these cases, the maxima observed in STM images do not necessarily coincide with the maxima of the surface topography. This is an important point to remember in the following chapters. Likewise one has to be careful when adsorbates are present on the surface since they alter the LDOS. They can either be imaged as protrusions or depressions depending on whether they enhance or deplete the LDOS at the Fermi level [33].

2.1.4 Scanning tunneling spectroscopy

The main application of the STM is, as the name implies, as a microscope. However, another application of the STM, which can be used to complement the imaging, is scanning tunneling spectroscopy (STS). In fact, the original idea of building the STM was not to build a microscope but rather to perform spectroscopy locally on an area less than 10 nm in diameter [27].

The concept of the STS technique follows from Equation 2.12. The equation implies that if the DOS of the tip is constant, then the conductance (I/V) plotted as a function of V reflects the LDOS of the surface. The low bias approximation of the Tersoff-Hamann approach is, however, often violated in practice. Selloni *et al.* [34] suggested, using the Wentzel-Kramers-Brillouin (WKB) approximation scheme, that the results of Tersoff and Hamann could quantitatively be generalized for modest voltages as:

$$I \propto \int_0^{eV} \rho_s(r, \varepsilon) \rho_t(r, -eV + \varepsilon) T(\varepsilon, eV, r) d\varepsilon \quad (2.14)$$

where $\rho_s(r, \varepsilon)$ and $\rho_t(r, \varepsilon)$ are the density of states of the sample and tip at the location r and energy ε measured with respect to their individual Fermi levels. For negative sample bias $eV < 0$, and for positive sample bias $eV > 0$. The tunneling transmission probability, $T(\varepsilon, eV, r)$, for electrons with energy ε and applied bias voltage V is given as:

$$T(\varepsilon, eV) = \exp\left(-\frac{2z\sqrt{2m_e}}{\hbar}\sqrt{\frac{\phi_s + \phi_t}{2} + \frac{eV}{2} - \varepsilon}\right) \quad (2.15)$$

where z is the distance between the tip and the sample, and ϕ_s and ϕ_t are the work functions of the sample and tip, respectively. Differentiation of Eq. 2.14 gives:

$$\begin{aligned} \frac{dI}{dV}(V) \propto & \rho_s(r, eV)\rho_t(r, 0)T(eV, eV, r) \\ & + \int_0^{eV} \rho_s(r, \varepsilon)\rho_t(r, -eV + \varepsilon) \frac{dT(\varepsilon, eV, r)}{dV} d\varepsilon \end{aligned} \quad (2.16)$$

Although the tunneling transmission probability $T(\varepsilon, eV, r)$ is usually unknown, the expression from the WKB approximation in Eq. 2.15 states that $T(\varepsilon, eV, r)$ is a smooth, monotonically increasing function of the applied bias voltage. At any fixed location the bias dependence of $T(\varepsilon, eV, r)$ thus contributes a smoothly varying “background” on which the spectroscopic information is superimposed. The structure in dI/dV as a function of V can therefore usually be attributed to the structure in the density of states via the first term in Eq. 2.16.

The information obtained by tunneling spectroscopy is, however, always a convolution of the electronic structures of the sample and the tip, as is evident from Eq. 2.16. To exclude a strong influence of the electronic structure of the tip in the tunneling spectroscopy results, it is thus desirable to use a tip with a featureless electronic structure. The state of the tip can be examined by acquiring spectra on a surface with a known electronic structure, e.g. a graphite surface as in Chapter 7, to see whether the electronic structure of the tip introduces features in the STS spectrum.

The experimental process of acquiring STS spectra is performed in parallel with the constant current STM imaging in order to relate the spectra directly to the surface structure beneath the tip. In the selected point, the tip position is frozen, the feedback loop controlling the z -position of the tip is momentarily interrupted, and the bias voltage (V) is ramped in a preset interval while the tunnel current (I) is measured simultaneously to produce current vs voltage I - V characteristics [35]. The I - V characteristic is subsequently smoothed to eliminate any noise features in the raw data before the dI/dV curve is obtained by numerical differentiation. For the analysis of the data, the dI/dV curves are displayed as a function of the bias voltage, and the position of features in the spectrum can then directly be related to electronic signatures and their energetic position relative to the Fermi level. The convention for presenting data is that the bias voltage refers to the voltage of the sample relative to the tip, i.e. positive (negative) voltages correspond to sample states above (below) the Fermi level when dI/dV is plotted as a function of V .

In the investigation of electronic states of metals and semiconductors, the energy range of interest often extends several electron volts on either side of the Fermi level. This may cause problems because $T(\varepsilon, eV, r)$ displays a very strong dependence on V when the voltage becomes an appreciable fraction of the sample and tip work functions. This is unfortunate since the V -dependence of $T(\varepsilon, eV, r)$ may distort features in the

spectrum. Feenstra *et al.* [36] proposed a simple but effective solution to this problem. They showed that normalization of dI/dV by dividing with I/V reflects the electronic density of states reasonably well since the normalization effectively cancels out the exponential dependence of $T(\varepsilon, eV, r)$ on V .

In Chapter 7, the STS technique is utilized to explore the conductivity properties of Mo_6S_6 nanowires. The STS results will be presented as normalized $(dI/dV)/(I/V)$ spectra.

2.2 Density functional theory

The information contained in STM images is only concerned with the electronic structure of the surface, and no direct conclusion can thus be drawn about the chemical identity of the surface structures. This lack of chemical sensitivity and the fact that STM in general reflects a convolution of the geometric and the electronic structure of the surface often makes it a difficult task to correlate the observed structures, e.g. of complex clusters and molecular adsorbates, to their atomistic structure on the surface. Complementary techniques are thus often essential to STM experiments in order to obtain a self-contained study. In recent years an interplay between STM and density functional theory (DFT) has proven to be a very powerful combination. DFT has become the main theoretical technique when it comes to elucidate energetics and geometrical and electronic structures related to surfaces [37, 38]. Furthermore, since a DFT calculation yields the electronic structure, it is fairly easy to extract the LDOS at the Fermi level of the system. This method gives the possibility of simulating constant current STM images by plotting the contours projected at an appropriate distance from the sample.

DFT has also been useful for the work presented in this thesis, and several simulated STM images will be presented to support the structural assignment of experimentally observed features of both MoS_2 nanoclusters and Mo_6S_6 nanowires. The calculations concerning the MoS_2 nanoclusters were performed in the group of J.K. Nørskov at the Technical University of Denmark, and the calculations on the Mo_6S_6 nanowires were performed by S. Gemming at Forschungszentrum Dresden-Rossendorf. My own contribution to the theoretical studies has been limited to the level of discussion and suggestions, and the computational details and parameters have to a large extent been left out in the forthcoming chapters. However, a short description of the theory behind DFT will be presented in the following.

2.2.1 Basic equations in DFT

The foundation of any theory describing a system of interacting electrons and atoms is the time-independent Schrödinger equation:

$$\hat{H}\Psi(\mathbf{r}_1, \mathbf{r}_2, \dots, \mathbf{r}_N) = E\Psi(\mathbf{r}_1, \mathbf{r}_2, \dots, \mathbf{r}_N) \quad (2.17)$$

where \hat{H} is the Hamilton operator, E is the energy of the system, and $\Psi(\mathbf{r}_1, \mathbf{r}_2, \dots, \mathbf{r}_N)$ is the many-body wave function that contains all information about the physical state of

the system containing N electrons. The complexity of solving the Schrödinger equation increases, however, rapidly with increasing numbers of particles involved, and approximations are thus required in order to address surface science problems. The first approximation used for most solid state systems is the Born-Oppenheimer approximation, which states that the motion of the atomic nuclei is slow enough, compared to the motion of the electrons, to treat the electrons as being free to move in an external potential set up by the static nuclei.

The basic idea in DFT is to reduce computational costs even further by focusing on the electron density $n(\mathbf{r})$ rather than on the many-body wave function Ψ . The foundation of DFT is two theorems by Hohenberg and Kohn [39]:

Theorem 1 The external potential $v_{ext}(\mathbf{r})$ is a unique functional of the electron density $n(\mathbf{r})$.

Theorem 2 The ground state energy can be obtained variationally: the electron density $n_0(\mathbf{r})$, which minimizes the total energy, is the exact ground state density.

The first theorem implies that the hamiltonian and consequently the total ground state energy can be expressed as a functional of the electron density:

$$E[n] = T[n] + V_{ee}[n] + V_{ext}[n] = F[n] + V_{ext}[n] \quad (2.18)$$

where $T[n]$ is the kinetic energy, $V_{ee}[n]$ is the electron-electron interaction energy, and $V_{ext}[n]$ is the energy associated with the external potential $v_{ext}(\mathbf{r})$. The second theorem provides a minimization scheme for finding the exact ground state energy and electron density if $F[n]$ is known. The theorems by Hohenberg and Kohn do, however, not give any guide lines on how to derive $F[n]$.

Kohn and Sham provided a solution to this problem [40]. The foundation of the Kohn-Sham approach is the introduction of a non-interacting reference system with the same energy as the interacting. The starting point is Eq. 2.18 where the classical electrostatic energy has been separated out from $F[n]$:

$$E[n] = G[n] + \frac{1}{2} \iint \frac{n(\mathbf{r})n(\mathbf{r}')}{|\mathbf{r} - \mathbf{r}'|} d\mathbf{r} d\mathbf{r}' + \int n(\mathbf{r})v_{ext}(\mathbf{r}) d\mathbf{r} \quad (2.19)$$

where the functional $G[n]$ does not depend on $v_{ext}(\mathbf{r})$ like $F[n]$. Kohn and Sham split $G[n]$ into two terms, a kinetic contribution from the non-interacting electron gas, $T_s[n]$ and the exchange-correlation energy, $E_{xc}[n]$. By construction $E_{xc}[n]$ is the difference between the exact ground state energy and the sum of $T_s[n]$ and the last two terms in Eq. 2.19, and contains all non-classical corrections to the energy. By applying the variational principle of quantum mechanics, Kohn and Sham derived a set of single-electron Schrödinger equations known as the Kohn-Sham equations:

$$\left[-\frac{1}{2}\nabla^2 + v_{eff}(\mathbf{r}) \right] \psi_i(\mathbf{r}) = \epsilon_i \psi_i(\mathbf{r}) \quad (2.20)$$

where the set of single-electron wave functions must correspond to the electron density:

$$\sum_{i=1}^N |\psi_i(\mathbf{r})|^2 = n(\mathbf{r}) \quad (2.21)$$

and the effective potential $v_{eff}(\mathbf{r})$ is comprised of the total electrostatic potential and the derivative of the exchange-correlation energy:

$$v_{eff}(\mathbf{r}) = v_{ext}(\mathbf{r}) + \int \frac{n(\mathbf{r}')}{|\mathbf{r} - \mathbf{r}'|} d\mathbf{r}' + \frac{\partial E_{xc}[n]}{\partial n(\mathbf{r})} \quad (2.22)$$

In a DFT calculation, the Kohn-Sham equations are solved self-consistently by first choosing a trial $n(\mathbf{r})$ from which $v_{eff}(\mathbf{r})$ and a set $\psi_i(\mathbf{r})$ can be evaluated, and finally a new $n(\mathbf{r})$ can be found. This is repeated in an iterative way until convergence is reached. The total energy can then be found as:

$$E = \sum_{i=1}^N \epsilon_i - \frac{1}{2} \iint \frac{n(\mathbf{r})n(\mathbf{r}')}{|\mathbf{r} - \mathbf{r}'|} d\mathbf{r} d\mathbf{r}' + E_{xc}[n] - \int \frac{\partial E_{xc}[n]}{\partial n(\mathbf{r})} n(\mathbf{r}) d\mathbf{r} \quad (2.23)$$

The Kohn-Sham equations are in principle exact. However, in practice the exchange-correlation energy $E_{xc}[n]$ has to be approximated because its exact functional form is unknown. Kohn and Sham used the local density approximation (LDA) in which the exchange-correlation energy is solely determined by the electron density:

$$E_{xc}[n] = \int n(\mathbf{r}) \epsilon_{xc}(n(\mathbf{r})) d\mathbf{r} \quad (2.24)$$

The LDA approximation assumes a slowly varying electron density which in fact is not true for surfaces where the density decreases exponentially due to the decay of the wave functions into the vacuum region. In fact, Kohn and Sham pointed out in their original paper that, “We do not expect an accurate description of chemical binding” within in LDA approximation [40]. This statement has, however, proved to be too pessimistic since the LDA-based calculations have turned out to give qualitative agreement with experimental values for a number of physical surface properties [41]. However, the LDA approximation fails in some applications, i.e. the binding energy of adsorbates are overestimated on the order of 1-2 eV in LDA-based calculations [38]. For this reason other and more elaborate approximations have been introduced. In the generalized gradient approximation (GGA), the exchange-correlation energy is a function of both the density and the gradient of the density:

$$E_{xc}[n] = \int n(\mathbf{r}) \epsilon_{xc}(n(\mathbf{r}), \nabla n(\mathbf{r})) d\mathbf{r} \quad (2.25)$$

The calculations presented in this thesis concerning the MoS₂ nanoclusters were carried out using the GGA-based Perdew-Wang 91 (PW91) functional, and the calculations on the Mo₆S₆ nanowires were carried out using the gradient-corrected Perdew-Burke-Ernzerhof (GGA-PBE) functional. The GGA approximation, however, also fails when the electron density varies too fast. In particular van der Waals interactions are not taken

into account in standard DFT calculations [42], which becomes an issue in Chapter 7 where the DFT calculations on the Mo_6S_6 nanowires predict a larger interwire distance in a wire bundle compared to the experimentally observed.

The self-consistent DFT energy represents the ground state energy at zero-pressure and zero-temperature. In order to investigate the stability of different edge terminations under the conditions of the experiments and even under realistic hydrotreating conditions, it is desirable to extend the DFT results to finite temperatures and pressures. This can be achieved by constructing a thermodynamic model where the edge free energies are expressed in terms of their DFT energies and the chemical potential of the involved species. A thorough derivation of the equations needed to calculate the edge free energy of MoS_2 is found in Ref. [43]. This thermodynamical approach is applied in calculating the edge free energies (γ) of the different Co- and Ni-promoted edge structure in Chapter 5.

CHAPTER 3

A hydrotreating model catalyst

In this chapter, the preparation of a hydrotreating model catalyst will be described. Furthermore, the main results of previous studies in the SPM group of non-promoted MoS₂ nanoclusters will be briefly summarized as these results form an important foundation for the work presented in the present thesis.

3.1 Introduction

The hydrotreating catalyst has been the subject of countless studies throughout the years using a large number of different catalyst characterization techniques [21, 44, 45]. The traditional catalyst characterization tools are, however, often not capable of obtaining information on an atomic level, which is essential for a deeper understanding of the catalyst and its working mechanism. Accordingly, surface science model studies have been performed on, e.g. single crystal MoS₂(0001) surfaces [46, 47]. These studies together with infrared adsorption spectroscopy (IRAS) of chemisorbed probe molecules [21, 48], such as CO and NO, have, however, revealed that the (0001) basal plane of MoS₂ is completely inert, suggesting that only the edges of the MoS₂-based phase are catalytically active. It is thus desirable to have a more complex model system that is more true to the technical catalyst. From *in situ* extended X-ray absorption fine structure (EXAFS) studies, it has been found that the active MoS₂ phase is present as particles with a size of 10-20 Å under typical operating conditions [49, 50]. A good model system should, accordingly, consist of dispersed particles in the same size-range.

In this chapter, the procedure to synthesize a model system consisting of dispersed MoS₂ nanoclusters will be described. Furthermore, the main results of previous studies in the SPM group of non-promoted MoS₂ nanoclusters will be briefly summarized as these results form an important foundation for the work presented in the present thesis.

3.2 The model support

The most common support material in hydrotreating catalysis is alumina (γ -Al₂O₃) or alternatively silica (SiO₂). Both materials are, however, electrically insulating, and imaging by STM is thus not possible. Instead a Au(111) surface is chosen as a model support. The Au(111) surface holds advantages in terms of dispersing the active cataly-

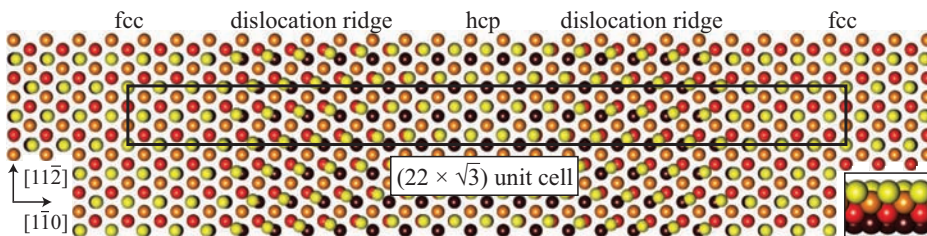


Figure 3.1. Ball model of the reconstruction of the Au(111) surface. The surface is characterized by a $(22 \times \sqrt{3})$ unit cell (indicated by the rectangular box) in which the gold atoms in the topmost layer are compressed, leaving 23 surface gold atoms distributed over 22 bulk sites in the unit cell along the $[1\bar{1}0]$ direction. This compression results in alternating broad fcc and narrow hcp stacking regions. The insert in the lower right corner displays a side view of the model showing the stacking of the layers.

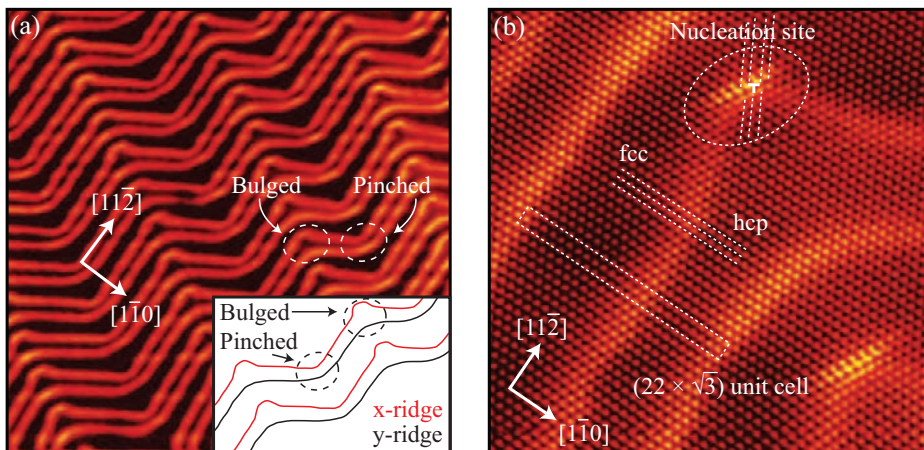


Figure 3.2. STM images of the clean Au(111) surface. (a) Large-scale STM image ($802 \text{ \AA} \times 795 \text{ \AA}$) illustrating the “herringbone” surface reconstruction of Au(111). The bulged and the pinched elbow sites are indicated together with the directions of the crystal. The inserted sketch illustrates x and y dislocation ridges. (b) Atom-resolved STM image of the Au(111) surface ($141 \text{ \AA} \times 135 \text{ \AA}$, $I_t = 1.55 \text{ nA}$, and $V_t = -39.1 \text{ mV}$). The surface is characterized by a $(22 \times \sqrt{3})$ unit cell (indicated with a rectangle), in which the position of the topmost Au atoms are gradually shifted from fcc to hcp sites. The bright dislocation ridges reflect Au atoms in bridge sites in the transition region and have a corrugation less than $\sim 0.2 \text{ \AA}$. The elbows of the x -ridges are associated with a surface dislocation (indicated by a \top), which is the preferential nucleation site of a large range of metals deposited from the vapor phase.

tic material into nanometer-sized clusters, which makes it the preferred model support in the present studies. However, in Chapter 6 the complexity of the model system is taken one step further. This chapter is devoted to studying the effects of more realistic support materials, i.e. a graphite and a rutile TiO_2 surface.

3.2.1 The Au(111) surface

The clean Au(111) surface displays the very characteristic “herringbone” reconstruction in STM images (see Fig. 3.2), which provides an ideal regular array of nucleation sites for epitaxial growth of highly dispersed metals clusters. The reconstruction of the Au(111) surface is driven by a reduced coordination of the surface atoms [51, 52] and is characterized by a $(22 \times \sqrt{3})$ unit cell in which the gold atoms in the topmost layer are compressed gradually by $\sim 4.5\%$ along the $[1\bar{1}0]$ direction [53]. Due to this contraction, the unit cell contains 23 surface gold atoms distributed over 22 bulk sites, resulting in alternating broad fcc and narrow hcp stacking regions running parallel along the $[11\bar{2}]$ as shown in Fig. 3.1. The gold atoms located near bridge locations appear in the STM images as bright dislocation ridges separating the fcc and hcp domains, as observed in

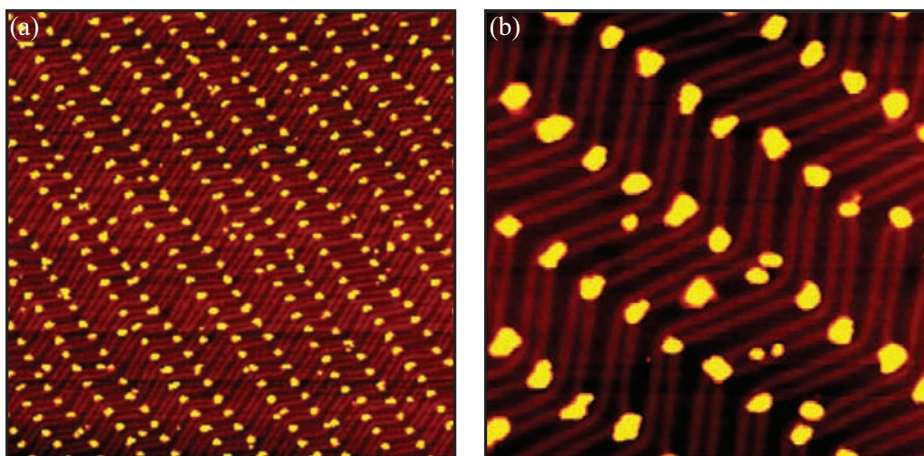


Figure 3.3. (a) STM image ($2000 \text{ \AA} \times 2000 \text{ \AA}$) of Mo deposited on the Au(111) surface at room temperature. (b) Zoom-in ($600 \text{ \AA} \times 600 \text{ \AA}$) showing that the Mo clusters nucleated in the elbow region of the x -ridges.

Fig. 3.2b. Approximately every 140 \AA , long-range elastic interactions introduce domain boundaries where the dislocation ridges bend by alternating $\pm 120^\circ$ [54]. These bends form the zig-zag pattern referred to as the “herringbone” reconstruction. On a length scale even larger than the image size of Fig. 3.2a, three rotational co-existing domains appear to relieve the surface stress isotropically. At the domain boundaries, where the dislocation ridges bend, two different types of elbows are observed: a pinched and a bulged elbow (see Fig. 3.2a).

In this thesis, the regular spaced elbows of the herringbone reconstruction are used as a nanotemplate to disperse the deposited metals (Mo, Co, Ni, and Fe) into nanoclusters of a similar size. Figure 3.3 shows an STM image of Mo deposited on the Au(111) surface, and Mo is indeed observed to nucleate at both the pinched and the bulged elbows of the herringbone reconstruction. The deposited Mo is thus observed to self-organize in equally sized $\sim 30 \text{ \AA}$ wide nanoclusters dispersed evenly onto the entire surface. The high degree of dispersion and the narrow particle-size distribution constitute a favorable situation for the subsequent synthesis of MoS_2 nanoclusters since it enables direct access of gaseous H_2S and ensures a homogeneous sulfidation of the clusters during crystallization.

The mechanism by which metals nucleate in the elbows of herringbone reconstruction has been investigated previously, and it has been observed that only a selected range of metals, including V, Mn, Fe, Co, Ni, Mo, Ru, and Pd nucleate in this particular manner [55–61], whereas metals, such as Al, Cu, Ag, and Au do not [62–64]. A closer look at the Mo clusters nucleated in the elbows (Fig. 3.3b) reveals that the metal clusters nucleate and grow from the “ x -ridges” (see insert in Fig. 3.2a). At the elbow sites, the bend of the x -ridge is associated with a dislocation (indicated with by \top in Fig. 3.2a),

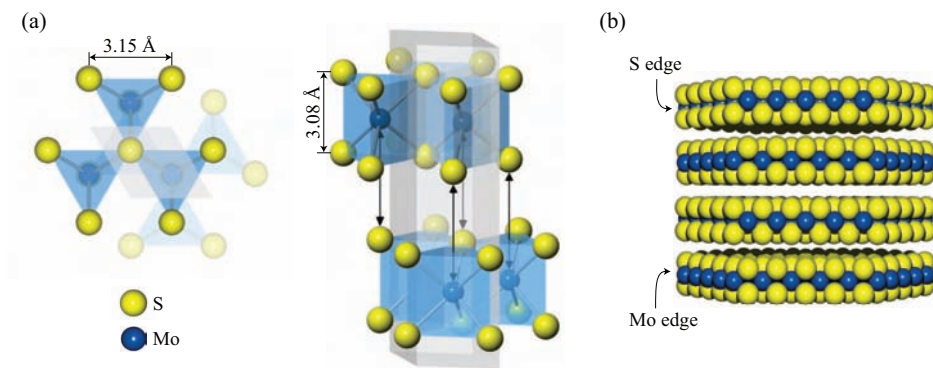


Figure 3.4. (a) Top and side view of the crystal structure of 2H-MoS₂. In the 2H-stacking adjacent S-Mo-S slabs are rotated by 60° with respect to each other and shifted so Mo atoms in one slab are placed over S atoms in the other and vice versa, as indicated by the black arrows. The distance between the Mo layers is 6.15 Å. The light gray parallelepiped shows the unit cell. (b) A ball model of a hypothetical hexagonal MoS₂ cluster with the 2H-stacking. Notice the alternating edge termination. A ($\bar{1}010$) S edge in one layer is directly above a ($10\bar{1}0$) Mo edge in the layer below and vice versa.

which is not present at the bend of the γ -ridge. The dislocation is characterized by a Au atom with a reduced (five) and another atom with an increased (seven) in-plane coordination. Whereas the bright dislocation ridges, which constitute the herringbone pattern, are mainly ascribed to a geometrical shift in the surface corrugation, electronic effects must clearly also play a role at the dislocation site. The altered electronic structure localized around the dislocation site may be prone to interact with the severely under-coordinated ad-atoms. Behm *et al.* [59] have proposed that the nucleation takes place by a two-step mechanism in which a few highly strained gold atoms near the dislocation first are kicked out in an exchange process with the ad-atoms, and the following nucleation then occurs on top of the of the substitutional ad-atoms. The distinction between metals that do or do not grow by this mechanism is explained by the energy gain associated with the initial exchange of gold atoms with different metal atoms.

3.3 Synthesis of MoS₂ nanoclusters

Prior to the actual synthesis of the MoS₂ nanoclusters, the Au(111) single-crystal is sputter-cleaned by 1.5 kV Ar⁺ ion bombardment followed by an annealing at 900 K for 10 min. This procedure generates a clean surface with a regular herringbone pattern as determined by Auger electron spectroscopy (AES) and STM (Fig. 3.2). The parameter space associated with the synthesis of MoS₂ nanoclusters is immense since parameters, such as total Mo coverage, the H₂S exposure, and the substrate temperature, all influence the outcome of the preparation. In the preparation that produces the most homogeneous

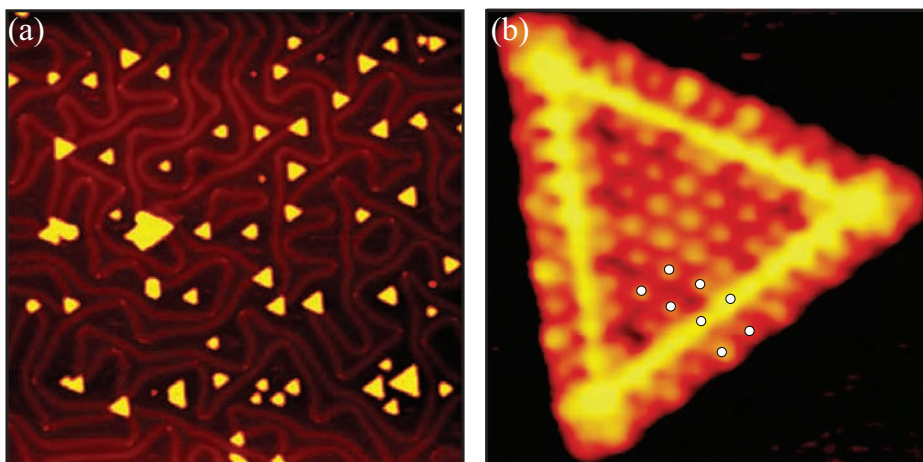


Figure 3.5. (a) STM image ($744 \text{ \AA} \times 721 \text{ \AA}$) of MoS_2 nanoclusters synthesized on the $\text{Au}(111)$ surface. (b) Atom-resolved STM image ($41 \text{ \AA} \times 40 \text{ \AA}$, $I_t = 1.28 \text{ nA}$, and $V_t = 5.2 \text{ mV}$) of a triangular single-layer MoS_2 .

ensemble of clusters in terms of size and morphology, Mo is deposited at 400 K by physical vapor deposition in a sulfiding H_2S atmosphere corresponding to a background pressure of 10^{-6} mbar. The deposition continues for 10 min until a coverage corresponding to $\sim 10\%$ of a monolayer is reached. In order to obtain full crystallinity of the clusters, the sample is post-annealed to 673 K for 15 min while maintaining a sulfiding atmosphere. Before presenting the outcome of the synthesis, the most common crystal structure of MoS_2 will be introduced.

3.4 Crystal structure of MoS_2

MoS_2 (molybdenite) is a layered compound consisting of trilayer S-Mo-S slabs held together by weak van der Waal interactions [65]. Each trilayer slab consists of two hexagonal (0001) planes of S atoms and an intermediate hexagonal layer of Mo atoms, which are trigonally prismatic coordinated to the six surrounding S atoms as shown in Fig. 3.4a. The most common allotrope of MoS_2 adopts the 2H-stacking. In 2H- MoS_2 the unit cell extends over two S-Mo-S slabs, and the Mo atoms in one slab are placed on top of the S atoms in the other, and vice versa as shown in Fig. 3.4.

3.5 Non-promoted MoS_2 nanoclusters

The synthesis procedure is seen from the STM image in Fig. 3.5a to produce dispersed nanoclusters with a distinctive triangular shape. The atom-resolved STM image of a

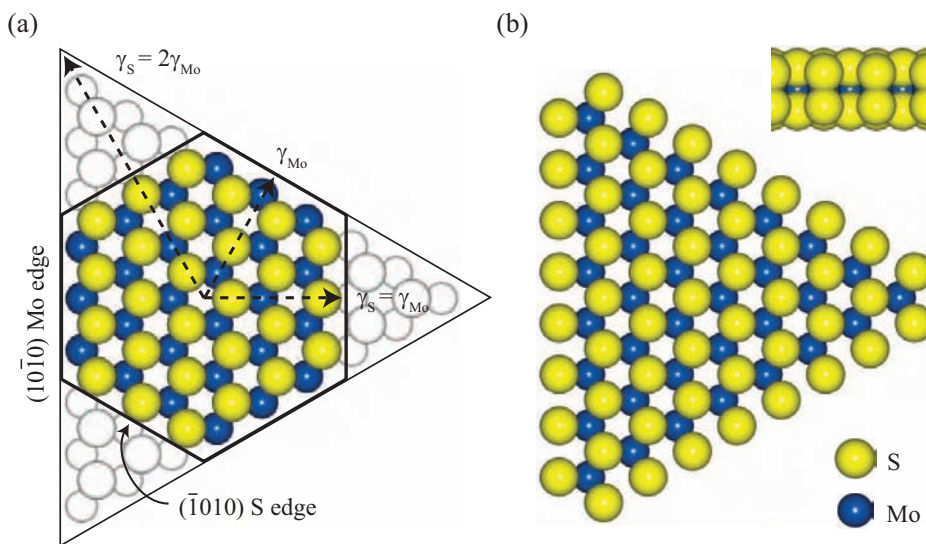


Figure 3.6. (a) Illustration of the Wulff construction of an MoS₂ nanocluster exposing the (0001) basal plane. The figure illustrates the dependence of the equilibrium morphology on the relative edge free energies (γ) of the two low-index edges of MoS₂: the $(10\bar{1}0)$ Mo edge and the $(\bar{1}010)$ S edge, respectively. If the ratio of edge free energies exceeds a factor 2, the shape will be perfect triangular, whereas a ratio in the interval from 1 to 2 results in hexagonally truncated shapes. (b) Top and side view of a ball model of the triangular single-layer MoS₂ nanocluster displaying $(10\bar{1}0)$ Mo edges fully saturated with sulfur dimers.

cluster in Fig. 3.5b illustrates that the clusters contain a plane of hexagonally arranged protrusions with an inter-atomic spacing of 3.15 ± 0.05 Å. This distance matches exactly the lattice distance found for the MoS₂(0001) plane. As pointed out in Chapter 2 low bias, constant current STM images reflect in general a rather complicated convolution of the electronic and geometric structure of the surface. Since this is true in particular for oxides and sulfides, which generally exhibit a band gap, and the lattices of the sulfur and molybdenum atoms furthermore are identical, it cannot *a priori* be determined whether the hexagonally arranged protrusions reflect the S atoms in the surface layer or the Mo atoms in the second layer. Recently, however, simulated STM images from DFT calculations (see Figs. 3.7b and 3.7c) have shown that the protrusions in low bias STM images of the MoS₂(0001) basal plane can be attributed to the topmost layer of S atoms [43]. This finding is also in accordance with previous theoretical studies of layered MoS₂ slabs [66, 67]. Since the hexagonal arrangement of protrusions in STM images does not change by varying the tunneling parameters, the triangular clusters are interpreted as MoS₂ nanoclusters with the (0001) basal plane oriented parallel to the Au(111) surface and with the protrusions reflecting the S atoms in the topmost layer.

The average cluster height is 2.0 ± 0.3 Å, which is less than the geometrical distance

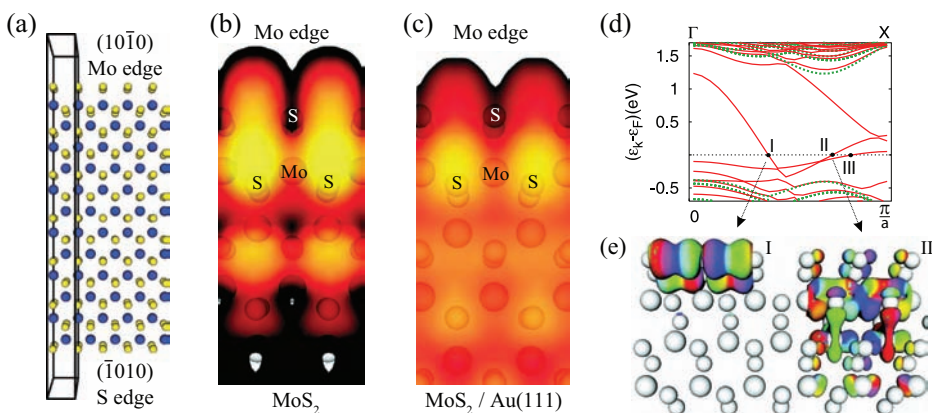


Figure 3.7. (a) The unit cell used in the DFT calculations of single-layer MoS₂. (b) and (c) Simulated STM images of the (10 $\bar{1}$ 0) Mo edge with sulfur dimers with and without Au(111) substrate effects included, respectively. The main effect of the Au(111) substrate is seen to be associated with the basal plane. (d) The calculated band structure for MoS₂. The red lines belong to an MoS₂ slab exposing the (10 $\bar{1}$ 0) Mo edge and the ($\bar{1}$ 010) S edge and the green lines correspond to an infinite MoS₂ layer. The infinite layer clearly shows a band gap, whereas the edge terminated system displays three bands crossing the Fermi level. (e) The contours of the electronic wave functions associated with the edge states localized entirely on the (10 $\bar{1}$ 0) Mo edge (I and II). The last edge state (III) (not shown) is associated with the ($\bar{1}$ 010) S edge (100% S).

between the top and the bottom S layers in a single-layer MoS₂ (see Fig. 3.4a). The cluster height is, however, found to be bias dependent and approaches asymptotically the geometrical value of a single MoS₂ layer with increasing bias [68], and it is thus concluded that the MoS₂ clusters consist of a single S-Mo-S layer, i.e. only one of the two building blocks in the unit cell of 2H-MoS₂ is present.

3.5.1 Morphology of non-promoted MoS₂ nanoclusters

The very strong preference for clusters with a triangular shape shows that this is the equilibrium shape under the conditions of the experiment. The equilibrium shape of an MoS₂ nanocluster is governed by the relative edge free energies of two different low-index edge terminations of the MoS₂(0001) basal plane, that is, the (10 $\bar{1}$ 0) Mo edge and ($\bar{1}$ 010) S edge, respectively. The shape of a cluster can be quantified in the so-called Wulff construction (see Fig. 3.6a), which states that the equilibrium shape minimizes the total free energy of the cluster, i.e. the sum over all edge free energies times the corresponding edge length ($\sum_i \gamma_i \times l_i$) [69, 70]. The plotted vectors with a common origin have a length corresponding to the edge free energies (γ_{Mo} and γ_{S}) of the (10 $\bar{1}$ 0) Mo edge and ($\bar{1}$ 010) S edge, respectively. The inner envelope of the tangent plane of the end points of the radius vectors describes the equilibrium shape of the cluster. If

the relative stability of one edge exceeds a factor of two compared to the other, a triangular shape will result as observed in the experiments (Fig. 3.5b). On the other hand, comparable stability will result in a hexagonally truncated shape, and in the limit where they are equal, the shape will be perfectly hexagonal. It should be noted that the Wulff construction is a thermodynamical equilibrium description, and the minor presence of metastable clusters with shapes different from triangular, i.e. truncated triangular, elongated hexagonal etc. reveals that some kinetic limitations are present. Similarly, corner and other finite size effects, which become increasingly important as the cluster size is reduced, are not included in this description [71]. Indeed, in Chapter 5 it will be shown that Ni-promoted MoS₂ nanoclusters display a size dependent shape.

3.5.2 Edge structure of MoS₂ nanoclusters

The identity of the edges displayed by the triangular clusters is inferred from a comparison between atomically resolved STM images, such as Fig. 3.5b, and DFT calculations [72]. The identification rests on two primary observations:

- (1) The outermost row of protrusions are observed to be *out of registry* with the basal plane atoms as indicated by the white circles in Fig. 3.5b.
- (2) The presence of a pronounced bright brim located adjacent to the outermost row of protrusions.

These observations cannot readily be explained by a simple geometric model of the edges. Instead, the appearance of the edges observed by the STM reflects a convolution of electronic and geometric features of the MoS₂ edge.

Both the shift of edge protrusions out of registry and the pronounced bright brim can only be reproduced in DFT-based STM simulations of a (10 $\bar{1}$ 0) Mo edge fully saturated by sulfur dimers [43, 73, 74]. The DFT calculations, furthermore, show that the (10 $\bar{1}$ 0) Mo edge is metallic as opposed to the interior of the MoS₂, which is semiconducting like bulk MoS₂. Imaging of the basal plane of the MoS₂ clusters is, however, possible at all biases due to the effect of the Au(111) substrate that renders the interior of the MoS₂ weakly metallic due to charge donation [43]. This observation is also seen in the simulated STM image in Fig. 3.7c where the effects of the Au(111) substrate is included.

The distinctive features of the (10 $\bar{1}$ 0) Mo edge are associated with two metallic edge states with bands penetrating into the band gap region of MoS₂ and crossing the Fermi level as observed in Fig. 3.7d. One of the edge states (I) originates from the overlap of p_x orbitals between the S dimers terminating the (10 $\bar{1}$ 0) Mo edges as seen from the plot of the wave function contours in Fig. 3.7e. The overlapping p_x orbitals yields a maximum in local density of states, and consequently, as seen from the simulated STM image of the (10 $\bar{1}$ 0) Mo edge (Fig. 3.7b), the STM primarily images the interstitial region between the S dimer pairs as bright, which accounts for the shifted position of the edge protrusions in the experimental images (Fig. 3.5b). The second edge state (II) is related to the fully sulfided (10 $\bar{1}$ 0) Mo edge and has a quite complicated structure extending into the first few rows counted from the edge and inwards. This state is primarily responsible for the STM imaging of the bright brim on the clusters.

Based on the good agreement between the experimental images and the simulations, it was concluded that the triangular MoS_2 clusters are terminated by a $(10\bar{1}0)$ Mo edge fully saturated by sulfur dimers (Fig. 3.6b). The triangular equilibrium shape of unsupported MoS_2 under the present synthesis conditions was later confirmed by cluster DFT calculations performed by Schweiger *et al.* [74].

The presence of the brim structure is catalytically highly interesting since previous studies have showed that the brim sites are active for hydrogenation and C-S splitting of thiophene even on the fully sulfided edges [75, 76]. The catalytic properties of the MoS_2 -based catalysts are thus not only determined by under-coordinated sites, such as sulfur vacancies as traditionally believed, but also by the brim structure.

Larger sulfur containing molecules, such as dibenzothiophene and alkyl-substituted dibenzothiophenes (see Fig. 1.4), can undergo HDS via two different reaction pathways [77]: (i) a direct desulfurization (DDS) route that leads to the formation of biphenyls and (ii) a hydrogenation route (HYD) where one of the benzene rings is hydrogenated prior to the sulfur removal. The HYD route is especially important for the sterically hindered substituted dibenzothiophenes where the substituted groups prevent the interaction of the sulfur atom with the active site in the DDS route. Consequently, the desulfurization of substituted dibenzothiophenes proceeds mainly via the HYD route. The brim sites enable hydrogenation of these highly sterically hindered molecules and may thus be the key to ultra-deep desulfurization of fuels where desulfurization of substituted dibenzothiophenes is a prerequisite.

CHAPTER 4

Size-dependent structure of MoS₂ nanoclusters

In this chapter, the structural progression of MoS₂ nanoclusters is followed as a function of their size, and it is shown that the equilibrium structure is altered when the cluster size is reduced.

4.1 Introduction

Within the area of nanomaterials it is well known that “*small is different*”, which implies that nanostructures may have new functional properties. Properties, such as conductivity, color, reactivity, magnetism, and melting point, may thus be entirely different for the nanomaterial compared to the same properties for a material with macroscopic dimensions [78]. The dimensions of a material is therefore an important parameter to consider in the development of new nanomaterials. Not least in catalysis, where the active materials today are confined to a limited number of metals, tuning the size of the catalytic particles may help in the development of new and better catalysts.

In the previous chapter, the atomic-scale structure of triangular single-layer MoS₂ nanoclusters was summarized based on previous work within the Århus SPM group [43, 79]. However, these studies were concerned with the larger MoS₂ clusters (> 500 Å²).

In this chapter, the study of the atomic-scale structure of MoS₂ nanoclusters is extended to include the smallest clusters (100-500 Å²), and it is shown that the equilibrium structure displays a very strong size dependence driven by the tendency to optimize the sulfur excess at the cluster edges.

4.2 Experimental details

The synthesis details follow the procedure described in Section 3.3. However, it is possible to favor the formation of the smallest nanoclusters (< 500 Å²) by lowering the post-annealing temperature to 623 K and decreasing the amount of Mo deposited onto the surface (~7-8% ML).

4.3 “Magic” sized MoS₂ nanoclusters

Figure 4.1 displays the distribution of the size of the triangular MoS₂ nanoclusters. The histogram was constructed by carefully measuring the area of the individual triangular nanoclusters in large-scale STM images, such as Fig. 3.5a. The envelope of the distribution is seen to follow a typical profile expected for a ripening scenario [80]. The histogram, however, exhibits a fine structure with distinct maxima reflecting that certain “magic” sized clusters are thermodynamically favored. This finding is surprising since the crystal structure of MoS₂ does not impose such restrictions. The distinct maxima of the histogram allow a clear discrimination between different clusters sizes, and each peak can thus be assigned to a particular cluster size by matching their apparent size in atom-resolved STM images in terms of the number of Mo atoms (n) at the edge of an MoS₂ triangle. The vertical dashed lines in the histogram indicate the estimated cluster sizes in terms of n . Surprisingly, the fine structure of the cluster size distribution reveals that larger clusters belonging to the sequence with even $n = 8, 10, 12, \text{ or } 14$ are greatly favored over clusters with an odd number ($n = 7, 9, 11, \text{ or } 13$). Clusters with an odd n

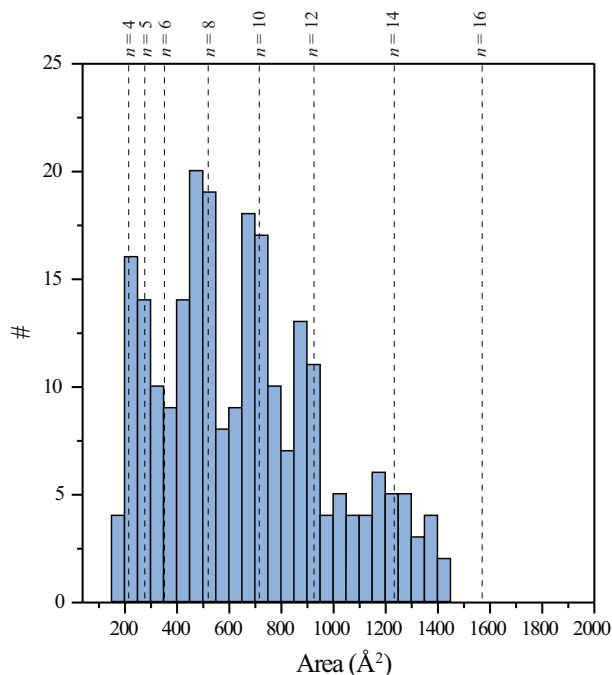


Figure 4.1. Size distribution of the triangular MoS_2 nanoclusters. The histogram was constructed by carefully measuring the area of the individual triangular nanoclusters in large-scale STM images, such as Fig. 3.5a. The vertical lines indicate the estimated clusters size in terms of the number of Mo atoms (n) along the edge of an MoS_2 triangle.

can occasionally be observed in direct analysis of atom-resolved STM images, but the odd numbered clusters are greatly underrepresented.

4.4 Size-dependent atomic-scale structure

To gain further insight into the factors controlling the size and shape of the triangular nanoclusters and thus the origin of the “magic” sized MoS_2 nanoclusters, the structure of the clusters was analyzed in detail in atom-resolved STM images (see Fig. 4.2).

4.4.1 $(10\bar{1}0)$ Mo edge terminated clusters

The larger clusters (Figs. 4.2a-4.2d) display the two distinct characteristics of the clusters treated in Section 3.5: a bright brim located adjacent to the outermost row of protrusions and a shift of half a lattice constant of the outermost protrusions relative to the S lattice of the basal plane. It is thus concluded that these clusters reflect triangular MoS_2

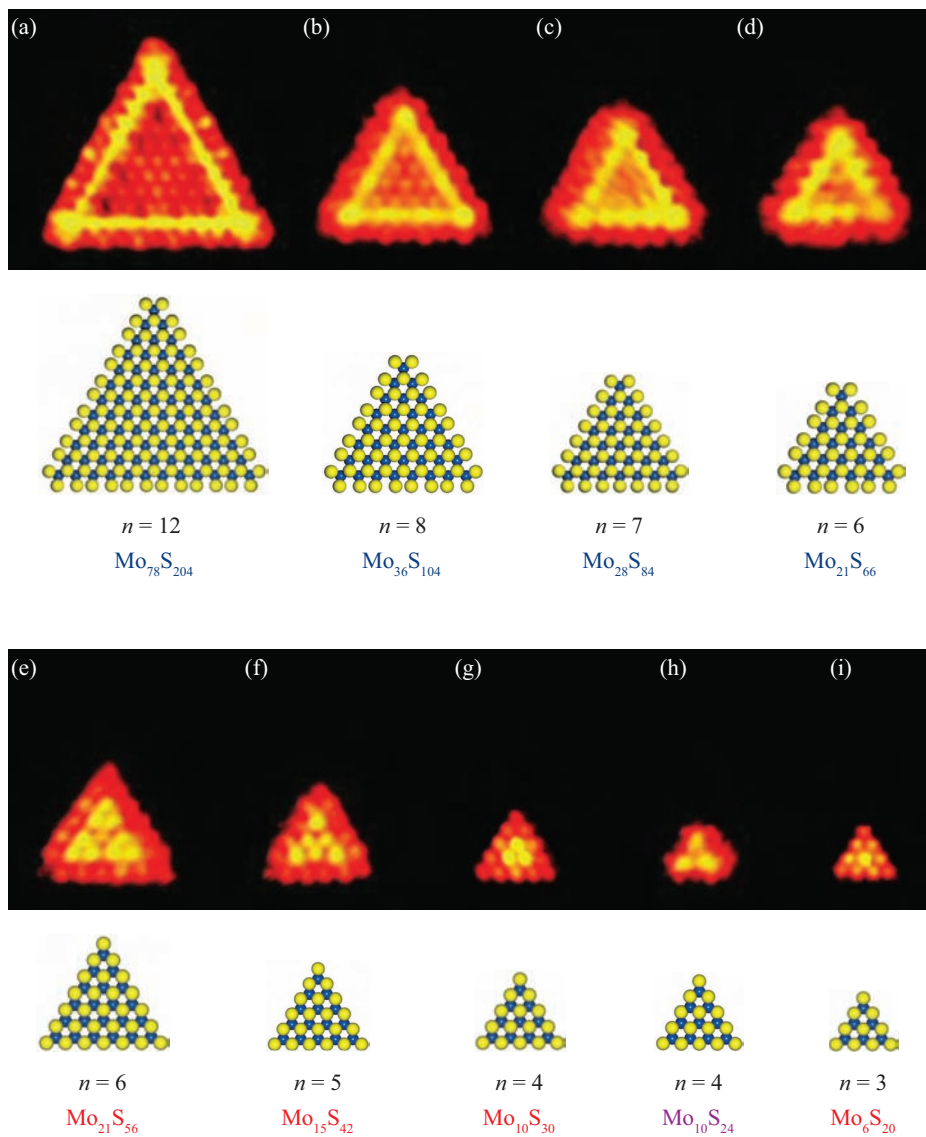


Figure 4.2. Nine atomically resolved STM images of MoS₂ nanoclusters of different sizes in the range $n = 3 - 12$, where n denotes the number of Mo atoms at the edge of the MoS₂ triangle. Below each STM image is a cluster ball model representing the actual cluster size and structure. Color code - Mo: blue and S: yellow.

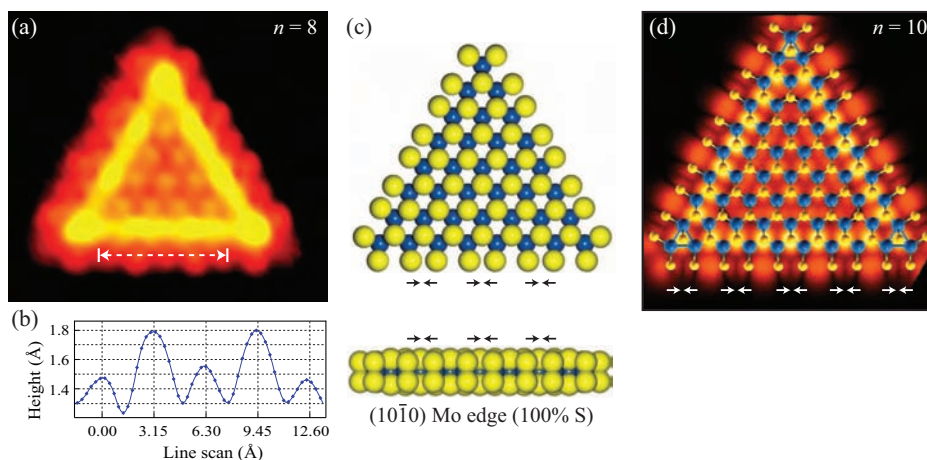


Figure 4.3. (a) STM image of an $n = 8$ triangular nanocluster. (b) Line scan showing a double period pattern present in clusters with an even n and $n \geq 6$. (c) Ball model of the cluster depicted in (a). The clusters is terminated by fully sulfided $(10\bar{1}0)$ Mo edges displaying an alternating contraction and extension of the gap between dimer pairs, which gives rise to the double period pattern in the STM images, as shown in the DFT-based STM simulation in (d) (adapted from Ref. [81]).

nanoclusters terminated by a $(10\bar{1}0)$ Mo edge fully saturated with sulfur dimers (100% S). In Section 3.5.2 it was demonstrated how the shifted position of the edge protrusions is caused by a maximum of LDOS in the interstitial region between sulfur dimer pairs due to overlapping p_x orbitals of the sulfur dimers. The STM thus images the interstitial region between the S dimer pairs as bright, and consequently the number of Mo atoms, n , (equal to the number of sulfur dimers) is in reality always the number of protrusions counted in the STM images *plus* one.

A closer inspection of the edge structure of the larger MoS_2 nanoclusters reveals that the sulfur dimers reconstruct at the edge. As illustrated in the case of $n = 8$ in Fig. 4.3, a bright-dark alternating pattern of protrusions is observed along the edge. The line scan in Fig. 4.3b shows that the pattern is repeated with a periodicity of exactly twice the 3.15 Å distance between the sulfur dimers. Recent DFT calculations suggest that the double periodicity can be explained by a slight reconstruction of the sulfur dimers [43, 74, 81]. If the lateral distance between the between two sulfur dimers is decreased, the overlap between the p_x orbitals is changed; the destructive interference between the lobes of these orbitals becomes stronger, and the resulting intensity of the protrusion is weakened. If on the other hand the distance between the two sulfur dimers is increased, the destructive interference becomes weaker, and the intensity of the protrusion is enhanced. As a result, the edges appear in STM images with alternating bright-dark protrusions as demonstrated in the STM simulation in Fig. 4.3d. Interestingly, Schweiger *et al.* [74] have, based on clusters calculations for n up to 11, reported that the double periodicity

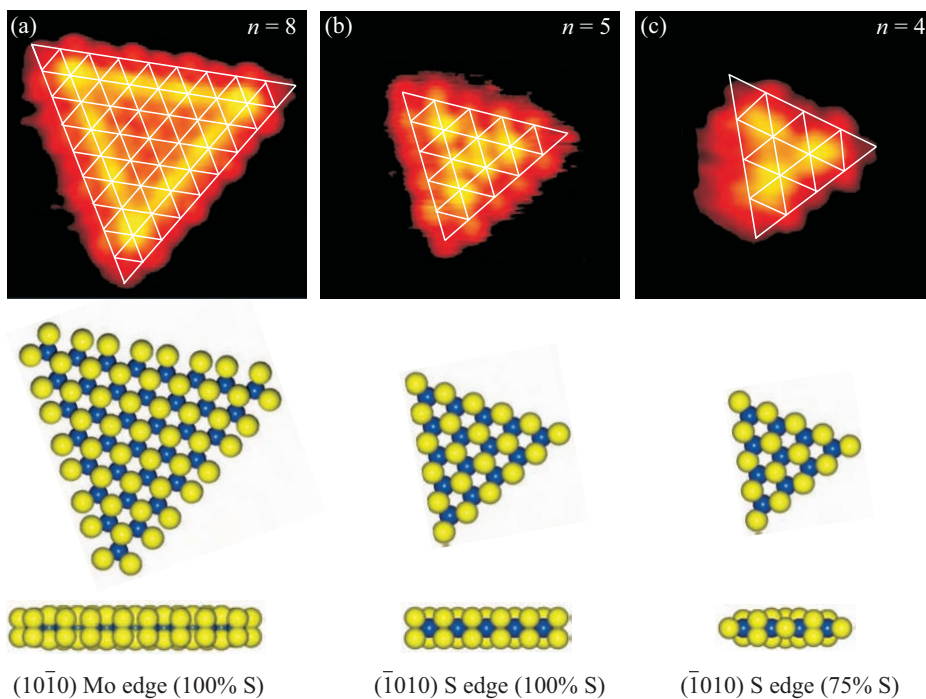


Figure 4.4. STM images of triangular nanoclusters with: (a) $n = 8$, (b) $n = 5$, and (c) $n = 4$. The superimposed grids show the registry of the outermost row of protrusions with the basal plane sulfur atoms. The atomic-scale structure of the three clusters is shown in the ball models below the STM images.

pattern is dependent on the parity of the edge, i.e. it is only energetically favorable for the dimers to reconstruct when the number of edge dimers is even. This finding is in excellent agreement with the present experimental findings where the (10 $\bar{1}0$) Mo edge (100% S) terminated clusters with even n (Figs. 4.2a, 4.2b, and 4.2d) all display the distinct double periodicity, whereas the less abundant clusters with odd n (Fig. 4.2c) do not. The preference for clusters to assemble with an even number of sulfur dimers (Mo atoms) along the edge can thus be understood in terms of frustration effects occurring at the cluster corners. If an odd number of dimers is present, one terminal sulfur dimer cannot be paired, which leads to a less stable cluster. The strong preference for clusters with an even number of Mo atoms along the edge indicates that the cluster morphology is controlled by the edge structure to a great extent.

4.4.2 ($\bar{1}010$) S edge terminated clusters

As the size of the triangular nanoclusters is reduced below six Mo atoms ($n = 6$) along the edge, an unexpected transition occurs. The transition is clearly demonstrated in

Figs. 4.2d and 4.2e. The cluster in Fig. 4.2e displays 5 clear protrusions at the edges (not counting the corner atoms), which is the same number of edge protrusions as for the slightly larger cluster in Fig. 4.2d.

However, whereas the cluster in Fig. 4.2d is terminated by $(10\bar{1}0)$ Mo edges (100% S), as demonstrated in the previous section, the cluster in Fig. 4.2e as well as the even smaller clusters in Figs. 4.2g-4.2i have a pronounced different appearance in the STM images. The characteristic bright brim is replaced by a hexagonal lattice of clearly resolved protrusions, and a grid superimposed on the clusters clearly demonstrates that the outermost rows of protrusions are now *in registry* with the basal plane atoms as opposed to the larger clusters (see Fig. 4.4). In addition, the outermost rows of protrusions of the $n = 4$ cluster depicted in Fig. 4.4c are imaged with a lower relative intensity, and they display a pronounced buckling structure.

The edge structure observed for the clusters depicted in Figs. 4.2e-4.2i matches very closely that of the $(\bar{1}010)$ S edge. The $(\bar{1}010)$ S edge has previously been experimentally observed by STM for hexagonally truncated, single-layer MoS_2 nanoclusters synthesized in a mixture of hydrogen and hydrogen sulfide (sulfo-reductive conditions) [72]. Both the experimental images of the hexagonally truncated MoS_2 nanoclusters and simulated STM images from DFT [43] show that the fully sulfided $(\bar{1}010)$ S edge appears as the clusters in Figs. 4.2e-4.2i with clearly resolved bright protrusions behind the outermost row of protrusions, which are imaged slightly fainter and *in registry* with the basal plane atoms. The close match implies, that for the smallest clusters the $(\bar{1}010)$ S edge (100% S) is the energetically most favored edge termination.

For the cluster with $n = 4$ (Fig. 4.4c), the buckling structure observed at the edge suggests a third structure with less than 100% S coverage. The observed edge structure is proposed to be a partially saturated $(\bar{1}010)$ S edge with a 75% S coverage, which is found by DFT calculations to be only slightly less stable than the fully sulfur saturated $(\bar{1}010)$ S edge [43, 82]. The buckling structure is associated with the geometric arrangement of single and double S atoms placed in an alternating fashion along the edge (Fig. 4.4c).

Thus, based on the STM observations, it is concluded that triangular MoS_2 nanoclusters have an edge structure that is dependent on the actual size of the clusters.

4.5 Origin of the size effect

The origin of the size effect is linked to the stoichiometry of the nanoclusters. The overall stoichiometry of the triangular MoS_2 nanoclusters changes with size owing to the variation in the fraction of edge atoms relative to bulk atoms. In Fig. 4.5 the ratio of sulfur to molybdenum atoms (N_S/N_{Mo}) is plotted as a function of the cluster size in terms of n for triangles terminated by five of the most relevant MoS_2 edges. Table 4.1 summarizes the formula used for the calculations of N_S/N_{Mo} . The upper curve in Fig. 4.5 (filled squares) represents MoS_2 triangles terminated by fully sulfided $(10\bar{1}0)$ Mo edges, and it is seen that the sulfur excess relative to the bulk stoichiometry increases very steeply for the smallest clusters. Around $n = 6$, the N_S/N_{Mo} ratio jumps significantly above a factor of three. Triangles with a lower S coverage, or terminated by $(\bar{1}010)$ S edges, have a different scaling with n . The curve for triangles terminated with

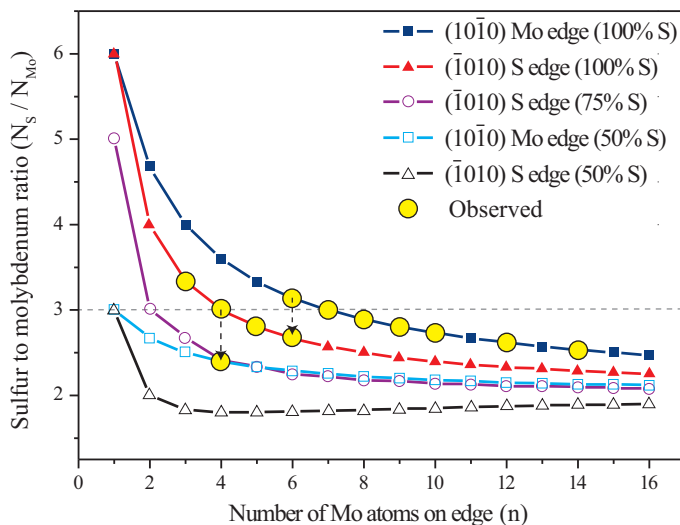


Figure 4.5. The ratio of sulfur atoms to molybdenum atoms (N_S/N_{Mo}) calculated as a function of the number of Mo atoms at the edge (n) for triangular Mo_xS_y nanoclusters, where $x = N_{Mo}$ and $y = N_S$. The five curves each represent clusters terminated with the most stable configurations corresponding to either the $(10\bar{1}0)$ Mo edge with 50% or 100% sulfur coverage or the $(\bar{1}010)$ S edge with 50%, 75%, or 100% sulfur coverage. The corresponding analytical expressions for the N_S/N_{Mo} ratio as a function of n are given in Table 4.1. The yellow circles denote the clusters observed in atom-resolved STM images for which the edge structure is identified.

fully sulfided $(\bar{1}010)$ S edges is presented by solid triangles, and for $n = 4$ it is seen that the N_S/N_{Mo} reaches a factor of three. These crossing points coincide precisely with the sizes for which both the transition from the $(10\bar{1}0)$ Mo edge to the $(\bar{1}010)$ S edge and the transition from the fully sulfided $(\bar{1}010)$ S edge to a 75% S coverage are observed, respectively. Hence, this observation suggests that the transitions are related to a supersaturation of sulfur in the clusters. In particular, it seems that clusters with a S:Mo stoichiometry of more than $\sim 3.5:1$ are not favored. The edge termination of the triangles is thus determined not only by the tendency to lower the edge free energy by exposing the most stable $(10\bar{1}0)$ Mo edge, but also by a counteracting tendency for edge restructuring to reduce sulfur excess.

4.6 Implications for catalysis

The size-dependent shape of the MoS_2 nanoclusters is not just an interesting nanoscience phenomenon but may also help improve the industrial catalyst. It is well known that only the edges of the MoS_2 nanoclusters are catalytic active; the basal plane is completely inactive, and since the chemical and thus catalytic properties are affected

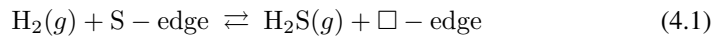
Edge type (S coverage)	N_{Mo}	N_{S}
(10 $\bar{1}$ 0) Mo edge (100% S)	$\frac{1}{2}n(n+1)$	$n(n+5)$
(10 $\bar{1}$ 0) Mo edge (50% S)	$\frac{1}{2}n(n+1)$	$n(n+2)$
($\bar{1}$ 010) S edge (100% S)	$\frac{1}{2}n(n+1)$	$n(n+3)+2$
($\bar{1}$ 010) S edge (75% S)	$\frac{1}{2}n(n+1)$	$n(n+3)+2-3n/2$, for even n $n(n+3)+1-3(n-1)/2$, for odd n
($\bar{1}$ 010) S edge (50% S)	$\frac{1}{2}n(n+1)$	n^2+2

Table 4.1. Stoichiometry and composition of Mo_xS_y nanoclusters as a function of the number of Mo atoms at the edge (n).

when the edge structure is changed, the present study shows that the size of the catalytic particles is an important parameter to consider. The theoretical framework used in Refs. [43, 74] to estimate the edge free energies of MoS_2 as a function of the chemical potential of sulfur could be applied to provide further insight in this regard and may be used to estimate key parameters determining the catalytic properties of the MoS_2 nanoclusters, such as the sulfur bonding strength (ΔE_{S}), or the tendency to dissociate hydrogen. Both parameters are expected to exhibit a correlated variation with size as observed for the structural changes for clusters because the different edge types are known to have very different affinities to sulfur and hydrogen.

4.6.1 Sulfur vacancies

The sulfur bonding strength has a direct influence on the formation of sulfur vacancies at the edges, that is, sites where Mo atoms have incomplete coordination to sulfur. Fully sulfided MoS_2 nanoclusters are generally not believed to be the most active ones in HDS catalysis since they are sulfur-saturated and thus presumably incapable of adsorbing sulfur containing molecules. Before the HDS reaction can take place, the cluster needs to be reduced with hydrogen to create sulfur vacancies. In a simple description, sulfur vacancies are in equilibrium with hydrogen and dihydrogensulfide gases:



where \square denotes a sulfur vacancy. If equilibrium is assumed, the fraction of vacancies at edge sites can in a simple kinetic model be expressed as:

$$\theta_{\square} = \frac{1}{1 + \frac{P_{\text{H}_2\text{S}}}{P_{\text{H}_2}} e^{\Delta E_{\text{S}}/k_B T}} \quad (4.2)$$

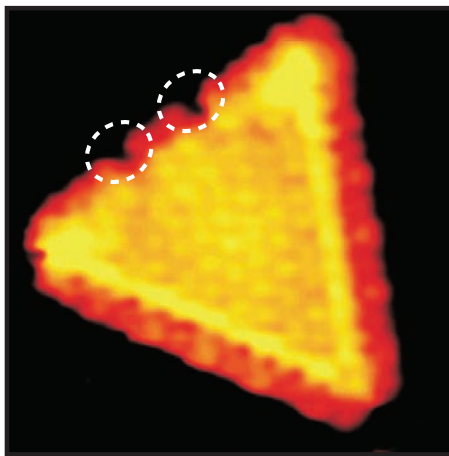


Figure 4.6. Atom-resolved STM image ($46 \text{ \AA} \times 47 \text{ \AA}$) of a $(10\bar{1}0)$ Mo edge terminated MoS_2 nanocluster exposed to atomic hydrogen. The two sulfur vacancies (indicated by white circles) are present on one of the edges.

where $P_{\text{H}_2\text{S}}$ and P_{H_2} are the partial pressures of H_2 and H_2S , respectively, ΔE_{S} is the formation energy associated with a vacancy, which is negative if the formation of a vacancy is favorable. The expression states that a high ratio of H_2 to H_2S combined with high temperature favors vacancy formation. Under these conditions the vacancy concentration will thus be high if the reaction is not too endothermic. The expression in Eq. 4.2 clearly demonstrates the direct dependence of vacancy formation on ΔE_{S} and hence the edge structure.

However, after exposing MoS_2 nanoclusters to molecular hydrogen gas (H_2), the STM images do not show any changes at the edges that can be related to vacancy formation, irrespectively of size of the MoS_2 nanoclusters. This apparent lack of reactivity of the clusters with molecular hydrogen is most likely due to the rather large dissociation energy of the H_2 molecule (4.52 eV) [32], which may cause the reaction to be severely activated. The extensive gap of a least thirteen orders of magnitude between the industrial process pressures and the ones realized under the present experimental conditions may then explain the apparent low possibility of reacting sufficiently activated hydrogen molecules with edge S atoms to form vacancies.

To surmount the reaction barrier, the MoS_2 clusters can instead be reduced by highly reactive atomic hydrogen. The predissociation of hydrogen and the subsequent dosage are performed by placing the sample facing a glowing hot tungsten filament in a background atmosphere of hydrogen ($P_{\text{H}_2} = 1 \cdot 10^{-6}$ mbar). As a result, small amounts of hydrogen molecules dissociate on the filament and then find their way onto the sample [83]. Prior to the atomic hydrogen treatment, the sample was heated to ~ 500 K, and this temperature was maintained throughout the exposure due to the close vicinity of the hot W filament.

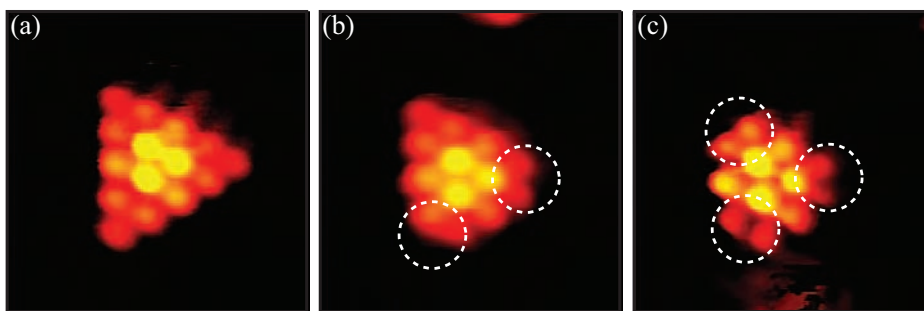


Figure 4.7. Three atom-resolved STM images ($30 \text{ \AA} \times 30 \text{ \AA}$) of three $(\bar{1}010)$ S edge terminated MoS_2 nanoclusters. The clusters in (b) and (c) have been exposed to atomic hydrogen and display two and three corner sulfur vacancies, respectively, as indicated by the white circles.

After the atomic hydrogen treatment, neither size distribution nor the shape of the MoS_2 nanoclusters were changed. However, STM images with atomic resolution clearly demonstrate that sulfur vacancies are formed at the edges. The preferential location of the sulfur vacancies is dependent on the structure of the edge. On the larger $(10\bar{1}0)$ Mo edge terminated MoS_2 nanoclusters, the sulfur vacancies are found to be located on the edges (Fig. 4.6), whereas the preferred location of the sulfur vacancies on the smaller $(\bar{1}010)$ S edge terminated MoS_2 nanoclusters is at the corners of the clusters (Fig. 4.7).

This finding could suggest that the vacancy formation on the $(\bar{1}010)$ S edge is energetically less favorable compared to that of the $(10\bar{1}0)$ Mo edge. However, recent DFT calculations [43] indicate that the vacancy formation energy is lower at the $(\bar{1}010)$ S edge (100% S) ($\Delta E_S = 0.23 \text{ eV}$) than at the $(10\bar{1}0)$ Mo edge (100% S) ($\Delta E_S = 0.49 \text{ eV}$ ¹). These calculations, however, also show that hydrogen adsorbs strongly ($\Delta E_H = -1.26 \text{ eV}$) on the fully sulfided $(\bar{1}010)$ S edge. The large gain of energy associated with hydrogen adsorption on the $(\bar{1}010)$ S edge suggests that hydrogen in fact stabilizes sulfur on the $(\bar{1}010)$ S edges. Accordingly, dosing large amounts of atomic hydrogen does not lead to sulfur vacancies but only adsorbed hydrogen, which explains why no sulfur vacancies were observed on the $(\bar{1}010)$ S edge. A similar observation has previously been made for hexagonally truncated MoS_2 nanoclusters synthesized in a mixture of hydrogen and hydrogensulfide (sulfo-reductive conditions). Exposing these clusters to atomic hydrogen did not lead to vacancy formation at the $(\bar{1}010)$ S edges either [72]. The corner sulfur atoms of the triangular $(\bar{1}010)$ S edge terminated nanoclusters presumably do not experience the same stabilizing effect of adsorbed hydrogen since sulfur vacancies here are readily formed. The present study, however, shows that it is in fact possible to have sulfur vacancies at the edges of a $(\bar{1}010)$ S edge terminated cluster. The smallest clusters (Fig. 4.4c) are seen to contain spontaneously formed sulfur vacancies at the edge due to the edge restructuring to reduce the sulfur excess.

The observation that the nature of the formed vacancies depends on the actual size of

¹Without S dimer pairing.

the MoS₂ nanoclusters is highly interesting since the results thus suggest that tailoring the catalytic nanoparticles to a specific size may help optimize the performance of the desulfurization catalyst.

4.7 Conclusion

In the present chapter, it was demonstrated that triangular MoS₂ nanoclusters exhibit a highly size-dependent structure. The MoS₂ nanoclusters, independent of their size, all display a very distinct triangular shape. However, a comprehensive analysis of the size distribution revealed that certain “magic” clusters with an even number of Mo atoms (n) along the edge are favored. The preference of even n clusters was shown to be due to a frustration effect occurring at the cluster corners. All large clusters ($n \geq 6$) are terminated by sulfur dimers, and these S₂ dimers have a tendency to pair up. If an odd number of dimers is present, one terminal S₂ dimer cannot be paired, thus leading to a less stable cluster.

The study furthermore showed that if the cluster size is reduced below $n = 6$, the edge structure of the clusters changes from a (10 $\bar{1}$ 0) Mo edge termination to a ($\bar{1}$ 010) S edge termination. As the particle size is reduced, the actual stoichiometry of the nanoparticles deviates from the bulk MoS₂ value as the relative S content increases. This change in edge structure occurs to lower the sulfur to molybdenum ratio in the particles since too S rich particles are unstable.

In future studies, it would be interesting to perform optical spectroscopy studies [84–86] or reactivity studies on size-selected MoS₂ nanoclusters to investigate the variation of their chemical or electronic properties as a function of size and search for optimum performance of this nanomaterial, not only in regard to HDS but also as, e.g. a potential photocatalyst [87] or for hydrogen production [88].

CHAPTER 5

Promoter atoms

In the present chapter, the effects of Co and Ni promoter atoms on the MoS₂-based model catalyst are investigated. The promoter atoms are found to have a profound influence on the cluster morphology, and the exact position of the promoter atoms is determined from atom-resolved STM images. In the end of this chapter, the study is extended to include Fe and Cu as promoter atoms, and it is shown that shape of the MoS₂ nanoclusters has a direct dependence on the type of promoter atom.

5.1 Introduction

The activity of the MoS₂-based catalyst increases dramatically when either Co or Ni is added. Since only a small fraction of Co or Ni relative to Mo is required, Co and Ni are considered to be *promoters* rather than catalysts in their own right. Not only is the overall hydrotreating reactivity generally found to be increased by more than an order of magnitude, but the specific selectivity with respect to hydrodesulfurization (HDS), hydrodenitrogenation (HDN), and hydrogenation (HYD) is also found to be dependent on the type of promoter atoms.

Several attempts have been made to correlate the structure of the active promoted phases to the reactivity and selectivity typically by a combination of analytical techniques and measurements of the HDS or HYD activity [21, 44, 45]. Recently, general agreement seems to have been reached on the so-called “CoMoS” model, which originally was proposed by Topsøe, Clausen, and co-workers [89–91]. In the CoMoS model, Co is present in three different phases (see Fig. 5.1):

- (i) **Co:Al₂O₃**: Co atoms dissolved in the Al₂O₃ support.
- (ii) **Co₉S₈**: The thermodynamically stable cobalt sulfide.
- (iii) **CoMoS**: A bimetallic sulfide compound of Co, Mo, and S. This phase has an MoS₂-like structure into which the Co atoms are incorporated. The phase is non-stoichiometric with respect to the Co/Mo ratio, and no unit cell can be defined in a crystallographic sense.

All three phases are found to co-exist in the catalyst under operation, but only the CoMoS structure is found to be associated with an appreciable catalytic activity. This phase is in the CoMoS model described as being essentially MoS₂-like, but with additional Co atoms embedded at the perimeter of the cluster. Since only the edges of MoS₂ are reactive, it has been proposed that the Co atoms located at the edges create new and more reactive sites, e.g. in the form of new types of sulfur vacancies at the Co promoter atoms [92].

The promoting effect of Co is, however, still under intensive debate since the exact position of the promoting atoms cannot be directly determined with traditional catalyst characterization tools [50, 93, 94]. The Ni-promoted catalyst has been subject to fewer studies compared to the Co-promoted. Similar to the Co-promoted catalyst, a NiMoS phase is found [21, 95, 96], but no direct information about the location of the promoting Ni atoms has been revealed.

In this chapter, the model system consisting of gold-supported MoS₂ nanoclusters will be extended to include the effect of promoter atoms. The first part of the chapter is concerned with the morphology and atomic-scale structure of the industrial employed CoMoS and NiMoS nanoclusters. In the second part the morphological investigation is extended to include MoS₂ clusters promoted with Fe and Cu, the so-called FeMoS and CuMoS structures. It is well known that CoMoS and NiMoS display a superior catalytic activity over the Fe- and Cu-promoted catalysts. However, from both a scientific and industrial point of view it is highly interesting to investigate why Co and Ni are better promoters compared to Fe and Cu.

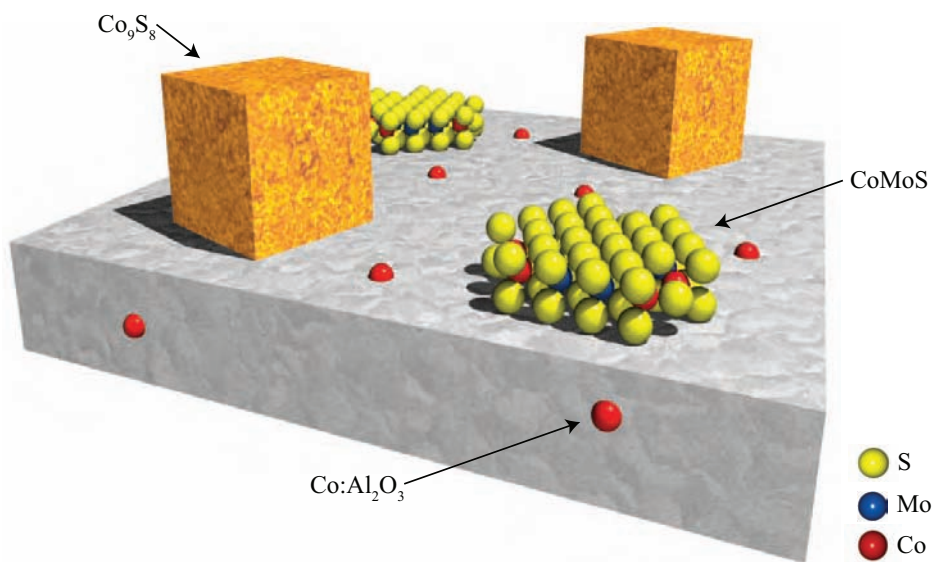


Figure 5.1. Schematic illustration of the CoMoS model. Under reaction conditions, Co is present in three different phases: (i) Co dissolved in the Al_2O_3 , (ii) a thermodynamically stable cobalt sulfide (Co_9S_8), and (iii) the catalytically active CoMoS nanoclusters consisting of a non-stoichiometric bimetallic sulfide.

5.2 Experimental details

In order to create the CoMoS and NiMoS nanoclusters, different synthesis procedures were investigated, and it was found that the tendency to form such a phase is highly dependent on the preparation method. This finding is not surprising since changes in preparation parameters of the industrial CoMo or NiMo-based catalysts also strongly influence the phase distribution [21].

For both Co- and Ni-promoted systems, the formation of first non-promoted MoS_2 , by the preparation described in Section 3.3, followed by a deposition of Co or Ni in a sulfiding atmosphere did not lead to the formation of a bimetallic phase, but instead produced well-separated MoS_2 nanoclusters and cobalt or nickel sulfide islands (similar to the structures shown in Figs. 5.2a and 5.2b). In order to form the bimetallic CoMoS or NiMoS phase, Mo should instead be co-deposited together with either Co or Ni from the e-beam evaporator in the sulfiding atmosphere consisting of H_2S . The exact order of deposition was found to be crucial. The most efficient method involved first deposition of only Mo in a sulfiding atmosphere to form sulfided Mo embryos followed by co-deposition of additional Mo together with Co or Ni to form a capped layer of a bimetallic sulfide. The sample was then annealed to 673 K while maintaining the sulfiding atmosphere in order to crystallize the bimetal-sulfide nanoclusters. The total

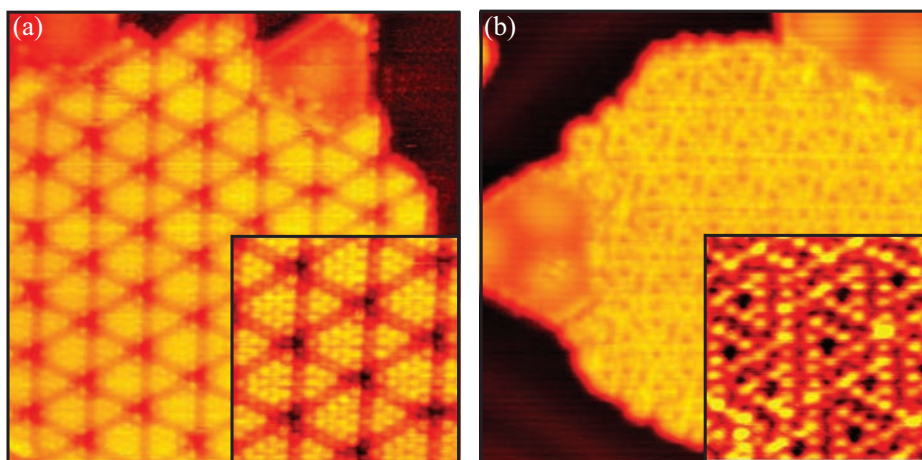


Figure 5.2. STM images of: (a) Cobalt sulfide ($150 \text{ \AA} \times 150 \text{ \AA}$, insert $60 \text{ \AA} \times 60 \text{ \AA}$) and (b) Nickel sulfide ($175 \text{ \AA} \times 175 \text{ \AA}$, insert $50 \text{ \AA} \times 50 \text{ \AA}$). The inserts show atom-resolved STM images of the structures.

coverages were 10% of a monolayer (ML) for Mo and 4% ML for Co or Ni, respectively.

5.3 Characterization of CoMoS and NiMoS

The synthesis procedure described above produces two significantly different surface structures for both the Co- and Ni-promoted model systems:

- (i) Large patches of cobalt or nickel sulfide islands, respectively, predominantly formed next to the Au(111) step edges.
- (ii) Well-dispersed CoMoS or NiMoS nanoclusters formed on the terraces of the Au(111) substrate.

The former is formed as a result of excess amounts of Co or Ni relative to the available number of substitutional sites on the MoS_2 nanoclusters. The predominant growth at the substrate step edges is initiated by a high mobility of Co and Ni on the Au(111) surface in the presence of H_2S . This could be observed directly by recording *in-situ* STM movies of the formation of cobalt or nickel sulfide islands after H_2S was introduced to Co or Ni clusters deposited on the Au(111) surface. The detailed sulfidation process of Co nanoclusters is treated in Chapter 8. Cobalt and nickel sulfides do, however, not have an appreciable HDS reactivity [21], and the following discussion will thus be concentrated on the, from a catalytical point of view, more interesting crystalline CoMoS and NiMoS structures nucleated on the Au(111) terraces.

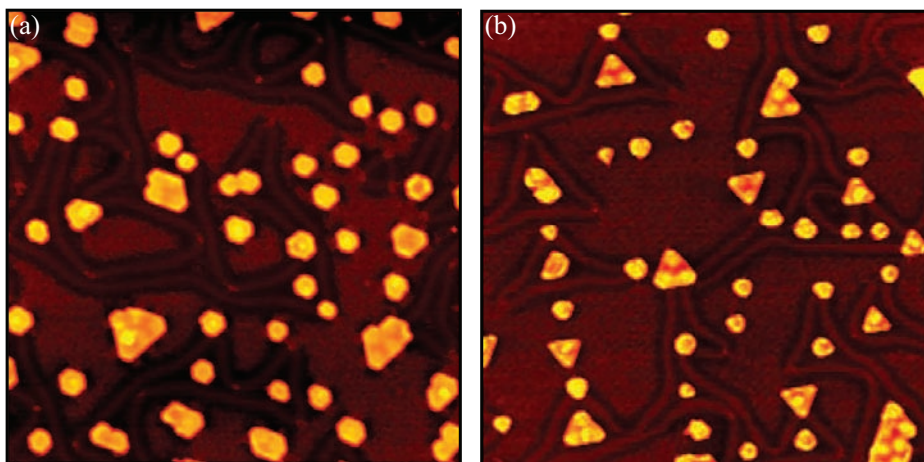


Figure 5.3. STM images of the Co- and Ni-promoted model systems synthesized in a sulfiding atmosphere at 673 K. (a) CoMoS ($700 \text{ \AA} \times 700 \text{ \AA}$). (b) NiMoS ($700 \text{ \AA} \times 700 \text{ \AA}$).

The main indication of the formation of a promoted phase is, for both the Co- and Ni-promoted systems, a pronounced shift in the morphology of the synthesized structures relative to non-promoted MoS₂. Two large-scale STM images of the CoMoS and NiMoS nanoclusters are shown in Fig. 5.3. The majority of the clusters in both the Co- and Ni-promoted systems is found to be crystalline nanoclusters with a height corresponding to a single S-Mo-S layer. However, in contrast to the triangular shape found for the non-promoted MoS₂ nanoclusters, the promoted clusters clearly exhibit non-triangular shapes. The changes in the morphology relative to the non-promoted MoS₂ nanoclusters are invoked only by the presence of promoter atoms (all other synthesis parameters were the same), and the observed shift in morphology is therefore directly attributed to the incorporation of promoters into the MoS₂ structure, that is, the formation of a CoMoS or NiMoS phase, respectively.

Atomically resolved STM images of both the CoMoS and NiMoS nanoclusters reveal a flat and perfectly crystalline basal plane consisting of hexagonally arranged protrusions with an interatomic spacing of 3.15 \AA (see Figs. 5.4a, 5.8a, and 5.10a). The similarities in low-bias STM images with the non-promoted MoS₂ nanoclusters imply that the protrusions are associated with the topmost sulfur atoms in the S-Mo-S layer.

Since the internal structure of the CoMoS and NiMoS clusters coincides with that of the non-promoted MoS₂ nanoclusters, the promoted clusters are indeed “MoS₂-like” as described in the CoMoS model. The main impact of Co and Ni promoters is thus primarily observed to be concerned with the edges of the clusters. The truncated morphology of the promoted clusters can be explained as a result of a perturbation of the edge free energy of the two low-index edges of MoS₂ driven by the affinity of Co or Ni to replace Mo at the edges. The addition of Co and Ni thus changes the relative stability of the different types of edges and therefore also the equilibrium cluster shape in accordance

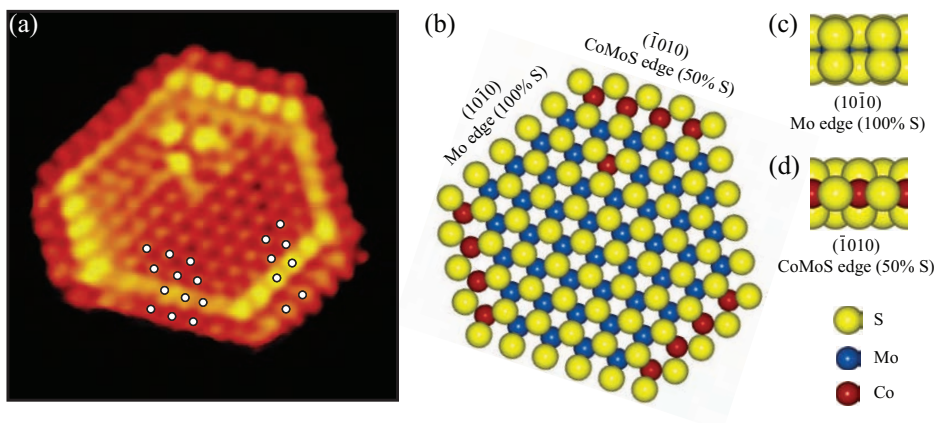


Figure 5.4. (a) Atom-resolved STM image ($51 \text{ \AA} \times 52 \text{ \AA}$, $I_t = 0.81 \text{ nA}$, and $V_t = 95.2 \text{ mV}$) of a hexagonally truncated CoMoS nanocluster supported on Au(111). The superimposed white dots illustrate the registry of protrusions on both types of edges. (b) A ball model of the CoMoS nanocluster exposing the non-promoted $(10\bar{1}0)$ Mo edges with a 100% coverage of sulfur and $(\bar{1}010)$ CoMoS edges fully substituted with Co and with a sulfur coverage of 50%. (c) Side view of the $(10\bar{1}0)$ Mo edge. (d) Side view of the Co-substituted $(\bar{1}010)$ CoMoS edge.

with the Wulff construction discussed in Section 3.5.

Co and Ni change the morphology in different ways, which indicates that Co and Ni adopt different positions at the MoS_2 nanocluster edges. Accordingly, the detailed equilibrium morphology and atomic-scale structure of CoMoS and NiMoS will be analyzed separately.

5.4 CoMoS

The majority of the cobalt-promoted crystalline nanoclusters is found to have a truncated triangular (or almost hexagonal shape). The remaining part of the clusters is observed to have more irregular shapes or shapes resulting from a merge of two or more clusters and will thus not be discussed here.

The predominant hexagonal morphology directly implies that both types of low-index edge terminations of MoS_2 are exposed in the cobalt-promoted clusters, that is, the $(10\bar{1}0)$ Mo edge and the $(\bar{1}010)$ S edge, respectively. In atom-resolved STM images of the CoMoS clusters, two different kinds of edges can clearly be identified (see Fig. 5.4a).

One edge type is characterized by the position of the outermost protrusions located with the regular 3.15 \AA interatomic distance, but clearly *out* of registry with the basal plane S atoms. Furthermore, this edge is identified by a brim along the edge with a height of $0.4 \pm 0.1 \text{ \AA}$ above the basal plane. A line scan across the brim perpendicular to the edge is shown in Fig. 5.5b along with a line scan across the $(10\bar{1}0)$ Mo edge on

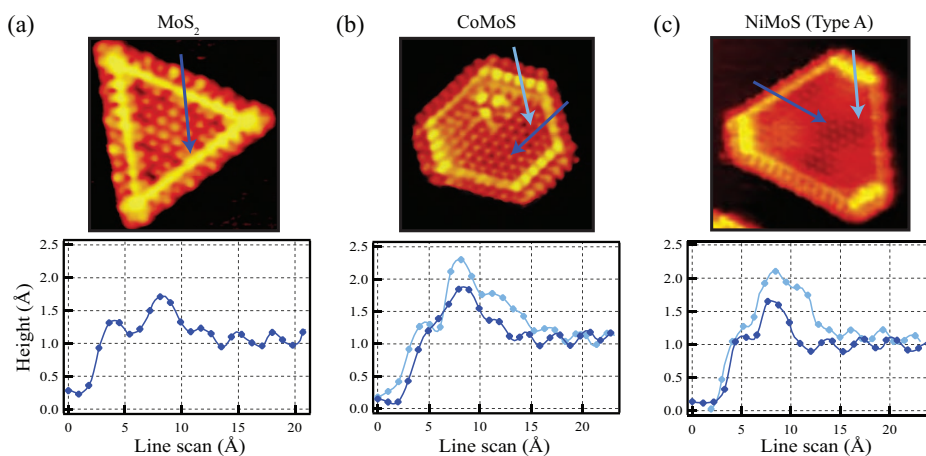


Figure 5.5. Line scans showing the brim height of: (a) The $(10\bar{1}0)$ Mo edge of the non-promoted MoS_2 clusters. (b) The $(10\bar{1}0)$ Mo edge (dark-blue) and the $(\bar{1}010)$ CoMoS edge (light-blue) of the CoMoS clusters. (c) The $(10\bar{1}0)$ Mo edge (dark-blue) and the $(\bar{1}010)$ NiMoS edge (light-blue) of the NiMoS type A clusters.

a non-promoted MoS_2 cluster for comparison (Fig. 5.5a). This type of edge is found to be completely identical to the fully sulfided $(10\bar{1}0)$ Mo edges (100% S) observed for the non-promoted MoS_2 triangles described in Section 3.5. The strong qualitative and quantitative similarities therefore suggest that this type of edge should be identified as non-promoted $(10\bar{1}0)$ Mo edge fully sulfided with one sulfur dimer per Mo edge atom (Fig. 5.4c).

The other type of edge must be the $(\bar{1}010)$ S edge according to the symmetry of the $\text{MoS}_2(0001)$ plane. Since Co appears to have no effect on the $(10\bar{1}0)$ Mo edges, the morphological shift to a hexagonally truncated shape is therefore concluded to be induced by the affinity for Co to be located *only* at the $(\bar{1}010)$ S edges, which will be termed the $(\bar{1}010)$ CoMoS edges from here on. This finding is consistent with recent DFT studies that show a clear preference for substitution of Mo with Co at the $(\bar{1}010)$ S edges [82, 97].

The superimposed white dots near the $(\bar{1}010)$ CoMoS edge in Fig. 5.4a reveal that the outermost row protrusions are located *in* registry with the basal plane S lattice. Compared to the position of the basal plane S lattice, however, a slight displacement of ~ 0.5 Å perpendicularly away from the edge is observed. The $(\bar{1}010)$ CoMoS edge furthermore displays a very bright brim extending along the edge in the row immediately behind the edge protrusions. The brim structure is, with a height of 0.9 ± 0.2 Å above the basal plane atoms, imaged significantly brighter than the brim on the $(10\bar{1}0)$ Mo edge. This is also observed in the line scans of the two types of edges in Fig. 5.5b. Furthermore, it can be seen in Fig. 5.4a that the bright brim structure on the $(\bar{1}010)$ CoMoS edge consists of well-defined protrusions, whereas no systematic corrugation is measured along the brim

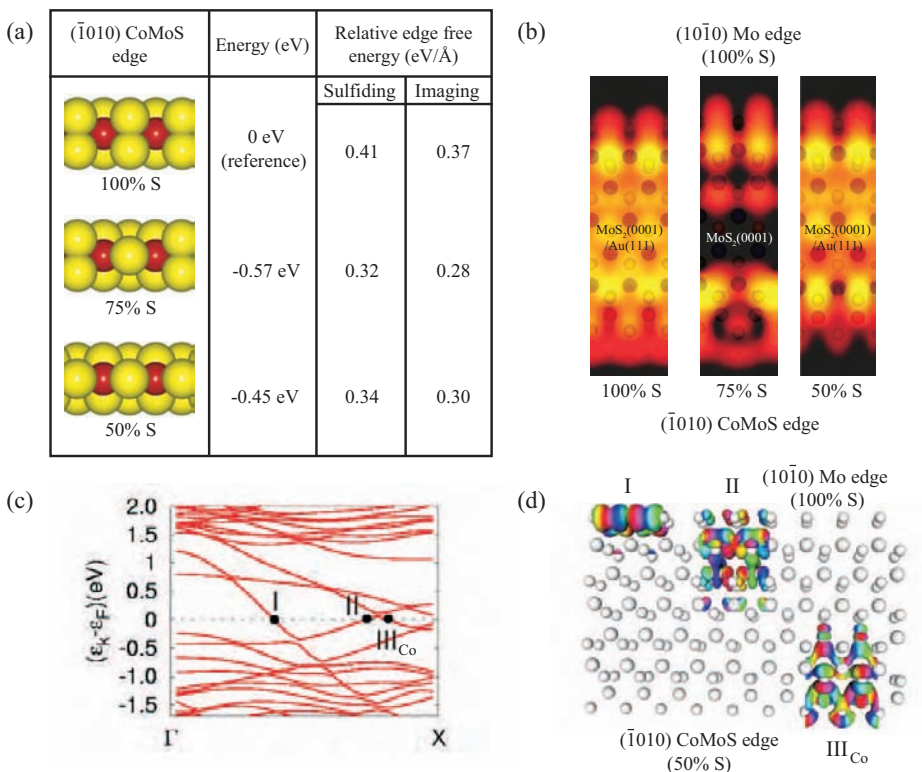


Figure 5.6. (a) DFT results for fully Co-substituted $(\bar{1}010)$ CoMoS edges with 100%, 75%, and 50% sulfur coverage, respectively. (b) STM simulations of $(\bar{1}010)$ CoMoS edges with 100%, 75%, and 50% sulfur. (c) The band structure of an MoS_2 slab exposing a $(10\bar{1}0)$ Mo edge (100% S) and a $(\bar{1}010)$ CoMoS edge (50% S). The electronic bands I and II are associated with metallic edge states on the non-promoted $(10\bar{1}0)$ Mo edge, whereas the metallic edge state III_{Co} is located on the $(\bar{1}010)$ CoMoS edge. (d) Plot of the wave function contours associated with the three metallic edge states in the CoMoS cluster.

on the $(10\bar{1}0)$ Mo edge.

Based on the detailed atomic-scale information provided by the STM images, the structural model shown in Fig. 5.4b is proposed for the the CoMoS nanoclusters. In this model, Co atoms have substituted all Mo atoms along the $(\bar{1}010)$ CoMoS edges of the hexagonally truncated nanocluster, and the outermost protrusions on these edges are assumed to be bridge-bonded S monomers leaving the Co atoms tetrahedrally coordinated.

The coordination of the Co atoms to sulfur is, however, not straight-forwardly inferred from the experimental STM images alone, and DFT calculations were therefore performed to support the STM studies. The theoretical work investigated the energetic stability of the Co-substituted $(\bar{1}010)$ CoMoS edge for several coverages of S. Three of

the investigated edge terminations are shown in Fig. 5.6a with coverages of 50%, 75%, and 100% sulfur, respectively. Edge terminations with a sulfur coverage lower than 50% are not discussed here since such configurations were found to be very unstable in accordance with previous calculations [98, 99].

As shown in Fig. 5.6a, the 50% S coverage (monomer) and 75% S-coverage are considerably more stable in energy than the fully sulfided (100% S) edge termination (dimer). The difference in edge free energy between the 50% S coverage and the intermediate 75% S coverage is on the other hand only $0.02 \text{ eV}/\text{\AA}$, and both structures are therefore likely candidates to match the experimental images. The atom-resolved STM images show, however, no evidence of a periodicity of more than one lattice distance along the outermost row of sulfur atoms on the Co-substituted ($\bar{1}010$) CoMoS edges. The configuration with 75% S coverage can therefore be ruled out since this structure would clearly give rise to a periodicity of two lattice distances. Likewise, configurations with Co only substituting a fraction of the Mo atoms, as have been proposed earlier [82, 97], can also be excluded since this would also give rise to periodicities larger than one atomic distance, which was not observed at all.

An STM simulation of the fully Co-substituted ($\bar{1}010$) CoMoS edge with a 50% S coverage is shown in the right part of Fig. 5.6b. The simulation is seen to reproduce the edges observed in the experimental STM images of CoMoS well. It is observed in the simulated image that the protrusions at the edge reflect the position of the bridging monomer S atoms and that a bright brim is present adjacent to the edge atoms towards the basal plane. As in the experimental image, the brim shows a significant corrugation parallel to the edge, and in the simulation, it is observed that the protrusions on the brim reflect the positions of the S atoms on the basal plane that are nearest neighbors to the substituted Co.

It is important to emphasize that the bright brim of the ($\bar{1}010$) CoMoS edge does not reflect S atoms located physically higher. Instead, the appearance of the brim region is, as for the ($10\bar{1}0$) Mo edge described in Section 3.5.2, associated with a perturbation of the electronic structure at the edges of the clusters and the existence of localized one-dimensional edge states. These edge states can be seen in the electronic band structure of an MoS₂ slab with a ($\bar{1}010$) CoMoS edge in Fig. 5.6c. In the band structure diagram, *three* bands are seen to penetrate into the band gap region of MoS₂ and cross the Fermi level. Edge states I and II are associated with the ($10\bar{1}0$) Mo edge and are the same as those shown in Fig. 3.7d for the non-promoted cluster. The edge state III_{Co} is, however, located directly at the ($\bar{1}010$) CoMoS edge as seen in the plot of the wave function contours in Fig. 5.6d. This edge state is localized on the outermost four rows of atoms counted from the edge and is responsible for the very intense bright brim on the ($\bar{1}010$) CoMoS edge.

The simulation of the ($\bar{1}010$) CoMoS edge (50% S) in Fig. 5.6b does not fully reproduce the appearance for the S monomers since they are imaged with a much lower intensity than in the experimental image. This can partly be associated to a limitation in the Tersoff-Hamann model used for the simulation and partly to an effect of the gold substrate. The theoretical model for STM simulations does not include tip-cluster forces [100] and does not reproduce STM tip induced relaxations of the surface atoms. This effect is expected to be most pronounced for loosely bound and more

isolated atoms, and the observed discrepancy may therefore be associated with a tip-induced upward relaxation of the S monomers, which would significantly enhance the corrugation at the monomer positions.

However, in light of the good qualitative agreement of the simulation with the experimental images and the fact that simulations of other edge configurations exhibited much larger discrepancies or were found to be energetically much less favorable when taking into account the sulfiding conditions of the experimental synthesis, it is concluded that the Co-substituted ($\bar{1}010$) CoMoS edge has a 50% sulfur coverage under the conditions of the STM experiment.

5.4.1 Promotional effect of Co

The proposed Co-promoted edges with sulfur monomers in Fig. 5.4d are seen to have intrinsic undercoordinated sites, and from a catalytic perspective this more open structure may be an attractive situation enabling adsorption of sulfur containing reactants. Furthermore, the resemblance of the promoted brim associated with the metallic edge state III_{Co} with that of the non-promoted MoS_2 nanoclusters is very interesting for a catalytical standpoint because the metallic brim sites on the $(10\bar{1}0)$ Mo edge are relatively strong adsorption sites active in the hydrogenation and C-S splitting of thiophene molecules as discussed in Section 3.5.2. In particular it is speculated that the close vicinity of the metallic brim sites and the edge sites on the $(\bar{1}010)$ CoMoS edge, which contains intrinsically undercoordinated Co atoms, may provide a favorable environment for reaction.

5.5 NiMoS

The Ni-promoted model catalyst is subject to an even more radical change of particle morphology due to the addition of Ni. The STM image in Fig. 5.3b shows the morphology of NiMoS clusters located on the Au(111) surface. All clusters are observed to have a truncated shape, but in contrast to the Co-promoted system, the NiMoS clusters are divided into two co-existing types of clusters. These can be distinguished in terms of size and exact shape, and will be referred to as NiMoS *type A* and NiMoS *type B*, respectively in the following. The two types of NiMoS clusters are depicted in the atom-resolved image in Fig. 5.7a and have the following morphological characteristics:

- **Type A** clusters are characterized by a hexagonally truncated shape similar to that of CoMoS.
- **Type B** clusters are smaller than type A clusters and have a more complex morphology that is best described as being dodecagonal (12-edges).

The distribution of NiMoS type A and type B is very sensitive to the exact post-annealing temperature of the preparation. The cluster size distributions in Fig. 5.7b illustrate this effect for three different post-annealing temperatures. At the lowest temperature (673 K) the size distribution displays the typical poisson-shaped distribution expected from

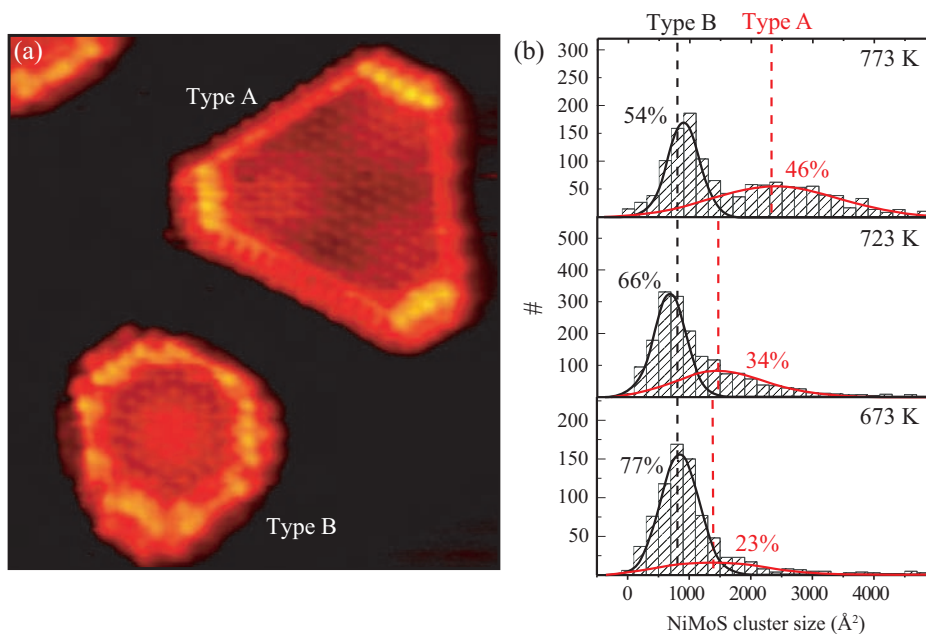


Figure 5.7. (a) STM image ($90 \text{ \AA} \times 100 \text{ \AA}$, $I_t = 0.50 \text{ nA}$, and $V_t = -600 \text{ mV}$) of the two types of NiMoS clusters. (b) Cluster size distributions (Bin size = 200 \AA^2) at 673 K, 723 K, and 773 K, respectively. The peaks in the bimodal distributions are for clarity fitted with gaussians.

nucleation and growth on a uniform substrate. The clusters have an average size of 800 \AA^2 , and only a small shoulder corresponding to larger clusters is observed. As the temperature is increased, the distribution shifts to a clear bimodal distribution with a peak remaining at the original position of 800 \AA^2 and a much broader peak at higher average size that increases in intensity and shifts to higher values as the temperature is increased. The gradual redistribution of the cluster size is attributed to a higher surface mobility at increased temperatures.

From a correlation between the cluster shape and size, it is found that the peak fixed at 800 \AA^2 , independently of the post-annealing temperature, is associated with the dodecagonally shaped NiMoS type B, whereas the larger clusters exclusively adopt the shape corresponding to truncated triangular NiMoS type A. Even after prolonged sulfidations up to 1 hour at the post-annealing temperatures, the unexpected bimodal distribution remained the same, indicating that the observation is not the result of kinetic limitations during growth. Interestingly, this finding shows that the equilibrium shape of NiMoS (i.e. the ratio of edge free energies) seems to be intimately linked to the size of the clusters. This result is in contrast to the Co-promoted system, which showed no systematic variation in the ratio of edge free energies (γ_S/γ_{Mo}) as a function of cluster size.

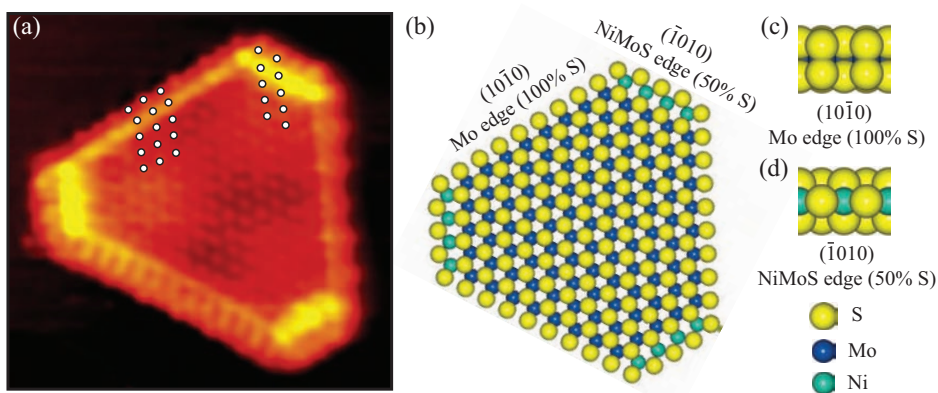


Figure 5.8. (a) An atom-resolved STM image of a NiMoS type A cluster ($61 \text{ \AA} \times 61 \text{ \AA}$, $I_t = 0.51 \text{ nA}$, and $V_t = -600 \text{ mV}$). The superimposed white dots illustrate the registry of protrusions both on the longer $(10\bar{1}0)$ Mo edges and shorter $(\bar{1}010)$ NiMoS edges. (b) A ball model of the NiMoS type A cluster exposing the non-promoted $(10\bar{1}0)$ Mo edges with 100% sulfur coverage and $(\bar{1}010)$ NiMoS edges fully substituted with Ni and with a 50% sulfur coverage. (c) Side view of the $(10\bar{1}0)$ Mo edge. (d) Side view of the Ni-substituted $(\bar{1}010)$ NiMoS edge.

Despite the structural similarities expected for Ni and Co promoters, this result shows that differences do exist in the morphologies, and they may explain the different selectivity of CoMoS and NiMoS in hydrotreating. Both types of NiMoS have sizes that are expected to play a role in the technical catalyst, and accordingly both type A and B structures are analyzed from atom-resolved STM images in the following.

5.5.1 NiMoS Type A

An atomically resolved STM image of one of the larger, truncated triangular NiMoS type A clusters is shown in Fig. 5.8a. The hexagonal morphology implies that both the $(10\bar{1}0)$ Mo edges and $(\bar{1}010)$ S edges are exposed in resemblance with the CoMoS clusters.

The longer edges are characterized by a bright brim measured to be 0.4 \AA high on average relative to the basal (see Fig. 5.5c) and edge protrusions that are shifted half a lattice constant compared to the basal plane S atoms, i.e. they are imaged *out* of registry. Furthermore, these edges display the superstructure originating from a periodic contraction/expansion of the distance between sulfur dimer pairs along the edges, which was also observed for the non-promoted MoS₂ triangles as discussed in Section 4.4.1. These edges are thus observed to be completely identical to the non-promoted $(10\bar{1}0)$ Mo edge with a 100% S coverage of dimerized S₂ units observed for both the non-promoted MoS₂ clusters (Fig. 3.5b) and the CoMoS clusters (Fig. 5.4a). The substitution of Ni promoter atoms therefore appears to be disfavored at the $(10\bar{1}0)$ Mo edges under the

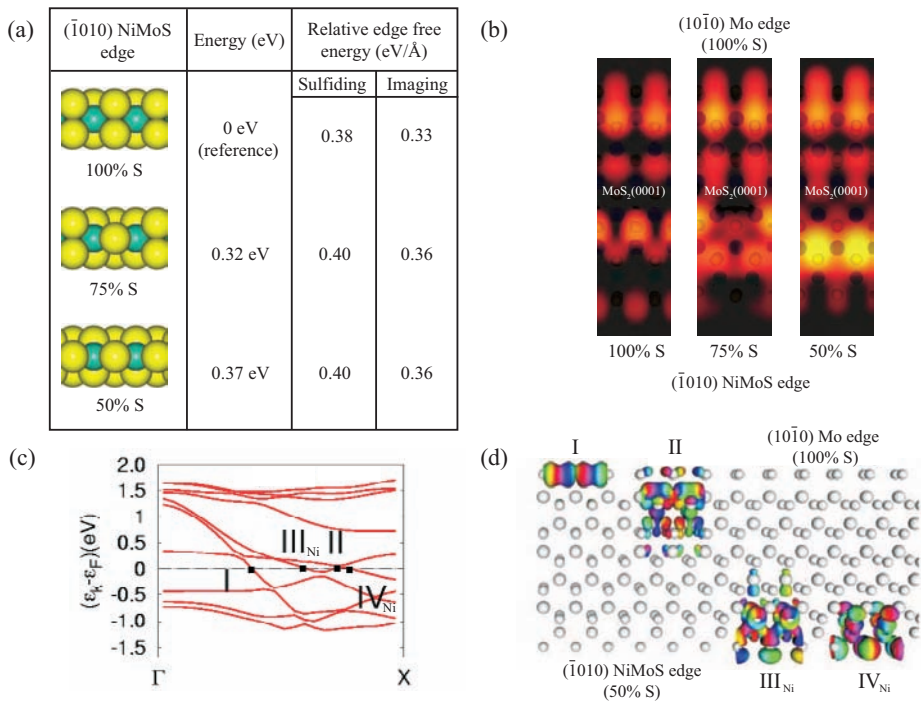


Figure 5.9. (a) DFT results for fully Ni-substituted (100% Ni) $(\bar{1}010)$ NiMoS edges with 100%, 75%, and 50% sulfur coverage, respectively. (b) STM simulations of $(\bar{1}010)$ NiMoS edges with 100%, 75%, and 50% sulfur, respectively. (c) The band structure of an MoS_2 slab exposing a $(10\bar{1}0)$ Mo edge (100% S) and a $(\bar{1}010)$ NiMoS edge (50% S). The electronic bands I and II are associated with metallic edge states on the non-promoted $(10\bar{1}0)$ Mo edge, whereas the metallic edge states III_{Ni} and IV_{Ni} are located on the $(\bar{1}010)$ NiMoS edge. (d) Plot of the wave function contours associated with the four metallic edge states in the NiMoS cluster.

conditions of the experiment, and the effect of Ni is thus exclusively observed to take place on the $(\bar{1}010)$ S edges for the NiMoS type A clusters.

The shorter edges must according to the symmetry of the clusters be the $(\bar{1}010)$ S edges, from here on termed $(\bar{1}010)$ NiMoS edges. As seen in Fig. 5.8a the $(\bar{1}010)$ NiMoS edges are associated with a very intense bright brim in the second row behind the edge and a row of edge protrusions that are imaged *in* registry with the basal plane atoms. This is similar to the CoMoS clusters, but the height of the brim of the $(\bar{1}010)$ NiMoS edges is measured to be $0.8 \pm 0.1 \text{ \AA}$ above the basal plane, which is slightly lower than that of the $(\bar{1}010)$ CoMoS edges (line scans of both types of edges can be seen in Fig. 5.5). The outermost protrusions on the $(\bar{1}010)$ NiMoS edges are, as for the CoMoS system, shifted a small distance ($\sim 0.8 \text{ \AA}$) away from the edge, indicating that S atoms may have moved outwards.

It has previously been proposed that $(\bar{1}010)$ S edges with alternating Mo and Ni atoms should be energetically feasible [99]. This seems, however, not to be the case since no patterns with periodicities larger than one atomic distance are observed on the $(\bar{1}010)$ NiMoS edges in atom-resolved STM images of NiMoS type A clusters, and a partial Ni substitution would give rise to such patterns. The $(\bar{1}010)$ NiMoS edges of the NiMoS type A cluster are therefore associated with an edge in which Ni atoms have replaced all the Mo atoms at the edge positions. The outermost S atoms are proposed to be bridge-bonded monomers, as shown in Fig. 5.8d.

Solid support of this interpretation is provided in terms of theoretical calculations of the energetics and STM simulations of the Ni-promoted $(\bar{1}010)$ NiMoS edge. Five sulfur terminations of the fully Ni-substituted $(\bar{1}010)$ NiMoS were considered with sulfur coverages ranging from 0% to 100%. The two most reduced edges (0% and 25%) could immediately be rejected since these were found to be energetically very unstable, and they are thus not considered further. The three most stable configurations corresponding to 50%, 75%, and 100% sulfur coverage are shown in Fig. 5.9a.

A fully sulfided $(\bar{1}010)$ NiMoS edge is the most stable in terms of edge free energy with the 75% and 50% S coverages being about 0.03 eV/\AA less stable. All three sulfur coverages are thus comparable in energy and are therefore likely candidates to match the experiment from an energetic point of view. However, the 75% S coverage can clearly be rejected, as in the CoMoS case, since it is expected to introduce a superstructure with a double period, which was not observed experimentally.

Of the 100% and 50% sulfur coverage only the simulation of the 50% sulfur coverage is found to match the experimental images (see Fig. 5.9b). The 50% S coverage is 0.03 eV/\AA less stable than the 100% S coverage. However, a small offset in energy due to a corner effect might change the stability of these rather short edges (10-20 \AA). The simulation of the $(\bar{1}010)$ NiMoS edge (50% S) matches the experimental images very closely, both quantitatively and qualitatively. Protrusions on the $(\bar{1}010)$ NiMoS edge (lower part of the simulation in Fig. 5.9b) are seen to reflect sulfur monomers, and as in experimental STM images, a bright brim is located on the sulfur atoms in the second row behind the edge.

The observed edge structure can, as for the CoMoS system, be related to edge states that render the Ni-substituted edge metallic. The band structure in Fig. 5.9c is calculated for a slab terminated at one edge by the non-promoted, fully sulfided $(10\bar{1}0)$ Mo edge at one edge and the $(\bar{1}010)$ NiMoS edge with a 50% sulfur coverage at the other. Four bands are clearly observed to cross the Fermi level. From the plot of the wave function contours (Fig. 5.9d), edge states I and II are found belong to the $(10\bar{1}0)$ Mo edge, whereas edge states III_{Ni} and IV_{Ni} are located on the $(\bar{1}010)$ NiMoS edge. Edge state III_{Ni} is similar to edge state III_{Co} of the $(\bar{1}010)$ CoMoS edge (Fig. 5.6d) and is the one giving rise to the bright brim, but edge state IV_{Ni} has no CoMoS counterpart. This edge state has a p_z -like geometry on the front S atoms and may play a role in the different activity and selectivity of NiMoS compared with CoMoS.

As for the CoMoS system, it is noted that the simulation of the $(\bar{1}010)$ NiMoS in Fig. 5.9b does not fully reproduce the experimental image at the position of the S monomers, but again the slightly dimmer appearance in the simulation may be explained by a discrepancy of the simulation neglecting tip-induced upward relaxation of the out-

ermost S atoms. On the other hand, the Tersoff-Hamann model correctly predicts the brim height of the $(\bar{1}0\bar{1}0)$ NiMoS edge to be 0.49 Å relative to the brim on the $(10\bar{1}0)$ Mo edge, which gives it a total height of 0.89 Å relative to the basal plane.

Based on the good agreement between the simulation and the experimental images, it is concluded that the truncated hexagonal NiMoS type A clusters are terminated by fully sulfided non-promoted $(10\bar{1}0)$ Mo edges and fully Ni-substituted $(\bar{1}0\bar{1}0)$ NiMoS edges with a 50% coverage of sulfur. The atomic scale morphology, the location of the promoter atoms, and the sulfur coverage of CoMoS and NiMoS type A clusters are thus observed to be completely identical.

5.5.2 NiMoS Type B

A NiMoS type B cluster is depicted in the atom-resolved STM image in Fig. 5.10a. The type B clusters are smaller in size and have a markedly different cluster shape than the type A clusters. The shape of NiMoS type B clusters can be described as being dodecagonal, i.e. clusters that expose 12 edges. This shape cannot be described as a simple low-index edge truncated shape of a triangle as in the Wulff-type model in Fig. 3.6a. Instead, a model that includes edges with higher Miller indices is required. As shown in Fig. 5.10b, a model where an MoS_2 hexagon exposing $(10\bar{1}0)$ Mo edges and $(\bar{1}0\bar{1}0)$ NiMoS edges is truncated at the corners by six new edges of the $(11\bar{2}0)$ type matches the experiment closely. Hence, the addition of Ni seems not only to stabilize the $(\bar{1}0\bar{1}0)$ NiMoS edges but also high-index edges of the $(11\bar{2}0)$ type in the smaller clusters¹.

The Ni-substituted $(\bar{1}0\bar{1}0)$ NiMoS edges are readily identified in the atom-resolved image in Fig. 5.10a since they are imaged in the same way as the $(\bar{1}0\bar{1}0)$ NiMoS edges of the larger NiMoS type A clusters (Fig. 5.8a). They are thus concluded to have a 50% S coverage as in Fig. 5.10c. Note that one of the $(\bar{1}0\bar{1}0)$ NiMoS edges in Fig. 5.10a shows a dark spot in the row of the bright protrusions (indicated by a black dashed circle). This is most likely a result of an only partial substitution of Mo with Ni, leaving a single Mo atom in the otherwise fully Ni-substituted $(\bar{1}0\bar{1}0)$ NiMoS edge as indicated by the red dashed circle in Fig. 5.10b. This was, however, only rarely observed and should therefore only be considered as a single defect rather than a stable structure.

The $(10\bar{1}0)$ Mo edges, from here on termed $(10\bar{1}0)$ NiMoS edges, which are rotated 60° relative to the $(\bar{1}0\bar{1}0)$ NiMoS edges, are also exposed in the dodecagonal NiMoS type B clusters. The zoom-in on the $(10\bar{1}0)$ NiMoS edge of a NiMoS type B cluster in Fig. 5.11a shows that the $(10\bar{1}0)$ NiMoS edge seems to be very different from the $(10\bar{1}0)$ Mo edges of the larger NiMoS type A clusters (Fig. 5.8a). First of all, the brim in the middle part of the edge is almost reduced to the level of the basal plane, whereas it has a much higher intensity near the corners. It is seen in the line scans in Fig. 5.12 that the intensity of the two bright spots matches the intensity of the brim on the $(\bar{1}0\bar{1}0)$ NiMoS edge. This match implies that the two bright spots should be attributed to Mo atoms being substituted with Ni atoms at the two edge positions near the corners between a $(10\bar{1}0)$ NiMoS edge and the two $(11\bar{2}0)$ high-index edges. This is shown in detail in the

¹It should be noted that the cluster in the experimental image (Fig. 5.10a) only contains 11 edges, i.e. only five out of six possible corners have been truncated by Ni to form $(11\bar{2}0)$ edges.

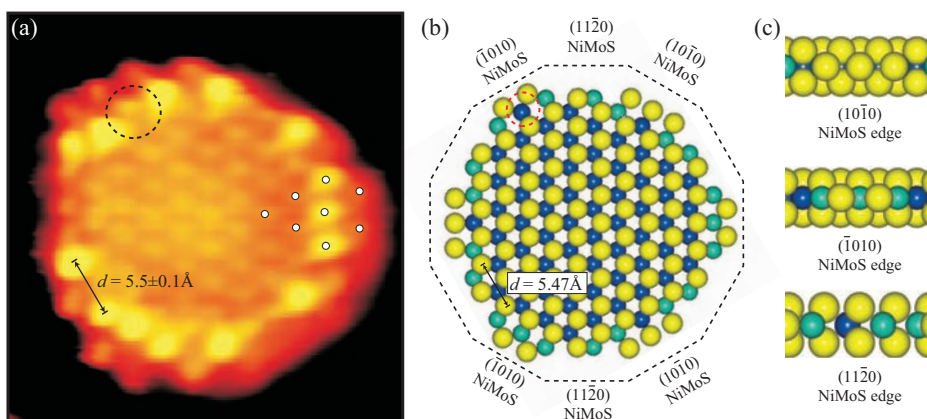


Figure 5.10. (a) Atom-resolved STM image ($39 \text{ \AA} \times 40 \text{ \AA}$, $I_t = 0.44 \text{ nA}$, and $V_t = -520 \text{ mV}$) of a NiMoS type B nanocluster supported on Au(111). The superimposed white dots illustrate the registry of protrusions at the $(\bar{1}010)$ S edge. (b) Ball model of type B NiMoS. (c) Side view of the $(10\bar{1}0)$ NiMoS, $(\bar{1}010)$ NiMoS, and $(11\bar{2}0)$ NiMoS edges, respectively.

ball model of the $(10\bar{1}0)$ NiMoS edge in Fig. 5.11b. In this way, the $(10\bar{1}0)$ NiMoS edge exhibits a partial substitution of Ni. It is, however, emphasized that substitution of Mo atoms with Ni atoms only seems to be favored at positions adjacent to a $(11\bar{2}0)$ edge, and clearly the substitution appears to be linked to the overall cluster size because the larger NiMoS type A clusters show no evidence of Ni on the $(10\bar{1}0)$ Mo edges. Since Ni was added in excess amounts during the synthesis, the observed partially Ni-substituted $(10\bar{1}0)$ NiMoS edge can be considered as an intrinsic and stable feature of the type B NiMoS clusters.

The outermost edge region of the $(10\bar{1}0)$ NiMoS type B edge has a very low intensity. This could indicate that sulfur atoms are missing compared to the fully sulfided $(10\bar{1}0)$ Mo edges of the NiMoS type A, CoMoS, and non-promoted MoS₂ nanoclusters. To elucidate the observed structure further, DFT calculations were performed for both a fully Ni-substituted edge and an edge with alternating Ni and Mo atoms representing $(10\bar{1}0)$ NiMoS edges that have parts with neighboring Ni-Ni and Ni-Mo parts, respectively.

The relative edge free energies in Figs. 5.11c and 5.11e are calculated with the same reference and are thus directly comparable. The fully Ni-substituted $(10\bar{1}0)$ NiMoS edge with 0% sulfur is the most stable. However, the difference in edge free energy relative to the most stable partially Ni-substituted edges is of the order of 0.04 eV/\AA . Hence, for short edges ($\sim 10 \text{ \AA}$), as in type B NiMoS, a partial Ni substitution cannot safely be neglected.

The fully Ni-substituted $(10\bar{1}0)$ NiMoS edge with 0% sulfur coverage represents the parts of the $(10\bar{1}0)$ NiMoS edge with neighboring Ni-Ni pairs near the corners as shown in Fig. 5.11b. A DFT-based simulation of this edge (Fig. 5.11d) reproduces a bright region behind the Ni row, as observed in the experimental images. This brim

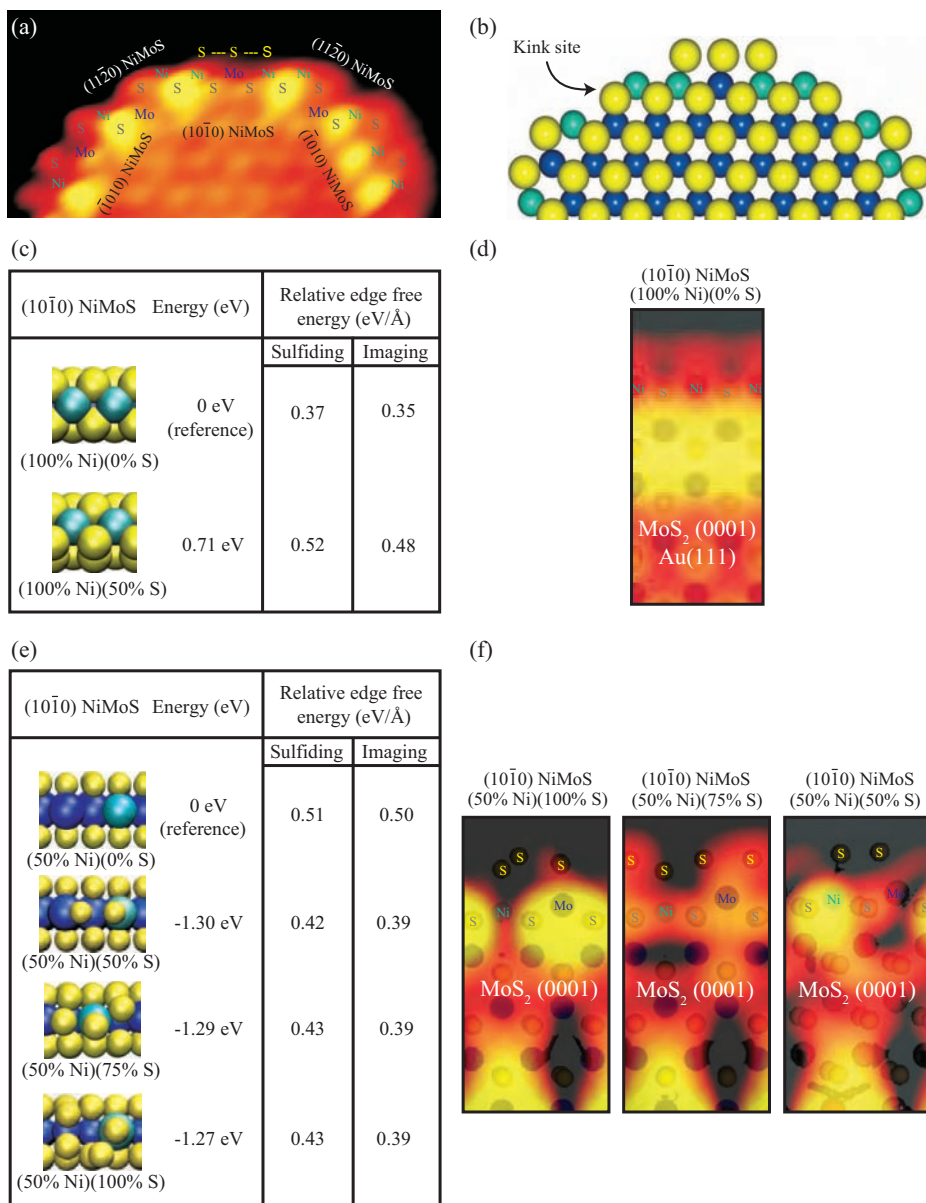


Figure 5.11. (a) Zoom-in on a type B NiMoS nanocluster. (b) A top view ball model. (c) DFT results for a fully Ni-substituted (100% Ni) (10 $\bar{1}$ 0) NiMoS edge. (d) STM simulation of a (100% Ni) (10 $\bar{1}$ 0) NiMoS edge with 0% S. (e) DFT results for a (50% Ni) (10 $\bar{1}$ 0) NiMoS edge. (f) STM simulations of (50% Ni) (10 $\bar{1}$ 0) NiMoS edges with 100%, 75%, and 50% S, respectively.

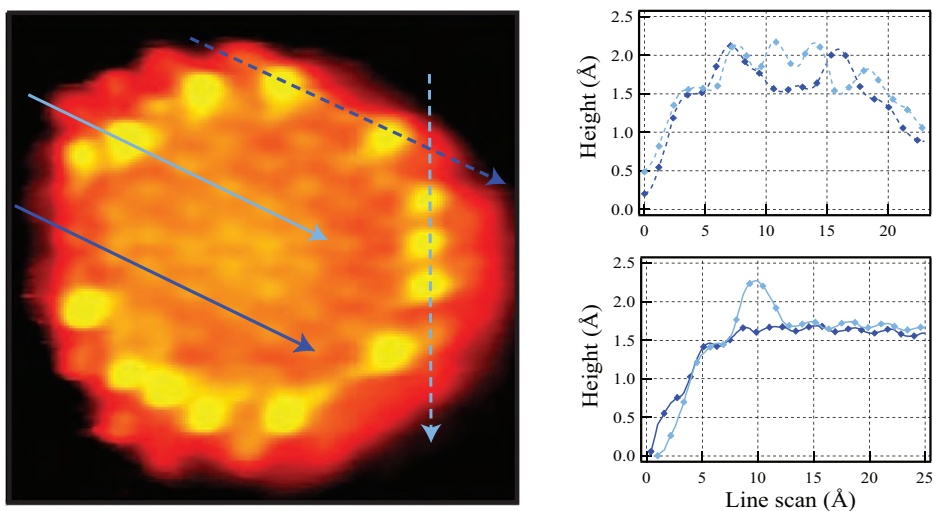


Figure 5.12. STM image and line scans illustrating the edge structure of a NiMoS type B cluster. The dark-blue line scans are on the $(10\bar{1}0)$ NiMoS edge and the light-blue on the $(\bar{1}010)$ NiMoS (Dashed line: Parallel with the edge and on the brim. Full line: Perpendicular on the edge). It can be seen (full dark-blue line) that the brim in the middle part of the $(10\bar{1}0)$ NiMoS edge is reduced to the level of the basal plane. Near the corners the $(10\bar{1}0)$ NiMoS edge displays, however, two bright spot with an intensity that matches the intensity of the $(10\bar{1}0)$ NiMoS edge brim as seen from the dashed line scans.

region has a comparable height to the brim on the Ni-substituted $(\bar{1}010)$ NiMoS edge. Moreover, the outermost edge region in which no S atoms are present indeed has a very low intensity.

Due to the higher affinity of Mo to sulfur, the situation is likely different in the middle part of the edge where both Ni and Mo are present at neighboring sites on the edge. Fig. 5.11e shows the three sulfur coverages in the range 50-100% found to be the most likely edge terminations for a $(10\bar{1}0)$ NiMoS edge exposing alternating Ni and Mo atoms (50% Ni substitution).

All three investigated sulfur coverages in the range 50-100% are very close in terms of edge free energy (<0.01 eV/Å). However, the STM simulations of the edges with 100% and 75% sulfur show no clear match with the experimental image (Fig. 5.11f left and middle). Instead the 50% S covered edge (Fig. 5.11f right) reproduces the experimental STM image, including the bright protrusion behind the Ni site and a depleted intensity behind the Mo site. Furthermore, it is seen that S atoms adsorbed on both Ni and Mo are associated with a very low intensity, as also observed in the experimental images.

Based on the qualitative similarities of the experimental STM images and the simulated images, a partly Ni-substituted $(10\bar{1}0)$ Mo edge, as shown in Fig. 5.11b, is proposed

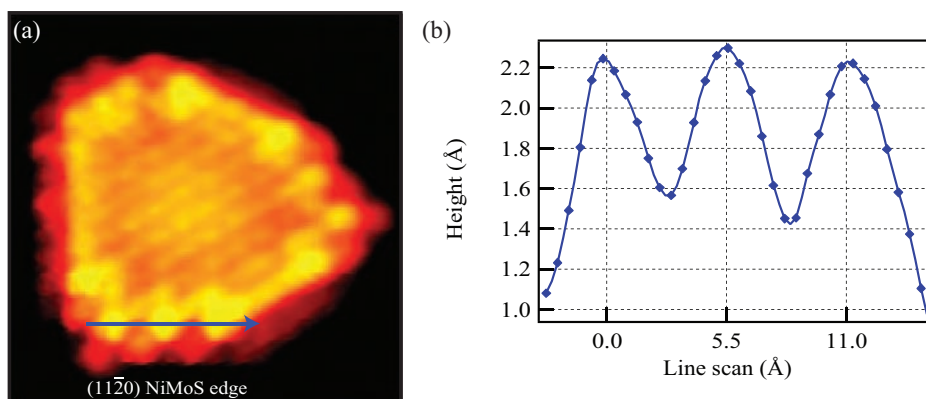


Figure 5.13. (a) Atom-resolved STM image ($43 \text{ \AA} \times 43 \text{ \AA}$, $I_t = 0.81 \text{ nA}$, and $V_t = -733 \text{ mV}$) of a NiMoS type B cluster displaying a $(11\bar{2}0)$ NiMoS edge spanning two unit cells. (b) Line scan along the $(11\bar{2}0)$ NiMoS edge as indicated by the arrow in (a).

for the type B clusters.

The short edges on each side of the $(10\bar{1}0)$ NiMoS edge in Fig. 5.11a have the $(11\bar{2}0)$ structure. They are primarily identified by their orientation 30° relative to the $(10\bar{1}0)$ and $(\bar{1}010)$ edges and by the two bright protrusions (Fig. 5.10a) separated by 5.5 \AA . This distance matches precisely the interatomic periodicity of 5.47 \AA in the direction parallel to the $(11\bar{2}0)$ edges of MoS_2 (Fig. 5.10b). The observation of these edges in equilibrium structures is highly interesting since high-index edge terminations normally have been considered to be too energetically unfavorable.

The Ni on the $(11\bar{2}0)$ edge is structurally similar to the Ni on the $(10\bar{1}0)$ NiMoS edge but has a lower sulfur coordination at the corner because only sulfur monomers are present on the neighboring $(\bar{1}010)$ NiMoS edge. The more open structure of the corner site may provide an attractive site for hosting reactive sulfur vacancies during reaction conditions, and clearly an improved understanding of the catalytic relevance of such sites in future DFT and STM investigations is important. Typically the $(11\bar{2}0)$ edges are very short, spanning only a single unit cell, and thus could be considered as a corner effect for the finite-size clusters. Surprisingly however, clusters with $(11\bar{2}0)$ edges two or three unit cells wide were occasionally observed as seen in Fig. 5.13. The abundance of these edge terminations suggests that the $(11\bar{2}0)$ edge termination must have a comparable edge free energy to the more closely packed $(10\bar{1}0)$ and $(\bar{1}010)$ edges for this cluster size. The existence of $(11\bar{2}0)$ edges has also recently been observed in a high-angle annular dark-field scanning transmission electron microscopy (HAADT-STEM) study [101].

Cluster DFT calculations of NiMoS clusters of different sizes could shed more light on the observed size-dependent affinity for Ni substitution and the NiMoS morphology. They could also help determine whether the $(11\bar{2}0)$ edges should be considered a stable edge termination of NiMoS or a corner effect that dominates only the smallest NiMoS

clusters.

5.6 Comparison with X-ray absorption results

It is interesting to compare the present STM and DFT results with previous X-ray absorption fine structure (XAFS) studies, which have provided information on the average interatomic distances and coordination numbers of Co or Ni promoter atoms for supported CoMoS and NiMoS particles, respectively. In order to avoid the influence from promoter atoms in other structures than the CoMoS and NiMoS (e.g. promoter atom dissolved in the alumina support), the measurements were typically performed on carbon-supported catalysts.

For CoMoS, the structural surroundings of the Co present in carbon-supported Co-Mo sulfide catalysts were studied by means of X-ray absorption near edge structure (XANES) spectroscopy at the Co K-edge. By comparison of XANES spectra of the catalysts with those of Co_9S_8 and CoS_2 model compounds, it was concluded [49, 106, 107] that the Co atoms in the CoMoS state have a distorted 5- to 6-fold S coordination. Furthermore, EXAFS studies showed that on average every Co atom is in contact with 2 Mo atoms at a distance of 2.80 Å [106]. From a comparison of the XANES structure of carbon-supported sulfided Ni-Mo catalysts with well-defined model structures, it was concluded [95, 96, 108] that the Ni atoms have a sulfur coordination number below 6, i.e. different from an octahedral-like S coordination. The Ni atoms in NiMoS were suggested to be located in a square pyramid of 5 S atoms at a distance of about 2.21 Å from the S atoms. Furthermore, EXAFS results showed that on average every Ni atom is surrounded by 1-2 Mo atoms at a distance of 2.84 Å [109].

Tables 5.1 and 5.2 summarize the main XAFS results in the literature for the coordination number and interatomic distances of Co-S, Co-Co, Ni-S, and Ni-Ni obtained from studies of Co-Mo and Ni-Mo sulfided catalysts (Refs. [49, 102–105] for Co and Refs. [95, 96, 108, 109] for Ni). The tables also contain the corresponding interatomic distances and coordination numbers taken from the detailed models of the promoted edges in CoMoS or NiMoS in the STM experiments and DFT calculations. To make a direct comparison to the XAFS values, the STM/DFT values from this study were cal-

	$N_{\text{Co-S}}$	$d_{\text{Co-S}}$	$N_{\text{Co-Co}}$	$d_{\text{Co-Co}}$
CoMoS STM/DFT	4.5-5.3	2.10	1.3-1.7	3.22
XAFS	4.9-5.5	2.20-2.26	0.6-1.2	2.6-2.9

Table 5.1. Coordination numbers and interatomic distances for Co in CoMoS. The XAFS data are compiled from Refs. [49, 102–105]. Typical uncertainties of the XAFS values are around $\sim 20\%$ for nearest neighbors. Interatomic distances (STM/DFT) are based on the calculated structures.

culated from the weighted average coordination of all Co or Ni atoms in the proposed CoMoS and type A and B NiMoS models (Figs. 5.4b, 5.8b, and 5.10b). The average coordination values of the promoters are functions of the cluster size and shape (degree of truncation) because corner or edge promoter atoms have a different coordination, and for small cluster sizes, this is a particularly important effect. It is the general trend that the sulfur coordination increases when corner sites start to dominate and the promoter-promoter coordination decreases towards one. The STM experiments typically reveal edges 2 to 6 unit cells wide for both Co- and Ni-promoted edges, and the data range listed in the tables therefore reflects the actual variation in the size and truncation of the observed CoMoS and NiMoS nanoclusters.

The agreement of the CoMoS XAFS data with the present findings is good in terms of both coordination number and interatomic distances. The XAFS measurements in general estimate a slightly higher sulfur coordination to Co ($N_{\text{Co-S}} \approx 4.9\text{-}5.5 \pm 1$) compared to the STM experiments. However, it is worth noting that many of the CoMoS clusters had one or more Co atoms substituted at bulk sites (see Fig. 5.4). These Co atoms are six-fold coordinated to sulfur, and the presence of Co bulk inclusions may thus shift the average Co-S coordination upwards. Furthermore, the Co-Co coordination is found to be slightly lower ($N_{\text{Co-Co}} = 0.6\text{-}1.2 \pm 1$) compared to the STM-based model ($N_{\text{Co-Co}} = 1.3\text{-}1.7$). This finding may indicate that the Co substitution of CoMoS clusters is incomplete, or that the CoMoS clusters in the industrial alumina-supported catalysts are slightly smaller than those in the present experiment.

For NiMoS, the agreement between XAFS data and the present STM/DFT results is also good. XAFS estimates a Ni coordination number to sulfur of $N_{\text{Ni-S}} \approx 4.7\text{-}5.6 \pm 1$, which is in good agreement with the values found for the type A NiMoS nanoclusters. In the type B NiMoS, Ni is substituted at three different type of sites with similar or lower sulfur coordination, that is, on the $(\bar{1}010)$ NiMoS edges, on the $(10\bar{1}0)$ NiMoS edges, and on the $(11\bar{2}0)$ NiMoS edges. This produces a slightly lower average S coordination number compared with that for type A NiMoS. In the case of NiMoS, inclusions on the basal plane, which would indicate the presence of six-fold coordinated Ni, is never observed. The values found for the Ni-S coordination could thus indicate that predom-

	$N_{\text{Ni-S}}$	$d_{\text{Ni-S}}$	$N_{\text{Ni-Ni}}$	$d_{\text{Ni-Ni}}$
Type A NiMoS STM/DFT	4.5-5.3	2.14	1.3-1.7	3.22
Type B NiMoS STM/DFT	4.0-4.6	2.14	1.0-1.2	3.21
XAFS	4.7-5.6	2.12-2.24	1.0	3.21

Table 5.2. Coordination numbers and interatomic distances for Ni in NiMoS. The XAFS data are compiled from Refs. [95, 96, 108, 109]. Typical uncertainties of the XAFS values are around $\sim 20\%$ for nearest neighbors. Interatomic distances (STM/DFT) are based on the calculated structures.

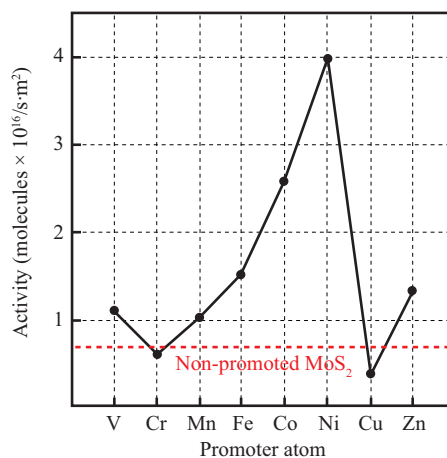


Figure 5.14. HDS activity of dibenzothiophene for a range of promoted MoS_2 -based catalysts. From Ref. [110].

inantly NiMoS type A particles are present in the industrial Ni-Mo sulfided catalysts. However, the values are very sensitive to the actual cluster size, and a comparison of the Ni-Ni coordination actually shows a better match with type B NiMoS clusters compared to type A clusters.

The proposed models for CoMoS and NiMoS are thus observed to be fully consistent with XAFS data for industrial sulfided Co-Mo and Ni-Mo catalysts. Nonetheless, it is emphasized that only one preferential site of Ni was considered in previous models, and it is in general unclear whether one or more NiMoS morphologies were present in the previous studies. It should also be taken into account that the XAFS data were obtained on samples exposed to HDS relevant conditions (H_2/H_2S mixture), whereas the structures analyzed here are formed in a highly sulfiding atmosphere. Regardless, there is nothing to indicate a lower sulfided state of NiMoS or CoMoS in the XAFS experiments since the sulfur coordination is estimated to be slightly higher in the XAFS experiments compared to the STM experiments.

5.7 Promoter-dependent (Fe, Co, Ni, and Cu) shape of MoS_2 nanoclusters

It is well known that CoMoS and NiMoS display a superior catalytic activity over Fe- and Cu-promoted MoS_2 structures (so-called FeMoS and CuMoS structures) [21]. Harris and Chianelli [110] measured the HDS of dibenzothiophene for a range of promoted MoS_2 -based catalysts and found the “volcano” plot displayed in Fig. 5.14. The plot clearly shows that Co- and Ni-promoted catalysts display the highest catalytic activity. Consequently, the vast majority of studies have been performed on Co- and Ni-promoted

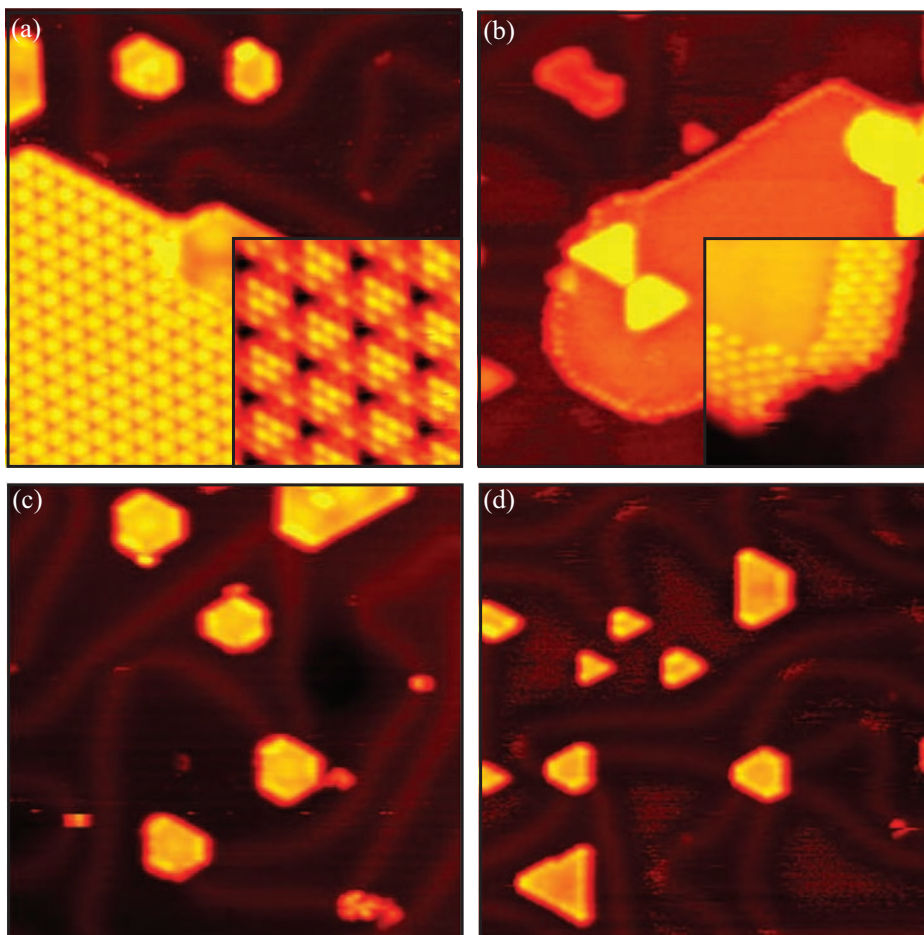


Figure 5.15. (a) and (b) STM images of: Iron sulfide ($275 \text{ \AA} \times 275 \text{ \AA}$, insert $50 \text{ \AA} \times 50 \text{ \AA}$), and Copper/Copper sulfide ($275 \text{ \AA} \times 275 \text{ \AA}$, insert $55 \text{ \AA} \times 55 \text{ \AA}$), respectively. The inserts show atom-resolved STM images of the structures. (c) and (d) STM images of FeMoS nanoclusters ($250 \text{ \AA} \times 250 \text{ \AA}$) and CuMoS nanoclusters ($300 \text{ \AA} \times 300 \text{ \AA}$), respectively.

systems and only very little is known about systems promoted by iron or copper, which are the neighboring elements to Co and Ni in the periodic table.

The Fe- and Cu-promoted MoS₂-based nanoclusters can be synthesized by the same procedure described in the beginning of the present chapter. The synthesis is seen, as for the CoMoS and NiMoS case, to produce two significantly different types of surface structures: (i) iron sulfide islands (Fig. 5.15a), and in the case of copper, metallic Cu islands where only the rim of the islands is sulfided (Fig. 5.15b), form primarily at the Au(111) step edges, and (ii) well-dispersed FeMoS and CuMoS nanoclusters on the

	FeMoS	CoMoS	NiMoS	CuMoS
l_S/l_{tot}	0.48 ± 0.01	0.42 ± 0.01	0.33 ± 0.01	0.17 ± 0.01

Table 5.3. The mean values of the l_S/l_{tot} ratios.

terraces of the Au(111) substrate (Figs. 5.15c and 5.15d).

Atom-resolved images of the copper- and iron-promoted nanoclusters (Figs. 5.16a and 5.16d, respectively) reveal that morphology of the CuMoS and FeMoS phase is identical to that of CoMoS and NiMoS type A (Figs. 5.16b and 5.16c, respectively). Both CuMoS and FeMoS nanoclusters possess three edges that are characterized by the position of the outermost protrusions located with the regular 3.15 Å interatomic distance, but clearly out of registry with the basal plane S atoms. Furthermore, this type of edge is identified by a brim along the edge with a height of 0.4 ± 0.1 Å above the basal plane. These edges are thus identical to the edges of the non-promoted MoS₂ nanoclusters and are accordingly ascribed to fully sulfided (10 $\bar{1}$ 0) Mo edges. The symmetry of the MoS₂ crystal structure dictates that the remaining three edges must be ($\bar{1}$ 010) S edges. These edges are characterized by an intense bright brim located behind the outermost row of protrusions, which are located in registry with the basal plane atoms. These two observations characterize the promoted ($\bar{1}$ 010) S edges of the CoMoS and NiMoS type A structures, and from this strong resemblance it is concluded that the ($\bar{1}$ 010) S edges of the CuMoS and FeMoS phase are fully substituted with Cu and Fe, respectively, and have a sulfur coverage of 50%.

However, differences do exist between the morphologies of the FeMoS, CoMoS, NiMoS, and CuMoS nanoclusters. Surprisingly, the shape of the promoted MoS₂ nanoclusters shows a direct dependence on the type of promoter atom. From the series of STM images of the promoted MoS₂ nanoclusters displayed in Fig. 5.16, it can be seen that the degree of truncation increases when going from copper, over nickel and cobalt, to iron. This systematic trend is confirmed in a detailed measurement of the distribution of the ratio of the length of the promoted ($\bar{1}$ 010) S edges to the total edge length (l_S/l_{tot}) for the four different types of promoted MoS₂ nanoclusters² (Fig. 5.17a). The color plots of the distribution of l_S/l_{tot} in Fig. 5.17b clearly reveal that the l_S/l_{tot} ratio increases when going from Cu over Ni and Co to Fe. The mean values of the l_S/l_{tot} ratios are displayed in Tabel 5.3. The CuMoS clusters thus appear almost triangular with only at slight degree of truncation, whereas the FeMoS clusters exhibit a clear hexagonal shape. The catalytically superior CoMoS and NiMoS clusters are located in between with an intermediate degree of truncation.

The shape dependence on the type of promoter atoms is not due to a lack of promoter atoms during the synthesis since the total coverage of the promoter metal was kept constant at ~4% ML. Syntheses where the promoter coverage was raised from ~4% ML to up to ~20% ML did not lead to a significant change in cluster shape. In fact the general

²For NiMoS, only type A clusters are included in this analysis.

observation was that when the MoS₂ nanoclusters reach a saturation of promoter atoms, which depends on the type of promoter atom, deposition of additional promoter atoms on the surface just leads to larger promoter metal sulfide islands. This observation reveals that the promoter-dependent shape reflects that different types of promoter atoms have different tendencies to be incorporated into the MoS₂ structure.

Several theoretical studies have sought to explain trends in the promotional effect by the different ability of the promoter atoms to weaken metal sulfur bonds [82, 97, 110]. However, the present study clearly shows that the promoter atoms not only change the strength of the metal sulfur bond, but a profound change in shape is also observed as a function of promoter type. A recent DFT study by Moses *et al.* [111] investigated different reaction pathways for the HDS of thiophene over different non-promoted MoS₂ edges structures. They found that the HDS process via the HYD route is initiated by a hydrogenation step that occurs at a brim site preferentially on the (10 $\bar{1}$ 0) Mo edge, and the subsequent S-C scission occurs at a vacancy site at the ($\bar{1}$ 010) S edge. These results thus suggest that both types of low-index edge terminations need to be present for a high HDS activity.

In this regard, it is highly interesting that the degree of truncation, and hence the ratio of the lengths of the (10 $\bar{1}$ 0) Mo edge and ($\bar{1}$ 010) S edge, is found to depend on the type of promoter atom in a systematic way. This could suggest that a high HDS activity is not only the result of the ability of the promoter atoms to weaken the metal sulfur bond, but also that an optimum ratio between the (10 $\bar{1}$ 0) Mo and promoted ($\bar{1}$ 010) S edges is important, and that this optimum is achieved by using either cobalt or nickel as promoter.

It should, however, be noted that a recent DFT study [112] of the HYD and DDS pathways on the Co-promoted ($\bar{1}$ 010) S edges show an increased hydrogenation activity of the Co-promoted brim sites compared to the brim sites of the non-promoted (10 $\bar{1}$ 0) Mo edge. This does, however, not rule out an interplay between the edges of the promoted catalytic particles. It could thus be speculated that certain additives or supports combined with promoter atoms may stabilize an optimum ratio between the (10 $\bar{1}$ 0) Mo and promoted ($\bar{1}$ 010) S edges for design of catalysts with specific HYD/DDS properties.

5.8 Conclusion

In conclusion, the presented results in this chapter clearly demonstrate that promoter atoms have a pronounced effect on the morphology of the clusters. In the case of CoMoS and NiMoS type A, the change in cluster shape to hexagonally truncated in contrast to the triangular non-promoted clusters is driven by the affinity of Co and Ni to be located *only* at the ($\bar{1}$ 010) S edges. These fully Co- or Ni-substituted ($\bar{1}$ 010) S edges are, based on comparison of experimental STM images and DFT calculations, proposed to have a sulfur coverage of 50%, leaving the promoter atoms in a tetrahedral environment. From a catalytic point of view, this more open structure may be an attractive situation that enables adsorption of sulfur containing reactants.

The smaller NiMoS type B clusters have a shape resembling a dodecagon. Surprisingly, this observation shows that Ni, due to a stronger affinity of Ni to the edges, can

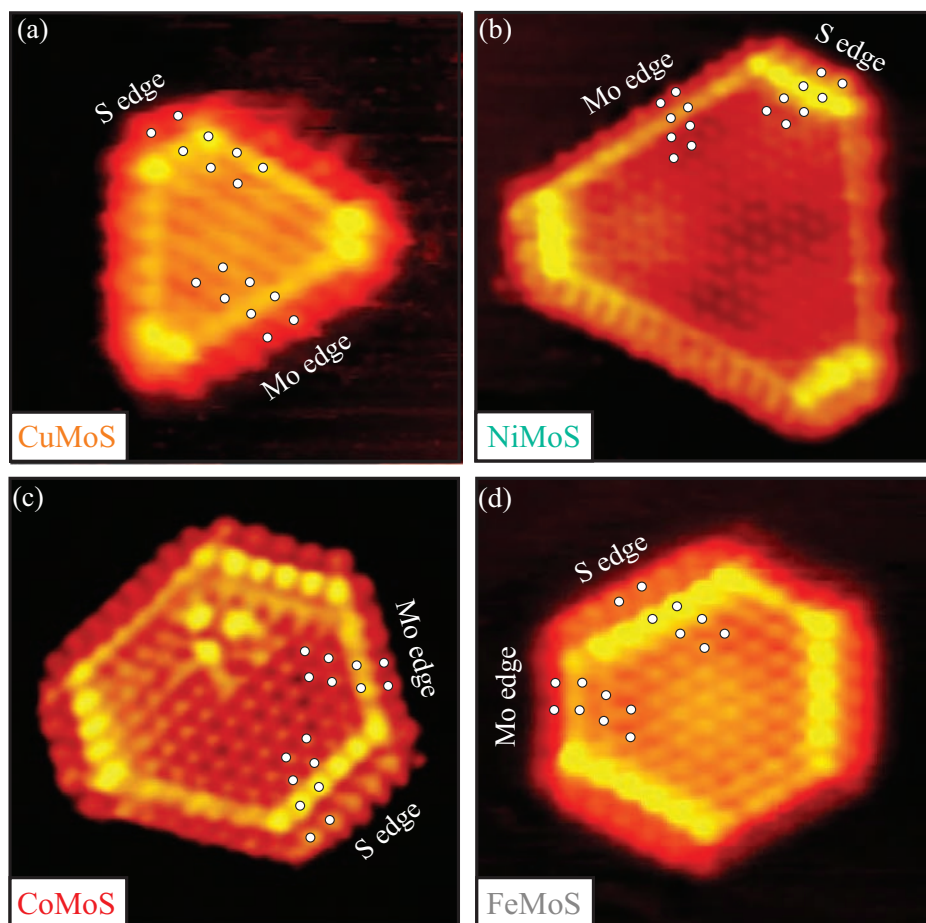


Figure 5.16. (a)-(d) Atom-resolved STM images of CuMoS ($50 \text{ \AA} \times 50 \text{ \AA}$, $I_t = 0.660 \text{ nA}$, and $V_t = -3.4 \text{ mV}$), NiMoS ($67 \text{ \AA} \times 65 \text{ \AA}$, $I_t = 0.500 \text{ nA}$, and $V_t = -600 \text{ mV}$), CoMoS ($51 \text{ \AA} \times 52 \text{ \AA}$, $I_t = 0.81 \text{ nA}$, and $V_t = 95.2 \text{ mV}$), and FeMoS ($50 \text{ \AA} \times 50 \text{ \AA}$, $I_t = 0.790 \text{ nA}$, and $V_t = -132 \text{ mV}$) nanoclusters, respectively. The white dots illustrate the position of the protrusions.

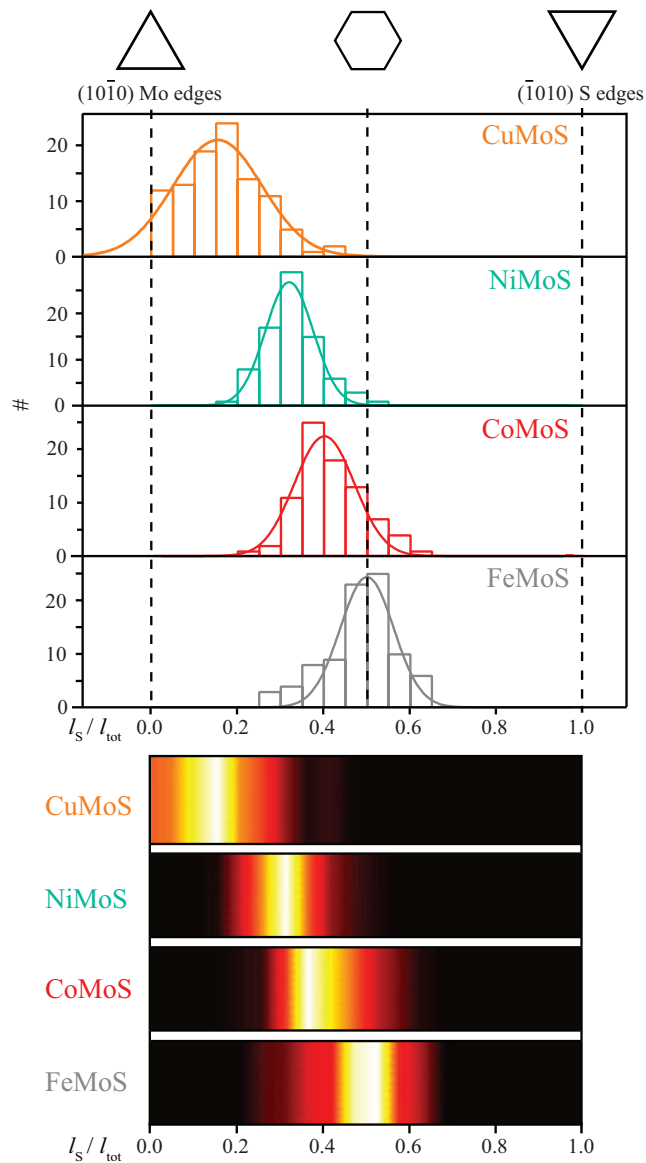


Figure 5.17. (a) Distribution of the ratio of the length of the $(\bar{1}010)$ S edges to the total edge length (l_S/l_{tot}) for CuMoS, NiMoS, CoMoS, and FeMoS, respectively. (b) Color plots of the ratio clearly illustrate that the proportional length of the $(\bar{1}010)$ S edges increases when going from copper over nickel and cobalt to iron in the periodic table.

stabilize the high-index $(11\bar{2}0)$ type of edges in MoS_2 , which are normally not considered in structural models. The presence of the NiMoS type B clusters clearly demonstrates that differences do exist in the morphologies of the CoMoS and NiMoS model catalysts. These differences may explain the different selectivity of CoMoS and NiMoS in the hydrotreating process.

Expanding the study to include iron and copper as promoter atoms showed that the degree of truncation of the clusters is dependent on the specific type of promoter atom in a systematic way.

CHAPTER 6

Support effects

In this chapter, the model system is taken one step further with an investigation of MoS₂ nanoclusters on a graphite and a rutile TiO₂ support, respectively, in order to study the effects of a more realistic support.

6.1 Introduction

The strength and nature of the cluster-support interaction are parameters known to influence the reactivity of the technical hydrotreating catalyst [21, 113–115]. The most widely used support material for the MoS₂-based hydrotreating catalyst is γ -alumina, which is in general believed to exert a stronger interaction on the active MoS₂-based nanoclusters compared to other supports, such as silica, carbon, or titania [21]. Though a strong support interaction is advantageous for synthesizing small MoS₂ clusters with a high edge dispersion that remain stable during operation, an increase in activity has been correlated with the existence of so-called type II CoMoS structures. These structures are assumed to be cobalt-promoted MoS₂ having a weak support interaction, as opposed to the less active type I CoMoS structures, which interact strongly with the support [116–119]. The lower activity of the type I structures is usually attributed to the formation of Mo-O-Al linkages to the support, which modifies the coordination and bonding of the reactive edge sites. This explanation is supported by a recent theoretical study by Hinnemann *et al.* [119], which showed that both the electronic edge structure and the bonding strength of sulfur at the cluster edges were greatly influenced by the presence of oxygen linkages to the support.

The more active type II structures typically form at higher sulfiding temperatures by breaking the Mo-O-Al linkages [120], but the higher temperatures also lower the degree of edge dispersion due to sintering, which leads to a loss of activity. Different methods have been developed to prevent this problem, including the use of chelating agents [121], but also the choice of substrate can be used as a means of optimizing the formation of type II structures.

In this regard, it is highly interesting to investigate the influence different substrates have on the morphology of the MoS₂ nanoclusters. Due to the insulating nature of alumina, it is not possible to investigate alumina-supported MoS₂ nanoclusters with STM. However, STM investigation of several other hydrotreating relevant support materials is possible. In this chapter two model substrates are investigated: a graphite surface and a rutile TiO₂ surface.

6.2 Graphite support

Graphite, as support material for MoS₂ nanoclusters, is very interesting since carbon-supported MoS₂-based catalysts have previously been found to exhibit a very high HDS reactivity [91, 122–124]. This was correlated with the presence of type II CoMoS structures.

In this section, STM is used to investigate carbon-supported MoS₂ nanoclusters. From high-resolution STM images, it is found that MoS₂ nanoclusters synthesized at low temperature in a sulfiding atmosphere preferentially grow as single-layer clusters, whereas clusters synthesized at 1200 K grow as multi-layer slabs. Furthermore, atom-resolved STM images provide information on the atomic-scale structure and morphology of the graphite-supported MoS₂ nanoclusters, and it is shown that STM is sensitive

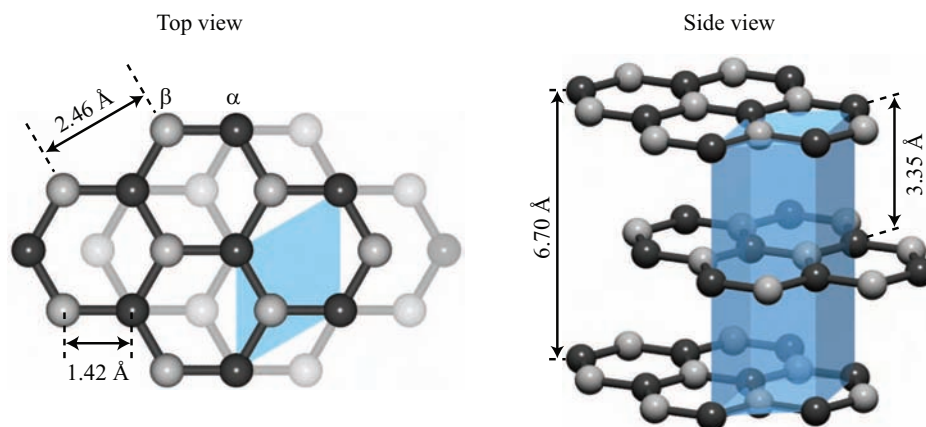


Figure 6.1. Ball model (top and side view, respectively) of the HOPG(0001) surface with two different carbon atoms - α and β sites. Only the β sites are imaged in STM images. The light-blue parallelepiped shows the unit cell.

to the MoS₂/graphite interface, thus allowing an investigation of the bonding of MoS₂ to graphite.

6.2.1 HOPG surface

The graphite sample used in the experiments was a highly oriented pyrolytic graphite (HOPG) sample. The HOPG(0001) surface exposes a honeycomb structure consisting of sp^2 hybridized carbon atoms that occupy non-equivalent sites within the two-dimensional surface unit cell: α carbon atoms, which have a neighbor in the underlying layer, and β carbon atoms, which have none as shown in the ball model in Fig. 6.1.

6.2.2 Experimental details

Prior to the experiments, the HOPG sample was cleaved in air with adhesive tape to expose the atomically flat (0001) basal plane. After transfer to the UHV chamber, the sample was thoroughly degassed at 1200 K in order to provide a clean and adsorbate free substrate. When the HOPG surface was imaged at this stage, the STM revealed clean and atomically flat terraces extending typically over several hundred nanometers. An atomically resolved STM image of the clean HOPG surface is shown in Fig. 6.2a.

It has previously been shown in detail that STM only resolves the β -sites of the graphite surface [125–127]. This is due to the fact that STM images in general reflect a convolution of the geometric and the electronic structure of the surface as discussed in Section 2.1.3. The β -atoms of the graphite surface are associated with a higher LDOS at the Fermi level compared to the α atoms, and consequently the β -sites are imaged as protrusions by the STM, although they do not physically protrude from the surface. The

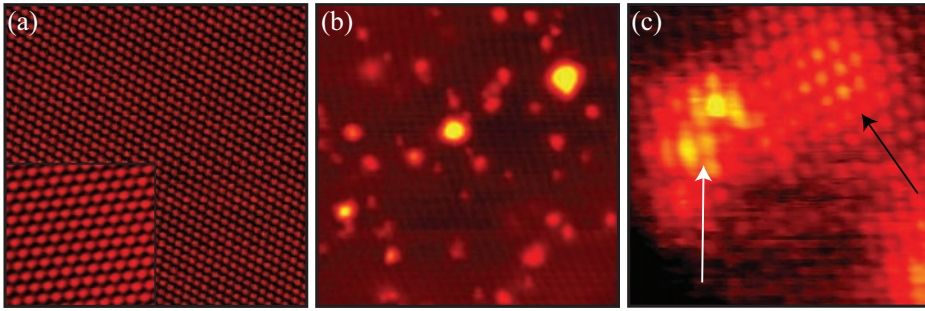


Figure 6.2. (a) STM image ($80 \text{ \AA} \times 80 \text{ \AA}$, $I_t = 0.44 \text{ nA}$, and $V_t = -9.8 \text{ mV}$) of the β -site atoms in the clean and flat HOPG surface. The insert shows a zoom-in ($30 \text{ \AA} \times 30 \text{ \AA}$, $I_t = 0.24 \text{ nA}$, and $V_t = -7.9 \text{ mV}$). (b) STM image ($400 \text{ \AA} \times 400 \text{ \AA}$) of a defect covered HOPG surface after the Ar^+ ion sputtering. (c) STM image ($80 \text{ \AA} \times 80 \text{ \AA}$, $I_t = 0.44 \text{ nA}$, and $V_t = -9.8 \text{ mV}$) of the two types of defects on the HOPG surface.

distance between protrusions in the high symmetry directions is measured to be 2.46 \AA in STM images, such as Fig. 6.2a, which is in accordance with the interatomic distance between the β -sites.

STM images of metallic Mo evaporated onto the pristine HOPG surface reveal that the nucleation density of Mo was quite low, and there was a tendency for Mo to agglomerate at the step edges at the synthesis temperatures. Due to the presumably weak bonding of Mo to the (0001) graphite plane, it was thus not possible to synthesize highly dispersed MoS_2 nanoclusters on the pristine HOPG surface. Instead, a procedure involving a slight ion bombardment with low-energetic Ar^+ ions (20 s at 150 V acceleration voltage) of the surface results in a well-dispersed system. Fig. 6.2b shows an STM image of the HOPG surface after the ion bombardment and a flash annealing to 900 K. The ion bombardment is observed to introduce a low density of defects on the HOPG surface ($\sim 4 \cdot 10^{-4} \text{ defects/\AA}^2$).

The defects can be divided into two distinctive types as seen in Fig. 6.2c. One type (black arrow) has as an almost circular dome-like structure displaying the undisturbed lateral atomic arrangement of the (0001) HOPG surface, whereas the other (white arrow) exhibits a distorted atomic structure. The dome-like defects are attributed to interstitial atoms, either Ar or C [128–130]. This type of defect is only rarely observed after the annealing to 900 K due to the desorption/mobility of the interstitials [130]. The more abundant distorted type of defect appears unaffected of the annealing. The origin of this type of defect is associated with a distortion of the surface atoms due to the formation of vacancies since the Ar^+ ions are above the threshold ($33.6 \pm 1 \text{ eV}$) for creating vacancies [131]. The seemingly counter-intuitive protruding imaging of defects caused by vacancies is explained by a vacancy-induced enhancement of the LDOS [130, 132]. These vacancy defects are typically also associated with a long-range electronic perturbation on the HOPG surface, leading to a $(\sqrt{3} \times \sqrt{3})R30^\circ$ superstructure in the STM images (see Fig. 6.3). This appearance is in good agreement with previous studies of

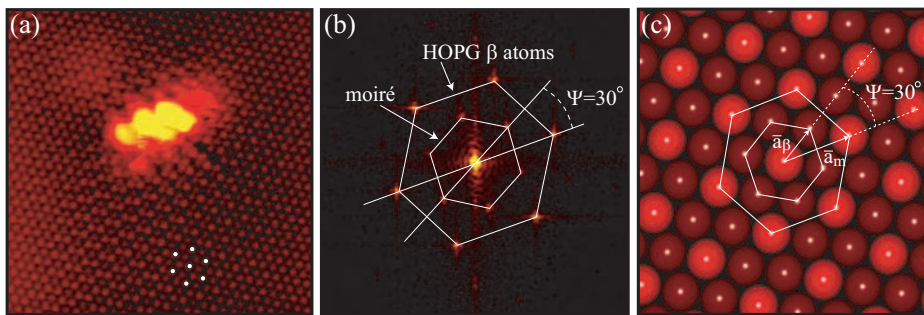


Figure 6.3. (a) Zoom-in ($75 \text{ \AA} \times 75 \text{ \AA}$, $I_t = 0.11 \text{ nA}$, and $V_t = -9.8 \text{ mV}$) on a defect. The white dots indicate the $(\sqrt{3} \times \sqrt{3})R30^\circ$ superstructure. (b) Fourier transform of the HOPG surface depicted in (a) in the region with the superstructure. The angle between the high symmetry direction of the superstructure and the β sites is found to be 30° . (c) Ball model of the $(\sqrt{3} \times \sqrt{3})R30^\circ$ superstructure (light colored balls).

superstructures on HOPG caused by defects in the topmost layer [133–135].

The synthesis procedure of the nanocrystalline MoS_2 clusters follows the preparation described in Section 3.3. Molybdenum ($\sim 10\%$ of a monolayer) was first deposited onto the defective HOPG substrate at 400 K by physical vapor deposition in a sulfiding H_2S atmosphere corresponding to $5 \cdot 10^{-6}$ mbar. In order to facilitate full sulfidation and crystallization of the clusters, it was necessary to increase the post-annealing temperature significantly compared to the 673 K for the synthesis on Au(111). In accordance with previous findings for the gold-supported systems [68] and a number of other studies for high surface area catalysts [101, 136], it was found that the crystallinity, morphology, and stacking of the MoS_2 nanostructures are dependent on the exact temperature used for the annealing step. As will be shown in the following sections, clusters synthesized at a temperature of 1000 K consist predominantly of a single S-Mo-S layer, whereas the clusters synthesized at 1200 K reflect crystalline multi-layer MoS_2 clusters of 2 to 6 S-Mo-S layers. Clusters synthesized at lower temperatures but at the same pressures used for the sulfidation step showed a relatively poor crystalline order.

6.2.3 Morphology of graphite-supported MoS_2 nanoclusters

Figures 6.4a and 6.8a show large-scale STM images of the surface following the synthesis at 1000 K and 1200 K, respectively. In both cases, it is observed that the synthesis produces well-dispersed, nanocrystalline clusters on the HOPG surface. The atomically resolved STM images in Fig. 6.4b and Fig. 6.10a of nanoclusters synthesized at 1000 K and 1200 K, respectively, reveal a perfectly crystalline basal plane consisting of hexagonally arranged protrusions with an average interatomic spacing of 3.15 \AA . This agrees with the interatomic spacing of the (0001) basal plane of MoS_2 , and it is thus concluded that the clusters are MoS_2 clusters aligned with the $\text{MoS}_2(0001)$ face in parallel with the graphite substrate.

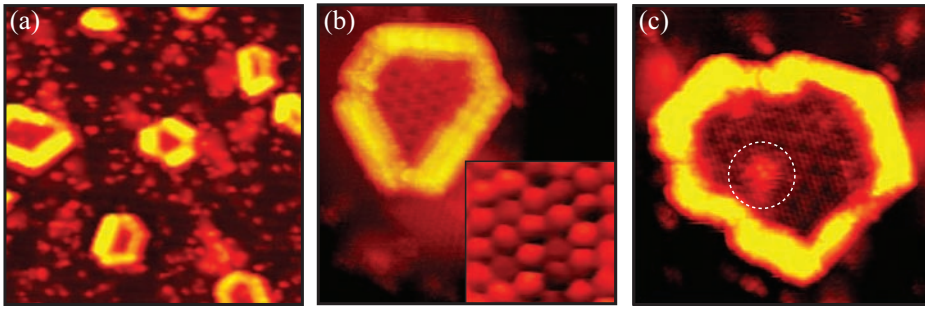


Figure 6.4. (a) STM image ($430 \text{ \AA} \times 430 \text{ \AA}$) of single-layer MoS_2 nanoclusters on HOPG. (b) STM image ($150 \text{ \AA} \times 150 \text{ \AA}$, $I_t = 0.35 \text{ nA}$, and $V_t = -743 \text{ mV}$) of a single-layer MoS_2 nanocluster. The insert ($17 \text{ \AA} \times 16 \text{ \AA}$, $I_t = 0.25 \text{ nA}$, and $V_t = -525 \text{ mV}$) shows a zoom-in on the basal plane showing the hexagonal arrangement of the topmost S atoms. (c) STM image ($150 \text{ \AA} \times 150 \text{ \AA}$) of a single-layer MoS_2 nanocluster on top of a defect in the HOPG surface (indicated by a white dashed circle).

The most striking difference between clusters prepared at the two different post-annealing temperatures is the apparent cluster height. In the common 2H- MoS_2 stacking of MoS_2 described in Section 3.4, the unit cell consists of two S-Mo-S layers separated by 6.15 \AA (see Fig. 3.4). The basal plane of the MoS_2 clusters synthesized at 1000 K has an apparent height of $4.0 \pm 0.3 \text{ \AA}$ relative to the HOPG measured from the basal plane of the cluster, and it is therefore concluded that these clusters reflect *single-layer* MoS_2 nanoclusters.

The apparent height of the clusters synthesized at 1200 K is significantly larger than the expected interlayer distance. It is therefore concluded that the clusters prepared at 1200 K represent *multi-layer* MoS_2 nanoclusters, i.e. consisting of two or more S-Mo-S layers. A height distribution measured for the synthesized clusters represents a measure of the stacking, and it is found that the predominant part of the clusters has heights that fall in the range from $\sim 18 \text{ \AA}$ up to 36 \AA . When this is compared to the nominal step height of $\text{MoS}_2(0001)$ of 6.15 \AA , it is concluded that these values reflect cluster stacking from 3-5 and in rare cases even up to 6 S-Mo-S layers. As expected, the cluster coverage at 1200 K is lower than the coverage of clusters synthesized at 1000 K due to the stacking since the total amount of Mo was kept fixed. Taking the height into consideration, the total MoS_2 coverage is found to be $\sim 12\text{-}16\%$ of a monolayer for both systems.

It is clearly observed in the STM images in Fig. 6.4a and Fig. 6.8a that both the single- and multi-layer clusters preferentially adopt a hexagonal morphology. As discussed in Section 3.5, the hexagonal morphology indicates that the stability of the $(10\bar{1}0)$ Mo edge and $(\bar{1}010)$ S edge is comparable. In the 2H- MoS_2 unit cell, the two S-Mo-S layers are translated and rotated 60° about the c axis so that S atoms in one layer are placed on top of Mo atoms in the next layer. The edges of a multi-layer cluster will thus expose both $(10\bar{1}0)$ Mo and $(\bar{1}010)$ S edge terminations in an alternating fashion (see Fig. 3.4b) and thus tend to cancel out any difference in edge free energies. Multi-layer

MoS₂ nanoclusters are consequently expected to grow in a perfect hexagonal shape in good agreement with the STM observations (see Fig. 6.8b).

It is, however, more surprising that the single-layer clusters display a hexagonally truncated shape, as opposed to the triangular shape found for the single-layer MoS₂ nanoclusters on a Au(111) substrate, as showed in Section 3.5. This change may, however, be explained by a change in synthesis parameters. The shape of MoS₂ clusters is known both experimentally [72, 101, 137, 138] and theoretically [74, 98] to be influenced by different synthesis parameters, such as the chemical potential of both hydrogen and sulfur (pressure, temperature), and the presence of promoter atoms as discussed in detail in the previous chapter.

The increase in post-annealing temperature in this experiment, from 673 K to 1000 K compared to the synthesis on Au(111), was necessary to achieve full crystallinity of the clusters at the applied H₂S pressures. The increased temperature leads to a lower chemical potential of sulfur [139]. This lowering changes the relative stability of the two types of edges, shifting the equilibrium shape from triangular exposing only (10 $\bar{1}$ 0) Mo edges toward hexagonally truncated exposing both types of edges [74]. A similar effect is observed when a mixture of H₂S and H₂ is used for the synthesis [72]. Furthermore, hydrogen adsorbs quite strongly on the fully sulfided ($\bar{1}$ 010) S edge and stabilizes the ($\bar{1}$ 010) S edge compared to the (10 $\bar{1}$ 0) Mo edge [43, 72, 140]. Hydrogen is always present during the synthesis in this experiment due to decomposition of H₂S and the fact that commercially available H₂S gas with the highest nominal purity always contains about 0.2% hydrogen. It is therefore plausible that ($\bar{1}$ 010) S edges on single-layer MoS₂ synthesized on HOPG, apart from a stabilizing effect from the increased temperature, furthermore experience an additional stabilization from hydrogen, which makes the stability of the ($\bar{1}$ 010) S edges comparable to that of the (10 $\bar{1}$ 0) Mo edges resulting in a hexagonally truncated cluster shape, as observed in the experiment.

6.2.4 Single-layer MoS₂ nanoclusters

In atom-resolved STM images of the single-layer MoS₂ clusters, a moiré superstructure is typically observed to be superimposed on the hexagonal lattice of sulfur atoms on the basal plane (Fig. 6.5). The moiré pattern arises from a rotation and lattice mismatch between MoS₂ and HOPG and thus reveals information on the structure of the MoS₂-graphite interface. According to the principle of epitaxial rotation, the relationship between the rotation angle, ψ_A , of the moiré structure relative to the MoS₂ lattice and the angle between the MoS₂ and substrate lattice, θ , is given as [141]:

$$\cos \theta = r_{SA} \sin^2 \psi_A + \cos \psi_A \sqrt{1 - r_{SA}^2 \sin^2 \psi_A} \quad (6.1)$$

where r_{SA} is the ratio of the substrate and MoS₂ lattice parameters. For the specific cluster in Fig. 6.6a (zoom-in on the basal plane) the angle ψ_A is found to be $22 \pm 1^\circ$, which gives θ a value of 5° if the lattice parameter for HOPG is taken to be the distance between voids of the honeycomb-structure on the HOPG surface (2.46 Å). The angle between the MoS₂ lattice and the voids on the HOPG can be measured directly in images with atomically resolution on both the MoS₂ and the HOPG and is found to be $5 \pm 1^\circ$

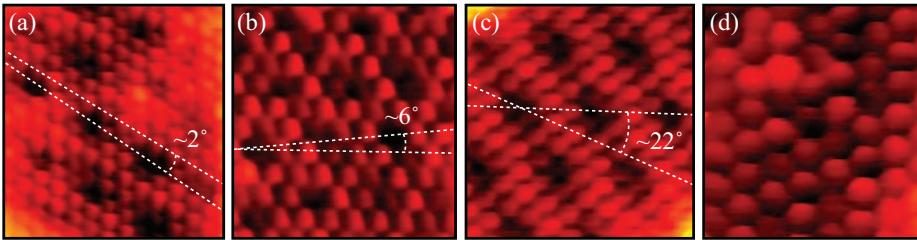


Figure 6.5. (a)-(c) STM images showing different moiré superstructures on the basal plane of single-layer MoS₂ nanoclusters. The rotation angles between the moiré structure and the MoS₂ lattice are approximately: 2°, 6°, and 22°, respectively. (d) STM image of an MoS₂ basal plane without a clear moiré pattern.

in good agreement with the above. A number of different periodicities of the moiré patterns are, however, observed on other clusters as shown in Fig. 6.5, which indicates that the rotation θ of the MoS₂ relative to the HOPG is arbitrary from cluster to cluster. This is also directly observed when comparing the relative orientation of MoS₂ clusters located on the same HOPG terrace in large-scale images (see, e.g. Fig. 6.4a).

The vertical corrugation in the moiré superstructures is measured in STM line scans to be 0.7-2 Å over the lateral distance of the specific moiré pattern (typically 9-12 Å). It is well known that MoS₂ is indeed very flexible perpendicular to the basal plane, which is exemplified by the formation of nanotubes and rag-like MoS₂ structures [136, 142-144]. The magnitude of the corrugation, e.g. in Fig. 6.6a, is however, unlikely to reflect a pure geometrical relaxation of the 2.39 Å Mo-S bonds in MoS₂ over such short distances. The moiré pattern is therefore also considered to be an electronic effect of the MoS₂ adlayer on HOPG. The existence of moiré patterns dominated by electronic effects has been explained by a three-dimensional extension of the MoS₂ wave functions around the Fermi level making them very sensitive to the substrate [66]. Furthermore, Kobayashi has showed that the amplitude of the superstructure produced at the interface propagates through the MoS₂ without decay [145]. If the position of the tip is above a certain crossover point, the signal detected by the STM will be dominated by the superstructure and not the topmost atomic structure. This is a result of the shorter wavelength and hence faster decay of the atomic structure.

A moiré pattern dominated by electronic effects is furthermore consistent with the fact that the voids in the honeycomb structure, which are associated with a low tunnel probability, seem to decide the structure of the moiré pattern rather than the geometrical structure of both types of carbon sites. The ball model in Fig. 6.6b of the specific cluster in Fig. 6.6a shows the HOPG lattice and a hexagonal lattice with an interatomic spacing of 3.15 Å corresponding to the interatomic distance in MoS₂. This lattice is rotated 5° compared to the HOPG lattice. As seen from the colored balls, the resulting superimposed cluster/HOPG-lattice structure explains the observed structure in the STM images accurately, if the dark regions (blue balls) are positioned directly over the voids in the HOPG lattice.

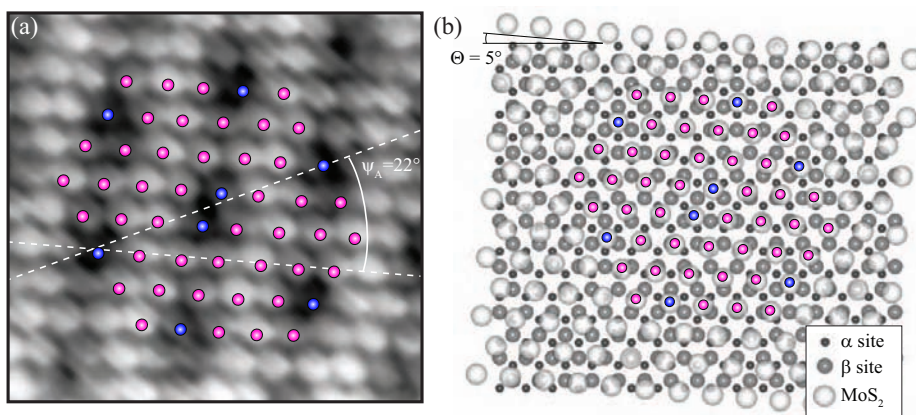


Figure 6.6. (a) STM image ($35 \text{ \AA} \times 33 \text{ \AA}$, $I_t = 0.24 \text{ nA}$, and $V_t = -1250 \text{ mV}$) showing a moiré superstructure on the basal plane of a single-layer MoS_2 nanocluster. (b) Ball model showing the HOPG lattice and an MoS_2 lattice rotated 5° with respect to each other. The colored balls show that the resulting superimposed cluster/HOPG-lattice structure explains the observed structure in the STM image accurately, if the dark regions (blue balls) are positioned directly over the voids in the HOPG lattice.

The necessity of introducing defects in the surface region in order to stabilize a high dispersion of MoS_2 on the plane HOPG(0001) surface clearly shows that defects play a role in the bonding of MoS_2 to graphite at elevated temperatures. The atom-resolved STM images provide information on the nature of the anchoring of the MoS_2 nanoclusters to the defects. In the atom-resolved images, the basal plane of the single-layer MoS_2 nanoclusters mostly appears with a perfect crystalline order reflecting that the topmost layer of graphite underneath is also perfectly crystalline. Occasionally, a distortion in the MoS_2 lattice on the basal plane of the clusters is observed (Fig. 6.4c), but a comparison of the defect density and the area of the individual clusters shows that the number of defects located underneath the basal plane is at least an order of magnitude lower than the expected average number of 5-8 defects per cluster. It is therefore concluded that no substantial bonding of basal plane sites underneath the MoS_2 clusters to the sites associated with defects in the graphite surface occurs.

In contrast, the appearance of the edges of the single-layer MoS_2 clusters suggests that defects are present in this region instead. The edges appear very bright in the atom-resolved STM images, indicating a high LDOS, but the crystalline ordering is clearly perturbed in several regions at the edges. Both the size and interspacing between the perturbed edge regions suggest that defects are present in the graphite support directly under the edges. The observations thus suggest that the bonding of the cluster to the substrate is predominantly formed by bonding of edge sites of the MoS_2 nanocluster. This conclusion is also consistent with the notion that edge sites typically have a higher interaction strength than the rather inert basal plane of MoS_2 [21]. Furthermore, the

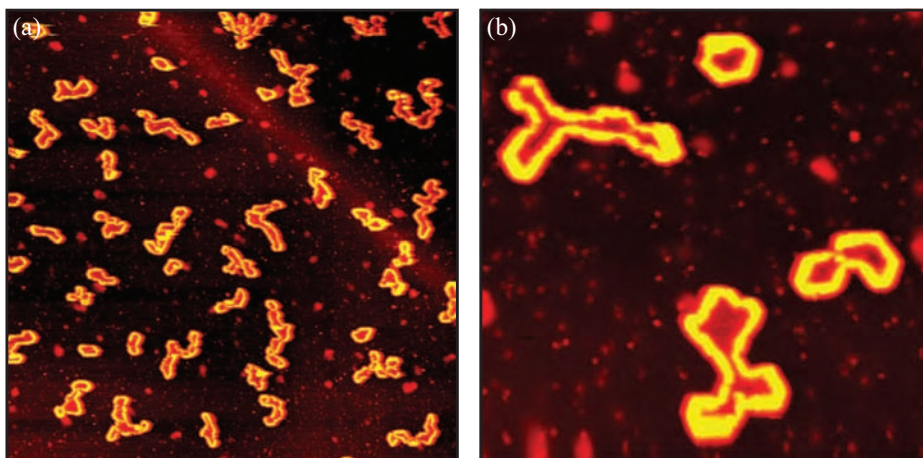


Figure 6.7. STM images of single-layer MoS_2 nanoclusters synthesized with 60 min of post-annealing. (a) STM image ($2500 \text{ \AA} \times 2500 \text{ \AA}$, $I_t = 0.560 \text{ nA}$, and $V_t = -1250 \text{ mV}$) and (b) ($750 \text{ \AA} \times 750 \text{ \AA}$, $I_t = 0.200 \text{ nA}$, and $V_t = -1250 \text{ mV}$).

defect-controlled anchoring of the clusters is in good agreement with the seemingly arbitrary rotation of the clusters with respect to the HOPG substrate since a bonding controlled by the basal plane sites of the MoS_2 would presumably favor certain rotations of the MoS_2 lattice with respect to the graphite.

The observation that defects control the anchoring of the MoS_2 was investigated further by controlling the cluster size. In separate experiments the duration of the 1000 K post-annealing step was increased from 15 min to a total of 60 min, which led to the formation of ~ 3 times larger single-layer MoS_2 nanoclusters (see Fig. 6.7). Again, none of the larger clusters show a significant concentration of defects being trapped under the MoS_2 basal plane despite the larger size confirming the observation above. Although the longer annealing time in principal should favor the formation of a more homogeneous ensemble of clusters, the result is a much more complex morphology consisting of irregularly shaped single-layer clusters and clusters partly merged from the simpler shapes. The irregular cluster shapes cannot be explained by the simple Wulff-type arguments for a free MoS_2 cluster but are rather attributed to defects controlling the morphology during growth of the larger clusters. Presumably, the defects act as pinning sites during growth and their distribution thus forces the clusters to adopt irregular shapes that deviate from the expected for an unsupported cluster in thermodynamic equilibrium. The fact that defects seem to be present only at the edges furthermore suggests that the defects must be slightly mobile under the clusters and are transported to the edge region of the clusters during the post-annealing at 1000 K. Thus, two different driving forces seem to control the morphology during growth, namely, the minimization of edge free energy of the clusters and the mobility and availability of the adhesion points during growth. The next section shows how an increase in the annealing temperature during the

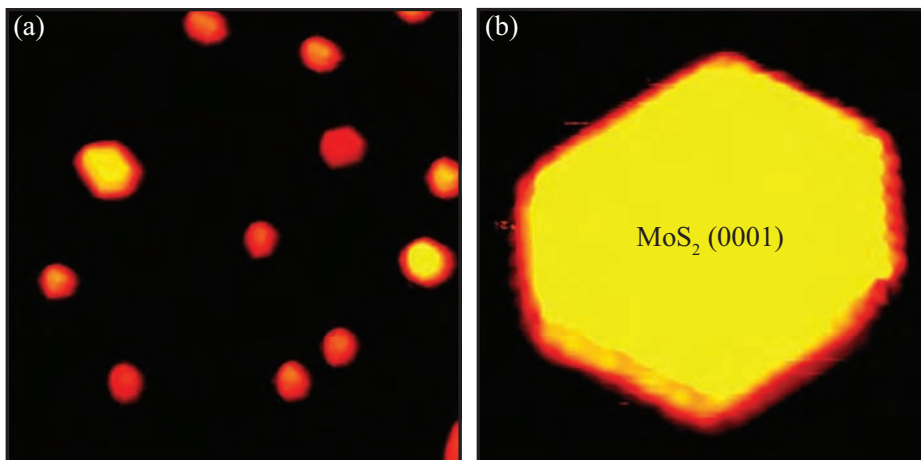


Figure 6.8. (a) STM image ($1000\text{\AA} \times 1000\text{\AA}$) of multi-layer MoS_2 nanoclusters on HOPG synthesized at 1200 K. (b) STM image ($69\text{\AA} \times 70\text{\AA}$) of a multi-layer MoS_2 nanocluster.

synthesis leads to a higher mobility of the defects and thus a more uniform morphology of the multi-layer MoS_2 clusters.

6.2.5 Multi-layer MoS_2 nanoclusters

At a post-annealing temperature of 1200 K following the Mo deposition, all MoS_2 nanoclusters appear as multi-layer clusters. The absence of single-layer clusters is explained by a preferential three-dimensional growth of stacked MoS_2 nanoclusters at 1200 K. Although the sputter-induced defects remain on the HOPG support after preparation at 1200 K, it is clearly not favorable enough to support two-dimensional growth of single-layer MoS_2 nanostructures. This finding reflects that the adhesion of the topmost layers of the MoS_2 nanoclusters on the lower layers is larger than that on the graphite(0001) plane or on the defects on the substrate. It is unlikely that the ordinary interlayer van der Waal bonding of the MoS_2 nanocluster basal plane is responsible for the preferential stacking. Instead, it is more likely that the stacking of the multi-layer MoS_2 nanoclusters is facilitated by interlayer bonding at sites near the cluster edge due to presence of the electronic edge states localized at the two outermost atomic rows. The complete absence of stacked structures at lower temperatures is then explained by a lower mobility of the surface species.

As opposed to the single-layer clusters no moiré pattern could be observed on the basal plane of the multi-layer clusters (see, e.g. Fig. 6.10a). Furthermore, the edges appear undistorted, and it thus not possible to observe individual anchoring points of the multi-layer clusters as was done for the single-layer MoS_2 clusters. However, the defects seem to control the morphology in an even more profound way than for the single-layer clusters. A direct comparison of the defect density on the surface before and after the

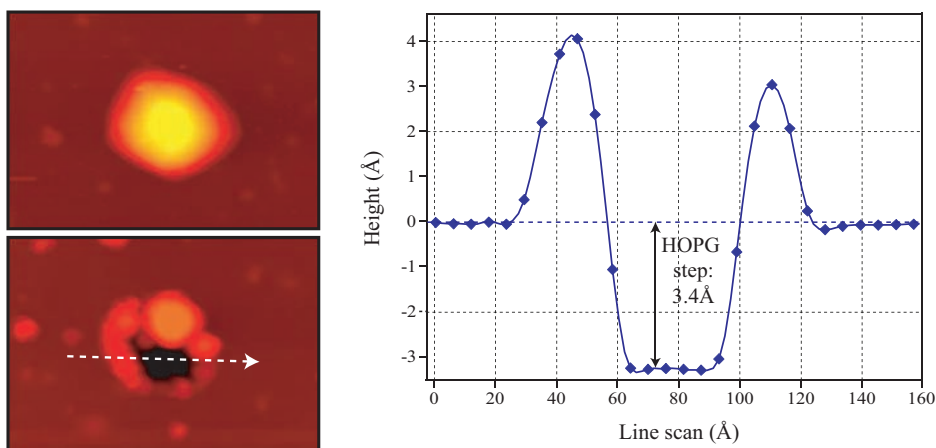


Figure 6.9. STM images ($250 \text{ \AA} \times 175 \text{ \AA}$) of a 30 \AA high multi-layer MoS_2 nanocluster before and after the cluster was moved by the fast-scanning STM tip. The line scan shows the profile of the pit in the HOPG surface after the tip removed the cluster.

synthesis at 1200 K reveals a decrease in the total number of defects by a factor of 2 to around $\sim 2 \cdot 10^{-4}$ defects/ \AA^2 . This finding indicates that the defects on the graphite become highly mobile at 1200 K and move either towards a step edge or alternatively start to agglomerate underneath the MoS_2 clusters.

Indeed, it was possible with the STM tip to remove the MoS_2 nanoclusters and thus expose the surface underneath. Such tip-induced lateral manipulations of the clusters could be induced by scanning the STM tip too fast across the surface for the feedback control to regulate the tip height accurately enough for the tip to clear the cluster during its path. As shown in Fig. 6.9, this procedure reveals a pit where the cluster was located originally. The line scan shows that the depth of the pit is 3.4 \AA , which corresponds precisely to the step height of HOPG. Furthermore, the atomic lattice in the pit could occasionally be resolved and revealed a hexagonal arrangement of atoms matching that of HOPG(0001). It is therefore suggested that the surface defects, introduced by the ion bombardment, agglomerate underneath the MoS_2 nanoclusters at 1200 K. The MoS_2 nanoclusters thus grow directly in the one atomic-layer deep pits of the HOPG, and the cluster substrate bonding is therefore not dominated by anchoring to point-like defects but rather pinning to steps in the pit. It is also observed that the overall morphology is significantly more uniform for the multi-layer clusters than for the single-layer clusters. This observation is linked to the higher mobility of the defects at 1200 K, which does not limit the growth and thus allows the cluster to adopt the equilibrium form of a free cluster.

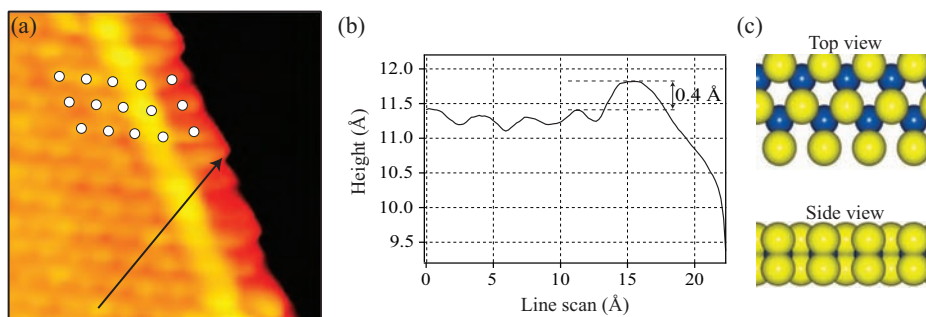


Figure 6.10. (a) Atom-resolved STM image ($36 \text{ \AA} \times 35 \text{ \AA}$, $I_t = 0.23 \text{ nA}$, and $V_t = -7.9 \text{ mV}$) showing the atomic-scale structure of the $(10\bar{1}0)$ Mo edge on a multi-layer MoS_2 nanocluster supported on HOPG. The superimposed grid on the basal plane sulfur atoms shows that protrusions at the edge are out of registry. (b) A line scan across the brim region of the $(10\bar{1}0)$ Mo edge. (c) Ball model (top and side view, respectively) of the $(10\bar{1}0)$ Mo edge fully saturated with sulfur dimers corresponding to the experiment.

6.2.6 Atomic-scale structure of multi-layer MoS_2 edges

In atom-resolved STM images (Figs. 6.10 and 6.11) the edge structures of the multi-layer MoS_2 nanoclusters are revealed, and since the edges do not appear perturbed by the HOPG defects, their structure can be analyzed in detail. As expected from the hexagonal morphology of the multi-layer clusters, two different types of edges aligned with a 120° angle between them are found in typical atom-resolved images, implying that one is the $(10\bar{1}0)$ Mo edge and the other is the $(\bar{1}010)$ S edge.

Figure 6.10a shows a zoom-in on one of the two edge types on a three-layer high hexagonal MoS_2 nanocluster. This edge is characterized by two predominant features: (i) protrusions at the edge are observed to be shifted *out* of registry relative to the basal plane S atoms and (ii) a narrow bright brim aligned in the direction parallel to the cluster edge just behind the outermost row of edge protrusions. These two observations are similar to the signatures that were used to unambiguously identify the fully sulfided $(10\bar{1}0)$ Mo edge in atom-resolved STM images of single-layer clusters grown on the gold support, as showed in Section 3.5.2. The qualitative accordance with previous observations therefore suggests that the edge analyzed in Fig. 6.10a reflects a fully sulfided $(10\bar{1}0)$ Mo edge on the multi-layer, graphite-supported MoS_2 clusters. For the multi-layer clusters the height of the brim above the basal plane is measured to be $\sim 0.4 \text{ \AA}$ (see Fig. 6.10b). Although one should be cautious about making direct comparison between the clusters synthesized on HOPG and gold, it is appealing that the brim height for the clusters synthesized on gold is also found to be 0.4 \AA .

The symmetry of the MoS_2 crystal structure implies that the other type of edges must be the $(\bar{1}010)$ S edges. This type of edge is shown in Fig. 6.11a. The primary indicators for the $(\bar{1}010)$ S edge in atom-resolved STM images of MoS_2 nanoclusters are again the registry of the protrusions at the edge and the location of the brim. A

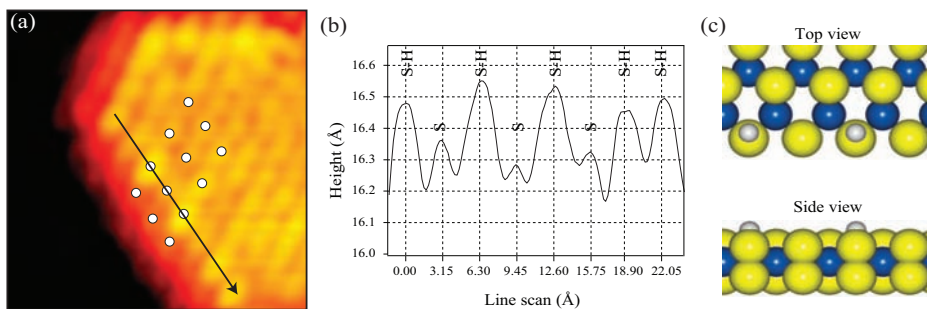


Figure 6.11. (a) Atom-resolved STM image ($41 \text{ \AA} \times 37 \text{ \AA}$, $I_t = 0.19 \text{ nA}$, and $V_t = 0.6 \text{ mV}$) of the $(\bar{1}010)$ S edge. The grid shows that the outermost protrusions on the $(\bar{1}010)$ S edge are imaged in registry with the basal plane S atoms. (b) A line scan along the bright brim on the $(\bar{1}010)$ S edge. Regions with lower intensity are associated with missing S-H groups. (c) Ball model of the $(\bar{1}010)$ S edge fully sulfided and with a fractional coverage of S-H groups representing the experimental image of the $(\bar{1}010)$ S edge.

superimposed grid shows that edge protrusions are placed *in* registry with the basal plane S atoms. Furthermore, the STM images also clearly show the existence of a brim located adjacent to the outermost row of protrusions. This brim is more intense than that of the corresponding $(10\bar{1}0)$ Mo edge also shown in the top left part of the image. In contrast to the brim of the $(10\bar{1}0)$ Mo edge, which shows no systematic corrugation along the brim, the position of individual protrusions along the brim region of the $(\bar{1}010)$ S edge is clearly resolved with the regular interatomic spacing of 3.15 \AA of MoS_2 . However, it is also apparent from the images that the protrusions in the brim region show a systematic variation in height. This is clearly observed in the line scan of Fig. 6.11b. Two types of brim protrusions are present with a difference in height of 0.2 \AA measured from peak to peak.

The difference in the intensity of the brim protrusions may be explained by hydrogen adsorption. The appearance of the $(\bar{1}010)$ S edges in the present study is quite similar to the $(\bar{1}010)$ S edges imaged for hexagonally truncated, single-layer MoS_2 nanoclusters synthesized in a mixture of hydrogen and hydrogen sulfide (sulfo-reductive conditions) [72]. In that case, a brim imaged 0.5 \AA above the basal plane was observed together with edge protrusions placed in registry. The edges with this signature were identified by a combination of DFT studies and STM as fully sulfided $(\bar{1}010)$ S edges with hydrogen adsorbed to form S-H groups. For comparison, the brim protrusions in Fig. 6.11a are $\sim 0.3 \text{ \AA}$ and $\sim 0.5 \text{ \AA}$ above the basal plane, respectively. Based on the similarities, it is tentatively suggested that the $(\bar{1}010)$ S edges of the multi-layer MoS_2 clusters also expose this kind of termination, despite that they are synthesized under sulfiding conditions since hydrogen is always present as pointed out in Section 6.2.3. It is therefore plausible that a fractional population of S-H groups is present even at the low hydrogen pressures present during synthesis in this experiment. Hydrogen adsorption on the $(\bar{1}010)$ S edge with a coverage less than 100% may thus explain the observation

of the different brim heights along the edge since bonding of H on the S adjacent to the brim will most likely change the characteristics of the electronic states associated with the brim. In this case, adsorbed H seems to lead to an enhancement of the brim. This configuration with a fractional population of S-H groups is shown in the ball model in Fig. 6.11c.

The observation of hydrogen adsorbates at the cluster edges is very interesting since both adsorption of the S containing molecule and dissociation of H₂ are required to facilitate the HDS reaction. In particular, the fractional occupation of hydrogen on the ($\bar{1}010$) S edge is interesting in this respect since free sites are thus available for vacancy formation or direct adsorption of the S containing molecule in the brim region, which subsequently can react with the adjacent atomic H specie.

6.3 TiO₂ support

Most metal oxides are large band gap semiconductors or insulators, which inhibits the use of most surface science techniques. Some of the oxides can, however, be made conducting by the introduction of defects, such as oxygen vacancies or metal interstitials, which are formed during the standard sputtering and annealing crystal preparation procedure under ultra-high vacuum conditions [146].

In recent year rutile titanium dioxide (TiO₂) has emerged as the prototypical oxide system for surface science studies. This is partly due to the technological versatility of TiO₂ and partly due to the ability to prepare conducting TiO₂ crystals under UHV conditions. TiO₂ is utilized in a vast number of technological applications ranging from white pigment in, e.g. paint and cosmetics, “self-cleaning” super-hydrophilic coatings for windows [147], the surface layer on Ti-based bio-compatible implants [148, 149], photocatalyst in, e.g. solar cells [150, 151], and active support in oxidation catalysts [15, 152].

Titanium dioxide has also been studied as a support for the MoS₂-based hydrotreating catalyst. TiO₂-supported MoS₂ catalysts in fact present three to five times higher intrinsic hydrodesulfurization and hydrogenation activities than alumina-supported ones with an equivalent Mo loading per area [115]. Alumina-supported catalysts have nevertheless been preferred due to a better porosity and higher specific surface area. However, within the last decade, many improvements in the preparation of oxide supports have been achieved, and TiO₂ supports with higher specific surface areas and larger pore diameters have been obtained [153, 154]. The TiO₂-supported MoS₂-based catalysts have thus recently been subject to renewed attention both experimentally and theoretically. Ramirez *et al.* suggested that the enhanced catalytic activity is related to the formation

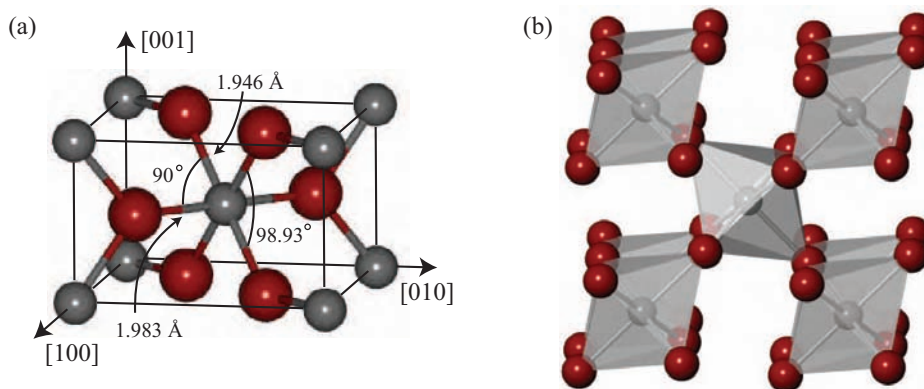


Figure 6.12. (a) The unit cell of bulk TiO₂. Each Ti atom is coordinated to six O atoms in a slightly distorted octahedron. The stacking of these octahedra in the crystal structure of rutile TiO₂ is shown in (b). Color code - Ti: gray and O: red.

of Ti³⁺ species under reaction conditions [155]. These Ti³⁺ species act as electron donors and inject electrons into the Mo 3*d* conduction band, which weakens the Mo-S bond. On the other hand recent DFT calculations have suggested that the origin of the high activity of the TiO₂-supported MoS₂-based catalysts is linked to the formation of edge-up MoS₂ particles due to an interaction between the MoS₂ edge planes and certain planes of anatase TiO₂ [156–158]. The role of the TiO₂ support and other supports in general is still under intensive debate, and scanning probe surface science studies may thus provide valuable information that could help unravel the effects of the TiO₂ and other supports.

While rutile crystals are readily available, sufficiently large and pure anatase crystals are difficult to obtain. The present study is thus performed on the rutile TiO₂(110) surface, which has been subject to intense surface science, including STM studies [159]. It is shown that single-layer MoS₂ nanoplatelets form on the rutile TiO₂(110) surface, thus allowing the first detailed atomic-scale investigation of MoS₂ nanoparticles on an oxide support. From high-resolution STM images it is found that the TiO₂ support controls the growth of the MoS₂ nanoplatelets both in terms of shape and orientation relative to the support.

6.3.1 Rutile TiO₂

Rutile TiO₂ has a tetragonal unit cell with two titanium and four oxygen atoms (Fig. 6.12a). Each Ti atom is surrounded by six oxygen atoms in a slightly distorted octahedron. In the bulk rutile TiO₂ crystal, the octahedra are stacked with their long axis alternating by 90°, resulting in three-fold coordinated oxygen atoms (Fig. 6.12b). Electronically rutile TiO₂ is a wide band gap semiconductor of ~ 3eV. The valence band consists predominately of O 2*p* states, while the conduction band primarily consists of Ti 3*d* states [160]. TiO₂ is, however, readily reduced by annealing under vacuum conditions. Upon reduction, bulk defects are introduced, which gives rise to a pronounced color change of the TiO₂ crystal from initially transparent to light- and eventually dark-blue [161].

The most stable facet of rutile TiO₂ is the (110) surface [146]. Due to the partly covalent nature of the bonds in TiO₂, this is not unexpected since the (110) surface is the one with the smallest number of dangling bonds [162]. The (110) surface is bulk terminated and can be created by cleaving a TiO₂ crystal perpendicular to the [110] direction (Fig. 6.13). The stoichiometric TiO₂(110) surface consists of alternating rows of fivefold coordinated titanium atoms, Ti(5f), and twofold coordinated oxygen atoms, O(2f), as illustrated in Fig. 6.13c.

6.3.2 Experimental details

The TiO₂(110) sample was cleaned by cycles of Ar⁺ sputtering, followed by annealing at 900 K for 20 min to restore a flat surface. The crystal used for this experiment had a dark-blue color, indicating O-deficient, bulk-reduced sample. Figure 6.14a shows an STM image of the TiO₂(110) surface. The surface appears with alternating parallel bright and dark rows and a number of bright protrusions on the dark rows. It is

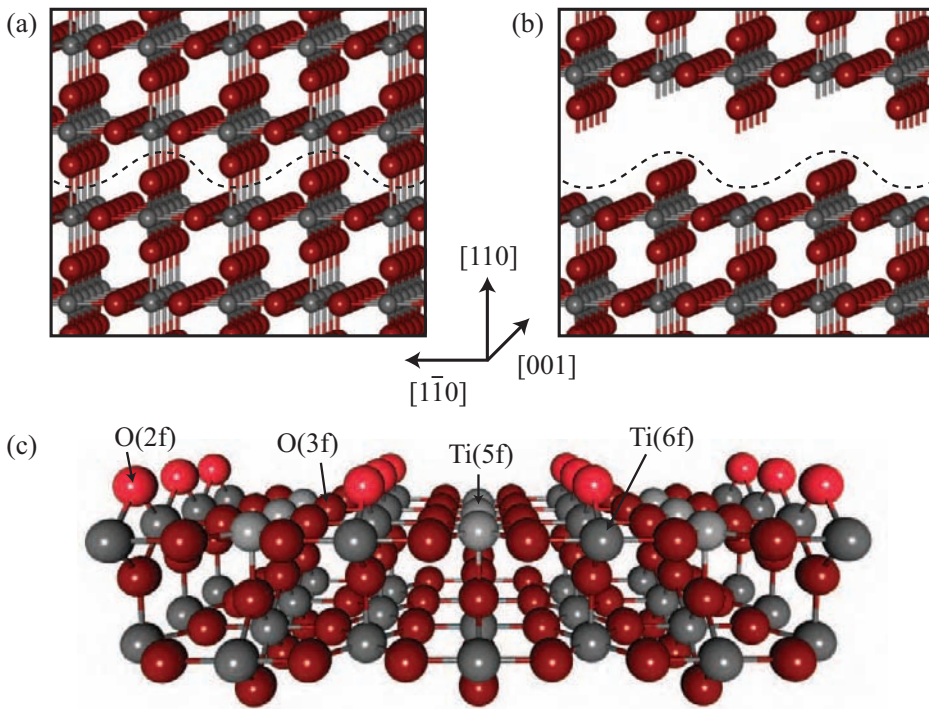


Figure 6.13. (a) The bulk TiO₂ crystal. (b) The TiO₂(110) surface is created by cleaving the crystal along the dashed line. (c) Ball model of the stoichiometric TiO₂(110) surface. The coordination of the individual atoms is indicated in the brackets. Color code - Ti: gray and O: red.

well known that the STM images of the TiO₂(110) surface are dominated by electronic effects, and counterintuitive the Ti troughs are imaged as the bright rows, whereas the geometric protruding bridging O rows are imaged as dark rows [159]. The bright protrusions located on the dark rows are associated with either oxygen vacancies or bridging hydroxyl groups [163]. Figures 6.14c-6.14e show three successive STM images of the same part of the TiO₂(110) surface, and it is observed that the bright protrusions are mobile on the surface. This is a clear indication that the bright protrusions are associated with OH groups. The bridging hydroxyl groups form as a result of dissociation of water from the rest gas in the oxygen vacancies created during the cleaning process of the TiO₂(110) surface [164].

The MoS₂ nanoplatelets were synthesized by the method described in Section 3.3. The Mo deposition was carried out in an H₂S atmosphere corresponding to $\sim 5 \cdot 10^{-6}$ mbar, and subsequently the sample was annealed to 900 K or 950 K for 10 min while maintaining the sulfiding atmosphere. H₂S has previously been shown to adsorb dissociative on a sputtered highly defective TiO₂(110) surface producing both H and S bound to Ti cations on the surface [165, 166]. However, the post-annealing step in the cleaning

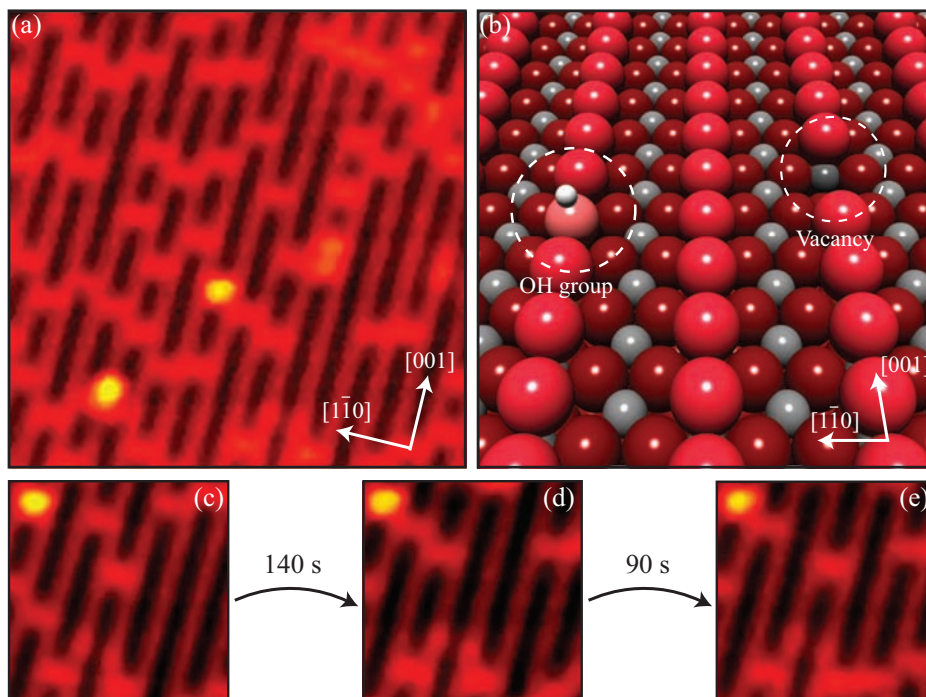


Figure 6.14. (a) STM image ($100 \text{ \AA} \times 100 \text{ \AA}$, $I_t = 0.490 \text{ nA}$ and $V_t = 1250 \text{ mV}$) of the clean reduced $\text{TiO}_2(110)$ surface. (b) Ball model of the $\text{TiO}_2(110)$ surface showing a bridging hydroxyl group and an oxygen vacancy. Color code - Ti: gray, O: red, and H: white. (c)-(e) Successive STM images of the same part of the surface showing the mobility of the OH groups.

procedure restores a $\text{TiO}_2(110)$ surface with only a low concentration of defects. Previous studies have shown that a nearly perfect $\text{TiO}_2(110)$ surface is inert to a variety of gases [167–170], and in agreement only trace amounts of sulfur is found with Auger electron spectroscopy (AES) after exposing the surface to H_2S . Subsequent STM on the $\text{TiO}_2(110)$ surface exposed to H_2S , during the synthesis of the MoS_2 nanoclusters, also images the surface with the well known alternating parallel bright and dark row appearance (see, e.g. Fig. 6.17a). Both AES and STM thus confirm that H_2S does not subject a low defect concentration $\text{TiO}_2(110)$ surface to a massive sulfur-induced transformation as previously observed for a surface exposed to elemental sulfur [171]. It is thus concluded that the MoS_2 nanoplatelets are synthesized on a low defect concentration $\text{TiO}_2(110)$ surface without major sulfur-induced transformations.

The sulfur pressure during the synthesis was observed to have pronounced effect on the synthesized molybdenum sulfide structures. A lower sulfur pressure ($< 1 \cdot 10^{-6}$ mbar) during the synthesis resulted in a very homogeneous ensemble of small ball-like structures on the surface (Fig. 6.15). The average size of these ball-like struc-

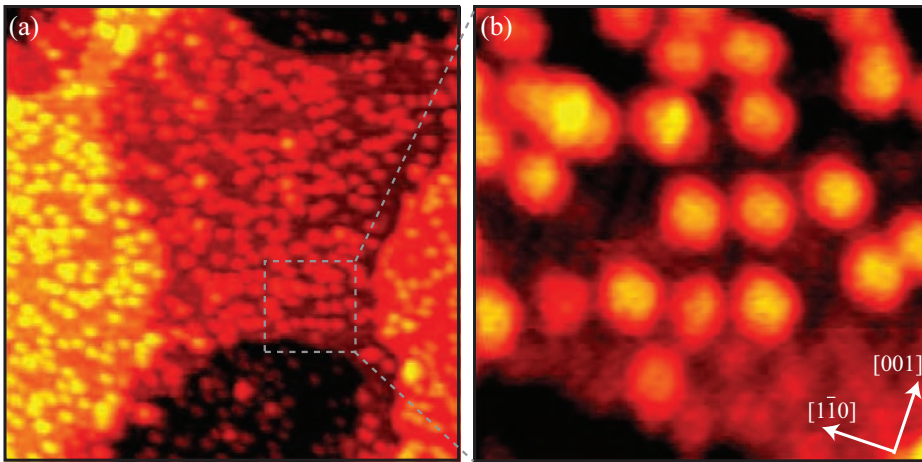


Figure 6.15. (a) STM image ($500 \text{ \AA} \times 500 \text{ \AA}$, $I_t = 0.580 \text{ nA}$ and $V_t = 1250 \text{ mV}$) of Mo_mS_n complexes on the TiO_2 (110) surface. (b) Zoom-in ($100 \text{ \AA} \times 100 \text{ \AA}$, $I_t = 0.860 \text{ nA}$ and $V_t = 1250 \text{ mV}$).

tures is measured in STM images to be $94 \pm 3 \text{ \AA}^2$. It is proposed that the ball-like structures are Mo_mS_n complexes, which act as precursors to the formation of MoS_2 nanocrystals. However, the low-pressure sulfiding conditions do not stabilize the sulfur-terminated edges of the S-Mo-S layers required for the stabilization of regular layered MoS_2 nanocrystals, and hence only at higher sulfur pressures ($> 5 \times 10^{-6}$ mbar) do the precursors agglomerate and crystallize into MoS_2 nanocrystals. A similar effect is observed for molybdenum sulfide nanostructures synthesized on a graphite surface. At low sulfur pressures the synthesis produces a Mo_6S_6 nanowire structure instead of MoS_2 nanoclusters. These Mo_6S_6 nanowires are the topic of Chapter 7.

6.3.3 Morphology of $\text{TiO}_2(110)$ -supported MoS_2 nanoplatelets

Figures 6.16a and 6.16b show large-scale STM images of the created structures on the $\text{TiO}_2(110)$ surface after synthesis with a post-annealing temperature of 900 K and 950 K, respectively. At both post-annealing temperatures, the synthesis is observed to produce a well-dispersed ensemble of MoS_2 nanoplatelets. The synthesis at 950 K generally produces longer platelets, however, the width of the platelets is observed to be fixed around a value of $\sim 36 \text{ \AA}$ independent of annealing temperature, as seen from the width distribution in Fig. 6.16c.

As observed for the $\text{Au}(111)$ -supported system [79], the apparent height of the MoS_2 nanoplatelets is observed to be dependent on the applied bias voltage as seen from Figs. 6.17a-6.17c. A strong dependence of the bias on the imaging is expected since MoS_2 is a semiconductor with a band gap of $\sim 1.2 \text{ eV}$. Accordingly, at high bias voltages ($>1000 \text{ mV}$) the platelets appear with a clear basal plane. At intermediate voltages

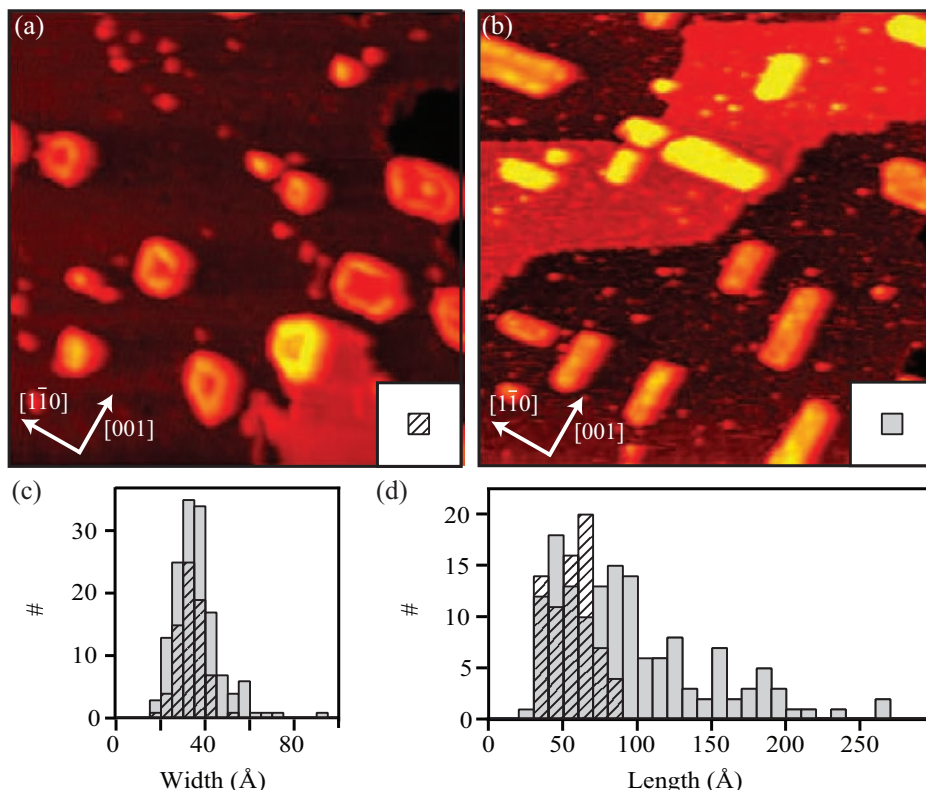


Figure 6.16. (a) and (b) STM images showing the synthesized MoS₂ nanoclusters on a TiO₂(110) surface. (a) is synthesized at 900 K (500 Å × 500 Å, $I_t = 0.320$ nA, $V_t = 1250$ mV) and (b) is synthesized at 950 K (1000 Å × 1000 Å, $I_t = 0.300$ nA, $V_t = 1250$ mV). (c) and (d) Width and length distribution of the MoS₂ clusters, respectively.

(100 mV - 1000 mV) the basal plane of the MoS₂ platelets becomes transparent to the STM, and the row structure of the TiO₂(110) surface can be observed through the MoS₂ platelet. At low bias voltages (<100 mV) the hexagonal lattice of MoS₂ with a lattice constant of 3.15 Å can clearly be observed with a small perturbation from the underlying Ti rows. Due to the strong dependence of the bias on the imaging, one should be cautious about performing height measurements. However, in images recorded at high bias voltages where the platelets show a clear basal plane, the platelets have an apparent height of 4.7 ± 0.5 Å, and it is thus concluded that the MoS₂ nanoplatelets consist of a single S-Mo-S layer.

On the TiO₂(110) surface, the MoS₂ platelets grow in an elongated hexagonal manner, and as a result, the platelets display both (10 $\bar{1}$ 0) Mo and ($\bar{1}$ 010) S edges. In STM images the two different edge terminations can clearly be distinguished. Figure 6.18a shows an STM image of a hexagonal MoS₂ nanoplatelet on the TiO₂(110) surface.

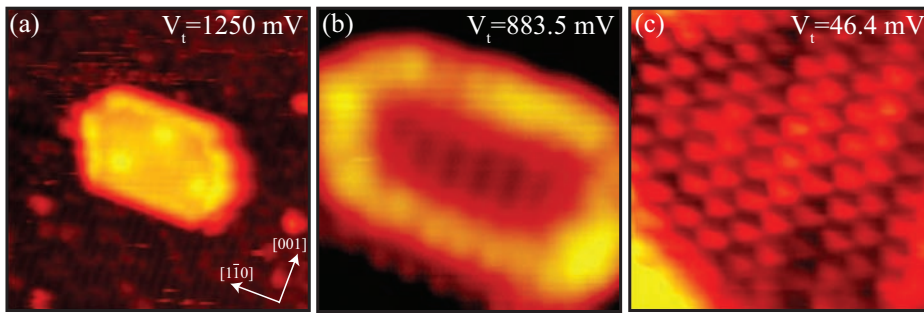


Figure 6.17. STM images showing the bias dependent imaging of the MoS₂ clusters. (a) ($200 \text{ \AA} \times 200 \text{ \AA}$, $I_t = 0.320 \text{ nA}$, $V_t = 1250 \text{ mV}$), (b) ($70 \text{ \AA} \times 70 \text{ \AA}$, $I_t = 0.260 \text{ nA}$, $V_t = 883.5 \text{ mV}$), and (c) ($30 \text{ \AA} \times 30 \text{ \AA}$, $I_t = 0.390 \text{ nA}$, $V_t = 46.4 \text{ mV}$).

Three of the edges, which are rotated 120° compared to each other, are imaged brighter relative to the remaining three edges as also clearly illustrated in an STM line scan across both edges (see Fig. 6.18b). It was not possible to obtain atom-resolved STM images of the edge structure of the TiO₂-supported MoS₂ platelets, and an identification of (10 $\bar{1}$ 0) Mo and ($\bar{1}$ 010) S edges from the position of the outermost row of protrusions is thus not possible, as was demonstrated for the graphite-supported system in the previous section. However, as also discussed in the previous section, the ($\bar{1}$ 010) S edges are associated with a brighter brim structure, and accordingly the edges with the more intense brim structure are proposed to be ($\bar{1}$ 010) S edges.

6.3.4 Support-controlled growth of MoS₂ nanoplatelets

Large-scale STM images, such as Fig. 6.16b, reveal that the nanoplatelets orient in two very distinct ways on the TiO₂ surface: parallel or perpendicular to the [001] direction of the TiO₂ surface. A more detailed analysis of the rotation relative to the [001] direction is shown in Fig. 6.19a and clearly confirms that nearly all of the platelets are oriented either parallel (0°) or perpendicular (90°) to the [001] direction. The clear bimodal orientation must be governed by the interface between the platelet and the support. The hexagonal lattice structure of MoS₂ implies that a 60° rotation of a platelet does not change the orientation of the MoS₂ lattice with respect to the TiO₂(110) surface. However, the clear absence of platelets with an orientation 30° or 60° relative to the [001] direction evidently shows that the interaction between the basal plane of the MoS₂ platelet and the support cannot play a major role in the bonding and hence orientation of the platelet to the support. This leaves the edges as the controlling parameter. As discussed in Section 6.2.5 in the case of multi-layer MoS₂ clusters on a HOPG support, the metallic edge states facilitate a strong bonding compared to basal plane sites. It thus seems likely that the edges also play a crucial role in the bonding of the platelet to the support in the present case.

The origin of two distinct orientations of the MoS₂ platelets and the very narrow

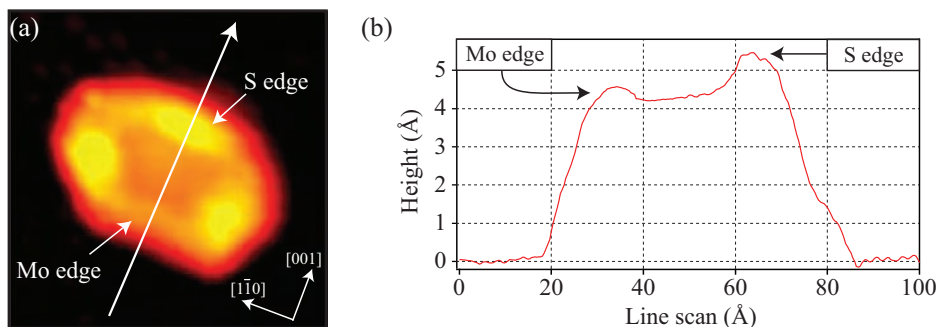


Figure 6.18. (a) STM image ($100 \text{ \AA} \times 100 \text{ \AA}$, $I_t = 0.350 \text{ nA}$, $V_t = 1250 \text{ mV}$) clearly showing that the MoS₂ platelet expose to different edge terminations: the $(10\bar{1}0)$ Mo and $(\bar{1}010)$ S edge, respectively. (b) Line scan across the cluster depicted in (a) as indicated by the white arrow.

width distribution can be directly correlated with the well-defined lattice mismatch between the MoS₂(0001) and TiO₂(110). Figures 6.20a and 6.20b display the specific width distribution for platelets oriented parallel and perpendicular to the [001] direction, respectively. The platelets oriented parallel have an average width of $38 \pm 1 \text{ \AA}$, which is slightly larger than the average width of $33 \pm 1 \text{ \AA}$ for the platelets oriented perpendicular. Both widths are controlled by the mismatch between the MoS₂ lattice and TiO₂(110) lattice. Figure 6.19b shows two slabs of MoS₂ on a TiO₂(110) surface where the bridging oxygen atoms are represented by the grid. One slab is oriented parallel and the other perpendicular to the [001] direction. The brim regions with enhanced bonding properties are shown in yellow and covers the first three rows from the edge. The position of the two slabs relative to the surface has been determined from atom-resolved STM images. Figure 6.20c shows the edge of a platelet oriented parallel to the [001] direction, and from the superimposed grid representing the position of the bridging oxygen atoms, it is observed that the brim structure is on top of two bridging oxygen rows running in the [001] direction. Accordingly, the model slab oriented parallel to the [001] direction in Fig. 6.19b has been placed with the yellow brim structure on top of two bridging rows in the [001] direction. Figure 6.19b reveals that in order for both platelet edges parallel to the [001] direction to have this particular strong bonding position on the TiO₂(110) surface, the platelet requires a width of 38.3 \AA . In a similar way, Fig. 6.20d shows the position relative to the TiO₂(110) surface for a platelet oriented perpendicular to the [001] direction, and Fig. 6.19b shows that these platelets require a width of 32.8 \AA to obtain this particular strong bonding structure under both platelet edges parallel to the $[\bar{1}\bar{1}0]$ direction. Both widths are in excellent agreement with the experimentally observed and show that the width of the platelets is determined by the underlying support.

The growth mode of MoS₂ platelets on the TiO₂(110) surface can thus be described as an initial nucleation and growth of an anchoring platelet edge to highly specific positions on the TiO₂(110) surface running either along the [001] or $[\bar{1}\bar{1}0]$ direction, which explains the bimodal orientation. The growth in the $[\bar{1}\bar{1}0]$ direction of a platelet oriented

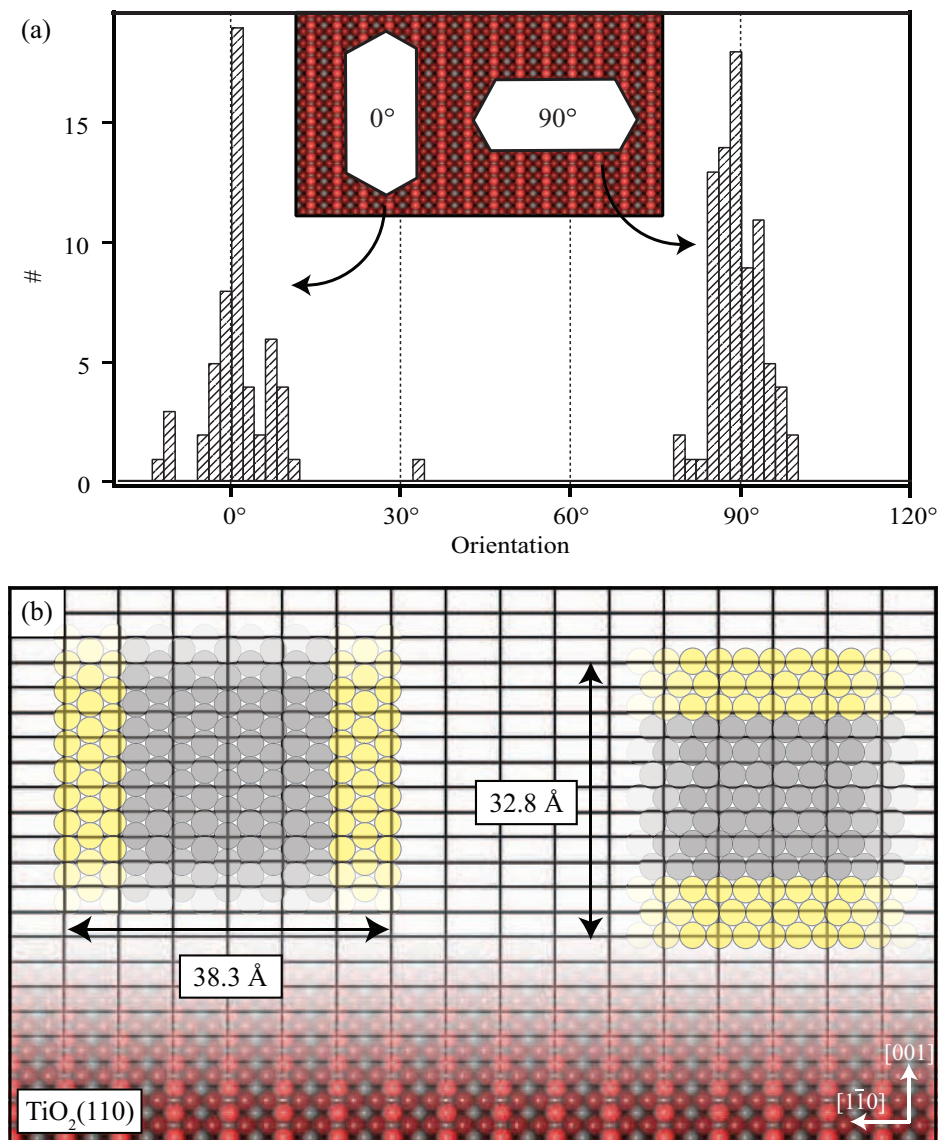


Figure 6.19. (a) Rotation distribution of the MoS₂ clusters on the TiO₂ surface with respect to the [001] direction. (b) Two slabs of MoS₂ on a TiO₂(110) surface where the bridging oxygen atoms are represented by the grid. The brim regions of the clusters are shown in yellow.

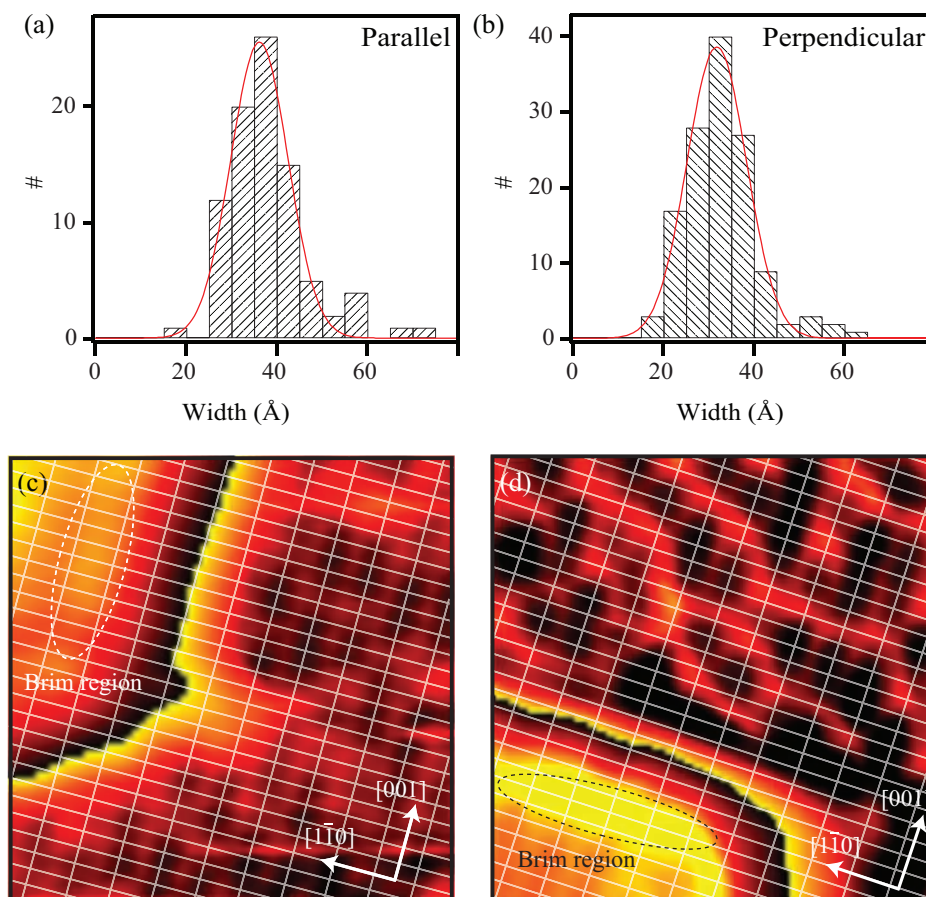


Figure 6.20. (a) and (b) Width distributions for clusters oriented parallel and perpendicular to the [001] direction, respectively. (c) and (d) show two STM images ($75 \text{ \AA} \times 75 \text{ \AA}$) of the edge region of a cluster oriented parallel and a cluster oriented perpendicular to the [001] direction, respectively. The grids show the position of the bridging oxygen atoms.

parallel to the [001] direction or in the [001] direction of a platelets oriented perpendicular to the [001] direction continues until the platelet is again able to make a strong bonding to the support. At this point when the platelet has two edges strongly bonded to the support, the platelet is restricted to grow parallel to the two strongly bonded edges with an elongated platelet shape as a result. This growth mode explains the narrow width distribution since the width of the platelets solely is determined by the well-defined mismatch between the MoS₂ lattice and lattice of the TiO₂(110) support.

It would be very interesting in future experiments to synthesize MoS₂ on another facet of rutile TiO₂, e.g. the (100) or (001) facet, with another lattice mismatch with respect to the MoS₂, to see whether the width of the synthesized MoS₂ nanoclusters is changed accordingly as expected from the present results. Furthermore, DFT calculations of MoS₂ on a rutile TiO₂(110) surface could shed more light on the exact nature of the bonding between the MoS₂ platelets and the support.

6.4 Conclusion

The studies presented in this chapter take the hydrotreating model system one step further by including the effects of more realistic support materials, that is, a HOPG and a rutile TiO₂(110) surface, respectively. The results show that the support affects the structure of the MoS₂ clusters in terms of, e.g. stacking and cluster shape. On the HOPG surface, the synthesized clusters are observed to display a very temperature-dependent morphology since the clusters prepared at 1000 K grow as single-layer clusters, whereas clusters prepared at 1200 K exclusively grow as stacked multi-layer clusters.

On the rutile TiO₂(110) surface, the MoS₂ clusters are observed to adopt two distinct orientations: parallel or perpendicular to the [001] direction, respectively. The clusters have an elongated hexagonal shape and a very narrow width distribution that is found to depend on the specific orientation. Both the bimodal orientation and the narrow width distribution was found to be linked to the well-defined mismatch between the MoS₂ lattice and the lattice of the TiO₂(110) surface. The TiO₂(110) surface is thus found to impose strong restrictions on the growth of the MoS₂ nanoclusters.

In future experiments, it would be highly interesting to include both the effect of promoter atoms and the effect of the support. Activity measurements have shown that the HDS activity of thiophene for the same Mo loading is promoted by Co by a factor of 7.6 on alumina but only by a factor of 3.3 on anatase [172]. This finding clearly suggests that the support does not only play a passive role but there is a synergy between the effects of support and the effects of the promoter atoms. Future STM studies of promoted TiO₂-supported MoS₂ nanoclusters may provide information on this synergy effect.

CHAPTER 7

Mo₆S₆ nanowires

An interesting spin-off study, from the experiments with synthesizing MoS₂ nanoclusters on the HOPG support, is concerned with the formation of Mo₆S₆ nanowires. In this chapter, a novel synthesis route to elementary pure Mo₆S₆ nanowires is presented, and the detailed atomic-scale structure is revealed using STM and DFT calculations. Furthermore, scanning tunneling spectroscopy (STS) is utilized to explore the electronic properties of the Mo₆S₆ nanowires.

7.1 Introduction

The common form of MoS_2 is the layered compound consisting of S-Mo-S sheets addressed in the previous chapters. However, chalcogenides of molybdenum and tungsten are among the most promising and versatile categories of compounds for the design of novel nanomaterials [136, 142, 143, 173, 174]. In particular, a variety of stable one- and two-dimensional molybdenum sulfide nanostructures have been discovered with unique combinations of mechanical, electronic, magnetic, and chemical properties completely different from those observed for the 3D bulk phase of these materials [175–179]. The layered MoS_2 can, e.g. wrap up into spectacular hollow fullerene-like structures and nanotubes in analogy to graphene sheets [144, 175]. Recently, novel one-dimensional molybdenum-sulfide nanowire structures have been proposed. These structures are not constructed from MoS_2 layers but instead have a solid interior built from Mo_6S_y subunits, ($y = 6$ or 9) [180–183].

Quasi-1D batches of molybdenum sulfide nanowires and chalcogenide (Se, Te) analogues have been synthesized previously in bulk inorganic synthesis using various dopants, such as alkali metals [180, 184] or iodine [185]. The counter-ions have been considered necessary to stabilize the nanowires in the previous synthesis protocols, and, e.g. in the case of iodine the dopant atoms are physically incorporated in random concentrations leading to a range of chalcocyanide isomers with a $\text{Mo}_6\text{S}_{y-z}\text{I}_z$ configuration ($y = 6$ or 9 and $z = \text{random}$). Accordingly, it has so far not been possible to experimentally examine the atomic structure of isolated non-doped, rigid Mo_6S_6 -type nanowires in a pure well-defined conformation and relate the structure to the detailed electronic properties of the nanowires. The dopants will most likely affect the conductivity of the individual wires, and from, e.g. a nanoelectronics perspective, it is of paramount importance to be able to synthesize wires with well-defined electrical and, hence, structural properties.

In this chapter, it is shown that synthesis of uniform bundles of elementally pure Mo_6S_6 nanowires is in fact possible on a graphite surface. From combined high-resolution scanning tunneling microscopy and spectroscopy studies and density functional theory calculations, the atomic-scale structure of the Mo_6S_6 nanowires is revealed, and furthermore it is demonstrated that the wires in this pure form are metallic in nature.

7.2 Experimental details

In outline, the synthesis procedure follows the method described in Section 6.2.2 for MoS_2 nanoclusters on a graphite surface. As in the case of the MoS_2 nanoclusters, the synthesis was performed on a highly ordered pyrolytic graphite (HOPG) substrate with induced defects from a slight Ar^+ ion bombardment. The key, however, to the selective synthesis of the Mo_6S_6 nanowires versus other sulfided Mo structures is a careful control of the sulfiding environment during the synthesis. The synthesis of the Mo_6S_6 nanowires was performed by physical vapor deposition of Mo onto the HOPG substrate followed by high-temperature sulfidation in a very low-pressure H_2S environment ($P_{\text{H}_2\text{S}} = 1 \cdot 10^{-6}$ mbar) at 1000 K. The selectivity towards Mo_6S_6 nanowire formation is explained by the

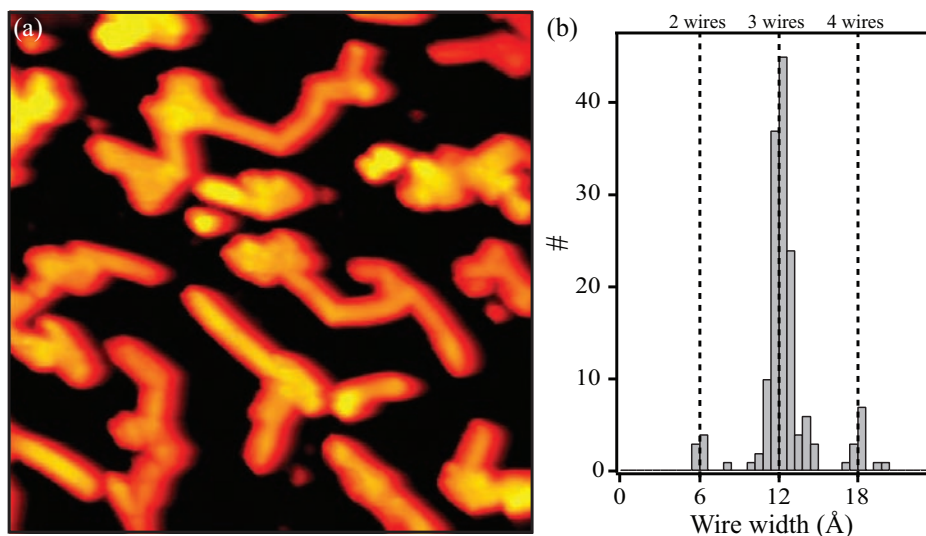


Figure 7.1. (a) STM image ($50 \text{ \AA} \times 50 \text{ \AA}$, $I_t = 0.230 \text{ nA}$, and $V_t = -1250 \text{ mV}$) of Mo₆S₆ wires on HOPG. (b) The width distribution of the wires.

fact that low-pressure sulfiding conditions do not stabilize the sulfur-terminated edges of the S-Mo-S layers required for layered MoS₂ nanocrystals. Indeed, if the H₂S pressure was increased by one order of magnitude, the synthesis results instead in single- or multi-layer MoS₂ nanoclusters with the regular 2H-MoS₂ stacking (Section 6.2). It is therefore concluded that synthesis of the nanowires from a metallic Mo precursor is successfully performed *only* in a mildly sulfiding environment.

7.3 Morphology of Mo₆S₆ nanowires

Figure 7.1a shows a large-scale STM image of Mo₆S₆ nanowires supported on the HOPG substrate. The Mo₆S₆ nanowires are distributed uniformly on the surface with no preferred orientation relative to the high-symmetry substrate directions, which indicates that the direct bonding of the Mo₆S₆ nanowires segments to the substrate is rather weak. The Mo₆S₆ nanowires are observed to consist of straight segments in between a number of bends and joints that are attributed to the initial random distribution of sputter-induced defects in the HOPG surface. The height and the width of the nanowires are observed from the STM images to be extremely uniform, with the apparent height of the Mo₆S₆ wires measured to be $9.0 \pm 0.1 \text{ \AA}$ relative to the substrate while the width of a typical nanowire segment is measured to be $12 \pm 2 \text{ \AA}$.

Figure 7.2 depicts an atomically resolved STM image of a nanowire segment, and the Mo₆S₆ nanowire is observed to consist of regularly spaced protrusions in three parallel rows, reflecting that the structure of the nanowires consists of three single Mo₆S₆ wires

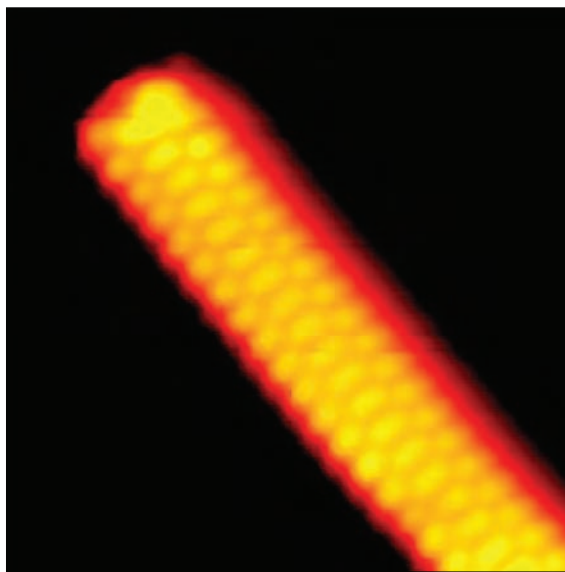


Figure 7.2. Atomically resolved STM image ($80 \text{ \AA} \times 80 \text{ \AA}$, $I_t = 0.220 \text{ nA}$, and $V_t = -9.8 \text{ mV}$) of a trimer Mo_6S_6 nanowire bundle.

(a trimer). The width distribution of the Mo_6S_6 nanowires in Fig. 7.1b clearly shows that predominantly wires corresponding to trimers are synthesized, revealing an unprecedented high selectivity ($> 90\%$) towards formation of a structurally singular nanowire conformation. From the width distribution, two other discrete width values are also observed but with a much lower count. These are attributed to dimer and tetramer Mo_6S_6 nanowires, but no wider nanowires were observed.

7.4 Preference for trimers

Gradient-corrected DFT calculations of the formation energies, E_f , (Table 7.1) reveal a clear preference for the trimer formation in agreement with the experimental width distribution histogram (Fig. 7.1b). The DFT calculations show that the individual Mo_6S_6 nanowires undergo a structural deformation when the wires are combined into bundles. The deformation energy of a central Mo_6S_6 wire, e.g. in a trimer or tetramer, is at least 0.24 eV per Mo_6S_6 unit higher than the value of the two outer Mo_6S_6 wires since a central wire has to form two contacts, and its geometry changes accordingly. Wider Mo_6S_6 bundles, such as pentamers, are thus expected to display an even higher formation energy, which explains why these wider bundles are not observed. In addition, E_b , the energy required for cleavage into unrelaxed free wires, shows that the wires are mechanically stable. The DFT calculations on trimer structure models predict that a slightly larger spacing of 12 \AA between the two outermost wires is preferred in the most stable

Configuration	E_f	E_b	d
(1) 	0	19	12.2
(2) 	3	25	13.9
(3) 	67	36	14.2
(4) 	88	47	13.8
(5) 	70	21	6.5
(6) 	15	50	18.3

Table 7.1. The energy of formation, E_f , with respect to the most stable trimer configuration (1), the energy barrier, E_b , against mechanical separation, and the spacing between the centers of the two outermost wires for selected low-energy dimer, trimer, and tetramer structures (all energies in meV/at, distances in Å).

trimer arrangement (configuration (1) in Table 7.1) compared to the experimental distance of 10 Å (see Fig. 7.4c). However, the DFT calculation partly neglects inter-wire dispersion forces, such as van der Waals forces, which lead to exaggerated distances in the bulk compound [42], and the other low-energy trimer structures selected from a large number of model structures do not interlock to the same extent as configuration (1), and accordingly they exhibit even larger equilibrium spacings of up to 14 Å (see Table 7.1). The calculated nanowire spacings for the dimers and tetramers are also slightly exaggerated compared to the experimental with calculated distances of 6.5 Å to 6.9 Å for the dimer and of 18 Å to 20 Å for the tetramer models.

7.5 Atomic-scale structure of Mo₆S₆ nanowires

The basic unit of the nanowire bundles observed by STM is the single Mo₆S₆ nanowire depicted in Fig. 7.3. The unit cell consists of an octahedral Mo₆ unit dressed by an exterior cap of six S atoms each coordinated to three Mo atoms (see Fig. 7.3a). The Mo₆S₆ nanowire is created by a face sharing repetition of these units forming a backbone of

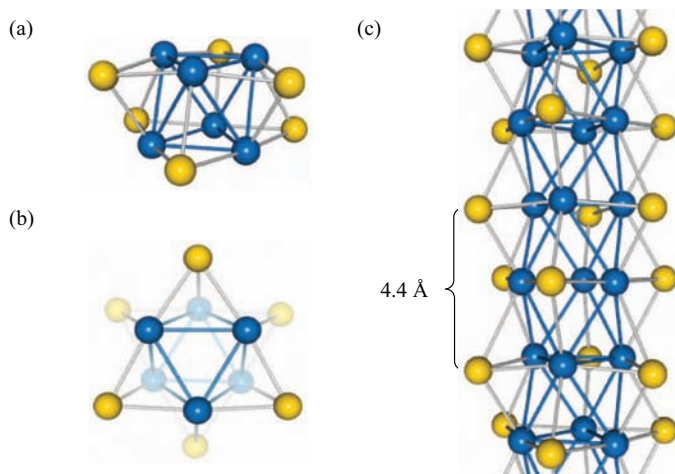


Figure 7.3. (a) The Mo_6S_6 building block. (b) End view of the Mo_6S_6 nanowire. (c) Side view of a single Mo_6S_6 nanowire. Color code - Mo: blue and S: yellow.

Mo_3 triangles arranged with the base up or down in an alternating fashion as depicted in Fig. 7.3b. The distance between Mo_6 units measured along a single wire is calculated by DFT to be 4.4 \AA , which is in perfect agreement with the periodicity determined from the STM line scans in Fig. 7.4b. Across the nanowire trimer the arrangement of protrusions on adjacent wires are shifted 2.2 \AA along the wire, which suggests that adjacent wires are rotated 60° with respect to each other, and that the two outermost wires have the same orientation. The structural model displayed in Fig. 7.4d illustrates the calculated equilibrium configuration of such wires (trimer configuration (1) in Table 7.1). The top part of the image shows an STM simulation superimposed on the structural model. For the simulation, the width of the trimer has been fixed to match the experimental geometry with a spacing of 10 \AA between the centers of the two outermost wires. The simulated STM image perfectly reproduces the shifted geometry observed on the nanowire in the experimental STM image. Figure 7.5 displays STM simulation of all trimer configurations in Table 7.1, and it is clearly observed that only configuration (1) reproduces the experimental STM images.

The STM simulation reveals that the bright protrusions separated by 4.4 \AA in the STM image reflect the position of the sulfur atoms exposed at the top of the nanowires. In the STM line scan across the wire slightly weaker protrusions with an interatomic distance of 2.6 \AA are observed (see Fig. 7.4c). From comparison with the simulated line scan in Fig. 7.4f, these features are observed to be associated with lower lying sulfur atoms in the central nanowire, thus confirming the orientation of the wires. Based on the both qualitative and quantitative good agreement between the STM and DFT results, it is concluded that the Mo_6S_6 nanowires selectively form as trimer configuration (1).

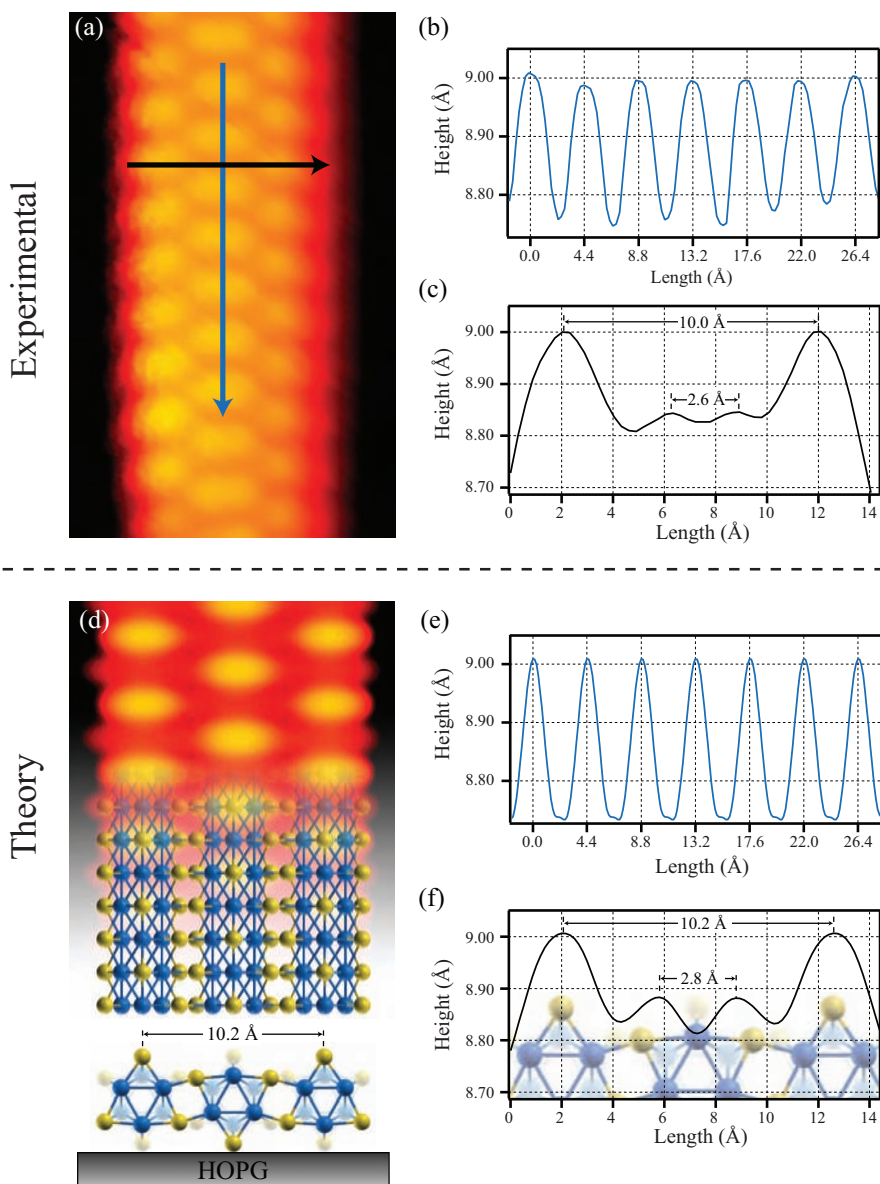


Figure 7.4. (a) STM image ($25 \text{ \AA} \times 53 \text{ \AA}$, $I_t = 0.210 \text{ nA}$, and $V_t = -9.8 \text{ mV}$) of a trimer Mo_6S_6 nanowire bundle. (b) Line scan along the row of protrusions on the nanowire in (a) as indicated by blue arrow. (c) Line scans across the nanowire in (a) as indicated by black arrow. (d) A DFT-based simulated STM image with the Mo_6S_6 structure embedded. (e) and (f) Simulated STM line scans equivalent to the line scans in (b) and (c).

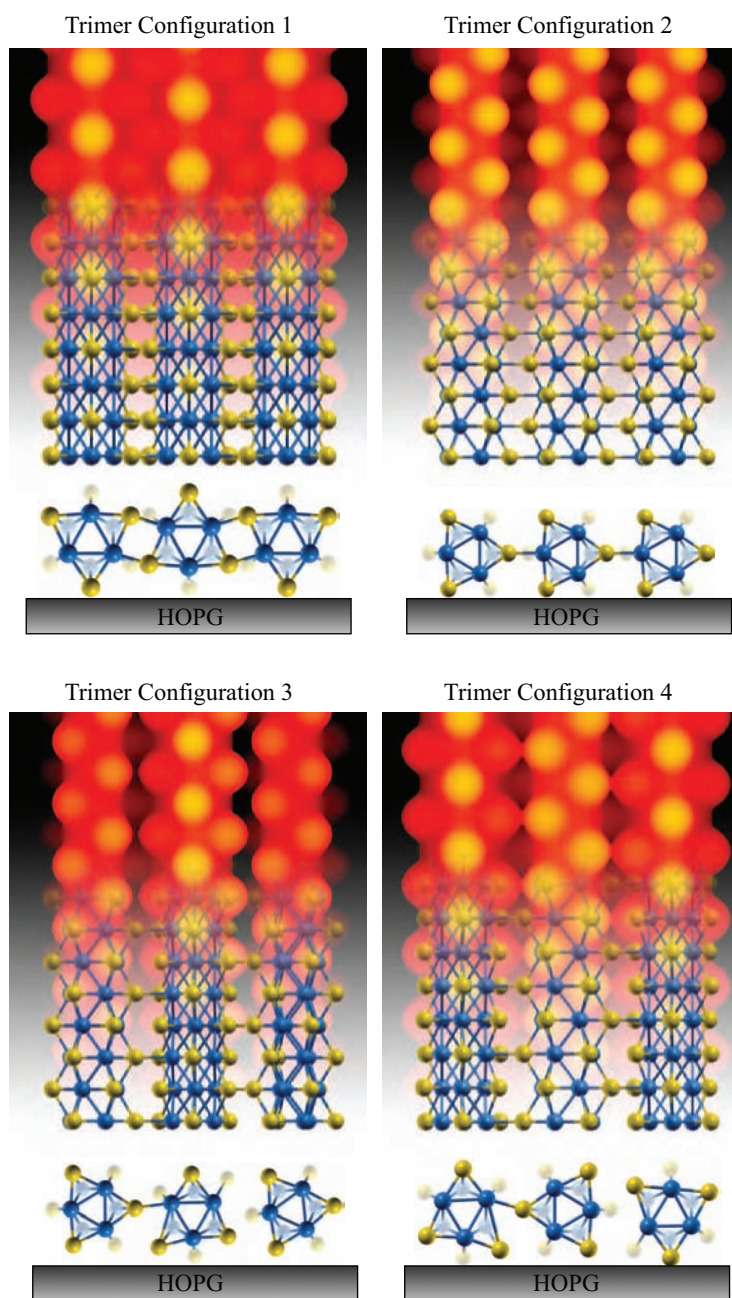


Figure 7.5. DFT-based simulated STM images of trimer wire configuration (1)-(4) in Table 7.1. Only configuration (1) matches the experimental STM images (see, e.g. Fig. 7.2).

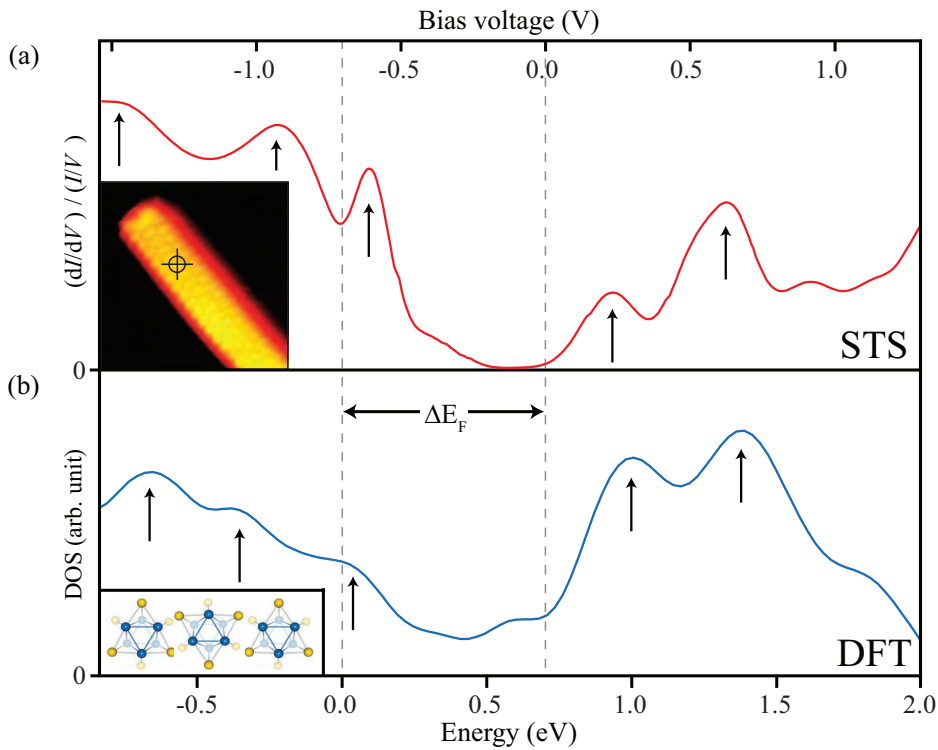


Figure 7.6. (a) Normalized conductance curve measured at the position indicated in the STM image. (b) DOS curve from DFT of trimer configuration (1) in Table 7.1 with the distance between the two outer wires fixed to the experimentally observed.

7.6 Electronic structure of Mo_6S_6 nanowires

To assess the potential of Mo_6S_6 nanowires for nanoelectronic applications, the conductivity properties of the nanowires can be explored by scanning tunneling spectroscopy (STS). The STS technique was introduced in Section 2.1.4, and here it will suffice to mention that with STS it is possible to probe the conductivity of the nanowires directly at the atomic scale by measuring the tunneling current (I) as a function of bias voltage (V) at a well-defined position of the nanowires. The measurement was performed at room temperature by disabling the scanning and the current feedback loop, and subsequently measuring the current I as a function of the bias voltage V applied to the sample at a specific position on the nanowire (Fig. 7.6a).

The uniformity of the tip states was investigated by recording STS spectra on the plain HOPG surface prior to the STS measurements on the Mo_6S_6 wires, and it was observed that tip states only had a minor influence on the recorded STS spectra, i.e. only changed the intensity of the observed features but not their position. The final output

of a STS measurement is a normalized conductance curve, $(dI/dV)/(I/V)$, which, as discussed in Section 2.1.4, can be shown to reflect the local density of states (LDOS) in a first-order (tip-independent) approximation.

The normalized STS conductance curve measured on the Mo_6S_6 nanowires displays a number of sharp peaks as seen in Fig. 7.6a. Such distinct peaks in the DOS spectra are due to van Hove singularities (VHS) in the density of states, as expected for a 1D nanowire system, and have previously been observed for, e.g. carbon nanotubes [186].

The fine structure in the experimental STS curves is well reproduced in the DOS plot in Fig. 7.6b resulting from the DFT calculations of the trimer configuration (1) with the distance between the two outer wires fixed to the experimental value. With respect to the band structure of a single Mo_6S_6 wire [187], the inter-wire interaction in the trimer introduces additional splittings of the signals in the vicinity of the Fermi level due to a weak elliptic elongation of the wires by 0.1-0.2 Å parallel to the surface normal. These splittings considerably improve the match with the measured STS spectrum beyond a merely qualitative comparison.

Hence, the present DFT calculations allow an assignment of the different characteristic features observed in the experimental STS spectra. The filled electronic bands just below the Fermi level are dominated by Mo d states with a small contribution from sulfur p states, whereas the conduction band above the Fermi level almost exclusively originates from Mo d states. Thus, the observed shift of the Fermi level in the experimental normalized conductance curve $(dI/dV)/(I/V)$ compared to the theoretical DOS curve ($\Delta E_F = 0.7$ eV) is a result of charge transfer from the substrate to mainly the Mo d states. Both the experimental normalized conductance results and the theoretical DOS curve exhibit non-zero values at and around the Fermi level (E_F), reflecting that the Mo_6S_6 nanowire trimers are one-dimensional conductors. The Mo_6S_6 nanowires are thus concluded to be very well suited as nanoscale metallic leads with a conductivity originating from Mo d states that create the metallic backbone of the Mo_6S_6 nanowires.

7.7 Conclusion

In the present chapter, a new route to synthesize and grow elementary pure Mo_6S_6 nanowires at mildly sulfiding conditions was revealed. From an interplay of STM and STS measurements and DFT calculations the atomic-scale geometric and electronic structures of the Mo_6S_6 nanowires were determined. The Mo_6S_6 nanowires was found to possess a unique geometry consisting of three interlocked ribbon-shaped Mo_6S_6 nanowires bundles and to be 1D conductors. The Mo_6S_6 nanowires thus possess uniquely well-defined structural and electronic properties and may therefore have a distinct advantage as compared to the structurally much less well-defined 1D carbon nanostructures, such as nanotubes [186] or the more recently discovered graphene nano-ribbons [188]. Furthermore, the sulfur termination of the wires may facilitate a strong and well-defined atomic bonding to metallic electrodes [189], which has previously proven to be crucial for a well-defined transport behavior in nanoscale electronic contacts.

CHAPTER 8

Sulfidation of Co nanoparticles

In this chapter, time-resolved STM is used to investigate a massive sulfur-induced transformation of a homogeneous array of Co nanoparticles into a new cobalt sulfide phase. The underlying atomistic mass-transport process is revealed and, surprisingly, found to be mediated exclusively by the formation and detachment of monosized Co_3S_4 complexes at the perimeter of the Co nanoparticles.

8.1 Introduction

When a system containing nanoparticles encounters changes in the surrounding gaseous environment, a dramatic shift in the nanoparticle morphology or a redistribution of the nanomaterial may be initiated by the interaction with gas molecules or atoms [190–192]. This change in morphology or dispersion may lead to an unfortunate transformation of the intended functional properties of the particular system. Such adverse gas-induced effects are particularly well documented for noble metals in heterogeneous catalysts where the preservation of catalytic activity and reaction selectivity relies on a high, uniform dispersion of active nanoparticles [193, 194].

The details of the underlying physical processes, such as adsorption, diffusion, and nucleation are, however, often far from understood. Much knowledge has been gained from studies on single-crystal surfaces, but key issues related to the atomistic nature of the species mediating the mass-transport often remain unsolved. Detailed insight into such processes for complex systems consisting of nanoparticles with multiple facets has, furthermore, been extremely difficult to achieve due to lack of techniques with the appropriate spatial and temporal resolution.

Co nanoparticles are the catalytically active phase in Fischer-Tropsch synthesis where hydrocarbons are synthesized from a mixture of H_2 and CO. It is well documented that the Co-based catalyst is permanently poisoned by sulfur. Several studies have been concerned with the effects of sulfur poisoning in terms of lifetime, selectivity, etc. [195–198], but the detailed poisoning mechanism is still debated [199–201].

In this chapter, STM is used to directly observe the dynamics of an adsorbate-induced transformation of cobalt nanoparticles exposed to H_2S . Furthermore, the diffusing monosized cobalt sulfide complexes are directly identified in time-resolved STM movies.

8.1.1 Historic background of Fischer-Tropsch synthesis

The synthesis of hydrocarbons from hydrogenation of CO took its beginning in 1902 when Sabatier and Senderens produced CH_4 using a Ni catalyst [202]. In 1920s the two German scientists Franz Fischer and Hans Tropsch demonstrated in their pioneering work that CO hydrogenation over iron, cobalt, or nickel catalysts produces a mixture of linear hydrocarbons [203–205]; The Fischer-Tropsch synthesis was born.

The development continued during the 1930s, where the first commercial Fischer-Tropsch plants were built, which enabled Germany to produce synthetic fuels during World War II. The production peaked in 1944, where 600,000 tons of transportation fuels were produced per year via gasification of coal and Fischer-Tropsch synthesis [206].

Since the end of World War II, the interest in Fischer-Tropsch synthesis has essentially been synchronized with the oil price as seen from Fig. 8.2. The present record-high oil price and significant advances in coal gasification technology for syngas (mixture of H_2 and CO) production [207,208] suggest that the Fischer-Tropsch synthesis has the potential to become a major contender on the global energy scene. Furthermore, synthetic fuels from Fischer-Tropsch synthesis hold the advantage of containing extremely low

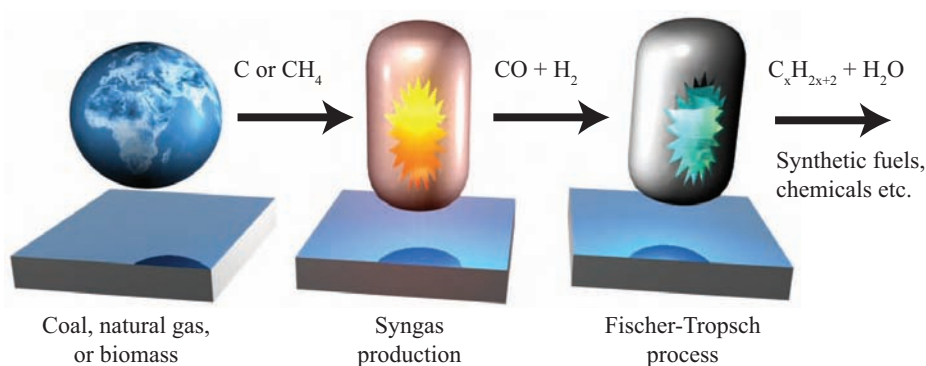


Figure 8.1. Illustration of the Fischer-Tropsch route to synthetic fuels. Linear hydrocarbons are synthesized from syngas (a mixture of H₂ and CO), which can be produced from either methane or coal.

levels of sulfur and aromatics, which is an environmental benefit with lower emission of SO₂ and particles during combustion [4].

8.1.2 Chemistry of Fischer-Tropsch synthesis

Fischer-Tropsch synthesis is in essence a carbon chain building process, where -CH₂-groups are put together. The overall reaction can be written as:



The reaction is highly exothermic with a reaction enthalpy of $\Delta H_{FT}^\circ = -165 \text{ kJ/mol}$, and it is therefore important to design the reactor to rapidly remove the heat to avoid overheating of the active catalytic particles, which would otherwise result in an increased rate of deactivation due to sintering and fouling.

The feed to the Fischer-Tropsch reactors is syngas, which can be produced from either gasification of coal with oxygen and steam or by steam reforming of methane:



The only metals that have a sufficient high Fischer-Tropsch activity for commercial application are Fe, Co, Ni and Ru [209]. However, Ru is simply too expensive¹, and Ni-based catalysts produce too much methane under industrial operating conditions, which leaves Fe and Co as the only viable catalysts. Iron is the cheaper of the two metals, but cobalt holds the advantage of higher activity and longer lifetime. Both the iron and cobalt catalyst are permanently poisoned by sulfur. The presence of even a few ppm sulfur in the reactant feed can limit catalyst lifetime to a few hours or days. This is

¹At present the price of ruthenium is $\sim 80,000$ times higher than that of scrap iron.

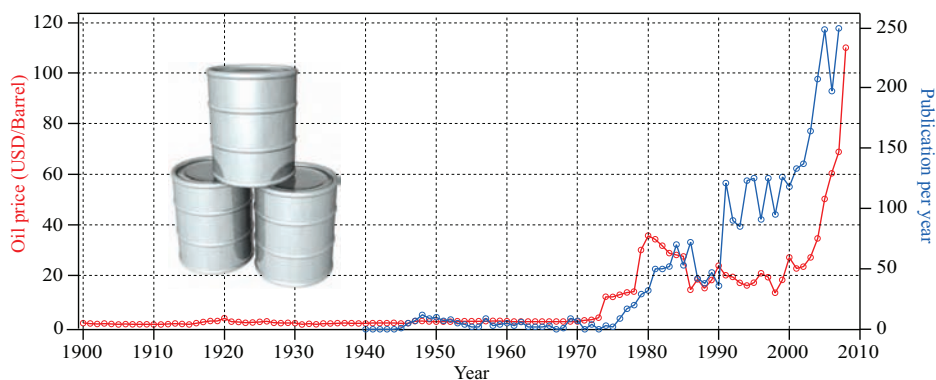


Figure 8.2. Graph illustrating an almost synchronized relationship between the interest in Fischer-Tropsch catalysis [210] and oil price [211].

particular severe in the case of the more expensive Co catalyst since a high metal dispersion and long lifetime is required to be able to offer a good balance between cost and performance.

8.2 Experimental details

The sulfur-induced transformation of Co nanoparticles was investigated by exposing dispersed Co nanoparticles to H_2S . Co nanoparticles were grown by deposition of Co onto a sputter-cleaned Au(111) substrate exposing the well known herringbone reconstruction, which acts as a template for creating Co nanoparticles with a uniform size and shape as described in Section 3.2.1. Co nanoparticles synthesized under these conditions were observed at RT to be static on the Au(111) surface and were characterized as truncated triangular, bilayer particles oriented with the close-packed Co(111) facet in parallel with the substrate. Less than 5% of the nanoparticles had Co also in the third layer. The sulfidation process was monitored by recording *in situ* STM movies of the Co nanoparticles at room temperature in a H_2S atmosphere ($P_{\text{H}_2\text{S}} = \sim 5 \cdot 10^{-8}$ mbar).

8.3 Phase identification

Figure 8.3 illustrates a series of snapshots of the same area of the sample taken from an STM movie (M1) recorded over a time span of ~ 80 hours. The STM movie can be watched in Ref. [212] as online supporting material. During the movie, it is possible to observe the gradual transformation of the well-dispersed hexagonally truncated Co nanoparticles into much larger irregular patches consisting of cobalt sulfide. In the STM movie, as illustrated in Fig. 8.4, three different primary phases can be identified by their atomic structure and apparent height in line scans in the individual frames: (i) the

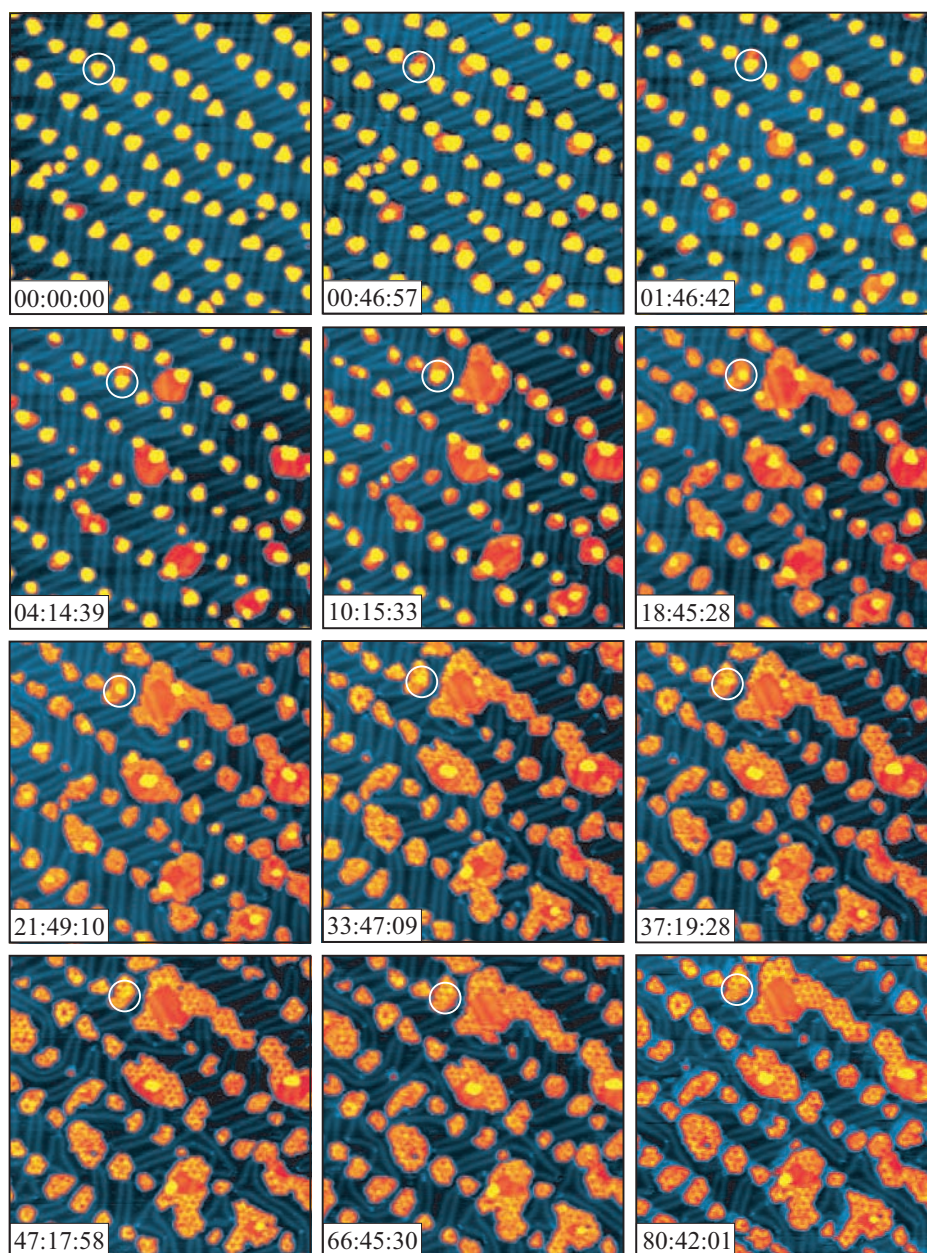


Figure 8.3. Time-lapse sequence of STM images ($700 \text{ \AA} \times 700 \text{ \AA}$, $I_t = 0.6 \text{ nA}$, and $V_t = -1250 \text{ mV}$) from an STM movie (M1) covering ~ 80 hr. When the Co nanoparticles are exposed to H_2S , they are gradually transformed into cobalt sulfide. One reference particle has been encircled on all images. The time (hr:min:s) is indicated in the lower left corner of the images.

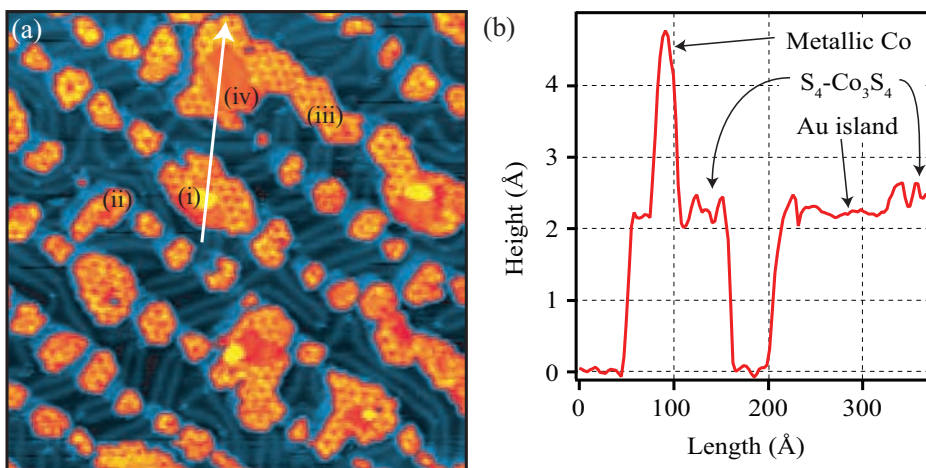


Figure 8.4. Four different phases are observed: (i) the metallic Co phase, (ii) amorphous cobalt sulfide, (iii) crystalline cobalt sulfide, and (iv) Au islands.

metallic Co phase, (ii) amorphous cobalt sulfide, and (iii) crystalline cobalt sulfide. The time-resolved and spatial evolution of each phase can thus be followed in detail during the corrosion process. Note that a fourth structure (iv) is present. This phase is identified in atom-resolved STM images as single-layer gold islands by having the same height as a step on the surface and the same lattice constant as seen from atomically resolved images (see Fig. 8.5b). The gold islands are much less corrugated than the cobalt sulfide structure but show as expected dislocation ridges. Images with atomic resolution show that the dislocation ridges indeed separate fcc from hcp stacking regions (Fig. 8.5b). The formation mechanism of the Au islands is well known and involves diffusing Au atoms. The rate of formation was observed to accelerate upon introduction of H₂S, indicating that sulfur also has an effect on the diffusion of gold adatoms as recently reported for the clean Au(111) surface exposed to SO₂ [213,214]. However, the cobalt sulfide formation process is expected to be independent of the presence of Au islands, and they will only marginally influence the final distribution of the sulfide on the surface.

8.4 Formation of Co sulfide

The steps of the decay of the Co nanoparticles and the corresponding growth of cobalt sulfide are illustrated in Fig. 8.6a where the areas have been measured directly in the STM images extracted from movie M1. In this analysis, no discrimination between crystalline and amorphous cobalt sulfide is made. As seen from Fig. 8.6a, the decay rate of the Co nanoparticles (circles and red curve) is initially very fast, but after a duration of 80 min, the decay rate decreases quite abruptly. Similar abrupt changes in the decay rate are also observed after 1000 min and 1500 min. The formation rate of the cobalt

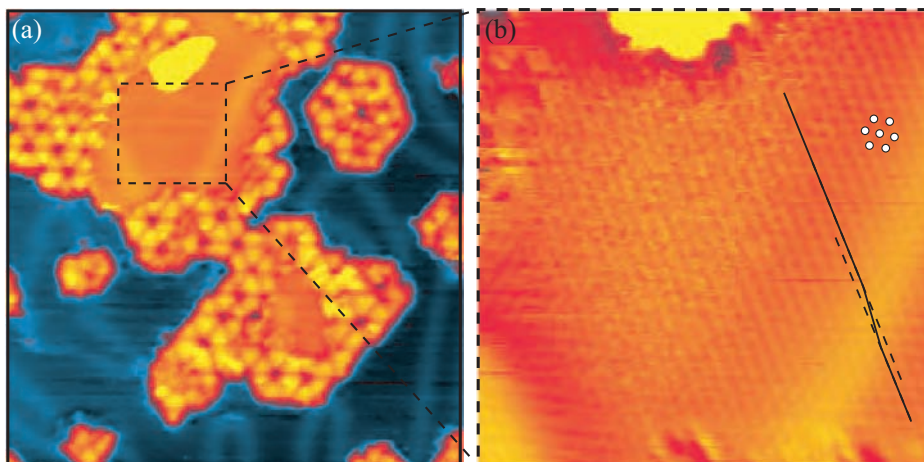


Figure 8.5. (a) STM image ($300 \text{ \AA} \times 300 \text{ \AA}$) showing a gold island with dislocation ridges embedded in the cobalt sulfide structure. (b) Zoom-in ($70 \text{ \AA} \times 70 \text{ \AA}$) of the marked area in (a). The white dots indicate the Au(111) lattice, and the lines show that the dislocation ridges separate the fcc from hcp stacking regions.

sulfide phase (triangles and blue curve) is observed to correlate exactly with the features of the metallic Co nanoparticle decay.

Several different decay scenarios are possible for the cobalt nanoparticles since the the decay rate may correlate with:

- (1) The particle area: $dA/dt \propto A$
- (2) The particle perimeter (circumference): $dA/dt \propto \sqrt{A}$
- (3) The arrival rate of sulfur: $dA/dt = \text{constant}$

From the analysis of the decay curve of large-scale images (Fig. 8.6a) and an another more precise analysis of a single bilayer Co nanoparticle imaged with a higher time resolution (Fig. 8.6b), it is seen that a $\sqrt{A} \propto -t$ correlation is found. It is thus concluded that the sulfur-induced corrosion process depends on the number of available sites on the perimeter of the nanoparticles. On the basis of the perimeter dependent decay, it is proposed that H_2S is initially physisorbed on the Au surface [215] (and not exclusively on the Co nanoparticles) and then diffuses to the cobalt nanoparticles and extracts the Co from perimeter sites. This scenario is further supported by STM images recorded at 163 K where physisorbed H_2S directly can be observed as a striped phase (Fig. 8.8c).

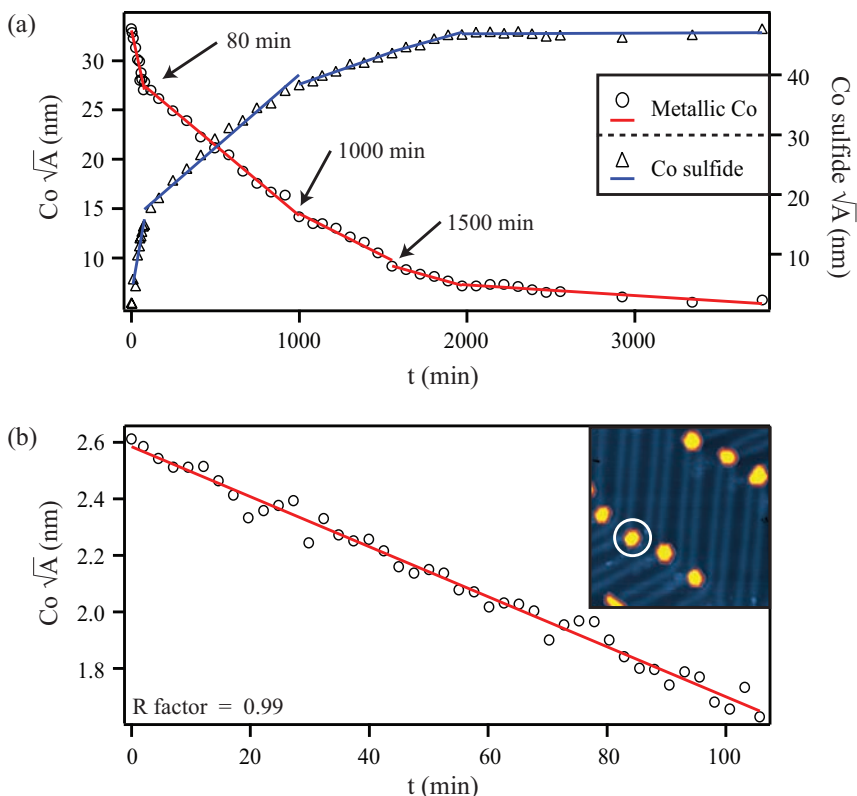


Figure 8.6. (a) Time evolution of cobalt nanoparticles and the cobalt sulfide, plotted as the square root of the area (from movie M1). (b) Same plot but of a single Co nanoparticle, marked with a white circle in the inserted STM image, from a second movie with higher resolution.

8.5 Diffusion Co_nS_m complexes

To observe and identify the diffusing species responsible for the mass transport, a movie (M2) with even higher time and spatial resolution was recorded (M2 can be watched in Ref. [212] as online supporting material). The snapshots, taken from the STM movie, are displayed in Figs. 8.7a-8.7d and show how larger features composed of several atoms disappear or reappear near the particle perimeter between consecutive scans. These frequent changes in the decay rate of individual particles indicate a more complex process than a single sulfur atom interacting with a single cobalt atom.

The temporal evolution of the two nanoparticles (Fig. 8.7e) shows that the decay of the particle area, which from the curve in Fig. 8.6 seemed to be continuous, actually consists of steps corresponding closely to complexes of a given size. The steps are, as indicated in Fig. 8.7e, all integral multiples of a smallest step size, which is found to

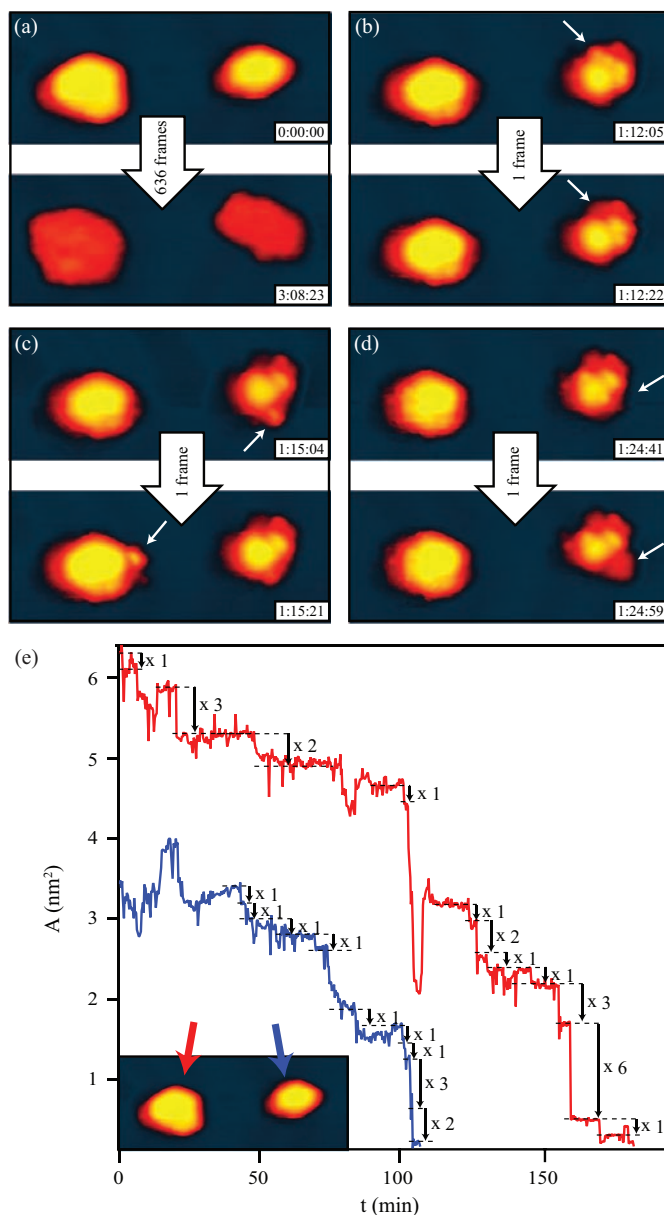


Figure 8.7. (a)-(d) Snapshots ($160 \text{ \AA} \times 65 \text{ \AA}$) from an STM movie (M2) showing the transformation of two Co particles into cobalt sulfide. The time (hr:min:s) is indicated in the lower right corner of the images. (a) First and last frame of the movie showing the metallic cobalt nanoparticles and the final cobalt sulfide islands, respectively. (b)-(d) STM images showing larger features (indicated by the white arrows) composed of several atoms disappearing or appearing between consecutive scans. (e) Area evolution of the two cobalt particles.

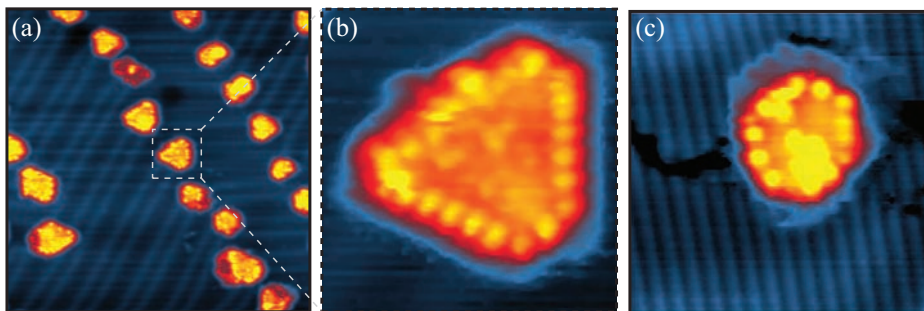


Figure 8.8. (a) STM image ($490 \text{ \AA} \times 490 \text{ \AA}$) of the Co particles exposed to H_2S and subsequently imaged at 173K. (b) A zoom-in ($69 \text{ \AA} \times 71 \text{ \AA}$, $I_t = 0.50 \text{ nA}$, and $V_t = -1.25 \text{ V}$) of the marked particle in (a) shows that the perimeter of the particle consist of small round protrusions. (c) STM image ($40 \text{ \AA} \times 40 \text{ \AA}$, $I_t = 0.53 \text{ nA}$, and $V_t = -625 \text{ mV}$) recorded at 163 K of a Co particle surrounded by a striped structure attributed to physisorbed H_2S .

be $20 \pm 2 \text{ \AA}^2$, suggesting that the decay proceeds stepwise by the formation of single monosized type of mobile Co_nS_m complex. The size of the mobile Co_nS_m complex suggests, when compared to the closed-packed density of Co, that a Co_nS_m complex contains 3 or 4 Co atoms.

8.5.1 Quench-and-look experiments

The diffusion of Co_nS_m complexes was generally too fast to be captured with high-resolution STM at room temperature. However, quench-and-look experiments at a lower temperature allow direct observation of the diffusing Co_nS_m complexes. The sulfidation process was initiated by exposing the sample to H_2S at room temperature, and after a few minutes, the sample was transferred into the cooled STM. In the resulting STM images recorded at 173 K, the truncated triangular shape of the Co nanoparticle is still clearly observed, but the perimeter of the nanoparticles contains several round protrusions (Fig. 8.8b). These protrusions are very uniform in size, and in full accordance with the step size in Fig. 8.7e, the area of the protrusions is found to be $21 \pm 2 \text{ \AA}^2$.

The formation of a rim of amorphous cobalt sulfide complexes may account for the decrease in the decay rate of the Co nanoparticles that is observed around 80 min in the graph of Fig. 8.6a. The reduced decay rate can be explained by the gradual saturation of sites at the rim, which hinders the sulfur from directly accessing the remaining metallic Co. The changes in the slope of the graph in Fig. 8.6a observed at later times corresponding to $\sim 1000 \text{ min}$ and $\sim 1500 \text{ min}$ are due to the fact that the rather few three layer high Co nanoparticles present in the movie M1 have a much slower apparent decay rate than the two layer high nanoparticles. The higher stability of the three layer high particles in the sulfiding atmosphere again suggests that H_2S mainly interacts at the interface between the Au substrate and the perimeter of the Co nanoparticles.

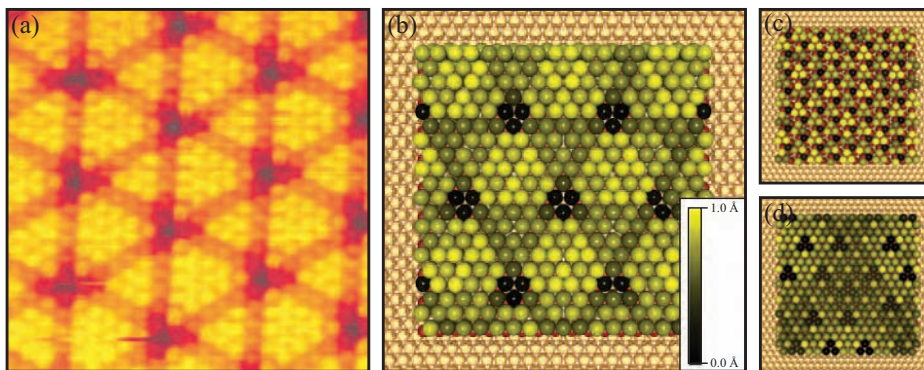


Figure 8.9. (a) An atom-resolved STM image ($70 \text{ \AA} \times 70 \text{ \AA}$, $I_t = 0.26 \text{ nA}$, and $V_t = -19.5 \text{ mV}$) of the cobalt sulfide structure. (b)-(d) Ball models of Co_3S_4 , CoS_2 , and Co_9S_8 on $\text{Au}(111)$, respectively. The color of the topmost layer of sulfur atoms represents the vertical positions as indicated by the color scale bar in (b).

8.6 Structure of cobalt sulfide

The cobalt sulfide phase is initially amorphous, but eventually all Co crystallizes into a structure that appears with a characteristic “mill-wheel” structure (see Fig. 8.9a). The cobalt sulfide has an apparent height of 2.60 \AA , and its top facet consists of hexagonally arranged protrusions with a lattice distance of $3.4 \pm 0.1 \text{ \AA}$.

Cobalt sulfides exist in a variety of different crystallographic structures, e.g. Co_9S_8 , Co_4S_3 , Co_3S_4 , CoS_2 , and CoS [216]. Three of these phases: Co_9S_8 (cobalt pentlandite), Co_3S_4 (linnaeite), and CoS_2 (cattierite), are stable at the temperatures of the present experiments [217]. All three crystal structures are cubic, and the hexagonal arrangement of topmost sulfur atoms in the observed structure thus suggest that the structure displays a (111) face. The observed interatomic distance in the “mill-wheel” structure matches, however, only that of the S atoms in Co_3S_4 ($d = 3.37 \text{ \AA}$). In support of this assignment, a recent XRD study [218] showed that the most stable phase is indeed Co_3S_4 when sulfur is in large excess.

Furthermore, a geometrical structure simulation of the Co_3S_4 structure (Fig. 8.9b) is found to be excellent accordance with the mill-wheel structure observed experimentally (Fig. 8.9a), whereas the simulations of the CoS_2 and Co_9S_8 structures do clearly not resemble the observed (Figs. 8.9c and 8.9d). The simulations were performed computationally by allowing the atoms in each layer of a single cobalt sulfide overlayer to make a vertical relaxation dependent on the position of the atoms in the layer beneath, and subsequently color the topmost sulfur atoms in a ball model of the cobalt sulfide slabs according to the vertical relaxation. Each (111) slab consists of a Co layer in between two sulfur layers since the height of these slabs is consistent with the measured height of the cobalt sulfide structure.

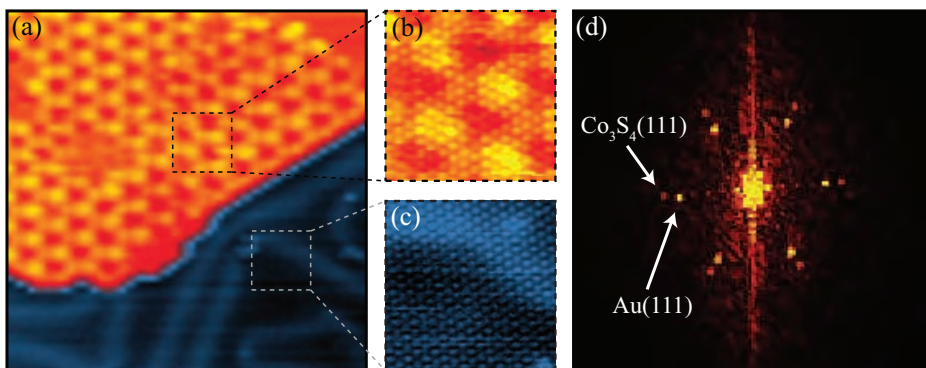


Figure 8.10. (a) STM image of cobalt sulfide on Au(111). (b) and (c) Atom-resolved zoom-ins on the cobalt sulfide and Au(111), respectively. (d) FFT image of the two images in (b) and (c) clearly showing the topmost sulfur atoms in the cobalt sulfide are aligned with the Au(111) atoms.

The fixed rotation of the overlayer could be determined in STM images with atomic resolution on both the cobalt sulfide and the Au(111) substrate. These images clearly show that the topmost sulfur atoms in the cobalt sulfide are aligned with the Au(111) lattice (Fig. 8.10). The resulting simulation of Co_3S_4 (Fig. 8.9b) shows a clear hexagonal structure consisting of triangles similar in size to those observed in the experimental STM image (Fig. 8.9a). Furthermore, the three corner S atoms, where the triangles join, have a low vertical position as indicated by the dark color, which is also in agreement with the experimentally observed STM images. The rather intriguing mill-wheel structure is therefore explained by a simple moiré structure reflecting the lattice mismatch between the non-rotated overlayer and substrate [141].

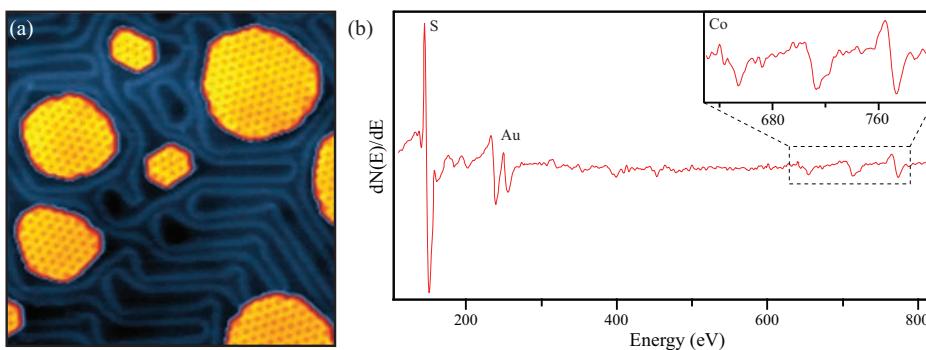


Figure 8.11. (a) STM image ($740 \text{ \AA} \times 740 \text{ \AA}$) showing cobalt sulfide islands after annealing to 573 K for 10 min. (b) AES spectrum of the $\text{S}_4\text{-Co}_3\text{S}_4$ structure.

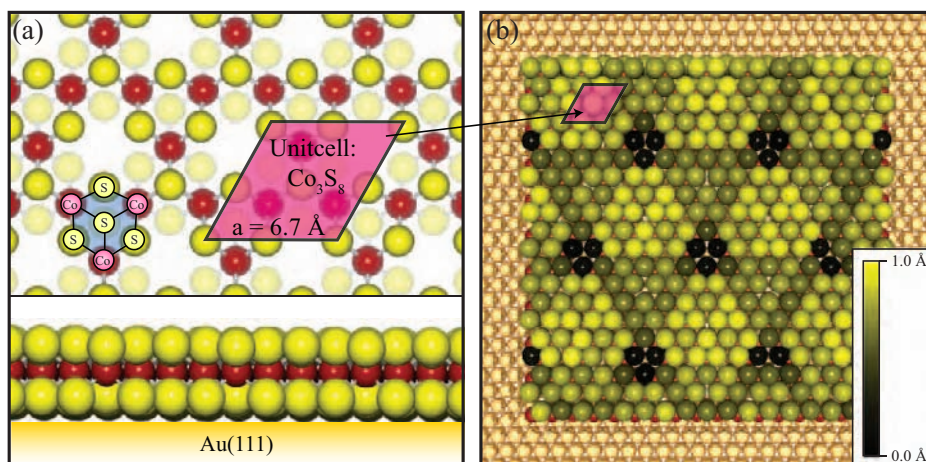


Figure 8.12. (a) Ball model, top and side view, respectively, of Au(111)-S₄-Co₃S₄.

A detailed ball model of the Co₃S₄ slab used in the geometrical structure simulation is shown in Fig. 8.12a. The structure can be viewed as a network structure composed of Co₃S₄ subunits held together by an additional four sulfur ligands. The expected size and shape of this subunit matches closely the 20-21 Å² wide diffusing complexes observed in the low-temperature STM images (Fig. 8.8b) and the quantized step decay of Co particles (Fig. 8.7e). Due to the stacking sequence Au(111)-S₄-Co₃S₄, the overall stoichiometry corresponds to a sulfur to cobalt ratio of 8 to 3, which is higher than that observed for any bulk cobalt-sulfide phase. Auger electron spectroscopy (AES), however, confirms this ratio. For this analysis larger more homogenous patches of the S₄-Co₃S₄ mill-wheel structure were synthesized by annealing the sample at 523 K in a H₂S atmosphere (Fig. 8.11a). A control AES spectrum under the same sulfidation conditions but without Co showed no traces of sulfur, confirming that all sulfur is indeed present as cobalt sulfide. Taking Auger selectivity factors into account, the peak-to-peak intensity of the AES spectrum (Fig. 8.11b) yields a sulfur to cobalt ratio of 2.7 ± 0.2 in perfect accordance with a 8 to 3 S:Co ratio. The stabilization of the sulfur excess is not surprising since the Au surface generally has a high affinity towards single-bonded sulfur compounds, such as thiols [219, 220].

8.7 Conclusion

An important conclusion from the present studies is that Co nanoparticles are structurally unstable in an even very mildly sulfiding environment. STM movies with a duration of up to 80 hours directly reveal that Co nanoparticles decay by a mechanism that involves the formation of volatile Co₃S₄ complexes at the particle perimeter. The complexes are continuously transported away, and the process should therefore occur for Co particles

of any larger size also. Interestingly, the whole process occurs with a very low energy barrier since it is observed at room temperature, and the implications are that sulfur levels even at a fraction of a ppb will significantly influence the distribution of Co. The present findings are thus of general interest for controlling the long-term stability of systems relying on a high dispersion of Co nanoparticles and show that modeling the dynamical behavior of such systems in a sulfiding environment needs to take Co_3S_4 complexes into account.

In relation to the Co-based Fischer-Tropsch catalyst, the findings suggest that the catalytic deactivation mechanism by sulfur poisoning may not only be due to site-blocking by sulfur, but may in fact be determined by an accelerated redistribution and sintering or even refacetting of the active Co nanoparticles, which may prevent full regeneration after exposure to sulfur.

CHAPTER 9

Summary and outlook

The increasing demand for fuels with low sulfur content has dramatically increased the efforts put into the development of new and more capable desulfurization catalysts. The MoS₂-based hydrotreating catalyst has thus been subject to intense research for the last decades, but despite numerous studies, a number of fundamental questions have remained unanswered. This is largely due to the fact that traditional spectroscopic techniques are unable to directly map the atomic-scale structure of the catalytic active nanoclusters.

The results reported in this thesis are based on the surface science approach to catalysis in order to elucidate some of these unanswered questions. The general approach was to synthesize promoted and non-promoted MoS₂ nanoclusters on well-characterized surfaces as model systems for hydrotreating catalysts and investigate these by scanning tunneling microscopy (STM).

The STM studies show in general that the structure of MoS₂ nanoclusters are highly dependent on numerous parameters, including the annealing temperature and the gas pressure during the synthesis, the specific gas composition (H₂:H₂S ratio), the inclusion of promoter atoms, the support, and even the mere size of the clusters changes the edge structure. The MoS₂-based nanoclusters thus constitute a highly complex model system, and the ability of the STM to image the morphology with atomic resolution is paramount to gain a fundamental understanding of the MoS₂-based hydrotreating catalyst on an atomic-scale level.

The three main topics concerning the MoS₂-based hydrotreating catalyst covered in this thesis are: the size-dependent structure of MoS₂ nanoclusters, the influence of promoter atoms on the structure with special emphasis on cobalt and nickel promoters,

and the effect of the support.

The STM results show that the non-promoted triangular MoS_2 nanoclusters are subject to a surprising change of edge termination between the two low-index edge terminations that occurs as the size of the nanoclusters is reduced. Larger clusters with more than six Mo atoms along the edge display the $(10\bar{1}0)$ Mo edge, whereas clusters with less than six Mo atoms along the edge display the $(\bar{1}010)$ S edge. The shift in edge structure is a result of sulfur saturation of the MoS_2 nanoclusters. As the cluster size is decreased, the actual stoichiometry of the nanoparticles deviates from the bulk MoS_2 value as the relative S content increases due to excess sulfur at the cluster edges. The change in edge structure occurs to lower the sulfur to molybdenum ratio in the clusters since too S rich clusters are unstable.

The size-dependent shape of the MoS_2 nanoclusters is not just an interesting nanoscience phenomenon but may also help improve the technical hydrotreating catalyst. It is well known that only the edges of the MoS_2 nanoclusters are catalytic active, the basal plane is totally inactive, and since the chemical properties are affected when the edge structure is changed, a change in the catalytic properties is expected. In future studies it would be highly interesting to perform reactivity studies on size-selected MoS_2 nanoclusters in a batch flow reactor to investigate the variation of reactivity as a function of size.

MoS_2 nanoclusters are not just interesting in relation to hydrotreating catalysis. A recent study by Jaramillo *et al.* [88] showed that the edges of the MoS_2 nanoclusters are active in the hydrogen evolution reaction. The rather large size of the MoS_2 clusters in that study indicates that the edge termination was dominated by $(10\bar{1}0)$ Mo edges. It would be highly interesting to prepare a sample with predominant $(\bar{1}010)$ S edge terminated clusters by the method described in Section 4.2 in order to directly compare the hydrogen evolution activity of the two different edge terminations.

The studies on the effects of promoter atoms show that the MoS_2 nanoclusters display a promoter dependent morphology, which is explained by the different affinities for Co and Ni to replace Mo at the edge sites of MoS_2 nanoclusters. In contrast to the triangular non-promoted MoS_2 nanoclusters, the CoMoS clusters exhibit a hexagonally truncated equilibrium shape dominated by both types of low-index edge terminations. The shift in morphology is linked to a preference for the Co atoms to be located only at the $(\bar{1}010)$ S edges.

The change in shape is even more pronounced for the NiMoS nanoclusters, which adopt two kinds of shapes with one type resembling a hexagon and another shaped like a dodecagon. Surprisingly, this observation shows that Ni can stabilize the high-index $(11\bar{2}0)$ type of edges in MoS_2 , which are normally not considered in structural models. This surprising difference is attributed to a stronger affinity of the Ni to the edges of the MoS_2 nanoclusters. Importantly, this shows that the location and coordination of the promoters atoms are different in NiMoS and CoMoS, which may explain the different selectivity observed in the industrial catalysts.

The inclusion of Co or Ni at the edges is found to affect both the electronic and geometric structure of the edges. The promoted edges in general have a lower sulfur coverage compared to the non-promoted edges and this may provide attractive sites for adsorption of sulfur containing molecules.

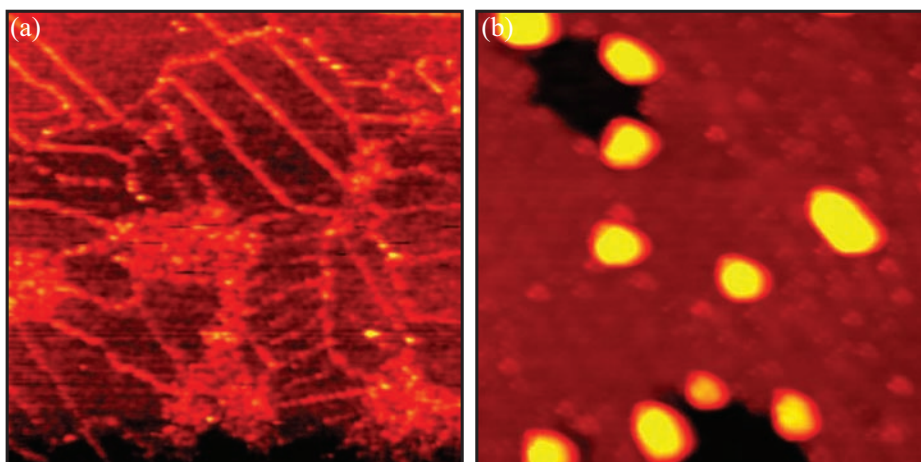


Figure 9.1. (a) STM image ($1000 \text{ \AA} \times 1000 \text{ \AA}$, $I_t = 0.43 \text{ nA}$, and $V_t = 1769 \text{ mV}$) showing a thin film of aluminium oxide grown on a NiAl(110) crystal. (b) STM image ($300 \text{ \AA} \times 300 \text{ \AA}$, $I_t = -0.53 \text{ nA}$, and $V_t = -1250 \text{ mV}$) of MoS₂ nanoclusters supported on the aluminium oxide thin film.

The studies of MoS₂ nanoclusters on a HOPG and on a rutile TiO₂(110) surface take the hydrotreating model studies one step further by including the effects of more realistic support materials. These studies show that the support affects the structure of the MoS₂ nanoclusters in terms of, e.g. stacking and cluster shape.

It would of course be highly interesting to study MoS₂ nanoclusters grown on alumina, but the insulating properties of Al₂O₃ inhibits STM imaging. It is, however, possible to form a thin film of aluminium oxide by oxidizing a NiAl(110) crystal [18, 221]. This allows an STM study of MoS₂ nanoclusters on a surface with an aluminium oxide structure. In preliminary studies a thin film of aluminium oxide has been prepared on a NiAl(110) crystal (see Fig. 9.1a). The synthesis of MoS₂ produces dispersed nanoclusters as observed in Fig. 9.1b, but no atom-resolved images have so far been obtained. Alternatively, atomic force microscopy (AFM), which does not require a conducting surface, could be used to image MoS₂ nanoclusters on a single-crystal α -Al₂O₃ support.

The studies presented in this thesis have mainly been concerned with the materials gap and thus conducted under UHV conditions. High-pressure STM could provide the means necessary to bridge the pressure gap. In particular a system where a high-pressure STM is combined with a reactor cell in a setup like that of Hendriksen and Frenken [222] would be a very powerful combination. Such a system would make it possible to directly relate the change in reactivity to the observed morphological changes of the model catalysts.

CHAPTER 10

Dansk resumé

Afbrænding af fossile brændstoffer, såsom diesel og benzin, er den primære kilde til svovludledning i atmosfæren. Denne udledning udgør et stort miljøproblem i form af eksempelvis syrerregn. Derudover har svovl også den uheldige effekt, at det ødelægger bilkatalysatoren, der renses udstødningsgassen. Disse negative effekter af svovl har de seneste år sat stor fokus på indholdet af svovl i brændstoffer, og mange lande heriblandt USA, Japan og EU-landene har markant skærpet grænseværdierne for svovlindholdet.

Svovlet fjernes fra råolien på olieraffinaderierne i en katalytisk proces, hvor den aktive katalysator består af molybdendisulfid (MoS_2) partikler, der har en størrelse på ganske få nanometer¹ (se Fig. 10.1). For at kunne leve op til de nye og skrappe grænseværdier for indholdet af svovl er det nødvendigt at udvikle nye og bedre katalysatorer.

Udviklingen hæmmes dog ofte af katalysatorers komplicerede struktur og virkemåde. De katalysatorer, der er på markedet i dag, er således primært udviklet på en empiriske måde, dvs. ved at forsøge sig frem med mere eller mindre kvalificerede gæt. Denne proces er imidlertid både tidskrævende og økonomisk tung, og udvikling af nye katalysatorer på baggrund af en fundamental forståelse af katalysatoren baseret på videnskabelige eksperimenter synes således særdeles attraktivt.

Den primære teknik benyttet i denne afhandling er skanning tunnel mikroskopet (STM). STM'et har en helt enestående opløsningsevne, der gør det muligt at se enkelte atomer på en overflade, dvs. mikroskopet gør det muligt direkte at se den atomare opbygning af de katalytiske partikler.

I denne afhandling studeres forskellige parametres indvirken på den MoS_2 -baserede

¹En nanometer er en milliardtedel af en meter.

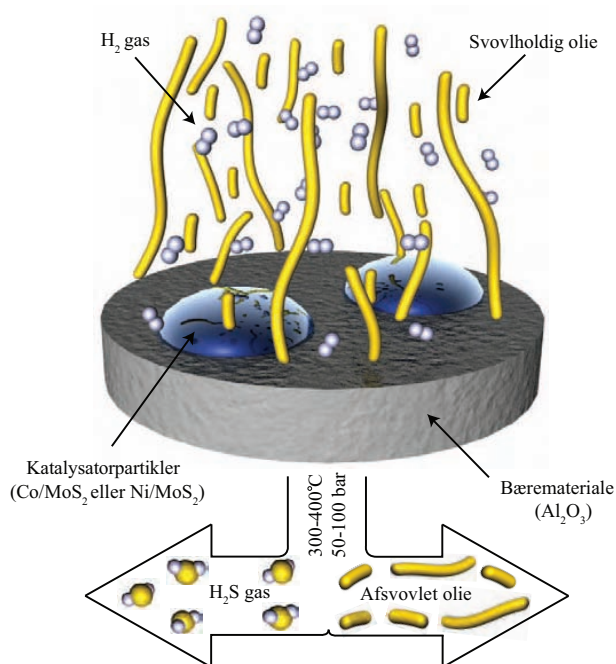


Figure 10.1. Skitse af katalysatoren som bruges til afsvovlingsprocessen af råolie. Brint og olie ledes gennem katalysatoren ved høj temperatur og tryk, hvorved svovl fjernes fra olien som svovlbrinte.

afsvovlingskatalysator. Da den industrielle katalysator er for kompliceret til at kunne studeres direkte, er der benyttet forsimplede modelsystemer til at studere eksempelvis effekten af partikelstørrelsen, bærematerialet og tilsætningen af promoter atomer (kobolt og nikkel). I det følgende vil studiet af partikelstørrelsen samt tilsætningen af promoteratomer kort resumeres.

Partikelstørrelsen

Inden for nanomaterialer er det velkendt at “small is different”, hvilket hentyder til, at nanostrukturer kan besidde helt nye egenskaber. Egenskaber som elektrisk ledningsevne, farve, reaktivitet, magnetisme og smeltepunkt kan således være fuldstændig anderledes for nanomaterialet sammenlignet med egenskaberne for materialet med makroskopiske dimensioner. Dimensionerne af et materiale er derfor en vigtig parameter at tage i betragtning i udviklingen af nye nanomaterialer. Ikke mindst i katalyse, hvor de aktive materialer i dag er begrænset til et relativt lille antal metaller, kan optimering af partikelstørrelsen måske være med til at udvikle nye og bedre katalysatorer.

Strukturen af MoS₂-nanopartikler viser sig at være afhængig af partikelstørrelsen. STM-billeder af ikke-promoterede MoS₂-nanopartikler viser, at partiklerne uanset stør-

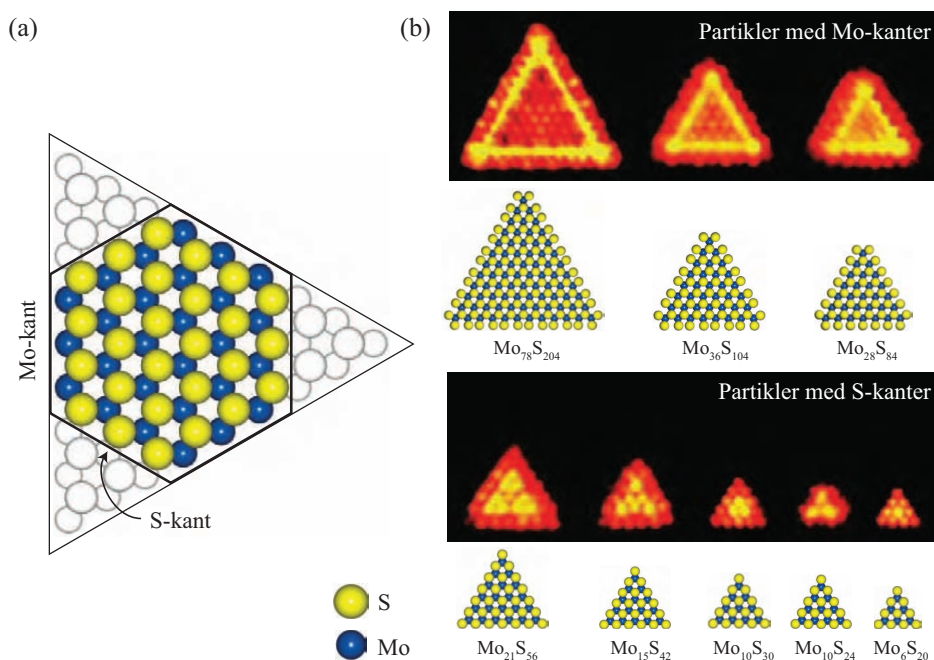


Figure 10.2. (a) Boldmodel af en MoS_2 -nanopartikel. En trekantet partikel kan antage to forskellige kantstrukturer. Enten afsluttes den udelukkende af såkaldte Mo-kanter eller også udelukkende af såkaldte S-kanter. (b) Otte atomart opløste STM-billeder af MoS_2 -nanopartikler med forskellig størrelse. Under hver partikel er en boldmodel svarende til strukturen af nanopartiklen. De større partikler i den øverste række afsluttes alle med Mo-kanter, mens de små partikler i den nederste række alle afsluttes med S-kanter.

relse antager en trekantet form. STM-billederne viser imidlertid også, at når størrelsen af MoS_2 -nanopartiklerne reduceres, sker en overraskende ændring af kantstrukturen. Den hexagonale krystalstruktur af MoS_2 betyder, at en trekantet nanopartikel kan antage to forskellige kantstrukturer. Enten afsluttes en partikel udelukkende af såkaldte Mo-kanter eller også udelukkende af såkaldte S-kanter, som vist i Fig. 10.2a.

De større MoS_2 -partikler, med seks eller flere Mo-atomer langs kanten, antager Mo-kanten fuldt besat med svovlatomer, mens de mindste MoS_2 -partikler med under seks Mo-atomer langs kanten antager S-kanten. Ændringen af kantstrukturen skyldes, at partiklernes svovl til molybdæn-forhold afviger fra 2:1 støkiometrien af MoS_2 . Årsagen til afvigelsen skyldes den ekstra mængde svovl, der findes på kanterne, idet eksempelvis en nøgen Mo kant uden svovl, som vist i Fig. 10.2a, ikke er energimæssig stabil. Når størrelsen af partiklerne mindskes, betyder den ekstra mængde svovl ved kanterne forholdsmæssigt mere, og svovl til molybdæn-forholdet stiger således med mindre partikler. Et for højt svovl til molybdæn-forhold (omkring 3:1) gør imidlertid partiklerne ustabile, men ved at skifte fra Mo-kanten til S-kanten kan partiklerne sænke deres svovl

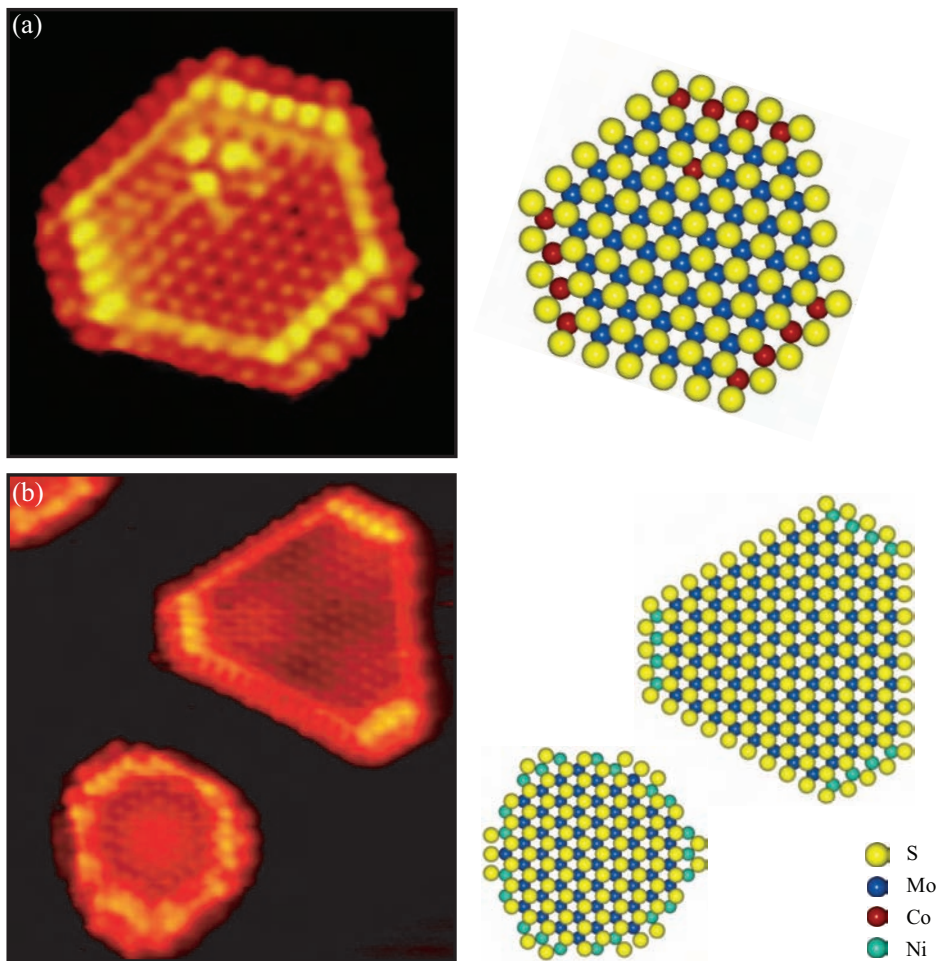


Figure 10.3. (a) STM-billede og boldmodel af en CoMoS-nanopartikel. (b) STM-billede og boldmodel af henholdsvis en sekskantet og en tolvkantet NiMoS-nanopartikel.

til molybdæn-forhold.

Ændringen af kantstrukturen som funktion af størrelsen er yderst interessant, idet det er på kanten af de katalytiske aktive MoS_2 -partikler, at svovlet fjernes. Ved at ændre på kantstrukturen ændres således også på partiklernes evne til at afsvoвле råolien, og resultaterne antyder derfor, at ved at skræddersy partiklerne til en optimal størrelse kan den industrielle katalysators evne til at fjerne svovl optimeres.

Promoteratomer

Den MoS_2 -baserede katalysators evne til at fjerne svovl forøges dramatisk, når ganske små mængder kobolt eller nikkel tilsættes. Årsagen til den gunstige effekt af disse såkaldte promoteratomer har været meget debatteret i litteraturen. Der synes dog at være opnået enighed om, at den forøgede katalytiske aktivitet skyldes såkaldte “CoMoS”- og “NiMoS-strukturer”, hvor henholdsvis kobolt- eller nikkelatomer er inkorporeret i kantstrukturen af de katalytiske MoS_2 -partikler og derved danner nye mere aktive sites.

Figur 10.3 viser STM-billeder af henholdsvis en CoMoS-partikel og to NiMoS-partikler. Billederne viser tydeligt, at tilsætningen af promoteratomer ændrer partikelformen fra trekantet til henholdsvis sekskantet, når kobolt tilsættes, og enten sekskantet eller tolvkantet, når nikkel tilsættes.

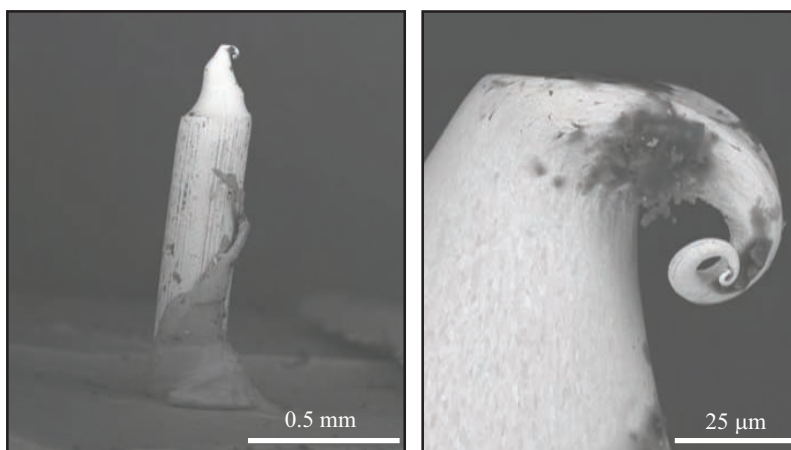
I tilfældet med sekskantede partikler stabiliserer kobolt og nikkel promoter atomerne S-kanten i forhold til Mo-kanten. De promoterede partikler danner dermed en helt ny type kant, hvor den yderste række Mo-atomer i S-kanten er udskiftet med enten Co eller Ni. Disse nye kanter har en lavere mængde svovl på kanten og tænkes således at være attraktive for adsorption af svovlholdig oliemolekyler og dermed årsagen til den forøgede aktivitet i forhold til de ikke-promoterede MoS_2 -partikler.

Den tolvkantede er unik for nikkel. NiMoS-partiklernes form hænger nøje sammen med partikelstørrelsen, idet kun de mindste NiMoS-partikler antager den tolvkantede form, mens de større alle antager den sekskantede. Den tolvkantede form skabes, hvis en sekskantet partikel trunkeres ved hjørnerne. Den nye type kant, der herved opstår, er meget fattig på svovl og kunne tænkes at være et attraktivt sted for svovlholdige oliemolekyler at adsorbere. Tilstedeværelsen af de tolvkantede NiMoS partikler viser ydermere, at der er forskel på CoMoS og NiMoS strukturerne, idet CoMoS-partikler udelukkende er sekskantede.

Acknowledgements

During the past four years as a PhD student, I had the great pleasure of not only being a part of the SPM group but also of the iNANO center, which has truly been an inspiring environment to work in. At this point I would thus like to gratefully acknowledge a number of people.

First and foremost, I would like to thank my supervisors Flemming Besenbacher and Jeppe Vang Lauritsen. I am deeply indebted to both, Flemming for his never ending enthusiasm and keen interest in the project, and Jeppe for his excellent guidance of me into the world of experimental surface science and many fruitful discussions. Erik Lægsgaard is also highly appreciated for his technical support in the laboratory.



Scanning electron microscopy (SEM) images of the STM tip used to record the majority of STM images presented in this thesis. However, after three years the tip had an unfortunate encounter with a graphite surface.

Furthermore, the theoreticians in the group headed by Jens K. Nørskov at the Technical University of Denmark (DTU), especially Poul Georg Moses and Berit Hinnemann, are greatly appreciated for their work on the HDS model catalyst systems. Likewise is theoretical work of Sibylle Gemming on the Mo_6S_6 nanowires highly appreciated. I would also like to thank Karina Morgenstern for good discussions concerning the sulfidation of the cobalt nanoparticles.

Throughout the project the link to the real world was maintained by the interaction with the catalyst company Haldor Topsøe A/S. Especially Bjerne S. Clausen and Henrik Topsøe are thanked for putting the results of the HDS model catalyst system into a larger context. Fruitful discussions with Stig Helveg are also acknowledged.

The many PhD students, not only in the SPM group but also at iNANO in general, have truly made everyday life a pleasant and enjoyable experience. I would like to thank Anders Tuxen, Martin Levisen, Jesper Matthiesen, Wei Xu, Lindsay Merte, Stefan Wendt, Jonas Ørbæk Hansen, Estephania Lira, and especially Jan Knudsen for good company in the lab. A special thank goes to Mona Robenhagen Jensen, Peter Herskind, Henrik Andersen, Martin Lorentzen, and Mads Hovgaard with whom I have had many scientific and non-scientific discussions. Annette Riisberg is thanked for proofreading the thesis. Finally, I would like to thank FysKem2000 and the buddies from chemistry without whom my 8 years at the University of Aarhus would have been much less happy.

Jakob Kibsgaard

Bibliography

- [1] V. Smil, “*Detonator of the population explosion*”, *Nature* **400**, 415 (1999).
- [2] The Nobel Foundation:
http://nobelprize.org/nobel_prizes/chemistry/laureates/1918/.
- [3] The Nobel Foundation:
http://nobelprize.org/nobel_prizes/chemistry/laureates/1931/.
- [4] I. Chorkendorff and J. W. Niemantsverdriet, “*Concepts of Modern Catalysis and Kinetics*”, (Wiley-VCH Verlag GmbH, Weinheim, 2003).
- [5] “*Handbook of Heterogeneous Catalysis*”, edited by G. Ertl, H. Knözinger, and J. Weitkamp (Wiley-VCH, Weinheim, 1997), Vol. 1-5.
- [6] G. A. Somorjai, “*Surface Chemistry and Catalysis*”, (Wiley, New York, 1994).
- [7] A. McNaught and A. Wilkinson, “*The IUPAC Compendium of Chemical Terminology*”, (Blackwell Science, Cambridge, 1997).
- [8] The Nobel Foundation:
http://nobelprize.org/nobel_prizes/chemistry/laureates/2007/.
- [9] P. Bernard, K. Peters, J. Alvarez, and S. Ferrer, “*Ultrahigh vacuum high pressure chamber for surface x-ray diffraction experiments*”, *Rev. Sci. Instrum.* **70**, 1478 (1999).
- [10] G. D. Moggridge, T. Rayment, R. M. Ormerod, M. A. Morris, and R. M. Lambert, “*Spectroscopic Observation Of A Catalyst Surface In A Reactive Atmosphere At High-Pressure*”, *Nature* **358**, 658 (1992).
- [11] D. F. Ogletree, H. Bluhm, G. Lebedev, C. S. Fadley, Z. Hussain, and M. Salmeron, “*A differentially pumped electrostatic lens system for photoemission studies in the millibar range*”, *Rev. Sci. Instrum.* **73**, 3872 (2002).
- [12] T. W. Hansen, J. B. Wagner, P. L. Hansen, S. Dahl, H. Topsøe, and C. J. H. Jacobsen, “*Atomic-resolution in situ transmission electron microscopy of a promoter of a heterogeneous catalyst*”, *Science* **294**, 1508 (2001).
- [13] P. L. Hansen, J. B. Wagner, S. Helveg, J. R. Rostrup-Nielsen, B. S. Clausen, and H. Topsøe, “*Atom-resolved imaging of dynamic shape changes in supported copper nanocrystals*”, *Science* **295**, 2053 (2002).
- [14] S. Helveg, C. Lopez-Cartes, J. Sehested, P. L. Hansen, B. S. Clausen, J. R. Rostrup-Nielsen, F. Abild-Pedersen, and J. K. Nørskov, “*Atomic-scale imaging of carbon nanofibre growth*”, *Nature* **427**, 426 (2004).

- [15] M. Haruta, N. Yamada, T. Kobayashi, and S. Iijima, "Gold catalysts prepared by coprecipitation for low-temperature oxidation of hydrogen and of carbon-monoxide", *J. Catal.* **115**, 301 (1989).
- [16] M. Valden, X. Lai, and D. W. Goodman, "Onset of Catalytic Activity of Gold Clusters on Titania with the Appearance of Nonmetallic Properties", *Science* **281**, 1647 (1998).
- [17] C. T. Campbell, "Ultrathin metal films and particles on oxide surfaces: Structural, electronic and chemisorptive properties", *Surf. Sci. Rep.* **27**, 1 (1997).
- [18] K. H. Hansen, T. Worren, S. Stempel, E. Lægsgaard, M. Baumer, H. J. Freund, F. Besenbacher, and I. Stensgaard, "Palladium nanocrystals on Al_2O_3 : Structure and adhesion energy", *Phys. Rev. Lett.* **83**, 4120 (1999).
- [19] B. J. McIntyre, M. Salmeron, and G. A. Somorjai, "A variable pressure/temperature scanning tunneling microscope for surface science and catalysis studies", *Rev. Sci. Instrum.* **64**, 687 (1993).
- [20] E. Lægsgaard, L. Österlund, P. Thosttrup, P. B. Rasmussen, I. Stensgaard, and F. Besenbacher, "A high-pressure scanning tunneling microscope", *Rev. Sci. Instrum.* **72**, 3537 (2001).
- [21] H. Topsøe, B. S. Clausen, and F. E. Massoth, "Hydrotreating Catalysis, Science and Technology", (Springer Verlag, Berlin, 1996), Vol. 11.
- [22] A. C. Byrns, W. E. Bradley, and M. W. Lee, "Catalytic desulfurization of Gasolines by cobalt molybdate process", *Ind. Eng. Chem.* **35**, 1160 (1943).
- [23] Commission of the European Communities:
Legislative document - COD/2007/0019.
- [24] P. Sarrazin, J. Bonnardot, S. Wambergue, F. Morel, and C. Gueret, "New mild hydrocracking route produces 10-ppm-sulfur diesel", *Hydrocarbon Processing* **84**, 57 (2005).
- [25] S. J. Smith, R. Andreas, E. Conception, and J. Lurz, "Historical Sulfur Dioxide Emissions 1850-2000: Methods and Results", PNNL Research Report (2004).
- [26] G. Binnig, H. Rohrer, C. Gerber, and E. Weibel, "Surface Studies by Scanning Tunneling Microscopy", *Phys. Rev. Lett.* **49**, 57 (1982).
- [27] G. Binnig and H. Rohrer, "Scanning tunneling microscopy – from birth to adolescence", *Rev. Mod. Phys.* **59**, 615 (1987).
- [28] The Nobel Foundation:
http://nobelprize.org/nobel_prizes/physics/laureates/1986/.
- [29] E. Lægsgaard, F. Besenbacher, K. Mortensen, and I. Stensgaard, "A fully automated, 'thimble-size' scanning tunnelling microscope", *J. Microsc. Oxford* **152**, 663 (1988).
- [30] J. Tersoff and D. R. Hamann, "Theory and application for the scanning tunneling microscope", *Phys. Rev. Lett.* **50**, 1998 (1983).
- [31] J. Bardeen, "Tunneling from a Many-Particle Point of View", *Phys. Rev. Lett.* **6**, 57 (1961).
- [32] "Handbook of Chemistry and Physics", 74 ed. (CRC Press, Boca Raton, Florida, USA, 1994).
- [33] N. D. Lang, "Vacuum Tunneling Current from an Adsorbed Atom", *Phys. Rev. Lett.* **55**, 230 (1985).
- [34] A. Selloni, P. Carnevali, E. Tosatti, and C. D. Chen, "Voltage-Dependent Scanning-Tunneling Microscopy Of A Crystal-Surface - Graphite", *Phys. Rev. B* **31**, 2602 (1985).
- [35] R. M. Feenstra, W. A. Thompson, and A. P. Fein, "Real-Space Observation Of Pi-Bonded Chains And Surface Disorder On $Si(111)2 \times 1$ ", *Phys. Rev. Lett.* **56**, 608 (1986).
- [36] R. M. Feenstra, J. A. Stroscio, and A. P. Fein, "Tunneling Spectroscopy Of The $Si(111)2 \times 1$ Surface", *Surf. Sci.* **181**, 295 (1987).
- [37] B. Hammer and J. K. Nørskov, "Theory of Adsorption and Surface Reactions" in "Chemisorption and Reactivity on Supported Clusters and Thin Films", edited by R. M. Lambert and G. Pacchioni (Kluwer Academic Publishers, Netherlands, 1997), pp. 285–351.

- [38] B. Hammer and J. K. Nørskov, "Theoretical Surface Science and Catalysis - Calculation and Concepts", *Adv. Catal.* **45**, 71 (2000).
- [39] P. Hohenberg and W. Kohn, "Inhomogeneous Electron Gas", *Phys. Rev. B* **136**, B864 (1964).
- [40] W. Kohn and L. J. Sham, "Self-Consistent Equations Including Exchange and Correlation Effects", *Phys. Rev.* **140**, A1133 (1965).
- [41] R. O. Jones and O. Gunnarsson, "The Density Functional Formalism, Its Applications And Prospects", *Rev. Mod. Phys.* **61**, 689 (1989).
- [42] H. Rydberg, M. Dion, N. Jacobson, E. Schroder, P. Hyldgaard, S. I. Simak, D. C. Langreth, and B. I. Lundqvist, "Van der Waals density functional for layered structures", *Phys. Rev. Lett.* **91**, 126402 (2003).
- [43] M. V. Bollinger, K. W. Jacobsen, and J. K. Nørskov, "Atomic and Electronic Structure of MoS₂ Nanoparticles", *Phys. Rev. B* **67**, 085410 (2003).
- [44] R. Prins, V. H. J. de Beer, and G. A. Somorjai, "Structure and Function of the Catalyst and the Promoter in Co-Mo Hydrotreating Catalysts", *Catal. Rev.-Sci. Eng.* **31**, 1 (1989).
- [45] R. Prins, "Hydrodesulfurization, Hydrodenitrogenation, Hydrodeoxygenation and Hydrodechlorination" in "Handbook of Heterogeneous Catalysis", edited by G. Ertl, H. Knözinger, and J. Weitkamp (VHC, Weinheim, 1997), Vol. 4, p. 1908.
- [46] M. Salmeron, G. A. Somorjai, A. Wold, R. Chianelli, and K. S. Liang, "The adsorption and binding of thiophene, butene and H₂S on the basal plane of MoS₂ single crystals", *Chem. Phys. Lett.* **90**, 105 (1982).
- [47] M. H. Farias, A. J. Gellman, G. A. Somorjai, R. R. Chianelli, and K. S. Liang, "The CO Co-Adsorption and Racitons of Sulfur, Hydrogen and Oxygen on clean and Sulfided Mo(100) and on Mos₂(0001) Crystal Faces", *Surf. Sci.* **140**, 181 (1984).
- [48] N.-Y. Topsøe and H. Topsøe, "IR spectroscopic studies of the nature of surface sites in hydrotreating catalysts", *J. Electr. Spectr. Rel. Phenom.* **39**, 11 (1986).
- [49] B. S. Clausen, B. Lengeler, R. Candia, J. Als-Nielsen, and H. Topsøe, "EXAFS Studies of Calcined and Sulfided Co-Mo HDS Catalysts", *Bull. Soc. Chim. Belg.* **90**, 1249 (1981).
- [50] T. G. Parham and R. P. Merrill, "An EXAFS Study of the Structure of Supported Cobalt Molybdate catalysts as a Function of Sulfiding Temperature", *J. Catal.* **85**, 295 (1984).
- [51] R. J. Needs, M. J. Godfrey, and M. Mansfield, "Theory of surface stress and surface reconstruction", *Surf. Sci.* **242**, 215 (1991).
- [52] V. Fiorentini, M. Methfessel, and M. Scheffler, "Reconstruction Mechanism of fcc Transition Metal (001) Surfaces", *Phys. Rev. Lett.* **71**, 1051 (1993).
- [53] J. V. Barth, H. Brune, G. Ertl, and R. Behm, "Scanning Tunneling Microscopy observations on the reconstructed Au(111) surface: Atomic structure, long-range superstructure, rotational domains, and surface defects", *Phys. Rev. B* **42**, 9307 (1990).
- [54] S. Narasimhan and D. Vanderbilt, "Elastic Stress Domain and the Herringbone Reconstruction on Au(111)", *Phys. Rev. Lett.* **69**, 1564 (1992).
- [55] J. A. Stroschio, D. T. Pierce, R. A. Dragoset, and P. N. First, "Microscopic aspects of the initial growth of metastable fcc iron on Au(111)", *J. Vac. Sci. Tech. A* **10**, 1981 (1992).
- [56] B. Voigtländer, G. Meyer, and N. M. Amer, "Epitaxial Growth of thin magnetic cobalt films on Au(111) studied by scanning tunneling microscopy", *Phys. Rev. B* **44**, 10354 (1991).
- [57] K. Morgenstern, J. Kibsgaard, J. V. Lauritsen, E. Lægsgaard, and F. Besenbacher, "Cobalt growth on two related close-packed noble metal surfaces", *Surf. Sci.* **601**, 1967 (2007).

- [58] D. D. Chambliss, R. J. Wilson, and S. Chiang, "Nucleation of Ordered Ni Island Arrays on Au(111) by Surface-Lattice Dislocations", *Phys. Rev. Lett.* **66**, 1721 (1991).
- [59] J. A. Meyer, I. D. Baikie, E. Kopatzki, and R. J. Behm, "Preferential island nucleation at the elbows of the Au(111) herringbone reconstruction through place exchange", *Surf. Sci.* **365**, L647 (1996).
- [60] S. Strbac, O. M. Magnussen, and R. J. Behm, "Nanoscale Pattern Formation during Electrodeposition: Ru on Reconstructed Au(111)", *Phys. Rev. Lett.* **83**, 3246 (1999).
- [61] A. W. Stephenson, C. J. Baddeley, M. S. Tikhov, and R. M. Lambert, "Nucleation and growth of catalytically active Pd islands on Au(111)- $22 \times \sqrt{3}$ studied by scanning tunneling microscopy", *Surf. Sci.* **398**, 172 (1998).
- [62] B. Fischer, J. V. Barth, A. Fricke, L. Nedelmann, and K. Kern, "Growth and surface alloying of Al on Au(111) at room temperature", *Surf. Sci.* **389**, 366 (1997).
- [63] M. M. Dovek, C. A. Lang, J. Nogami, and C. F. Quate, "Epitaxial-Growth Of Ag On Au(111) Studied By Scanning Tunneling Microscopy", *Phys. Rev. B* **40**, 11973 (1989).
- [64] C. A. Lang, M. M. Dovek, J. Nogami, and C. F. Quate, "Au(111) autoepitaxy studied by scanning tunneling microscopy", *Surf. Sci.* **224**, L947 (1989).
- [65] R. G. Dickinson and L. Pauling, "The Crystal Structure of Molybdenite", *J. Am. Chem. Soc.* **45**, 1466 (1923).
- [66] K. Kobayashi and J. Yamauchi, "Electronic structure and scanning-tunneling-microscopy image of molybdenum dichalcogenide surface", *Phys. Rev. B* **51**, 17085 (1995).
- [67] A. Altibelli, C. Joachim, and P. Sautet, "Interpretation of STM images: The MoS₂ surface", *Surf. Sci.* **367**, 209 (1996).
- [68] J. V. Lauritsen, "Atomic-scale Study of a Hydrodesulfurization Model Catalyst", Ph.D Thesis, University of Aarhus (2002).
- [69] G. Wulff, "Zur Frage der Geschwindigkeit des Wachstums und der Auflösung der Krystallflächen", *Z. Kristallogr.* **34**, 449 (1901).
- [70] W. K. Burton, N. Cabrera, and F. C. Frank, "The Growth of Crystals and The Equilibrium Structure of Their Surfaces", *Trans. R. Soc. A* **243**, 299 (1951).
- [71] W. I. Winterbottom, "Equilibrium Shape Of A Small Particle In Contact With A Foreign Substrate", *Acta Metall.* **15**, 303 (1967).
- [72] J. V. Lauritsen, M. V. Bollinger, E. Lægsgaard, K. W. Jacobsen, J. K. Nørskov, B. S. Clausen, H. Topsøe, and F. Besenbacher, "Atomic-scale Insight into Structure and Morphology Changes of MoS₂ Nanoclusters in Hydrotreating Catalysts", *J. Catal.* **221**, 510 (2004).
- [73] M. V. Bollinger, J. V. Lauritsen, K. W. Jacobsen, J. K. Nørskov, S. Helveg, and F. Besenbacher, "One-dimensional metallic edge states in MoS₂", *Phys. Rev. Lett.* **87**, 196803 (2001).
- [74] H. Schweiger, P. Raybaud, G. Kresse, and H. Toulhoat, "Shape and Edge Sites Modifications of MoS₂ Catalytic Nanoparticles Induced by Working Conditions: A Theoretical Study", *J. Catal.* **207**, 76 (2002).
- [75] J. V. Lauritsen, M. Nyberg, R. T. Vang, M. V. Bollinger, B. S. Clausen, H. Topsøe, K. W. Jacobsen, F. Besenbacher, E. Lægsgaard, J. K. Nørskov, and F. Besenbacher, "The Chemistry of One-dimensional Metallic Edge States in MoS₂ Nanoclusters", *Nanotech.* **14**, 385 (2003).
- [76] J. V. Lauritsen, M. Nyberg, J. K. Nørskov, B. S. Clausen, H. Topsøe, E. Lægsgaard, and F. Besenbacher, "Hydrodesulfurization reaction pathways on MoS₂ nanoclusters revealed by scanning tunneling microscopy", *J. Catal.* **224**, 94 (2004).
- [77] M. Egorova and R. Prins, "Hydrodesulfurization of dibenzothiophene and 4,6-dimethylidibenzothiophene over sulfided NiMo/γ-Al₂O₃, CoMo/γ-Al₂O₃, and Mo/γ-Al₂O₃ catalysts", *J. Catal.* **225**, 417 (2004).

- [78] “*Nanocatalysis*”, edited by U. Heiz and U. Landman (Springer-Verlag, Berlin Heidelberg, 2007).
- [79] S. Helveg, J. V. Lauritsen, E. Lægsgaard, I. Stensgaard, J. K. Nørskov, B. S. Clausen, H. Topsøe, and F. Besenbacher, “*Atomic-scale Structure of Single-layer MoS₂ Nanoclusters*”, *Phys. Rev. Lett.* **84**, 951 (2000).
- [80] H. Brune, “*Microscopic view of epitaxial metal growth: nucleation and aggregation*”, *Surf. Sci. Rep.* **31**, 121 (1998).
- [81] T. S. Li and G. L. Galli, “*Electronic properties of MoS₂ nanoparticles*”, *J. Phys. Chem. C* **111**, 16192 (2007).
- [82] L. S. Byskov, J. K. Nørskov, B. S. Clausen, and H. Topsøe, “*DFT Calculations of Unpromoted and Promoted MoS₂-Based Hydrodesulfurization Catalysts*”, *J. Catal.* **187**, 109 (1999).
- [83] K.-H. Rieder and W. Stocker, “*Hydrogen-Induced Subsurface Reconstruction of Cu(110)*”, *Phys. Rev. Lett.* **57**, 2548 (1986).
- [84] J. P. Wilcoxon and G. A. Samara, “*Strong quantum-size effects in a layered semiconductor: MoS₂ nanoclusters*”, *Phys. Rev. B* **51**, 7299 (1995).
- [85] V. Chikan and D. F. Kelley, “*Size-dependent spectroscopy of MoS₂ nanoclusters*”, *J. Phys. Chem. B* **106**, 3794 (2002).
- [86] N. Bertram, J. Cordes, Y. D. Kim, G. Gantefor, S. Gemming, and G. Seifert, “*Nanoplatelets made from MoS₂ and WS₂*”, *Chem. Phys. Lett.* **418**, 36 (2006).
- [87] H. Tributsch and J. C. Bennett, “*Electrochemistry and photochemistry of MoS₂ layer crystals I*”, *J. Electroanal. Chem.* **81**, 97 (1977).
- [88] T. F. Jaramillo, K. P. Jørgensen, J. Bonde, J. H. Nielsen, S. Horch, and I. Chorkendorff, “*Identification of active edge sites for electrochemical H₂ evolution from MoS₂ nanocatalysts*”, *Science* **317**, 100 (2007).
- [89] H. Topsøe, B. S. Clausen, R. Candia, C. Wivel, and S. Mørup, “*In situ Mössbauer emission spectroscopy studies of unsupported and supported sulfided Co-Mo hydrodesulfurization catalysts: evidence for and nature of a Co-Mo-S phase*”, *J. Catal.* **68**, 433 (1981).
- [90] C. Wivel, R. Candia, B. S. Clausen, S. Mørup, and H. Topsøe, “*On the catalytic significance of a Co-Mo-S phase in Co-Mo/Al₂O₃ hydrodesulfurization catalysts: combined in situ Mössbauer emission spectroscopy and activity studies*”, *J. Catal.* **68**, 453 (1981).
- [91] H. Topsøe and B. S. Clausen, “*Importance of Co-Mo-S Type Structures in Hydrodesulfurization*”, *Catal. Rev.-Sci. Eng.* **26**, 395 (1984).
- [92] J. K. Nørskov, B. S. Clausen, and H. Topsøe, “*Understanding the trends in the hydrodesulfurization activity of the transition metal sulfides*”, *Catal. Lett.* **13**, 1 (1992).
- [93] O. Sørensen, B. S. Clausen, R. Candia, and H. Topsøe, “*HREM and AEM Studies of HDS Catalysts: Direct evidence for the Edge Location of Cobalt in Co-Mo-S*”, *Appl. Catal.* **13**, 363 (1985).
- [94] Y. Okamoto and T. Kubota, “*A model catalyst approach to the effects of the support on Co-Mo hydrodesulfurization catalysts*”, *Catal. Today* **86**, 31 (2003).
- [95] W. Niemann, B. S. Clausen, and H. Topsøe, “*X-ray adsorption studies of the Ni environment in Ni-Mo-S*”, *Catal. Lett.* **4**, 355 (1990).
- [96] S. P. A. Louwers and R. Prins, “*Ni EXAFS Studies of the Ni-Mo-S Structure in Carbon-Supported and Alumina-Supported Ni-Mo Catalysts*”, *J. Catal.* **133**, 94 (1992).
- [97] P. Raybaud, J. Hafner, G. Kresse, S. Kasztelan, and H. Toulhoat, “*Structure, Energetics, and Electronic Properties of the Surface of a Promoted MoS₂ Catalyst: An ab initio Local Density Functional Study*”, *J. Catal.* **190**, 128 (2000).

- [98] H. Schweiger, P. Raybaud, and H. Toulhoat, "Promoter sensitive shapes of Co(Ni)MoS nanocatalysts in sulfo-reductive conditions", *J. Catal.* **212**, 33 (2002).
- [99] M. Y. Sun, A. E. Nelson, and J. Adjaye, "On the incorporation of nickel and cobalt into MoS₂-edge structures", *J. Catal.* **226**, 32 (2004).
- [100] P. Sautet, "Images of Adsorbates with the Scanning Tunneling Microscope: Theoretical Approaches to the Contrast Mechanism", *Chem. Rev.* **97**, 1097 (1997).
- [101] M. Brorson, A. Carlsson, and H. Topsøe, "The morphology of MoS₂, WS₂, Co-Mo-S, Ni-Mo-S and Ni-W-S nanoclusters in hydrodesulfurization catalysts revealed", *Catal. Today* **123**, 31 (2007).
- [102] M. W. J. Crajé, S. P. A. Louwers, V. H. J. de Beer, R. Prins, and A. M. van der Kraan, "An EXAFS Study On The So-Called "Co-Mo-S" Phase In Co/C And Como/C, Compared With A Mössbauer Emission-Spectroscopy Study", *J. Phys. Chem.* **96**, 5445 (1992).
- [103] B. S. Clausen and H. Topsøe, "Insitu Studies Of Catalysts By XAFS And Mössbauer-Spectroscopy", *Hyperfine Interact.* **47-8**, 203 (1989).
- [104] J. T. Miller, W. J. Reagan, J. A. Kaduk, C. L. Marshall, and A. J. Kropf, "Selective hydrodesulfurization of FCC naphtha with supported MoS₂ catalysts: The role of cobalt", *J. Catal.* **193**, 123 (2000).
- [105] J. T. Miller, C. L. Marshall, and A. J. Kropf, "(CO)MoS₂/alumina hydrotreating catalysts: An EXAFS study of the chemisorption and partial oxidation with O₂", *J. Catal.* **202**, 89 (2001).
- [106] S. M. A. M. Bouwens, J. A. R. van Veen, D. C. Koningsberger, V. H. J. de Beer, and R. Prins, "Extended X-Ray Absorption Fine-Structure Determination Of The Structure Of Cobalt In Carbon-Supported Co And Co-Mo Sulfide Hydrodesulfurization Catalysts", *J. Phys. Chem.* **95**, 123 (1991).
- [107] H. Topsøe, R. Candia, N.-Y. Topsøe, and B. S. Clausen, "On the state of the Co-Mo-S model", *Bull. Soc. Chim. Belg.* **93**, 783 (1984).
- [108] S. M. A. M. Bouwens, D. C. Koningsberger, V. H. J. de Beer, S. P. A. Louwers, and R. Prins, "Exafs Study Of The Local-Structure Of Ni In Ni-MoS₂/C Hydrodesulfurization Catalysts", *Catal. Lett.* **5**, 273 (1990).
- [109] S. M. A. M. Bouwens, N. Barthe-Zahir, V. H. J. de Beer, and R. Prins, "The Role of Ni in Sulfided Carbon-Supported Ni-Mo Hydrodesulfurization Catalysts", *J. Catal.* **131**, 326 (1991).
- [110] S. Harris and R. R. Chianelli, "Catalysis By Transition-Metal Sulfides - A Theoretical And Experimental-Study Of The Relation Between The Synergic Systems And The Binary Transition-Metal Sulfides", *J. Catal.* **98**, 17 (1986).
- [111] P. G. Moses, B. Hinemann, H. Topsøe, and J. K. Nørskov, "The hydrogenation and direct desulfurization reaction pathway in thiophene hydrodesulfurization over MoS₂ catalysts at realistic conditions: A density functional study", *J. Catal.* **248**, 188 (2007).
- [112] P. G. Moses, "Transition metal sulfide catalysts - A DFT study of structure and reactivity", Ph.D Thesis, Technical University of Denmark (2008).
- [113] M. Breyse, J. L. Portefaix, and M. Vrinat, "Support effects on hydrotreating catalysts", *Catal. Today* **10**, 489 (1991).
- [114] F. Luck, "A Review Of Support Effects On The Activity And Selectivity Of Hydrotreating Catalysts", *Bull. Soc. Chim. Belg.* **100**, 781 (1991).
- [115] M. Breyse, P. Afanasiev, C. Geantet, and M. Vrinat, "Overview of support effects in hydrotreating catalysts", *Catal. Today* **86**, 5 (2003).
- [116] H. Topsøe and B. S. Clausen, "Active Sites and Support Effects in Hydrodesulfurization Catalysts", *Appl. Catal.* **25**, 273 (1986).
- [117] J. A. R. van Veen, E. Gerkema, A. M. van der Kraan, P. A. J. M. Hendriks, and H. Beens, "A ⁵⁷Co Mössbauer emission spectrometric study of some supported CoMo hydrodesulfurization catalysts", *J. Catal.* **133**, 112 (1992).

- [118] E. J. M. Hensen, V. H. J. de Beer, J. A. R. van Veen, and R. A. van Santen, "A refinement on the notion of type I and II (Co)MoS phases in hydrotreating catalysts", *Catal. Lett.* **84**, 59 (2002).
- [119] B. Hinnemann, J. K. Nørskov, and H. Topsøe, "A density functional study of the chemical differences between type I and type II MoS₂-based structures in hydrotreating catalysts", *J. Phys. Chem. B* **109**, 2245 (2005).
- [120] R. Candia, B. S. Clausen, J. Bartholdy, N.-Y. Topsøe, B. Lengeler, and H. Topsøe, (Verlag Chemie, Weinheim, 1984), Vol. II, p. 375.
- [121] L. Medici and R. Prins, "The Influence of Chelating Ligands on the Sulfidation of Ni and Mo in NiMo/SiO₂ Hydrotreating Catalysts", *J. Catal.* **163**, 38 (1996).
- [122] M. Breyse, B. A. Bennett, D. Chadwick, and M. Vrinat, "Structure and HDS Activity of Co-Mo Catalysts - a Comparison of Alumina and Carbon Supports", *Bull. Soc. Chim. Belg.* **90**, 1271 (1981).
- [123] J. C. Duchet, E. M. van Oers, V. H. J. de Beer, and R. Prins, "Carbon-supported sulfide catalysts", *J. Catal.* **80**, 386 (1983).
- [124] J. P. R. Vissers, B. Scheffer, V. H. J. de Beer, J. A. Moulijn, and R. Prins, "Effect of the Support on the Structure of Mo-Based Hydrodesulfurization Catalysts - Activated Carbon Versus Alumina", *J. Catal.* **105**, 277 (1987).
- [125] I. P. Batra, N. Garcia, H. Rohrer, H. Salemkink, E. Stoll, and S. Ciraci, "A Study Of Graphite Surface With STM And Electronic-Structure Calculations", *Surf. Sci.* **181**, 126 (1987).
- [126] D. Tomanek, S. G. Louie, H. J. Mamin, D. W. Abraham, R. E. Thomson, E. Ganz, and J. Clarke, "Theory And Observation Of Highly Asymmetric Atomic Structure In Scanning Tunneling Microscopy Images Of Graphite", *Phys. Rev. B* **35**, 7790 (1987).
- [127] S. Hembacher, F. J. Giessibl, J. Mannhart, and C. F. Quate, "Revealing the hidden atom in graphite by low-temperature atomic force microscopy", *Proc. Natl. Acad. Sci. USA* **100**, 12539 (2003).
- [128] H. Kang, K. H. Park, C. Kim, B. S. Shim, S. Kim, and D. W. Moon, "Point-Defect Formation On Graphite Surface Induced By Ion Impact At Energies Near Penetration Threshold", *Nucl. Instrum. Methods Phys. Res. Sect. B* **67**, 312 (1992).
- [129] D. Marton, H. Bu, K. J. Boyd, S. S. Todorov, A. H. Albayati, and J. W. Rabalais, "On The Defect Structure Due To Low-Energy Ion-Bombardment Of Graphite", *Surf. Sci.* **326**, L489 (1995).
- [130] J. R. Hahn and H. Kang, "Vacancy and interstitial defects at graphite surfaces: Scanning tunneling microscopic study of the structure, electronic property, and yield for ion-induced defect creation", *Phys. Rev. B* **60**, 6007 (1999).
- [131] D. Marton, K. J. Boyd, T. Lytle, and J. W. Rabalais, "Near-Threshold Ion-Induced Defect Production In Graphite", *Phys. Rev. B* **48**, 6757 (1993).
- [132] J. R. Hahn, H. Kang, S. Song, and I. C. Jeon, "Observation of charge enhancement induced by graphite atomic vacancy: A comparative STM and AFM study", *Phys. Rev. B* **53**, R1725 (1996).
- [133] B. An, S. Fukuyama, K. Yokogawa, and M. Yoshimura, "Evolution of Ar⁺-damaged graphite surface during annealing as investigated by scanning probe microscopy", *J. Appl. Phys.* **92**, 2317 (2002).
- [134] H. A. Mizes and J. S. Foster, "Long-Range Electronic Perturbations Caused By Defects Using Scanning Tunneling Microscopy", *Science* **244**, 559 (1989).
- [135] P. Ruffieux, O. Groning, P. Schwaller, L. Schlapbach, and P. Groning, "Hydrogen atoms cause long-range electronic effects on graphite", *Phys. Rev. Lett.* **84**, 4910 (2000).
- [136] R. R. Chianelli, E. B. Prestbridge, T. A. Pecoraro, and J. P. DeNeufville, "Molybdenum Disulfide in the Poorly Crystalline "Rag" Structure", *Science* **203**, 1105 (1979).
- [137] J. V. Lauritsen, S. Helveg, E. Lægsgaard, I. Stensgaard, B. S. Clausen, H. Topsøe, and F. Besenbacher, "Atomic-scale Structure of Co-Mo-S Nanoclusters in Hydrotreating Catalysis", *J. Catal.* **197**, 1 (2001).

- [138] J. V. Lauritsen, J. Kibsgaard, G. H. Olesen, P. G. Moses, B. Hinnemann, S. Helveg, J. K. Nørskov, B. S. Clausen, H. Topsøe, E. Lægsgaard, and F. Besenbacher, "Location and coordination of promoter atoms in Co- and Ni-promoted MoS₂-based hydrotreating catalysts", *J. Catal.* **249**, 220 (2007).
- [139] P.G. Moses - Personal communication.
- [140] P. Raybaud, J. Hafner, G. Kresse, S. Kasztelan, and H. Toulhoat, "Ab Initio Study of the H₂-H₂S/MoS₂ Gas-Solid Interface: The Nature of the Catalytically Active Sites", *J. Catal.* **189**, 129 (2000).
- [141] F. Grey and J. Bohr, "A symmetry Principle for Epitaxial Rotation", *Europhys. Lett.* **18**, 717 (1992).
- [142] Y. Feldman, E. Wasserman, D. J. Srolovitz, and R. Tenne, "High-Rate, Gas-Phase Growth of MoS₂ Nested Inorganic Fullerenes and Nanotubes", *Science* **267**, 222 (1995).
- [143] G. Seifert, H. Terrones, M. Terrones, G. Jungnickel, and T. Frauenheim, "Structure and Electronic Properties of MoS₂ Nanotubes", *Phys. Rev. Lett.* **85**, 146 (2000).
- [144] M. Remskar, "Inorganic nanotubes", *Adv. Mat.* **16**, 1497 (2004).
- [145] K. Kobayashi, "Moire pattern in scanning tunneling microscopy: Mechanism in observation of sub-surface nanostructures", *Phys. Rev. B* **53**, 11091 (1996).
- [146] V. E. Henrich and P. A. Cox, "The surface science of metal oxides", (Cambridge University Press, Cambridge, 1996).
- [147] R. Wang, K. Hashimoto, A. Fujishima, M. Chikuni, E. Kojima, A. Kitamura, M. Shimohigoshi, and T. Watanabe, "Light-induced amphiphilic surfaces", *Nature* **388**, 431 (1997).
- [148] B. Kasemo and J. Gold, "Implant surfaces and interface processes", *Adv. Dent. Res.* **13**, 8 (1999).
- [149] B. Kasemo, "Biological surface science", *Surf. Sci.* **500**, 656 (2002).
- [150] A. Fujishima, T. N. Rao, and A. Tryk, "Titanium dioxide photocatalysis", *J. Photochem. Photobiol. C* **1**, 1 (1999).
- [151] M. Grätzel, "Photoelectrochemical cells", *Nature* **414**, 338 (2001).
- [152] C. R. Henry, "Surface studies of supported model catalysts", *Surf. Sci. Rep.* **31**, 231 (1998).
- [153] V. Harle, J. P. Deloume, L. Mosoni, B. Durand, M. Vrinat, and M. Breysse, "Elaboration By Reaction In Molten Nitrates And Characterization Of Pure Titanium-Oxide With Large Surface-Area", *Eur. J. Solid State Inorg. Chem.* **31**, 197 (1994).
- [154] S. K. Maity, M. S. Rana, S. K. Bej, J. Ancheyta, G. M. Dhar, and T. Rao, "Studies on physico-chemical characterization and catalysis on high surface area titania supported molybdenum hydrotreating catalysts", *Appl. Catal. A* **205**, 215 (2001).
- [155] J. Ramirez, L. Cedeno, and G. Busca, "The role of titania support in Mo-based hydrodesulfurization catalysts", *J. Catal.* **184**, 59 (1999).
- [156] C. Arrouvel, M. Breysse, H. Toulhoat, and P. Raybaud, "A density functional theory comparison of anatase (TiO₂)- and gamma-Al₂O₃-supported MoS₂ catalysts", *J. Catal.* **232**, 161 (2005).
- [157] D. Costa, C. Arrouvel, M. Breysse, H. Toulhoat, and P. Raybaud, "Edge wetting effects of gamma-Al₂O₃ and anatase-TiO₂ supports by MoS₂ and CoMoS active phases: A DFT study", *J. Catal.* **246**, 325 (2007).
- [158] P. Raybaud, D. Costa, M. C. Valero, C. Arrouvel, M. Digne, P. Sautet, and H. Toulhoat, "First principles surface thermodynamics of industrial supported catalysts in working conditions", *J. Phys. Cond. Matt.* **20**, (2008).
- [159] U. Diebold, "The surface science of titanium dioxide", *Surf. Sci. Rep.* **48**, 53 (2003).
- [160] S. Munnix and M. Schmeits, "Electronic-Structure Of Ideal TiO₂(110), TiO₂(001), And TiO₂(100) Surfaces", *Phys. Rev. B* **30**, 2202 (1984).

- [161] U. Diebold, M. Li, O. Dulub, E. L. D. Hebenstreit, and W. Hebenstreit, "The relationship between bulk and surface properties of rutile $\text{TiO}_2(110)$ ", *Surf. Rev. Lett.* **7**, 613 (2000).
- [162] M. Ramamoorthy, D. Vanderbilt, and R. D. Kingsmith, "First-principles calculations of the energetics of stoichiometric TiO_2 surfaces", *Phys. Rev. B* **49**, 16721 (1994).
- [163] S. Wendt, R. Schaub, J. Matthiesen, E. K. Vestergaard, E. Wahlström, M. D. Rasmussen, P. Thostrup, L. M. Molina, E. Lægsgaard, I. Stensgaard, B. Hammer, and F. Besenbacher, "Oxygen vacancies on $\text{TiO}_2(110)$ and their interaction with H_2O and O_2 : A combined high-resolution STM and DFT study", *Surf. Sci.* **598**, 226 (2005).
- [164] S. Wendt, J. Matthiesen, R. Schaub, E. K. Vestergaard, E. Lægsgaard, F. Besenbacher, and B. Hammer, "Formation and splitting of paired hydroxyl groups on reduced $\text{TiO}_2(110)$ ", *Phys. Rev. Lett.* **96**, (2006).
- [165] K. E. Smith, J. L. Mackay, and V. E. Henrich, "Interaction Of SO_2 With Nearly Perfect And Defect $\text{TiO}_2(110)$ Surfaces", *Phys. Rev. B* **35**, 5822 (1987).
- [166] K. E. Smith and V. E. Henrich, "Interaction Of H_2S With High Defect Density $\text{TiO}_2(110)$ Surfaces", *Surf. Sci.* **217**, 445 (1989).
- [167] V. E. Henrich, "The Nature Of Transition-Metal-Oxide Surfaces", *Prog. Surf. Sci.* **14**, 175 (1983).
- [168] V. E. Henrich, "The Surfaces Of Metal-Oxides", *Rep. Prog. Phys.* **48**, 1481 (1985).
- [169] W. Gopel, G. Rocker, and R. Feierabend, "Intrinsic Defects Of $\text{TiO}_2(110)$ - Interaction With Chemisorbed O_2 , H_2 , CO , and CO_2 ", *Phys. Rev. B* **28**, 3427 (1983).
- [170] G. Rocker and W. Gopel, "Chemisorption Of H_2 And CO On Stoichiometric And Defective $\text{TiO}_2(110)$ ", *Surf. Sci.* **175**, L675 (1986).
- [171] E. L. D. Hebenstreit, W. Hebenstreit, and U. Diebold, "Adsorption of sulfur on $\text{TiO}_2(110)$ studied with STM, LEED and XPS: temperature-dependent change of adsorption site combined with O-S exchange", *Surf. Sci.* **461**, 87 (2000).
- [172] J. Ramirez, S. Fuentes, G. Diaz, M. Vrinat, M. Breyse, and M. Lacroix, "Hydrodesulfurization Activity And Characterization Of Sulfided Molybdenum And Cobalt Molybdenum Catalysts - Comparison Of Alumina-Supported, Silica Alumina-Supported And Titania-Supported Catalysts", *Appl. Catal.* **52**, 211 (1989).
- [173] J. A. Wilson and A. D. Yoffe, "Transition Metal Dichalcogenides", *Adv. Phys.* **18**, 193 (1969).
- [174] T. Yang, S. Okano, S. Berber, and D. Tomanek, "Interplay between structure and magnetism in $\text{Mo}_{12}\text{S}_9\text{I}_9$ nanowires", *Phys. Rev. Lett.* **96**, (2006).
- [175] M. Remskar, A. Mrzel, Z. Skraba, A. Jesih, M. Ceh, J. Demšar, P. Stadelmann, F. Lévy, and D. Mihailovic, "Self-assembly of subnanometer-diameter single-wall MoS_2 nanotubes", *Science* **292**, 479 (2001).
- [176] I. Popov, T. Yang, S. Berber, G. Seifert, and D. Tomaek, "Unique structural and transport properties of molybdenum chalcogenide nanowires", *Phys. Rev. Lett.* **99**, (2007).
- [177] J. V. Lauritsen, J. Kibsgaard, S. Helveg, H. Topsøe, B. S. Clausen, E. Lægsgaard, and F. Besenbacher, "Size-dependent structure of MoS_2 nanocrystals", *Nat. Nanotechnol.* **2**, 53 (2007).
- [178] J. P. Wilcoxon, T. R. Thurston, and J. E. Martin, "Applications of metal and semiconductor nanoclusters as thermal and photo-catalysts", *Nanostruct. Mater.* **12**, 993 (1999).
- [179] J. Zhang, J. M. Soon, K. P. Loh, J. H. Yin, J. Ding, M. B. Sullivan, and P. Wu, "Magnetic molybdenum disulfide nanosheet films", *Nano Lett.* **7**, 2370 (2007).
- [180] M. Potel, R. Chevrel, and M. Sergent, "New Pseudo-One-Dimensional Metals - $\text{M}_2\text{Mo}_6\text{Se}_6$ ($M = \text{Na}, \text{In}, \text{K}, \text{Tl}$), $\text{M}_2\text{Mo}_6\text{S}_6$ ($M = \text{K}, \text{Rb}, \text{Cs}$), $\text{M}_2\text{Mo}_6\text{Te}_6$ ($M = \text{In}, \text{Tl}$)", *Journal Of Solid State Chemistry* **35**, 286 (1980).

- [181] A. Meden, A. Kodre, J. P. Gomilsek, I. Arcon, I. Vilfan, D. Vrbanic, A. Mrzel, and D. Mihailovic, "Atomic and electronic structure of $Mo_6S_9-xI_x$ nanowires", *Nanotech.* **16**, 1578 (2005).
- [182] I. Vilfan, "Mo₆S₆ nanowires: structural, mechanical and electronic properties", *Eur. Phys. J. B Eur.* **51**, 277 (2006).
- [183] P. Murugan, V. Kumar, Y. Kawazoe, and N. Ota, "Assembling nanowires from Mo-S clusters and effects of iodine doping on electronic structure", *Nano Lett.* **7**, 2214 (2007).
- [184] L. Venkataraman and C. M. Lieber, "Molybdenum selenide molecular wires as one-dimensional conductors", *Phys. Rev. Lett.* **83**, 5334 (1999).
- [185] D. Vrbanic, M. Remškar, A. Jesih, A. Mrzel, P. Umek, M. Ponikvar, B. Jančar, A. Meden, B. Novosel, S. Pejovnik, P. Venturini, J. C. Coleman, and D. Mihailovic, "Air-stable monodispersed Mo₆S₃I₆ nanowires", *Nanotech.* **15**, 635 (2004).
- [186] J. W. G. Wildöer, L. C. Venema, A. G. Rinzler, R. E. Smalley, and C. Dekker, "Electronic structure of atomically resolved carbon nanotubes", *Nature* **391**, 59 (1998).
- [187] S. Gemming, G. Seifert, and I. Vilfan, "Li doped Mo₆S₆ nanowires: elastic and electronic properties", *Phys. Status Solidi B* **243**, 3320 (2006).
- [188] X. L. Li, X. R. Wang, L. Zhang, S. W. Lee, and H. J. Dai, "Chemically derived, ultrasmooth graphene nanoribbon semiconductors", *Science* **319**, 1229 (2008).
- [189] M. I. Ploscaru, S. J. Kokalj, M. Uplaznik, D. Vengust, D. Turk, A. Mrzel, and D. Mihailovic, "Mo₆S_{9-x}I_x nanowire recognitive molecular-scale connectivity", *Nano Lett.* **7**, 1445 (2007).
- [190] D. J. Coulman, J. Wintterlin, R. J. Behm, and G. Ertl, "Novel Mechanism For The Formation Of Chemisorption Phases - The (2x1)O-Cu(110) Added-Row Reconstruction", *Phys. Rev. Lett.* **64**, 1761 (1990).
- [191] J. D. Batteas, J. C. Dunphy, G. A. Somorjai, and M. Salmeron, "Coadsorbate induced reconstruction of a stepped Pt(111) surface by sulfur and CO: A novel surface restructuring mechanism observed by scanning tunneling microscopy", *Phys. Rev. Lett.* **77**, 534 (1996).
- [192] E. K. Vestergaard, R. T. Vang, J. Knudsen, T. M. Pedersen, T. An, E. Lægsgaard, I. Stensgaard, B. Hammer, and F. Besenbacher, "Adsorbate-induced alloy phase separation: A direct view by high-pressure scanning tunneling microscopy", *Phys. Rev. Lett.* **95**, (2005).
- [193] P. J. F. Harris, "Sulfur-Induced Faceting Of Platinum Catalyst Particles", *Nature* **323**, 792 (1986).
- [194] G. L. Bezemer, J. H. Bitter, H. Kuipers, H. Oosterbeek, J. E. Holewijn, X. D. Xu, F. Kapteijn, A. J. van Dillen, and K. P. de Jong, "Cobalt particle size effects in the Fischer-Tropsch reaction studied with carbon nanofiber supported catalysts", *J. Am. Chem. Soc.* **128**, 3956 (2006).
- [195] R. B. Anderson, F. S. Karn, and J. F. Shultz, "Factors In Sulfur Poisoning Of Iron Catalysts In Fischer-Tropsch Synthesis", *J. Catal.* **4**, 56 (1965).
- [196] A. L. Chaffee, I. Campbell, and N. Valentine, "Sulfur Poisoning Of Fischer-Tropsch Synthesis Catalysts In A Fixed-Bed Reactor", *Appl. Catal.* **47**, 253 (1989).
- [197] J. L. Li and N. J. Coville, "Effect of boron on the sulfur poisoning of Co/TiO₂ Fischer-Tropsch catalysts", *Appl. Catal. A* **208**, 177 (2001).
- [198] J. A. Kritzing, "The role of sulfur in commercial iron-based Fischer-Tropsch catalysis with focus on C-2-product selectivity and yield", *Catal. Today* **71**, 307 (2002).
- [199] C. H. Bartholomew and R. M. Bowman, "Sulfur Poisoning Of Cobalt And Iron Fischer-Tropsch Catalysts", *Appl. Catal.* **15**, 59 (1985).
- [200] C. H. Bartholomew, "Mechanisms of catalyst deactivation", *Appl. Catal. A* **212**, 17 (2001).
- [201] C. G. Visconti, L. Lietti, P. Forzatti, and R. Zennaro, "Fischer-Tropsch synthesis on sulphur poisoned Co/Al₂O₃ catalyst", *Appl. Catal. A* **330**, 49 (2007).

- [202] P. Sabatier and J. B. Senderens, "New methane synthesis", C.R. Hebd. Sean. Acad. Sci. **134**, 514 (1902).
- [203] F. Fischer and H. Tropsch, "Über die Synthese höherer Glieder der aliphatischen Reihe aus Kohlenoxyd", Ber. Dtsch. Chem. Ges. **56**, 2428 (1923).
- [204] F. Fischer and H. Tropsch, "Über die direkte Synthese von Erdöl-Kohlenwasserstoffen bei gewöhnlichem Druck (Erste Mitteilung)", Ber. Dtsch. Chem. Ges. **59**, 830 (1926).
- [205] F. Fischer and H. Tropsch, "Über die direkte Synthese von Erdöl-Kohlenwasserstoffen bei gewöhnlichem Druck (Zweite Mitteilung)", Ber. Dtsch. Chem. Ges. **59**, 832 (1926).
- [206] S. T. Sie, M. M. G. Senden, and H. M. H. V. Wechbm, "Conversion of natural gas to transportation fuels via the shell middle distillate synthesis process (smds)", Catal. Today **8**, 371 (1991).
- [207] D. Gray, M. Lytton, M. Neuworth, and G. Tomlinson, "The Impact of Developing Technology on Indirect Liquefaction", DOE report: MTR-80W326 (1980).
- [208] D. Gray, M. B. Neuworth, and G. Tomlinson, "Further Studies on Developing Technology for Indirect Liquefaction", DOE report: MTR-82W32 (1982).
- [209] M. E. Dry, "The Fischer-Tropsch process: 1950-2000", Catal. Today **71**, 227 (2002).
- [210] Web of knowledge:
<http://isiknowledge.com/>.
- [211] US Energy Information Administration:
<http://www.eia.doe.gov/>.
- [212] J. Kibsgaard, K. Morgenstern, E. Lægsgaard, J. V. Lauritsen, and F. Besenbacher, "Restructuring of Cobalt Nanoparticles Induced by Formation and Diffusion of Monodisperse Metal-Sulfur Complexes", Phys. Rev. Lett. **100**, 116104 (2008).
- [213] M. M. Biener, J. Biener, and C. M. Friend, "Revisiting the S-Au(111) interaction: Static or dynamic?", Langmuir **21**, 1668 (2005).
- [214] M. M. Biener, J. Biener, and C. M. Friend, "Sulfur-induced mobilization of Au surface atoms on Au(111) studied by real-time STM", Surf. Sci. **601**, 1659 (2007).
- [215] A. J. Leavitt and T. P. J. Beebe, "Chemical reactivity studies of hydrogen sulfide on Au(111)", Surf. Sci. **314**, 23 (1994).
- [216] "Pearson's handbook of crystallographic data for intermetallic phases", edited by P. Villars and L. D. Calvert (ASM International, Ohio, 1991), Vol. 1-4.
- [217] "Binary alloy phase diagrams", edited by T. B. Massalski (ASM International, Ohio, 1992), Vol. 1-3.
- [218] Y. D. Yin, R. M. Rioux, C. K. Erdonmez, S. Hughes, G. A. Somorjai, and A. P. Alivisatos, "Formation of hollow nanocrystals through the nanoscale Kirkendall Effect", Science **304**, 711 (2004).
- [219] G. E. Poirier, "Characterization of organosulfur molecular monolayers on Au(111) using scanning tunneling microscopy", Chem. Rev. **97**, 1117 (1997).
- [220] P. Maksymovych, D. C. Sorescu, and J. T. Yates, "Gold-atom-mediated bonding in self-assembled short-chain alkanethiolate species on the Au(111) surface", Phys. Rev. Lett. **97**, (2006).
- [221] R. M. Jaeger, H. Kuhlenbeck, H. J. Freund, M. Wuttig, W. Hoffmann, R. Franchy, and H. Ibach, "Formation Of A Well-Ordered Aluminum-Oxide Overlayer By Oxidation Of NiAl(110)", Surf. Sci. **259**, 235 (1991).
- [222] B. L. M. Hendriksen and J. W. M. Frenken, "CO Oxidation on Pt(110): Scanning Tunneling Microscopy Inside a High-Pressure Flow Reactor", Phys. Rev. Lett. **89**, 046101 (2002).